PREIONIZATION AND GAIN STUDIES IN FLUORINE BASED EXCIMER LASER GAS DISCHARGES

Anton Vladimirovich Azarov

This research was financially supported by the Dutch Technology Foundation STW (STW-project TTF5696)

The work was carried out at the Laser Physics and Non-Linear Optics Group at the Faculty of Science and Technology, University of Twente,P.O. Box 217, 7500 AE, Enschede, the Netherlands

ISBN 978-90-9023533-2

Printed by PrintPatners Ipskamp, Enschede, the Netherlands

PREIONIZATION AND GAIN STUDIES IN FLUORINE BASED EXCIMER LASER GAS DISCHARGES

DISSERTATION

to obtain
the degree of doctor at the University of Twente,
on the authority of the rector magnificus,
prof.dr. W.H.M. Zijm,
on account of the decision of the graduation committee,
to be publicly defended
on Thursday the 25th of September at 13.15

by

Anton Vladimirovich Azarov

born on the 13th of July 1978

in Bereznik, Russia

This dissertation is approved by:
Prof. Dr. K. J. Boller, the promoter
Dr. P. J. M. Peters, the assistant promoter

Abstract

Fluorine-based excimer gas lasers are powerful sources of coherent radiation in the UV and VUV part of the electro-magnetic spectrum. Due to their short wavelengths and high output power they are widely employed in high resolution material processing like micromachining and in lithography. In this field pattern sizes several times shorter than the used wavelength can be achieved using an immersion technique. However due to the short duration of the laser pulse (typically of few tens of ns for commercially available fluorine-based excimer lasers), the laser pulse makes only a few round-trips inside the laser resonator cavity. As the result, the optical quality of the laser beam of such an excimer laser is poor, leading to non optimal focusing conditions.

The purpose of this work was to investigate different methods and techniques to produce excimer lasers, based on fluorine containing gas mixtures, emitting optical pulse lengths of 100 ns or longer. In order to achieve this goal we have studied different gas discharge excitation techniques in a small scale discharge chamber (0.5 – 4 cm discharge gap, 5 cm electrodes diameter) at gas pressures varying from 2 to 5 bar. We have thoroughly investigated a pre - main pulse gas discharge pumping scheme with X-ray preionization and a single pulse excitation scheme with X-ray preionization.

As preionization source we investigated two homemade X-ray sources. We have developed a high voltage open barrier discharge device producing a fast electron beam directly in the gas. It was shown that it was possible to generate soft X-ray radiation (10 – 100 keV) directly in gases by means of this beam. With this and with an earlier developed traditional X-ray source the produced electron densities in different gases and gas mixtures have been measured. During our experiments we discovered that, apart from the well known direct electron generation in the gas, a substantial part of the measured preionization electrons were generated indirectly by the X-rays via the photo-electric effect at the electrode

With the single pulse excitation scheme we succesfully ignited a homogeneous discharge and were able to sustain it as a stable, homogeneous pulsed gas discharge in gas mixtures typically containing 5 % of Ar and 0.1 % of F_2 at a total gas pressure of 2 bar and an electrode distance of 1 cm. In this laser gas mixture the typical achieved peak power deposition density was 1 – 2 MW cm^{-3} with a pulse duration (FWHM) of ~ 100 ns. Under these conditions the observed spontaneous emission intensity was 119 kW cm^{-3} at the ArF^* excimer wavelenth (193 nm). The width of this emission signal was ~ 60 ns (FWHM). With a probe laser (λ = 193 nm) the amplification of the probe signal in the excited laser medium was measured. Under the same conditions a net gain was measured of ~ 34±20 % cm^{-1} with a FWHM of ~ 60 ns.

The combination of such high gain and the reasonably long optical pulse duration makes our gas discharge excitation system a promising device for the development of small scale fluorine-based excimer gas lasers. The short resonator length of several cm will result in a higher number of the intra cavity round-trips and thus to a better beam quality compared to the usual excimer lasers.

List of publications

Publications in refereed journals:

- Azarov A V, Peters P J M and Boller K-J, *Soft X-ray generation in gases by means of a pulsed electron beam produced in a high voltage barrier discharge*, Plasma Sources Sci. Technol., **16**, 110 (2007)
- Azarov A V, Peters P J M and Boller K-J, *Photo-electric effects in X-ray preionization for excimer laser gases*, J. Appl. Phys., **103**, 043301 (2008)
- Azarov A V, Peters P J M and Boller K-J, *Laser gain measurements at 193 nm in a small discharge cell containing ArF excimer laser gas mixtures*, Appl. Phys. B: Lasers and Optics, **90**, 455 (2008)
- Azarov A V, Mitko S V, Ochkin V N, Savinov S. Yu., *Non-self-sustained slab discharge as an efficient method for exciting an active laser medium*, Quantum Electronics, **33**, 419 (2003)
- Azarov A V, Mitko S V, Ochkin V N, *Xe laser pumped by fast electrons generated in a barrier discharge*, Quantum Electronics **32**, 675 (2002)

Contributions to international conferences:

- Azarov A V, Peters P J M and Boller K-J, *Spontaneous emission at 193 nm and gain measurements in F_2 containing excimer laser gas mixtures*, GCL/HPL 2006, Gmunden, Austria (2006), SPIE Proc. **6346**, 63460O-1 (2006)
- Azarov A V, Mitko S V, Ochkin V N, *An open barrier discharge as Xe laser pumping source*, Proc. IQEC / LAT 2002, Moscow, Russia (2002). Published in: Azarov A V, Mitko S V, Ochkin V N, *Open barrier discharge as Xe laser pumping source*, Proc. SPIE **5137**, 227 (2003)
- Azarov A V, Kuznetsov A A, Mitko S V, Ochkin V N, *High repetition rate non-self-sustained discharges at elevated gas pressures*, Proc. ESCAMPIG 16 / ICRP 5, Grenoble, France, vol. 1, p. 77 (2002)
- Azarov A V, Mitko S V, Ochkin V N, *An open barrier discharge as a source of kiloelectronvolt electron beam in moderate pressure gases*, Proc. ESCAMPIG 16 / ICRP 5, Grenoble, France, vol. 2, p. 305 (2002)

Other publications

- Azarov A V, Ochkin V N, *Effect of the field dependence of the coefficient of ion-electron emission on the characteristics of a normal cathode discharge*, J. Russian Laser Research, **25**, 138 (2004)
- Starostin S A, Peters P J M, Kindel E, Azarov A V, Mitko S V, Boller K-J, *Numerical study of the normal current density behaviour in a narrow-gap glow discharge*, e-Print archive of the Cornell University, New York, USA (2004) http://arxiv.org/abs/physics/0409047v1

- Azarov A V, Mitko S V, Ochkin V N, *The normal current density of a medium - pressure glow discharge in short gaps*, Bulletin of the Lebedev Physical Institute, **4**, 11 (2002)

Contributions to other conferences:

- Azarov A V, Peters P J M, Boller K-J, *Influence of the secondary electron emission coefficient on the value of normal current density in small gap glow discharges*, Proc. 16th NNV/CPS – symposium, Lunteren, the Netherlands, p.20 (2004)
- Azarov A V, Peters P J M, Boller K-J, *Pulsed longitudinal self-sustained and non-self-sustained discharges with pre-ionization by transversal barrier discharge*, Proc. of the 16th NNV/CPS – symposium, Lunteren, the Netherlands, p.13 (2004)

Contents

Introduction

Purpose of this work

In this thesis the results of our investigations within the framework of the project "Next generation of VUV fluorine based excimer lasers" supported by the Netherlands Technology Foundation (STW) are reported. The aim of the project was the development of long optical pulse (> 100 ns) gas discharge pumped excimer lasers operated in fluorine based laser gas mixtures. Excimer lasers like KrF^* (248 nm), ArF^* (193 nm) and F_2^* (157 nm) are thus the objects to study within the project.

At present KrF^* and ArF^* lasers are used in the mass production of integrated circuits in the semi-conductor industry. With the help of immersion techniques feature sizes of about 40 nm are obtained using the ArF^* excimer laser [1]. Despite the progress in the development of extreme ultraviolet (EUV) lithography at 13 nm [2, 3], EUV sources are inefficient and still generate radiation at low power which leads to long exposure times and low production speeds. Therefore excimer lasers are and will be widely employed in lithographic applications.

The F_2^* laser operates at a shorter wavelength than the KrF^* and ArF^* laser and provides a higher photon energy (~ 7.9 eV). This makes, for instance, micromachining possible of high bandgap materials like diamond (bandgap of 5.4 eV). Due to the strong absorption at this short wavelength a high surface quality and a low ablation threshold are reported for the processing of glass, fused silica and polymers like PET and PTFE [4 – 6]. The low ablation threshold promotes the use of the laser in thin film deposition [7 – 9].

Commercially available fluorine based excimer lasers deliver radiation in pulses with a typical duration of few tens of ns. Due to short duration of the optical pulse only a few of round-trips inside the laser cavity are possible resulting in a poor beam quality. With a longer optical pulse duration a better beam quality and therefore a better focusability of the laser beam is obtained.

In order to produce an optical laser pulse with a duration of ~ 100 ns or longer it is necessary to provide a stable, homogeneous electrical discharge in a multi-atmospheric laser gas mixture and with a high enough power deposition. Usually after some time discharge instabilities destroy the uniformity of the discharge and lead to shortening of the laser pulse. This is a typical problem for any high-pressure gas discharge although in halogen containing mixtures it is more severe due to the strong electron attachment of the electro negative halogen F_2 [10, 11]. The results of this work have thus a fundamental value because they are applicable to all rare gas halogen excimer lasers, especially those based on fluorine containing laser gas mixtures.

Some typical excimer laser gas mixtures are: He : F_2 and Ne : He : F_2 for F_2^* lasers and He : Ar : F_2 and Ne : Ar : He : F_2 for ArF^* lasers. It should be noted that the emitted 157 nm radiation from the F_2^* laser is in the vacuum ultraviolet region (VUV). This wavelength experiences a strong absorption in most solid optical materials and also in air, where it is absorbed mostly by O_2. As optically transparent materials at 157 nm are CaF_2 and MgF_2 available. The ArF^* excimer radiation at 193 nm does not experience such a strong absorption in air and there are more optical materials transparent at this wavelength. Therefore the ArF^* laser gas mixture was chosen as a test medium for our spontaneous emission and small signal laser

gain measurements in order to prove the capability of the developed discharge excitation scheme and to provide the optimized conditions for pumping long pulse excimer lasers.

Historical overview of the development of excimer lasers

The history of the laser starts in 1917 when Albert Einstein introduced the concept of stimulated emission [12]. However, it lasted until 1953 before Gordon, Zeiger and Townes realized the first amplifier device that used the effect of stimulated emission of radiation: an NH_3 microwave amplifier at a frequency of 24 MHz [13]. Their invention was called a *maser*, which is the acronym of: Microwave Amplification by Stimulated Emission of Radiation. Basov and Prochorov developed their maser independently at the same time [14].

In 1958 Schawlow and Townes [15] and Prochorov [16] independently proposed the use of a "leaking", so called open-type resonator. Using this approach the first *laser* (Light Amplification by Stimulated Emission of Radiation) was built by Maiman in 1960 [17]. It was the first solid state laser and consisted of a ruby rod optically pumped by a flash lamp. This ruby laser was oscillating at a wavelength of 694 nm.

The first gas laser was the He : Ne laser at a wavelength of 1.15 μm [18], it also was the first gas discharge laser. The well-known visible red line of the He : Ne laser, $\lambda = 632.8$ nm, was found one year later [19].

A large variety of different lasers has been developed since then: from solid state and gas lasers to pulsed and CW lasers spanning a large emission spectrum from far infra-red to VUV radiation. The pulse duration of modern lasers varies from fs to CW operation with pulse energies ranging from nJ to kJ. Consequently the peak power in the pulsed mode and average or CW mode varies over a wide region. For example, from μW and mW CW power for everyday and everywhere used diode lasers to hundreds of kW (CW or averaged power) for industrial CO_2 lasers. Recently peak powers in the TW region are made available on a laboratory scale with Ti:Sapphire lasers. In general lasers are classified on the basis of the employed lasing material: there are solid state (like ruby, Nd : YAG, Ti sapphire etc.), semi-conductor, dye, gas (like CO_2, He : Ne and others, including excimer lasers) and lasers based on the motion of free-electrons (free electron lasers, FEL).

Depending on their wavelength, pulse duration, output power and energy they are used in a lot of different applications like in CD / DVD / HD-DVD / "blue-ray" players and laser pointers, in tissue treatment in the medical applications (like surgery or eye correction, etc.), for lithography in the semi-conductor industry, for processing applications like material drilling, melting, welding and surface treatment in automobile, airplane, and building industry. Last but not least, lasers are very powerful instruments in science since all kind of nonlinear optical effects can be produced only by these powerful lasers.

The broad-band emission of *excimer* molecules was already known around 1930 when the UV emission of He_2^* was described [20]. The word "excimer" is a contraction of the words "excited dimer", a class of molecules which exists only a few ns in an excited state. Much later, other rare gas molecules like Ar_2^*, Kr_2^* and Xe_2^* were reported [21]. The first excimer laser was reported by Basov et al. in 1970 [22]. It used the stimulated emission from Xe_2^* molecules obtained by electron-beam excitation of cryogenically cooled xenon. Later in 1972 a high-pressure xenon gas was excited by a beam of electrons [23] and produced stimulated emission of Xe_2^* in the VUV at 172 nm.

Laser action in rare gas halogen mixtures excited by an electron beam were reported for the first time in 1975 for $XeBr^*$ and XeF^* [24, 25]. Because of technical limitations of e-beam pumping techniques and due to the large experience with gas discharge techniques for CO_2

lasers, almost at the same time the gas discharge pumping technique was applied for excimer lasers. For example, in 1976 XeF^*, KrF^* and ArF^* lasers pumped by an electrical, ultraviolet preionized, discharge in the laser gas mixture were reported [26]. Strictly speaking, rare gas halogen lasers are not excimer but *exciplex* (excited complex) lasers. However, the name exciplex lasers has never been accepted, so the whole class of rare gas and rare gas halogen lasers are commonly called excimer lasers.

In 1977 Rice et al. discovered the F_2^* laser at $\lambda = 157$ nm [27]. Halogen lasers like the F_2^* laser are, strictly speaking not excimer lasers as the halogen molecules have a stable ground state. For example, the laser transition in molecular fluorine takes place between an excited D' upper state which is ionic in character (i.e $F^+ - F^-$ strong binding) and an excited A' lower state which is weakly covalently bound. However, the formation chemistry of the excited upper state resembles that of the rare gas halogen excimers. Halogen lasers are operated, like the rare gas halogen excimer lasers, in mixtures of rare gases as a buffer gas and a small fraction of a halogen. They emit their optical radiation also in the UV and VUV region. Therefore halogen lasers like the molecular fluorine laser are also mentioned in the class of excimer lasers.

Structure of this thesis

To achieve a long pulse, stable, homogeneous gas discharge of rare gases halogen excimer mixtures we have investigated different pumping and gas preionization schemes. Firstly, a novel soft X-ray preionization source based on the generation of so-called "run away" electrons in a high voltage open barrier discharge was designed, build and extensively tested. Although the designed device is not yet fully developed to produce the desired level of the gas volume preionization, this novel soft X-ray source proved in principle the possibility of volume preionization of a gas medium at a moderate gas pressure of ~ 100 mbar directly by fast electrons with an energy of several tens of keV and by soft X-rays of the same photon energy. Therefore in our experiments later on a well known vacuum X-ray source based on a corona plasma cathode has been used to provide sufficient gas volume preionization at multi-atmospheric pressures.

With this X-ray source a significant contribution of the photo-electric effect at the cathode to the gas preionization has been discovered. Double (pre- and main) pulse and single pulse discharge excitation techniques have been investigated. A stabilizing role in the discharge characteristics due to the self-inductance of the laser chamber and connection cables has been found. With the vacuum X-ray source and a single pulse excitation scheme the power deposition density was found to be high enough to create and maintain a stable, homogeneous gas discharge with a pulse duration of ~ 100 ns in rare gas halogen mixtures at gas pressures of several bar. Spontaneous emission and small signal gain measurements in ArF^* excimer laser gas mixtures have been performed with this system.

In chapter 1 the theoretical backgrounds of lasers and gas discharge physics are presented. Furthermore some basic physics of the interaction of ionizing radiation with matter and a few definitions of non-metric units used in this thesis that are important for the understanding of this work are described,.

Chapter 2 is devoted to a novel soft X-ray source based on a high voltage pulsed barrier discharge. Apart from the design and properties of the developed X-ray source, the employed method of experimental data processing with low signal to noise ratio is described. The same signal processing method is used with small modifications in the experiments described in the following chapters. The main results, discussed within chapter 2 are published in [28].

A vacuum X-ray source based on a corona plasma cathode is described in chapter 3. It is used as the preionization source for creating homogeneous discharges in excimer laser gas

mixtures as investigated in chapters 4 and 5. The absolute values of the delivered doses and the distribution of the dose along the output window of the X-ray source are measured and presented. A high divergence of the generated X-ray beam is found in the experiments and is confirmed by numerical modeling. Also the preionization electron densities created by the X-ray pulse from this source in the discharge chamber filled with different gases and gas mixtures at different gas pressures and inter-electrode distances are measured. It was found that the photo-electric effect at the cathode due to absorption of X-rays by the cathode material contributes significantly to the preionization electron density. The main results, discussed within chapter 3 are published in [29].

Parametrical studies of X-ray preionized gas discharges excited by single pulse and double (pre- and main) pulse schemes in different gases at a pressure of 2 bar are described in chapter 4. It is shown that pulse forming circuits in both cases behave like LC networks although no additional inductors were included in the electrical schemes. So the current of a self-sustained glow discharge is limited by the circuit inductance, while the discharge voltage is determined by the steady-state voltage of the glow discharge. The double pulse excitation scheme is found to be redundant in our experiments because the single pulse excitation scheme is capable to provide a high enough power deposition density to create and to maintain homogeneous, stable glow discharges with pulse durations of ~ 100 ns.

In chapter 5 spontaneous emission and small signal gain measurements in ArF^* excimer laser gas mixtures at a wavelength of 193 nm are presented. The peak gain, as well as the temporal and spatial gain profiles, is reported here. A numerical model of the spatial gain distribution is developed and also described in chapter 5. The main results, discussed within chapter 5 are published in [30].

References:

[1] Y. Li, F. Zhang, Jpn, J, Appl. Phys. **46**, 2936 (2007)
[2] E.J. Takahashi, Y. Nabekawa and K. Midorikawa, Appl. Phys. Lett., **84**, 4 (2004)
[3] K.-Ch. Hou, S. George, A.G. Mordovanakis, K. Takenoshita, J. Nees, B. Lafontaine, M. Richardson, A. Galvanauskas, Optics Express **16**, 965 (2008)
[4] P.R. Herman, J.D. Moore and K. Beckley, in: *Digest of CLEO'95* (Optical Society of America, Washington DC, 1995), paper CThD1, p. 251
[5] Lamba Science no.**3**, Nov. 1990, published by: Lambda Physik, Göttingen, Germany
[6] P.E. Dyer, G.A. Oldershaw and D. Schudel, J. Phys. D **26**, 323 (1992)
[7] S. Inoue, T. Fujii, Y. Ueno and F. Kannari, IEEE Selected topics in Quant. Electr., vol.**1**, 908 (1995)
[8] Lambda Highlights no.**51**, March 1997, published by: Lambda Physik, Göttingen, Germany
[9] Y. Toyoshima, K. Kumata, U. Itoh and A. Matsuda, Appl. Phys. Lett., **51**, 1925 (1987)
[10] W.L. Nighan, Phys. Rev. A, **15**, 1701 (1977)
[11] W.L. Nighan, Phys. Rev. A, **16**, 1209 (1977)
[12] A. Einstein, Physik. Zeitshr., **18**, 121 (1917) (In German)
[13] J.P. Gordon, H.J. Zeiger and C.H. Townes, Phys. Rev., **95**, 282 (1954)
[14] N.G. Basov and A.M. Prochorov, Zh. Experim. i Teor. Fiz. (Sov. JETP) **27**, 431 (1954) (in Russian)
[15] A.L. Schawlow and C.H. Townes, Phys. Rev., **112**, 1940 (1958)
[16] A.M. Prochorov, Zh. Experim. i Teor. Fiz. (Sov. JETP) **34**, 1658 (1954) (in Russian)
[17] T.H. Maiman, Nature **187**, 493 (1960)
[18] A. Javan jr., W.R. Bennet and D.R. Herriott, Phys. Rev. Lett., **6**, 106 (1961).
[19] A.D. White and J.D. Rigden, Proc. IRE **50**, 1697 (1962)
[20] J.J. Hopfield, Phys. Rev., **35**, 1133 (1930)
[21] Y. Tanaka, J. Opt. Soc. Am., **45**, 710 (1955)
[22] N.G. Basov, V.A. Danilychev, Y.M. Popov and D.D. Khodkevich, JETP Lett., **12**, 329 (1970)
[23] H.A. Koehler, L.J. Ferderber, D.L. Redhead and P.J. Ebert, Appl. Phys. Lett., **21**, 198 (1972)
[24] S.K. Searles and G.A. Hart, Appl. Phys. Lett., **27**, 243 (1975)
[25] C.A. Brau and J.J. Ewing, Appl. Phys. Lett., **27**, 435 (1975)
[26] R. Burnham and N. Djeu, Appl. Phys. Lett., **29**, 707 (1976)
[27] J.K. Rice, A.K. Hays and J.R. Woodworth, Appl. Phys. Lett., **31**, 31 (1977)
[28] A.V. Azarov, P.J.M. Peters and K.-J. Boller, Plasma Sources Sci. Technol. **16**, 110 (2007)
[29] A.V. Azarov, P.J.M. Peters and K.-J. Boller, J. Appl. Phys. **103**, 043301 (2008)
[30] A.V. Azarov, P.J.M. Peters and K.-J. Boller, Appl. Phys. B: Lasers and Optics **90**, 455 (2008)

Chapter 1

Laser and gas discharge physics and interaction of ionizing radiation with matter

Theoretical aspects crucial for the physics behind the experiments described in this thesis are given in this chapter. The threshold pumping density for the laser, basics of the gas discharge physics, influence of the gas volume preionization on the discharge stability and uniformity, required electron preionization density and interaction of the X-ray radiation with matter are considered.

1.1 Purpose of this chapter

The physics of X-ray preionized gas discharge pumped lasers spans a broad area. It includes aspects of laser and gas discharge physics as well as the origin of X-ray production and the interaction of X-rays with matter. In this chapter some crucial theoretical physical aspects of this branch of physics are considered in order to derive some key laser parameters like the threshold laser pumping density and the electron preionization density. These are required for the development of an excimer laser based on a fluorine containing laser gas mixture. Further on some other physical phenomena that are not well known as, for instance, the electron "run away" effect are described in this chapter. Other theoretical aspects specific for each chapter are considered in the corresponding chapters.

1.2 Laser pumping

In order to make a laser lasing energy has to be fed into the laser medium. This can be done by a pumping mechanism. Examples of such a pumping mechanism are irradiating the medium by photons (called optical pumping), by high energetic electrons (called e-beam pumping) or alternatively by creating an electrical discharge in the gaseous laser medium. A detailed analysis of the pumping mechanism for a gaseous laser medium will be given in order to calculate the pumping requirements. It is expected that a certain level of pumping power is needed (called the threshold laser pumping density). The threshold laser pumping density is defined as the minimum power density deposited into a medium that is required to achieve lasing conditions or amplification of light in the medium. In the experiments described in this thesis the lasing medium is gas or mixture of different gases and the pumping power is deposited in the medium by an electrical discharge in the gas. The threshold laser pumping density is a key parameter in the development of gas discharge lasers. In order to estimate the threshold laser pumping density we used a model given in reference 1.

Consider a laser medium as a collection of identical particles, each having two different energy levels E_1 (lower state) and E_2 (upper state), $E_2 > E_1$, with populations N_1 and N_2. Other

energy levels exist in the medium but are not relevant here. The number of particles in the upper and the lower energy level depend on different processes:

- *Absorption of photons*: depending on the radiation field energy density ρ at $\nu = \nu_{12}$ and on the the population of the lower energy level; coefficient B_{12}.
- *Spontaneous emission*: only depending on the population of the upper energy level; coefficient A_{21}.
- *Induced* or *stimulated emission*: depending on the radiation field and the population of the upper level: coefficient B_{21}.
- *Direct population* of the upper level by other sources rather than light absorption at $\nu = \nu_{12}$, for instance, excitation by electron impact. Direct population of the upper level is described by the pumping rate P_2.
- *Non-radiative decay* of the upper level to the lower level, with coefficient D_2, which only depends of the population of the upper level.
- *Population of the lower state* with the rate P_1. It includes all possible channels except radiative and non-radiative transitions from the upper level E_2 to the lower level E_1.
- *Depopulation of the lower state* with coefficient D_1, which includes all possible channels except absorption of photons at $\nu = \nu_{12}$. It depends on the lower level population.

As a consequence the rate equation for the upper level E_2 can be written as:

$$\frac{dN_2}{dt} = -A_{21}N_2 + B_{12}\rho(\nu_{12})N_1 - B_{21}\rho(\nu_{12})N_2 + \\ + P_2 - D_2 N_2 \tag{1.1}$$

and for the lower level:

$$\frac{dN_1}{dt} = A_{21}N_2 - B_{12}\rho(\nu_{12})N_1 + B_{21}\rho(\nu_{12})N_2 + \\ + P_1 - D_1 N_1 \tag{1.2}$$

Equations 1.1 and 1.2 describe the dynamics of the population of the bound-bound transition $E_2 \leftrightarrow E_1$. In excimer lasers the lower state is repulsive and instead of Eqs. 1.1 and 1.2 only the rate equation of the upper state is important. Taking into account that the laser transition is bound-free the rate equation can be simplified to:

$$\frac{dN_2}{dt} = -A_{21}N_2 - B_{21}\rho(\nu_{12})N_2 + P_2 - D_2 N_2 \tag{1.3}$$

In the stimulated emission process, an incident photon with the resonant frequency ν_{12} forces a particle to experience a transition to the lower level emitting a photon with the same frequency, phase, polarization and propagation direction as the incident photon. Spontaneous emitted photons, on contrary, have a random phase, direction and polarization. Even the photon energy may vary in a relatively large range defined by spectral broadening due to different processes like the finite spontaneous emission lifetime, the Doppler broadening due to the thermal motion of the particles and collisional broadening. Thus, in small laser signal amplification experiments the stimulated emission dominates over the spontaneous emission ($A_{21} << B_{21}\,\rho(\upsilon_{12})$, for the given probe beam photons energy, polarization, phase and propagation direction). Therefore, the net loss or gain of photons per unit volume can be written as:

$$\frac{dN_{ph}}{dt} = N_2\,\rho(\nu_{12})\,B_{21} - N_1\,\rho(\nu_{12})\,B_{12} - \\ -k_a\,\rho(\nu_{12}) \tag{1.4}$$

where k_a is the photon loss rate due to absorption of photons in all other channels except for $E_1 \rightarrow E_2$ transition.

The change in irradiance of a monochromatic collimated beam with a low amplitude passing through a homogeneous medium as a function of distance is given by (Lambert-Beer) law:

$$\frac{dI(x)}{dx} = (g_0 - \alpha_0)\,I(x) \tag{1.5}$$

where:

$$\alpha_0 = \frac{h\nu}{c} k_a \tag{1.6}$$

is the small signal absorption coefficient, and:

$$g_0 = \left(N_2 - \frac{g_2}{g_1} N_1 \right) \frac{h\nu\, B_{21}}{c} = \left(N_2 - \frac{g_2}{g_1} N_1 \right) \sigma_{se} \tag{1.7}$$

is the small signal gain coefficient, taking into account thermal equilibrium, Boltzmann's statistic and statistic weights g_2 and g_1 of the upper and the lower levels. σ_{se} is the cross-section of the stimulated emission process.

In order to achieve light amplification the gain coefficient g_0 should exceed the absorption coefficient α_0 in Eq. 1.5. However, during one round-trip in the cavity the laser radiation experiences reflection at two mirrors with reflection coefficients R_1 and R_2 respectively. So the irradiance changes in one round trip inside the cavity from I_0 to I as:

$$I = I_0 R_1 R_2 \exp\left(2(g_0 - \alpha_0) L\right) \tag{1.8}$$

where L is the cavity length. Therefore, to achieve light amplification in one round-trip the gain coefficient should be higher than the threshold small gain value:

$$g_0 \geq g_{th} = \alpha_0 + \frac{1}{2L} \ln\left(\frac{1}{R_1 R_2}\right) \tag{1.9}$$

The threshold small signal gain includes photon losses due to absorption or scattering of photons in all other channels except for $E_1 \rightarrow E_2$ transition (impurities, etc.) and the optical cavity coupling factor.

The threshold laser pumping density is [1]:

$$P_{th} > \frac{8\pi h c^2 g_{th} \Delta\lambda}{\lambda^5} \tag{1.10}$$

According to Eq. 1.10 the threshold pump power density increases very rapidly with decreasing wavelength. For example, at $\Delta\lambda / \lambda = 10^{-2}$ and g_{th} = 5 % cm^{-1} a threshold pumping power density of ~ 12 kW cm^{-3} is required at $\lambda \sim 200$ nm, or ~ 36 kW cm^{-3} at $\lambda \sim 150$ nm or ~ 180 kW cm^{-3} at $\lambda \sim 100$ nm.

In these calculations it was assumed that all energy pumped into the medium is spent for the excitation of the upper level. Usually the excitation efficiency is much lower than 100% especially in the gas discharge pumped lasers. Therefore, gas discharge excited excimer lasers mixtures have to be pumped at MW's cm^{-3} levels in order to achieve lasing.

1.3 Gas discharge

The estimated pumping density of excimer lasers is at the MW cm^{-3} level. For a long pulse excimer laser it is therefore required to ignite and sustain an electrical discharge in the laser gas mixture at this high power deposition density level for a period of time of 100 ns or longer. The laser active medium should be excited in the entire volume of the optical resonator cavity or, at least, in a significant part of the cavity volume. The length of the excited medium and the volume along the optical path has to produce amplified radiation at a level high enough to compensate the losses in the cavity at the given pumping power density. The cross-section of the excited

medium in the transversal direction together with the cavity configuration determines the output laser beam aperture.

Electrical glow discharges in gases can be ignited and maintained in discharge cells, for example, with a long inter-electrode distance or in other words, long *gap* cells or with large area electrodes [2]. The first case is typical for low pressure gas discharge lasers as, for instance, the He-Ne laser. In these kind of lasers with longitudinal pumping the optical axis of the laser cavity is parallel to the discharge gap. In the second case, with transversal pumping typical for high pressure gas lasers, like excimer lasers, the optical axis is perpendicular to the discharge gap. The typical power deposition density into the glow discharge increases with the gas pressure due to increasing current density and voltage [2]. The probability of three particle collisions, which are responsible for the formation of the excimer molecules, increases also with the gas pressure. Therefore, creating a glow discharge in high pressure gas mixtures is very well suited for pumping of excimer lasers. A drawback of this excitation mode is that sooner or later instabilities occur in such type of discharge, developing easier at higher gas pressure and power deposition density [2].

The stability of an electrical discharge in gases is strongly dependent on the balance of charge carriers, electrons and ions, and their production and loss mechanisms. Any discharge instability can be attributed to a decease of the discharge or its transformation into another form, for example, into a spark or arc discharge due to any disturbance of the production and loss balance. In order to understand the origin of high pressure glow gas discharge instabilities and to learn how to avoid the development of instabilities and limitations, which development of discharge instabilities imply for gas discharge parameters like power deposition, discharge voltage and current, we need to study the different types of gas discharges and its important physical processes more in detail.

1.3.1 Gas discharge classification

Any gas is a dielectric in its usual state. Although due to cosmic rays and natural radioactivity some free electrons and ions exist in any gas, their concentration is very low under normal conditions. If volume filled by a gas is irradiated by a beam of photons with an energy higher than the ionization potential of the gas (usually in the UV, X-ray or gamma-ray region) or by beam of fast electrons or ions or by any other kind of ionizing radiation, free electrons (and ions) are formed in the gas medium. When subsequently an electric field is applied to the gas volume, the gas starts to conduct electrical current and the gas discharge is running. A gas discharge, in which, apart from the initiation of the discharge, an external source of ionization is necessary for the maintenance of the discharge, is called a *non-self-sustained discharge*.

Charged particles within a gas volume gain energy as they are accelerated in an applied electric field. On the other hand, they collide with other particles in the ionized gas but mostly with neutral atoms. After each collision the trajectory of the involved charged particle is changed to some angle up to 180^0 with respect to the initial trajectory. If a particle is scattered backwards, it is decelerated in the electric field. There are two types of collisions: elastic and inelastic collisions. In the first case the incident particle is only scattered to some angle but the states of the incident and the target particles are not changed, so neither excitation nor ionization takes place. Due to conservation of energy and momentum the incident particle energy is changed by $\sim 4\,\varepsilon\, m / M$, where ε is the energy of the incident particle, m is the incident particle mass and M is the target particle mass. Inelastic collisions leading to excitation or ionization of a target particle have a threshold energy ε_{th} for the incident particle. They thus occur only if the incident particle energy $\varepsilon > \varepsilon_{th}$. In these collisions the incident particle energy is decreased by ε_1, where $\varepsilon > \varepsilon_1 \geq$

ε_{th}. Therefore, in gases charged particles are not accelerated continuously like under vacuum conditions. Instead, the behavior of each kind of charged particles is described by their energy and momentum distribution functions. The entire ensemble for each kind of particles is characterized by the average energy and the average velocity (or momentum) of the ensemble as if the entire ensemble slowly drifts in the applied field with a speed called the *drift speed*. The drift speed is the average velocity of all particles of this type and the *average energy* corresponds to the width of the distribution functions, in other words to the *temperature* of the ensemble, for example, the electron and ion temperature, which are different from the gas temperature.

Electrons have the lowest mass of all charged particles present in a discharge. Therefore, their drift speed and average energy are the highest. The largest part of all kinetic processes in a discharge is due to electron collisions with neutrals. The energy and drift speed of the electrons increase with the applied electric field. If the electron energy is high enough, the electrons are able to ionize the gas and the concentration of charged particles increases. The discharge conductivity increases also. On the other hand, there are electron loss channels in gases as well. For instance, electrons diffuse out of the discharge volume, they recombine with positive ions and attach to electro-negative atoms and molecules. The rates for collisional ionization and electron losses depend on many different parameters. For example, the diffusion rate is proportional to the particle concentration gradient; the ionization and attachment rates are proportional to their frequencies, which are field dependent, and to the concentrations of electrons and neutrals. The recombination rate is proportional to the electron and the positive ion concentration, thus it is roughly proportional to the electron concentration squared. If the collisional ionization rate balances the losses rate, an external ionizer is no longer necessary. A discharge, where the collisional ionization in the gas volume due to applied field is high enough to maintain the discharge, is called a *self-sustained discharge*.

A self-sustained discharge can be ignited even in absence of the external ionizer if the applied field is high enough. As mentioned above, due to the natural background ionizing radiation a small density of free charged particles always exists in gases. The discharge starts from this seed charged particle concentration.

A self-sustained discharge, as well as a non-self-sustained discharge, is usually ignited between a pair of metallic electrodes, to which a voltage difference is applied. One of the electrodes is at positive potential, called *anode*, the other one is at negative potential and is called the *cathode*. Usually one of the electrodes is grounded, because it is only the potential difference between the anode and cathode that counts. In some discharges however, for example, in a corona discharge only one electrode is explicitly present. This electrode is set at a high positive or negative potential, In this case the environment surrounding the discharge area serves as the virtual (grounded) second electrode.

Electrons and negative ions in a gas discharge usually propagate from the cathode towards the anode and positive ions in the opposite direction, except for special case like a shock wave and streamers. The electrical current in the discharge flows from the anode to the cathode. The electron density increases along the discharge axis from the cathode to the anode due to collisional ionization but electrons are removed from the discharge volume at the anode. Apart from the ionization in the gas volume a source of electrons at the cathode is required for maintaining a self-sustained discharge.

In a glow discharge electrons are produced at the cathode mainly due to collisional emission. When an ion hits the cathode, it recombines with one of free electrons at the cathode surface and one additional electron is released from the cathode into the gas volume with a small probability. For slow ions this probability for electron emission is independent on the ion energy but is determined by the cathode work function and the ionization potential of the atom, from

which the incident positive ion is formed. This is the so called *potential emission*. The potential emission is believed to be the dominant emission process in a glow discharge [2]. For high energy ions and fast neutral atoms, which are formed due to charge transfer collisions in the gas, the electron emission probability depends on the incident particle energy. This process is called the *kinetic emission*. In some cases *photo-emission* of electrons at the cathode is also an important mechanism, however it is never the dominant emission process.

If the power deposition into the gas near the cathode is high, the cathode heating can become so significant that *thermal emission* at the cathode becomes the dominant process. This situation is observed in arc discharges. If the electric field strength at the electrode is very high and comparable to the nuclear field in atoms *field emission* starts at the cathode or in the gas surrounding the anode. For instance, corona discharges are ignited by the field emission. If an electrode has a sharp edge, for example, a needle tip, the electric field strength at the tip is increased very significantly compared to a plane-to-plane electrode configuration. This field enhancement also facilitates field emission very much. Under vacuum conditions, or at very low gas pressure, field emission is responsible for the electron production at or near the corona electrode, while at higher, for example, atmospheric pressure the corona discharge is maintained by potential emission.

The nature of the volumetric ionization of a gas also contributes to the different discharge structures. For a homogeneous glow discharge, especially at low gas pressures, the Townsend avalanche mechanism is a typical ionization form, while in spark and corona discharges a streamer-based ionization is observed.

1.3.2 Basics of the gas discharge physics

In general, all charged particles in a discharge are distributed in the phase space, that is in velocity – position coordinates, according to their distribution functions *f(t,* $\mathbf{x}$*,* $\mathbf{v}$*)*, where the space position and the velocity are given in bold letters to show their vector nature. The kinetic equation for such a distribution function was introduced by Boltzmann (see ref. 2 and refs. within):

$$\frac{\partial f(t,\vec{x},\vec{v})}{\partial t}+\vec{v}\frac{\partial f(t,\vec{x},\vec{v})}{\partial \vec{x}}+\frac{\vec{F}(\vec{x})}{m}\frac{\partial f(t,\vec{x},\vec{v})}{\partial \vec{v}} = P(t,\vec{x},\vec{v})-Q(t,\vec{x},\vec{v}) \quad , \tag{1.11}$$

where *F* is the force applied to the particle; equal to the electric field strength multiplied by the particle charge; *m* is the particle mass; *P* and *Q* are the position in phase space and time depended production and losses function, for example, due to ionization and recombination. In the case of a glow discharge a simple one dimensional *drift approximation* model can be applied [2]. The drift approximation is based on the drift speed of the particles and their average energy, thus the particles are treated as an ensemble moving with a drift speed in the applied field without solving the kinetic equation (Eq. 1.11).

With this approximation and assuming that only electrons and positive ions of one type are present in the discharge, Eq. 1.11 is then simplified to (for electrons and ions):

$$\frac{\partial n_e}{\partial t} = S + \nu_i\, n_e - \frac{\partial}{\partial x}\left[\mu_e\, n_e\, E(x)\right] - \beta\, n_e^2$$
$$\frac{\partial n_i}{\partial t} = S + \nu_i\, n_e - \frac{\partial}{\partial x}\left[\mu_i\, n_i\, E(x)\right] - \beta\, n_e^2 \qquad (1.12)$$

where S is the electron-ion pair production rate due to an external ionizer, ν_i is the collisional ionization frequency, β is recombination rate coefficient and μ_e and μ_i are the mobilities of electrons and ions in the applied electric field respectively. The recombination rate is actually $\beta\, n_e\, n_i$, but in a stationary state the discharge plasma is charge neutral $n_e \approx n_i$. A valid assumption in many cases is that there is no external ionizer and that the recombination rate is low. Further on it is known that in a stationary situation the time derivatives in Eq. 1.12 are zero. Under these conditions the changes in electron and ion current densities along the discharge axis are given by:

$$\frac{dj_e}{dx} = -\frac{dj_i}{dx} = \frac{\nu_i}{v_e}\, j_e(x) = \alpha\, j_e(x) \qquad (1.13)$$

where α is the Townsend ionization coefficient, which is the ratio of ionization frequency ν_i and electron drift velocity v_e. It is a function of the local electric field strength. The process governed by Eq. 1.13 is called *Townsend avalanche ionization*.

From Eq. 1.13 follows the conservation of the total current density along the discharge gap:

$$j_e(x) + j_i(x) = j(x) = const \qquad (1.14)$$

In the case of electro-negative gases attachment should be included in the rate equation 1.12 for electrons, the rate equation for negative ions should be added to Eq. 1.12, and the negative ion current density should be included in equation 1.14.

The electric field distribution along the discharge gap is determined by the applied voltage and the density of free charges:

$$\frac{dE}{dx} = \frac{e(n_i - n_e)}{\varepsilon_0} \qquad (1.15)$$

There ε_0 is the permittivity of vacuum. If the discharge plasma is charge neutral, that is $n_i \approx n_e$, like in the positive column of a glow discharge or in the entire plasma volume of a dark Townsend discharge, the field gradient is close to zero and the field is almost constant. On the other hand, in the cathode sheath of a glow discharge the ion density is much higher than the electron density. The field gradient is significant in the cathode sheath of a glow discharge and the electric field is distorted by the space charge of ions there.

Another example of field distortion by space charges is the formation of streamers or current filaments that are propagating from the cathode towards the anode [2]. In the starting phase of a streamer the charged particle density is low and ionization occurs in the Townsend avalanche regime (Eq. 1.13). The drift velocity of electrons in the applied electric field is larger than the one of positive ions, additionally electrons and positive ions move in opposite directions. As a result, a cloud of electrons moves with a much higher drift speed, forming the front of the avalanche, while the ions form the positively charged tail of the avalanche. As the electron density increases the electric field gradient also increases. At a certain moment the field distortion due to the space charge becomes so significant that a streamer is created. The electric field in the head of the streamer is so strong that the drift approximation is no longer valid. A significant number of electrons are accelerated to a high energy in this strong field due to the runaway effect. This effect will be discussed later in section 1.3.5. These fast electrons ionize the gas in front of the streamer head thereby increasing the propagation speed of the streamer and initializing new streamers. As a consequence, the streamer propagation velocity is much higher than the drift speed of electrons in the applied external electric field.

Apart from streamer formation, typically observed at high gas pressure (atmospheric and above) and, thus, high discharge voltage, the drift approximation with several additional assumptions and boundary and initial conditions qualitatively describes the properties of glow discharge very well.

1.3.3 Glow discharge

A glow discharge is one of the possible forms of a self-sustained discharge. For better understanding of its relation to other self-sustained forms of a gas discharge a schematic voltage – current characteristic of a self-sustained discharge is given in figure 1.1. The discharge cell is connected to a DC power supply with a voltage of V_0 through a load resistor R_0.

The *dark (Townsend) discharge* is described by the A – B part of the characteristic. This dark discharge burns at a voltage close to the *breakdown voltage* V_{br} of the gap determined by the breakdown law (Paschen curve). In the dark discharge the ionization rate is high enough to sustain the discharge without an external ionizer, thus it is a self-sustained discharge. On the other hand, the charge density is still low and the external applied field is not disturbed by the space charge. The electric field strength is constant along the discharge gap.

The part B – C is a transition region. The characteristic has a negative slope and the transition region is usually unstable state of a discharge, although with a very high impedance of the load resistor it is possible to observe a stable discharge in this transition region.

A glow discharge is observed in the C – D and D – E regions. The C – D region characterizes a *normal glow discharge* and the *D – E* region the *abnormal glow discharge*. In the normal glow discharge region the discharge voltage (V_n in figure 1.1) and the current density at the cathode is constant. However, the cathode area occupied by the discharge is proportional to the discharge current. This constant current density at the cathode is called the *normal cathode current density*. The normal mode of a glow discharge is observed until the discharge occupies the entire available area of the cathode. A further increase of the discharge current leads to an increase of the cathode current density and the transition into the abnormal glow discharge region.

In an abnormal glow discharge not only the discharge current is higher than in the normal glow discharge but also the cathode current density and the discharge voltage are higher. The abnormal discharge voltage increases with the discharge current. When the power deposition into the discharge reaches a critical value, a transition to an arc discharge occurs.

The E – F part in the graph characterizes the transition to the arc discharge region. This region is fundamentally unstable. The F – G region represents an arc discharge. The voltage of an arc discharge is much lower than the glow discharge voltage and the arc discharge current is much higher. Additionally, the arc discharge appears in a form of narrow channel, therefore the discharge current density increases very significantly after the transition to the arc discharge.

The actual discharge voltage V_d and current I_d are determined by the intersection of the discharge characteristic and the load line $V_d = V_0 - I_d R_0$, where V_0 is the power supply voltage and R_0 is the load resistance.

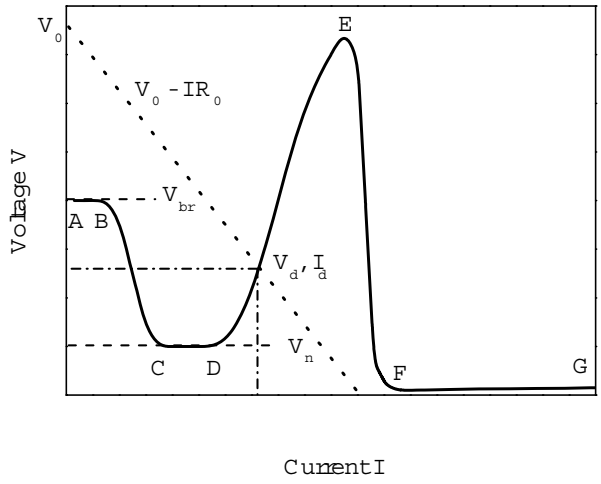

Figure 1.1. Schematic voltage – current characteristic of a self-sustained discharge (solid curve) connected to a DC power supply with a voltage of V_0 through a resistor R_0 and the load line (dotted) of the resistance.

The glow discharge in the normal and abnormal form at very low gas pressures (< 0.1 mbar) visually consists of dark and bright parts interleaved from the cathode to the anode. Subsequently the Aston dark space, the cathode glow, the cathode dark space, the negative glow, the Faraday dark space, the positive column glow and sometimes an anode dark space and anode glow are present. The width of all these parts, except for the positive column glow, is inversely proportional to the gas pressure. The positive column occupies the rest of the discharge gap. With an increase of the gas pressure the width of all these parts decreases and therefore the width of the positive column occupies increases. At atmospheric pressures the positive column occupies almost the entire gap length, and the interleaved dark and bright regions near the cathode and anode are so thin that it is impossible to resolve them.

All parts of the glow discharge near the cathode from the Aston dark space to the Faraday dark space form the cathode sheath. The cathode sheath and the positive column are the most important parts of a glow discharge. The cathode sheath is responsible for the maintenance of the

discharge as the electron current is built up in this region. The role of the positive column is to conduct the discharge current from the cathode sheath to the anode.

In the cathode sheath the ion density is much higher than the electron density $n_i >> n_e$ and it is so high that the distortion of the external electric field by the space charge is very significant. Here the electric field strength drops approximately linearly from a value of E_c at the cathode to almost zero at the edge of the cathode sheath:

$$\frac{dE}{dx} \approx \frac{E_c}{d_{cs}} \approx \frac{e\,n_i}{\varepsilon_0} \tag{1.16}$$

where d_{cs} is the thickness of the cathode sheath. The electric field strength is high and the Townsend ionization coefficient α, which increases rapidly with the electric field, is also high. Thus, the electron current is built up in this sheath with a thickness of d_{cs}.

Let's have a closer look to the electron current in the discharge. The electron emission starts at the cathode due to ion current hitting the cathode. Suppose the origin of the coordinates is at the cathode. Near the cathode $n_i >> n_e$, while in the positive column $n_i \approx n_e$, as will be discussed later. Therefore, the electron current near the cathode is less than the ion current. The ratio of the electron current to the ion current is determined by the mobilities of the electrons and ions. Because of the fact that $\mu_e >> \mu_i$ the electron current is much larger than the ion current in the positive column.

The electron current boundary condition at the cathode is:

$$j_e(0) = \gamma\, j_i(0) = \frac{\gamma}{1+\gamma}\, j_0 \tag{1.17}$$

where j_0 is the total current density (Eq. 1.14) and γ the electron emission coefficient. Taking into account that at the edge of the cathode sheath ($x = d_{cs}$) the total current is conducted mostly by electrons as in the positive column, the second boundary condition for the electron current is:

$$j_e(d) = j_0 \tag{1.18}$$

The solution of Eq. 1.13 for the electron current density with the boundary conditions given by Eqs. 1.17 and 1.18 gives a criterion for a self-sustained discharge:

$$\int_0^{d_{cs}} \alpha(E(x))\, dx = \ln\left(1 + \frac{1}{\gamma}\right) \tag{1.19}$$

This criterion (Eq. 1.19) is independent of the current density. It is valid for normal and abnormal glow discharges, and even for the dark discharge, although in the last case d is not the cathode sheath width but the discharge gap length. The voltage drop V_{cs} over the cathode sheath is:

$$V_{cs} = \int_0^{d_{cs}} E(x)\,dx \approx \frac{E_c\, d_{cs}}{2} \tag{1.20}$$

In a normal glow discharge the voltage drop $(V_{cs})_n$ over the cathode sheath does not depend on the total current and gas pressure. The voltage drop $(V_{cs})_n$ depends only on the cathode material and the gas composition [2]. The thickness of the cathode sheath is inversely proportional to the gas pressure, so the specific cathode sheath thickness is constant in a normal discharge $(p\, d_{cs})_n = const$. Therefore the electric field strength at the cathode is proportional to the gas pressure or $(E_c/p)_n = const$. The normal cathode current density j_n increases as the square of the gas pressure, so j_n/p^2 depends only on the cathode material and the gas composition [2].

In the abnormal discharge the cathode current density and the cathode voltage drop increase with the total discharge current. The relation between the cathode current density and cathode voltage drop in the normal and abnormal regime is:

$$\frac{V_{cs}}{(V_{cs})_n} = \sqrt{\left(\frac{j}{j_n}\right)} \tag{1.21}$$

where the $V_{cs}/(V_{cs})_n$ ratio is called the *degree of the discharge abnormality* [2].

The discharge voltage is higher than the cathode voltage drop because there is a voltage drop in the positive column determined by the positive column length and the electric field strength in the positive column. In the positive column neither the electron current nor the ion current increases. The positive column is usually wider than the discharge area at the cathode. If the positive column is not restricted by the discharge chamber walls the column width expands from the cathode discharge spot width near the cathode sheath to a certain value and is then constant farther away from the cathode. Therefore, the current density in the positive column is lower than the current density at the cathode but is constant along the discharge axis in the expanded region of the positive column. Of course, at the edges of the positive column diffusion of electrons is important, however close to the discharge axis it can be neglected. In this case Eq. 1.12 gives the electron density in the positive column:

$$n_e = \frac{\nu_i(E)}{\beta} \tag{1.22}$$

where ν_i is the ionization frequency that strongly depends on the electric field strength E. The recombination rate β depends on the average electron energy and thus on the electric field strength. However, this dependence is much weaker than the one of the ionization frequency and is therefore neglected here. On the other hand, the total positive column current equals the discharge current I. Thus the discharge current is:

$$I \approx S\, e\, \mu_e \frac{\nu_i(E)}{\beta} E, \tag{1.23}$$

where S is the cross-section area of the positive column.

The area S is not an independent parameter. In wall-dominated discharges, like in narrow discharge tubes, the positive column area is determined by the diameter of the tube where the discharge is ignited. So the electric field in the column is established in such a way that the column conducts the total discharge current I (Eq. 1.23). At a higher electric field strength the ionization frequency is higher and the electron density is higher (Eq. 1.22), so the positive column is able to conduct a much higher current (Eq. 1.23).

If the discharge is not restricted by the chamber walls, the width of the positive column is determined by electron diffusion. The radius of the positive column is roughly determined by the maximum distance that electrons can diffuse before they recombine and the radius of the cathode discharge spot.

Therefore, the electric field strength and the electron density in the positive column are established in such a way that the positive column conducts the same current as the cathode sheath. Although the field strength is much less than the electric field strength at the cathode, at a high gas pressure p and with a long discharge gap length d, so with the $p\,d$ value of several bar cm, the major part of the discharge voltage is contributed to the positive column voltage drop. Also under these conditions the entire visible glow of the glow discharge is due to the positive column, which occupies almost the entire discharge gap length.

1.3.4 Glow discharge instabilities

Glow discharge instabilities can be divided in two groups: instabilities near the electrodes and volumetric instabilities. From the previous section it is known that the electric field strength near the cathode in the glow discharge increases with the gas pressure. The degree of the discharge abnormality increases with the discharge voltage. If sharp edges are present on the cathode surface, like edges of the cathode or scratches in the surface, the electric field strength is further enhanced at these sharp edges. If the value of the local electric field is high enough, field emission of electrons starts. Increased electron emission leads to a higher current density and power deposition density at this point resulting in a higher local heating of the cathode. If due to field emission or any other reason the local cathode heating is increased significantly, thermal electron emission or field enhanced thermal emission starts. All these mechanisms result in an increase of the local current density. Although these considerations are based on theoretical arguments, discharge instabilities at the cathode were experimentally observed in excimer laser gas mixtures in form of “hot spots” [3, 4, 5]. The “hot spot” is a localized small area (~ 0.1 mm in diameter) of much brighter plasma, compared to the surrounding glow, in front of the cathode surface. Later in time, as the discharge evolves, filaments (thin channels of enhanced current

density) with higher brightness than the rest of the glow appear from the "hot spots". Later in time the filaments develop into microarcs [5] finally leading to short circuiting the discharge gap.

Volumetric instabilities occur in the bulk of the discharge plasma when the balance between the electron production and losses is disturbed. A good overview on discharge instabilities can be found in reference 2. Here we briefly describe the main mechanisms.

The *thermal* volumetric instability is a universal mechanism. The ionization frequency depends not only on the average electron energy and thus on the local electric field strength but on the gas temperature as well. The dependence of the ionization frequency on the gas temperature and the electric field strength, in the case then electron temperature T_e greatly exceeds the gas temperature T but $k\,T_e << I$, where I is the ionization potential, can be expressed as:

$$\nu_i = \varphi(T)\exp\left(-\frac{B\,p}{E\,k\,T}\right) \tag{1.24}$$

where $\varphi(T)$ is a (weak compared to the exponent) function of the gas temperature T; B is a specific coefficient for the given gas; p is the gas pressure; E is the electric field strength; k is the Boltzmann constant. Typically, $(B\,p) / (E\,k\,T) >> 1$. Therefore, the ionization frequency grows exponentially with an increase of the electric field strength and the gas temperature. The gas temperature increases with the power deposition density. A local increase of the gas temperature leads to a higher local ionization frequency and thus the local electron and current density increase. If heat transfer and electron diffusion cannot suppress this local increase in electron density, the instability evolves exponentially in time. At moderate power deposition densities this mechanism leads to contraction of the discharge positive column. This discharge contraction does not destroy the discharge stability and homogeneity. Instead, it provides a discharge transition from a broad diffuse form into a narrow and much denser form in which volumetric electron losses like recombination and attachment dominate over diffusion. Such a dense and constricted form of a glow discharge is observed in the experiments reported in this thesis. Spontaneous emission and small signal laser gain were measured in constricted discharges. However, higher power deposition density can cause an unbalanced contraction leading to the appearance of discharge filaments. Filaments in the discharge are clearly instabilities.

Eq. 1.24 describes the average ionization frequency of the electron ensemble in the drift approximation. In atomic gases as, for example, rare gases *electron – electron collisions* lead to thermalization and broadening of the electron energy distribution function (EEDF) into a Maxwell distribution function. Therefore, more electrons have a higher energy than the average value. The ionization cross-section strongly depends on the electron energy. The electron energy at which the ionization cross-section reaches the peak value greatly exceeds the typical average electron energy in glow discharges. The EEDF broadening due to electron – electron collisions therefore increases the average ionization frequency. This effect facilitates the development of thermal instabilities in atomic gases.

In molecular gases low energy electrons effectively excite vibrational and rotational states of the molecules. Vibrational excitation of molecules is effectively transformed into gas heating by a process called *V – T relaxation*. However, this relaxation process is rather slow compared to the excitation rate. Therefore, vibrationally excited states are accumulated and finally the

excitation energy is transferred into gas heating resulting in a significant change of the gas temperature. This mechanism enhances the thermal instabilities growth in molecular gases.

Another mechanism that can cause the development of a discharge instability in rare gases is *stepwise ionization* via metastable energy levels. For ionization from a metastable state much less energy is required than for ionization from the ground state. The lifetime of the metastable level is relatively long, therefore accumulation of atoms in metastable states is equivalent to the accumulation of easily ionized species in the gas mixture. The influence of the stepwise ionization on the discharge stability in He : F_2 and He : Kr : F_2 excimer laser gas mixtures is discussed in reference 6.

Electron – ion recombination in rare gas – halogen mixtures is a relatively slow process compared to *electron attachment*. Therefore in rare gas – halogen mixtures typical for excimer lasers the ionization is balanced by attachment rather than recombination. The steady-state conditions are determined by the following balance equation:

$$\nu_i(E) - k_a(E)\, n_a = 0 \tag{1.25}$$

where the ionization frequency ν_i stronger depends on the electric field E than the attachment rate coefficient k_a. The density of the electro-negative species is n_a and is formed mostly by halogen molecules (F_2, Cl_2 etc.). Electrons experience also attachment to halogen atoms like F, Cl etc., but their rate coefficient are several orders of magnitude less than the attachment rate coefficients of halogen molecules like F_2 etc. The decrease rate of halogen molecules due to dissociative attachment like $F_2 + e \rightarrow F^- + F$ is proportional to the electron and halogen molecule densities and to the attachment rate coefficient:

$$\frac{dn_a}{dt} \sim -k_a\, n_a\, n_e \tag{1.26}$$

If the local electron density increases, the halogen molecule density rate increases (Eq. 1.26) and the halogen molecule density n_a decreases. Thus, the electron production – losses balance (Eq. 1.25) is disturbed and ionization exceeds the attachment. The electron density increases further and the discharge instability evolves. This process is called *the local halogen depletion*. In reference 3 the influence of the local halogen depletion on the discharge stability is discussed. In addition, the halogen depletion rate increases due to other channels of halogen molecule dissociation, apart from the discussed dissociative attachment.

The mentioned instabilities evolve from a local perturbation of the gas temperature or electron concentration, which can occur even in a homogeneous discharge. If the discharge is non-homogeneous, the chance for the appearance of instabilities is greatly increased.

Another source for gas discharge instabilities is due to fast electrons with energy much higher than the average energy given by the EEDF. The interactions of these fast electrons can not be described in the drift approximation model. So, for example, the gas ionization they cause can not be described in terms of the local dependence on the electric field strength. Fast electrons locally increase the ionization rate above the average value given by the drift approximation and thus they are producing local disturbances in the spatial distribution of electrons and ions. Further

on gas discharge instabilities may evolve from these local disturbances. Fast electrons are, for example, produced by the so called "runaway" effect described in the next section.

1.3.5 The "runaway" effect

In a strong applied electric field the drift approximation model is not valid. A significant part of the electrons gains an energy much higher than the average electron energy determined by the potential difference along their path. This situation is observed in streamers. The electric field strength due to space charge in the streamer head is very high and fast electrons are produced there. These fast electrons propagate through the gas before the streamer and ionize the gas, producing new streamers and increasing the propagation velocity of the streamer. The electric field in the cathode sheath of a glow discharge is also high. Fast electrons with an energy of ~ 10^2 eV corresponding to a cathode voltage drop of ~ 10^2 V, must be taken into account in the EEDF of the cathode sheath even in a normal glow discharge [7]. In an abnormal glow discharge the specific width $p\,d$ of the cathode sheath decreases and the cathode voltage drop increases with an increase of the discharge current and voltage and therefore the electric field strength in the cathode sheath increases [2]. A beam of fast electrons generated in the cathode sheath of the abnormal glow discharge has been observed experimentally [8].

The production of fast electrons in a strong electric field occurs due to the so called *runaway effect*. A complete detailed overview on the runaway effect is given in reference 9. Here we present only the basic facts and the physical principles of the runaway effect.

The existence of fast electrons in gas discharges, especially in thunderstorm lighting, have been discussed since 1920's [10, 11]. Giovannelly proposed one of the first theories of the runaway effect in 1949 [12]. However, a detailed theory of the runaway effect appeared almost 10 years later. Dreicer derived the runaway criterion, and the required electric field strength in a fully ionized plasma in the late 50's [13]. The critical electric field strength required for the runaway effect is called the Dreicer field. A theory for weakly ionized gases was developed by Babych in early 60's [9].

When an electron moves in a gas due to the electric field, it can lose or gain energy depending on the angle between its propagation direction and the electric field strength vector. Assume that an electron moves against the field. Then the electric field accelerates the electron. On the other hand, the electron loses energy in collisions with other particles. The electron energy change $d\varepsilon$ along path dx can be written as

$$\frac{d\varepsilon}{dx} = eE - F(\varepsilon) \tag{1.27}$$

where e is the electron charge, E is the electric field strength and F is the effective "stopping" force, which describes the electron energy losses in collisions at the electron energy ε.

At low electron energies (comparable to the ionization potential of a gas I) the stopping force is usually expressed in terms of a cross-section for inelastic processes σ_k, the average energy loss ε_k in these inelastic processes and the density of collision particles N_k. Elastic collisions are also taken into account with a cross-section σ_{el} and particle density N_0. In collisions with atoms and molecules the electron is scattered at some angle. Due to conservation of momentum, the initial momentum of the electron is distributed between the electron and the target atom or molecule. Therefore, the electron velocity and kinetic energy decrease even in an

elastic collision. The average electron energy loss in an elastic collision is $4\,\varepsilon\,m\,M\,/\,(m+M)^2 \sim 4\,\varepsilon\,m\,/\,M$, where $m\,/\,M$ is the mass ratio of the electron and the target particle. In inelastic collisions a part of the electron kinetic energy is spent to excite or ionize the target atom or molecule. In an inelastic collisional ionization a secondary electron is produced usually with low kinetic energy. Thus, the average electron energy loss ε_k in an inelastic collision is at least equal or higher than the excitation energy E_{nm} of the $n \rightarrow m$ transition (in the case of excitation collision) or the ionization potential I (in the case of ionization collision). The electron energy loss depends also on the initial kinetic energy, the $m\,/\,M$ mass ratio and the average scattering angle. The cross-sections of elastic and inelastic collisions depend strongly on the initial electron kinetic energy.

As a result, the stopping force for electrons in a gas at low energy can be written as:

$$F(\varepsilon) = 4\frac{m}{M}\varepsilon\,\sigma_{el}(\varepsilon)\,N_0 + \sum_k \varepsilon_k(\varepsilon)\,\sigma_k(\varepsilon)\,N_k \tag{1.28}$$

At high electron energy ($\varepsilon >> I$) the major part of the electron energy losses is contributed to ionization. In this case the so called *continuous slow down approximation* (CSDA) is applicable. CSDA is based on the Bethe formula [14]:

$$F(\varepsilon) = \frac{4\pi n_e e^4}{\varepsilon}\left[\ln\left(\frac{\varepsilon}{I}\right) + \frac{1-\ln 2}{2}\right] \tag{1.29}$$

where n_e is the density of electrons in the medium bound to atomic nuclei with atomic number Z; $n_e = Z\,n_0$, where n_0 is the atom concentration in the medium. The term $(1 - \ln 2) / 2 \approx 0.153$ is important only at an electron energy $\varepsilon \sim I$. At higher electron energies ($\sim 10\,I$) it can be neglected. For electron energies even higher than this value the logarithmic term can also be neglected and the stopping force is given by the Thompson-Whiddington law (see ref. 15 and refs. within):

$$F(\varepsilon) \propto n_0\frac{Z}{\varepsilon} \tag{1.30}$$

The dependence of the electron stopping power (in keV cm^{-1}) on the electron energy (in eV) in N_2 at a gas pressure of 1 bar is given in figure 1.2. The experimental curve (1) is measured in the electron energy range from 10 eV to 10 keV [16]. The theoretical curve (2) is calculated by means of the ELSTAR computer code [17] (see also figure A.1 in the Appendix and references therein) in the energy range from 10 keV to 1 GeV. This computer code is based on the Bethe formula but the radiation losses (mostly Bremsstrahlung radiation) are taken into account. The radiation losses become significant at electron energies higher than ~ 1 MeV. The increase in stopping force in this region (2) is due to irradiative losses. The experimental results (1) and the calculated curve (2) coincide very well around the electron kinetic energy of 10 keV. The

stopping power in the energy region from ~ 80 eV to ~ 1 keV (3) is calculated according to the Bethe formula in reference 18. The stopping power measured in the experiments (1) differs a lot from the predictions of the Bethe formula (3) at electron energies lower than ~ 100 eV. This is because nitrogen is a molecular gas, and low energy electrons loose their energy in excitation of vibrational states of molecules. Vibrational excitations, as well as energy losses in elastic collisions, are not treated by the Bethe formula. In atomic gases, for instance, in rare gases, the stopping power follows the Bethe formula in the low energy region much closer, although elastic collisions are responsible for non-zero stopping power at $\varepsilon < I$. However, at electron energies higher than ~ 100 eV, where the maximum of the stopping power is reached, the experimental (1) and theoretical curve (3) coincide.

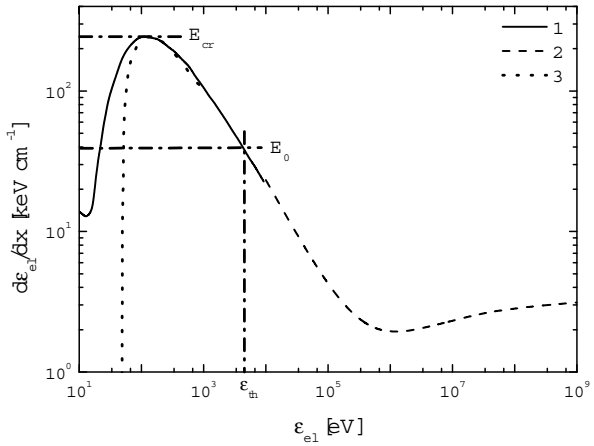

Figure 1.2. Electron stopping force in N_2 at a gas pressure of 1 bar. The experimental results (1) are from reference 16, and the theoretical curves are calculated with the ELSTAR code(2) [17] and the Bethe formula (3) [18].

It can be seen from figure 1.2 that the Bethe formula describes well the stopping power in gases in the electron energy region from ~ 0.1 – 1 keV to ~ 1 MeV. The maximum stopping power is reached at the electron energy $\varepsilon \approx 2.33\ I$, as follows from Eq. 1.29 for $ln(\varepsilon/I) = 1 - (1- ln\ 2)/2$. At this electron energy ($\varepsilon \approx 2.33\ I$) the stopping power $F_{max} \approx - (4\ \pi\ n_0\ Z\ e^4) / (2.33\ I)$. The ionization potential I in eV scales with Z as $13.6\ Z$ at $Z < 10$ [19] and as $9.76\ Z + 58.8\ Z^{0.19}$ at $Z \geq 10$ [20]. Therefore the electron energy, at which the stopping power is maximal, is mostly proportional to Z, while the peak value of the stopping force is mostly independent on Z but it is proportional to the gas density n_0: $F_{max} \sim n_0$. So, the stopping power is proportional to the gas density n_0 at any electron energy, and for $\varepsilon >> I$ it is proportional to Z: $F(\varepsilon) \sim n_0\ Z / \varepsilon$, as follows from Eq. 1.29.

The peak value of the stopping force determines the critical value of the electric field $E_{cr} = F_{max} / e$ (see figure 1.2, upper horizontal dash – dotted line). If the applied electric field strength

$E > E_{cr}$, then $d\varepsilon / dx > 0$ for any value of the electron energy ε (Eq. 1.27). Therefore, every electron regardless of its kinetic energy gains more energy due to acceleration in the field on its average free path between collisions than it loses due to collisions. So, electrons are accelerated continuously. This is the so-called *runaway effect*. For example, in N_2 at a gas pressure of 1 bar the critical electric field value $E_{cr} \approx 274$ kV cm^{-1}. The critical electric field strength is proportional to the gas density n_0 as well as the peak stopping force F_{max}, thus $E_{cr} / n_0 = \text{const}$. On the other hand, the gas breakdown field strength in nitrogen at 1 bar is ~ 30 kV cm^{-1}. Therefore, the electron runaway effect in gases can be observed only in a gas discharge.

Additionally, in gas discharges a small fraction of electrons have a kinetic energy $\varepsilon > I$. They experience a runaway effect even if the electric field strength is less than critical field strength. For example, if the electric field strength in the discharge is E_0 (lower horizontal dashed – dotted line in figure 1.2), then electrons with $\varepsilon > \varepsilon_{th}$ (vertical dashed – dotted line in figure 1.2) experience the run away acceleration.

As mentioned before the highest electric field strength in glow discharges is observed in the cathode sheath. A typical normal cathode voltage drop is ~ 10^2 V and the typical normal cathode sheath length $p\ d$ is less than or comparable to ~ 1 Torr cm [2]. So the electric field strength in the cathode sheath of a normal glow discharge at a gas pressure of 1 bar is ~ 10^2 kV cm^{-1}. In abnormal glow discharges the electric field strength in the cathode sheath is even higher [2]. Therefore, electrons from the high energy part of the EEDF can experience the runaway effect. For example, in reference 8 experimental results of the generation of fast electrons beams in an abnormal glow gas discharge are reported.

The generation of a fast electron beam based on a high voltage pulsed open barrier discharge and used as a soft X-ray generator as described in chapter 2 is due to the runaway effect described above.

1.3.6 Preionization

As discussed above, gas discharge instabilities develop from local disturbances of the electron and ion spatial distributions. Therefore, if a discharge is ignited non-uniformly in space, the chance for the development of an instability during the discharge is higher. Proper preionization of the gas volume facilitates a homogeneous gas gap breakdown and discharge ignition, especially at high gas pressures.

At low $p\ d$ values lower than ~ 100 Torr cm, where p is the gas pressure and d is the discharge gap length, gas breakdown occurs in the uniform Townsend avalanche mode. At high $p\ d$ values (~ bar cm) a gas breakdown in the form of a single spark or several sparks developed from initial streamers is usually observed without gas preionization. With proper volumetric preionization of the gas the uniform gas breakdown is obtainable even at a high $p\ d$ values [21, 22]. A streamer is created from an electron avalanche when the electric field due to the space charge of the avalanche is comparable to the applied external electric field. If single avalanches overlap in the plane perpendicular to the applied external field, the electric field due to their space charge is constant in this plane. Therefore a spatially uniform gas breakdown occurs. Proper volumetric preionization in a gas mixture can be achieved with high energetic photons (e.g. X-rays) which have a large penetration depth or by high energetic particles (e.g. electrons) with a lower penetration depth.

Suppose that each avalanche begins from a single electron produced in the gas by a preionization event and that the initial electron density is n_0. As the avalanche grows with time and moves towards the anode, electrons of the avalanche head diffuse. As a consequence, the radius of the avalanche head R at the time τ due to electron diffusion is:

$$R = \sqrt{4 D \tau} \tag{1.31}$$

where D is the diffusion coefficient. The diffusion coefficient D is expressed in terms of the electron mobility μ_e, the electron charge e and the average energy $<\varepsilon>$ as:

$$D = \frac{2\langle\varepsilon\rangle \mu_e}{3e} \tag{1.32}.$$

After a certain time τ_{cr}, when the space charge field is comparable to the external field E, the avalanche changes over into a streamer. The total number of electrons in the avalanche head at this moment is N_e. Assume that the avalanche head is a sphere and the electrons are distributed homogeneously in it. The avalanche head radius then can be expressed in terms of the total number of electrons and the external field strength:

$$R_{cr} = \sqrt{\frac{e N_e}{4\pi\varepsilon_0 E}} \tag{1.33}$$

N_e is determined by the ionization coefficient α, the electron drift velocity v_e and time τ_{cr} according to Eq. 1.13:

$$N_e = \exp(\alpha v_e \tau_{cr}) \tag{1.34}$$

From Eqs. 1.31 – 1.34 an equation for the critical avalanche radius is derived:

$$R_{cr} = \sqrt{\frac{8}{3}\frac{\langle\varepsilon\rangle}{\alpha e E}\ln\left(\frac{4\pi\varepsilon_0 E R_{cr}^2}{e}\right)} \tag{1.35}$$

This critical radius should be higher than the distance between the individual preionization electrons with density n_0 to cause an overlap of all avalanches. Therefore, the required electron preionization density should exceed a certain value:

$$n_e > \frac{1}{(2R_{cr})^3} \tag{1.36}$$

This preionozation electron density is estimated to be in the range from ~ 10^4 [22] to ~ 10^8 cm^{-3} [3] depending on the gas composition and pressure. In reference 3 a required preionization electron density of 10^7 – 10^8 cm^{-3} is reported for excimer laser gas mixtures at atmospheric pressures.

The purpose of gas preionization of high-pressure gas discharges is to create a uniform distribution of electrons in the whole gas volume and with a density high enough to provide overlapping of the avalanches. Under these conditions the cathode – anode gas gap is homogeneously conducting current and a homogeneous gas discharge is provided in the initial stage.

The development of a gas breakdown is not an instantaneous process. It is well known that the time needed for the gas breakdown decreases with the increase of the applied voltage. In pulsed discharges breakdown of the gas should occur within a time period shorter than the pulse duration. Due to this fact, the gas breakdown voltage in pulsed discharges should be higher than the static breakdown voltage [23, 24]. The discharge formation time is decreased by the amount of preionization. Therefore, the breakdown voltage decreases for the same pulse duration. A lower breakdown voltage facilitates impedance matching between the discharge excitation circuit and the discharge itself. As a consequence, the energy is coupled more efficiently into the discharge.

Preionization of a gas volume can be obtained by means of different techniques, for example, by UV radiation [25], X-ray radiation [24], an RF barrier discharge [26] or a short, high voltage pre-pulse [24, 27] prior to the main discharge. In this thesis an X-ray pulse was employed to produce the preionization of the gas volume. In the usual X-ray sources the photon energy is ~ 50 – 100 keV and higher. In rarified matter as, for example, gases, these X-ray photons are absorbed very weakly and have a large penetration range. On the other hand, a high photon flux is required for the creation of the required electron density of ~ 10^8 cm^{-3}. Soft X-rays with less photon energy are more attractive for the preionization of small scale high-pressure gas discharge systems ($p\ d$ ~ 1 – 10 bar cm) because they show a much larger X-ray photon absorption cross section in gases. In order to validate this statement we need to analyze the interaction of X-rays with matter.

1.4 X-ray absorption in matter

The X-ray dose absorbed in matter (gas, liquid or solid) in terms of energy per cm^3 or per kg is determined by the photon energy ε_{ph} and by the energy mass-absorption coefficient μ_e/ρ of matter at that photon energy. The probability of photon absorption decreases when the photon energy increases; on the other hand, the amount of energy absorbed in a single event increases. Suppose a photon flux F (in terms of photons per cm^2 per sec) with a photon energy ε_{ph} penetrating into a gas with mass density ρ_g. The path length of the X-ray beam in the gas is D. The amount of energy ΔE absorbed in the gas is given by:

$$\Delta E = F\left(1-\exp\left(-\left(\frac{\mu_e}{\rho}\right)_g \rho_g D\right)\right)\varepsilon_{ph} S \tau \qquad (1.37)$$

where S is the beam cross-section area and τ is the X-ray pulse duration. The energy mass-absorption coefficient $(\mu_e/\rho)_g$ is independent of the gas pressure and thus the gas mass density but it strongly depends on the photon energy. The energy dependence of the mass-absorption coefficient is given in the Appendix (see figure A.2) for different gases and solid materials.

Usually X-ray radiation penetrates into the discharge chamber through a metal foil or thin metal wall serving as the input window. In our experiments the input window of the discharge chamber is made of Al and has a thickness d of 1 mm. Therefore, the initial beam intensity is attenuated by a factor:

$$\exp\left(-\left(\frac{\mu}{\rho}\right)_{Al}\rho_{Al}\,d\right) \tag{1.38}$$

where $(\mu/\rho)_{Al}$ is the mass attenuation coefficient. The energy dependence of the mass attenuation coefficient for different gases and solid materials is also given in the Appendix (see figure A.3). The mass energy-absorption coefficient and mass attenuation coefficient describe different physical processes. The mass attenuation coefficient describes the attenuation of the X-ray beam including all processes, for example, elastic scattering of photons without change of the photon energy, while the mass energy-absorption coefficient refers to energy of the beam absorbed by matter due to photo-ionization, Compton scattering and other inelastic processes, leading to absorption of photons or changes in their energy.

Assume that an X-ray source produces a flux of F_0 photons per cm^2 per sec regardless of their energy. The X-ray beam with cross-section S and duration τ passes through the Al plate with thickness d = 1 mm and propagates in the discharge chamber along a path length D = 1 cm. The discharge chamber is filled with a gas or gas mixtures at a pressure of 5 bar. The absorbed dose D_a (in eV cm^{-3}) is given by the absorbed energy in the gas volume divided by the gas volume $V = D\,S$. The absorbed dose is:

$$D_a \propto \exp\left(-\left(\frac{\mu}{\rho}\right)_{Al}\rho_{Al}\,d\right)\left(1-\exp\left(-\left(\frac{\mu_e}{\rho}\right)_{g}\rho_g\,D\right)\right)\frac{\varepsilon_{ph}}{D} = \tag{1.39}$$
$$= \eta(\varepsilon_{ph})$$

where η is "efficiency" of the preionizer at the photon energy ε_{ph}. This "efficiency" is in terms of the average energy absorbed in the gas per cm per single photon of the initial X-ray beam.

The calculated "efficiency" dependence on the photon energy for the discharge chamber filled with He (a), Ne (b) and Ar (c) is plotted in figure 1.3. The mass density of Al is 2.7 g cm^{-3}, the mass density of He at a gas pressure of 5 bar is 1.66 10^{-4} g cm^{-3}, 8.39 10^{-4} g cm^{-3} for Ne and 1.66 10^{-3} g cm^{-3} for Ar. The "efficiency" is expressed in eV cm^{-1} because the photon energy ε_{ph} is in eV. One can see that for He (a) η increases almost monotonically with the photon energy except for a small minimum around ~ 13 to 18 keV. In Ne (b) and Ar (c) η increases sharply with the photon energy in the region below ~ 10 keV, reaches a peak value at ε_{ph} ~ 10 keV and decreases very fast at higher photon energy. In Ar (c) η decreases with the photon energy $\varepsilon_{ph} > 10$

keV, while in Ne (b) for ε_{ph} > 90 keV the "efficiency" slightly increases again with the photon energy.

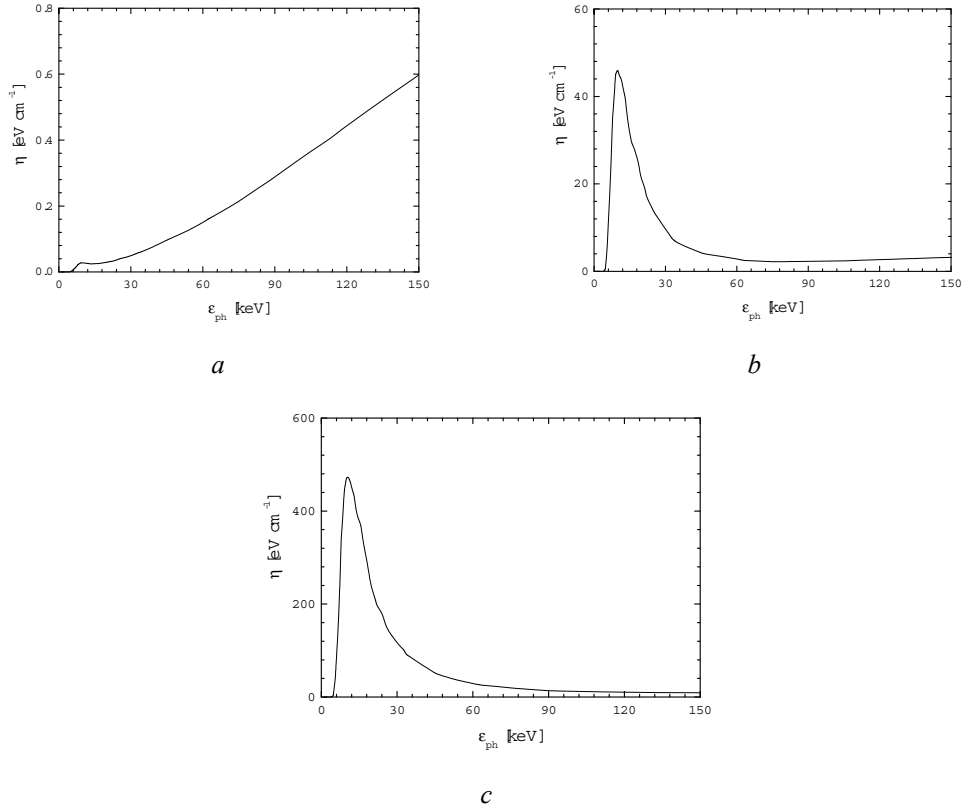

Figure 1.3. Calculated dependence of the "efficiency" η of the gas preionization on the photon energy ε_{ph} of X-ray fotons (Eq. 1.39) in He (a), Ne (b) and Ar (c) at a gas pressure of 5 bar. The X-ray input window is 1 mm thick and made of Al. The gas gap length is 1 cm.

The "efficiency" η (Eq. 1.39, figure 1.3) is determined by the transmittance of the Al window given by Eq. 1.38, the energy absorption in the gas given by Eq. 1.37 and the photon energy ε_{ph}. At photon energy below ~ 5 keV an Al window of 1 mm thickness absorbs the X-ray radiation almost entirely. At higher photon energy the transmittance increases rapidly, for example, at ε_{ph} = 5 keV the transmittance is ~ 1 %, at 10 keV it is ~ 50 % and at 20 keV it is ~ 90 %. At even higher photon energies the transmittance is high and increases slowly towards 100%, For instance, at 30 keV the transmittance is ~ 97 %, ~ 98.8 % at 50 keV and ~ 99.3 % at 100 keV. At photon energy higher than 100 keV the Al window transmittance is almost constant and ~ 100 %. In all three gases the absorption is weak at ε_{ph} > 5 keV and $(\mu_e/\rho)_g \rho_g D << 1$. Thus,

$$1-\exp\left(-\left(\frac{\mu_e}{\rho}\right)_g \rho_g D\right) \approx \left(\frac{\mu_e}{\rho}\right)_g \rho_g D \tag{1.40}$$

Therefore, the X-ray absorption in gases is proportional to the mass energy-absorption coefficient μ_e/ρ (see figure A.3 in Appendix), to the gas density and to the path length. In He the coefficient μ_e/ρ decreases drastically with the photon energy at $\varepsilon_{ph} < 20$ keV and slightly increases (by ~ 2.5 times) in the region from 20 to 150 keV. In Ne μ_e/ρ decreases fast in the photon energy region for 5 – 100 keV and it is almost constant from 100 to 150 keV. In Ar the mass energy-absorption coefficient drops fast with the photon energy increase in the entire range from 5 keV to 150 keV.

Therefore, in Ne (b) and Ar (c) high energy (~ 50 – 150 keV) X-ray photons are preferable from the transmittance point of view of the Al window, however they experience very weak absorption in the gases at these photon energies. So the advantage of a high window transmittance is drastically reduced by the decrease in absorption in these gases. The maximum "efficiency" of X-ray preionization in Ne and Ar with the given parameters of the experimental setup is expected at $\varepsilon_{ph} \sim 10$ keV. In He (a) the X-ray absorption does not change significantly in the photon energy range from 10 to 150 keV, and the increase of "efficiency" at $\varepsilon_{ph} > 30$ keV, where the Al window transmittance is almost constant (~ 100 %), is explained by the photon energy increase (see Eq. 1.39).

Taking into account Eq. 1.40, the "efficiency" given by Eq. 1.39 can be rewritten as:

$$\eta \approx \exp\left(-\left(\frac{\mu}{\rho}\right)_{Al} \rho_{Al}\, d\right)\left(\frac{\mu_e}{\rho}\right)_g \rho_g\, \varepsilon_{ph} \tag{1.41}$$

If the X-ray absorption in the gas is weak, the absorbed dose D_a is:

$$D_a = F_0\, \tau\, \eta \tag{1.42}$$

where F_0 is the photon flux (number of photons per cm^2 per sec) and τ is the X-ray pulse duration.

Analysis of Eq. 1.41 shows that for a thicker Al entrance window or higher Z materials, for example, Cu or Ni the maximum "efficiency" in Ne and Ar is observed at slightly higher photon energy and that in such a case the "efficiency" always decreases at any photon energy due to stronger X-ray absorption in the window. At every photon energy η and D_a in Ne and Ar increase with the gas pressure and thus the gas mass density ρ_g, although the maximum "efficiency" is reached at the same photon energy as long as the X-ray absorption in the gas is weak. In case of weak absorption in the gas neither the "efficiency" nor the absorbed dose depends on the gas gap length D. In He the "efficiency" and the dose D_a decrease with an increase of the window thickness or Z-number of the window material, and increase with the gas pressure.

The absorbed dose D_a is given in eV cm^{-3}. For the absorbed dose the unit rad, equal to 10^{-2} J kg^{-1}, is commonly used. The absorbed dose D_r expressed in rad is proportional to the ratio of D_a and the gas mass density ρ_g:

$$D_r = \frac{D_a}{\rho_g}\ 1.60218 * 10^{-16} \propto \frac{\eta}{\rho_g} \tag{1.43}$$

where ρ_g is in g cm^{-3}. For example, at photon energy of 100 keV the "efficiency" η is ~ 0.337 eV cm^{-1} in He, ~ 2.6 eV cm^{-1} in Ne and ~ 12.6 eV cm^{-1} in Ar. The η/ρ_g value is ~ 2.0 10^3 eV cm^2 g^{-1} in He, ~ 3.1 10^3 eV cm^2 g^{-1} in Ne and ~ 7.6 10^3 eV cm^2 g^{-1} in Ar. At a photon energy of 50 keV the η/ρ_g value is ~ 6.7 10^2, ~ 4.5 10^3 and ~ 2.7 10^4 eV cm^2 g^{-1} respectively and at a photon energy of 10 keV the values of these ratios are ~ 1.5 10^2, ~ 5.4 10^4 and ~ 2.8 10^5 eV cm^2 g^{-1}.

Therefore, our numerical model is in agreement with the well known fact that the dose absorbed in a gas increases with the Z-number of the gas under otherwise equal conditions. It also predicts that soft X-ray radiation (~ 10 keV) is more efficient as a gas preionization source for the most of the gases than shorter wavelength radiation with photon energies of ~ 50 - 150 keV.

1.5 Conclusion

Excimer lasers typically require a pumping power density in the order of magnitude of ~ MW cm^{-3}. A transversal glow gas discharge in a high pressure (few atmospheres) laser gas mixture between two electrodes at a short electrode distance (~ 1 cm) is able to provide the required pumping power density in the laser gas mixture. Therefore, such a system is a suitable excitation source for high pressure gas lasers. Although preionization of the gas volume does not guarantee a stable discharge during long pulses (> 100 ns), it is required for a uniform ignition of the discharge and, thus, increases the discharge stability. The required electron preionization density for a uniform gas breakdown in excimer laser gas mixtures at gas pressures of a few bar is ~ 10^8 cm^{-3}.

In systems with a longer electrode distance or higher gas pressures ($p\ d$ > 10 bar cm) hard X-ray preionization (photon energies of ~ 100 – 150 keV and higher) provides a more homogeneous distribution of the electron preionization density along the beam axis due to the weak absorption. Soft X-ray preionization with low energetic photons of ~ 10 keV is more efficient for short gap systems ($p\ d$ ~ 1 bar cm) than hard X-ray preionization due to the stronger absorption with the condition that the preionization electron density distribution along the beam axis is homogeneous enough. Therefore, if hard X-ray preionization is used in short gap systems, it requires a higher photon flux in terms of photons per cm^2 per second than soft X-ray preionization.

1.6 Non-metric physical units used in the thesis

In physics and mechanics, still a lot of different units and unit systems are used. In fact, they were adopted long time before the international recognition of the metric SI system, and sometimes they are more convenient and are also more accepted than the metric system units. In this thesis several old-style units are used for the gas pressure, energy or absorbed radiation dose.

Although the metric or international system of units (SI) is used in many countries like Russia or the Netherlands, units such as mile, inch or pound are still in use in countries like the United Kingdom and the United States of America.

The metric system unit for gas pressure is Pa. By definition 1 Pa is 1 N m^{-2} or alternatively 1 kg m^{-1} sec^{-2}. In this thesis the gas pressure is given in bar or Torr units. 1 Torr (equals 1 mm Hg) is the pressure produced on a surface by a column of Hg with a height of 1 mm due to gravity. 1 bar or 1 atmosphere (atm) is the standard atmospheric pressure. These units are related to each other as:

$$1 \text{ bar} = 10^5 \text{ Pa} = 705.06 \text{ Torr}$$

$$1 \text{ Torr} = 133.322 \text{ Pa} = 1.333\ 10^{-3} \text{ bar}$$

The metric system unit for energy is J, which is 1 N m or 1 kg m^2 sec^{-2}. In atomic and molecular physics, spectroscopy and gas discharge physics the energy unit electron-volt (eV) is commonly used. One electron-volt is the energy gained by an electron accelerated in vacuum by a potential difference of 1 V. The relation between eV and J is given by:

$$1 \text{ eV} = 1.60218\ 10^{-19} \text{ J}$$

where *e* is the elementary charge (the charge of an electron) in C.

In the metric system the Gy unit, which equals 1 J kg^{-1} or 1 m^2 sec^{-2}, is used for the absorbed dose of radiation. In this thesis another commonly used unit, the rad is used. The rad unit is part of the CGS system, which is very similar to the metric system but is based on cm, g and sec, instead of m, kg and sec. The absorbed dose unit refers to amount of radiation energy absorbed by a matter per unit of mass. The relation between Gy and rad is:

$$1 \text{ rad} = 10^{-2} \text{ Gy} = 10^{-2} \text{ J kg}^{-1}$$

Derived units like mbar, mrad or keV are produced in the usual way, or example, 1 mbar = 10^{-3} bar, 1 mrad = 10^{-3} rad and 1 keV = 10^3 eV, etc.

References:

[1] H.M.J. Bastiaens, PhD thesis, Univ. of Twente, The Netherlands, ISBN 90-365-141-69 (2000)
[2] Yu.P. Raizer, *Gas Discharge Physics*, Springer, London (1992)
[3] R.S. Taylor, Appl. Phys., B **41**, 1 (1986)
[4] R. Dreiskemper and W. Bötticher, IEEE Trans. Plasma Sci., **23**, 987 (1995)
[5] D. Mathew, H.M.J. Bastiaens, K.-J. Boller and P.J.M. Peters, Appl. Phys. Lett., **88**, 1 (2006)
[6] V.M. Borisov, V.P. Novikov and O.B. Khristoforov, High Temperature **24**, 1079 (1986)
[7] Yu. P. Raizer and M.N. Shneider, Fiz. Plazmy (Plasma Physics Reports) **15**, 318 (1989) (in Russian)
[8] Yu.S. Akishev, N.A. Djatko, A.P. Napartovich and P.I. Peretjatko, Zh. Tekh. Fiz., (Technical Physics) **59**, 14 (1989)
[9] L.P. Babych, *High-Energy Phenomena in Electric Discharges in Dense Gases: Theory, Experiment and Natural Phenomena*, ISTC Science and Technology Series, Vol. 2, Arlington, VA: Futurepast (2003)
[10] C.T.R. Wilson, Proc. Cambridge Philos. Soc., **22**, 534 (1924)
[11] A.S. Eddington, Nature (Suppl.) **25**, 2948 (1926)
[12] R.G. Giovanelly, Philos. Mag., **40**, 206 (1949)
[13] H. Dreicer, Phys. Rev., **115**, 238 (1959)
[14] H. Bethe, Ann. Phys., **5**, 325 (1930)
[15] M. Lamoureux, P. Waller, P. Charles and N.B. Avdonina, Phys. Rev., **E 62**, 4091 (2000)
[16] L.R. Peterson and A.E.S. Green, J. Phys. B: At. Mol. Phys., **1**, 1131 (1968)
[17] NIST database, ELSTAR, *http://physics.nist.gov/PhysRefData/Star/Text/contents.html*
[18] F. Salvat and J. Parellada, J. Phys. D: Appl. Phys., **17**, 185 (1984)
[19] R.D. Birkhof, *Encyclopædia of Physics,* vol. 34, ed. S. Flügge (Berlin, Springer), p. 58 (1958)
[20] M.J. Berger and S. M. Seltzer, *Studies in Penetration of Charged Particles in Matter*, Nucl. Sci. Ser. Rep. No 39; NAS-NRC Publ. No 1133 (Washington, DC: National Academy of Sciences), p. 205 (1964)
[21] J.I. Levatter and Sh.-Ch. Lin, J. Appl. Phys., **51**, 210 (1980)
[22] A.J. Palmer, Appl. Phys. Lett., **25**, 138 (1974)
[23] S.V. Mitko, Y.B. Udalov, P.J.M. Peters, V.N. Ochkin and K.-J. Boller, Appl. Phys. Lett., **83**, 2760 (2003)
[24] H.M.J. Bastiaens, S.J.M. Peeters, X. Renard, P.J.M. Peters and W.J. Witteman, Appl. Phys. Lett., **72**, 2791 (1998)
[25] R. Burnham and N. Djeu, Appl. Phys. Lett., **29**, 707 (1976)
[26] S. Nagai, K. Takehisa, T. Enami, T. Nishisaka, J. Fujimoto, O. Wakabayashi, H. Mizoguchi and A. Takahashi, Jpn. J. Appl. Phys., **38**, 7013 (1999)
[27] J.P. Reilly, J. Appl. Phys., **43**, 3411 (1972)

Chapter 2

Soft X-ray generation in gases by means of a pulsed high voltage barrier discharge

Fast electron beam generation is observed in a pulsed high voltage open barrier discharge. In this chapter the generation of such an electron beam and the propagation of the e-beam in gases are described. The production of soft X-ray radiation by stopping the electrons from the generated e-beam either directly in a gas or in a metal target is discussed.

2.1 Historical overview

In chapter 1 the advantage of soft X-ray radiation (~ 10 keV) compared to hard X-ray radiation (> 100 keV) as a preionization source for a gas volume has been discussed. It was shown that in a laser gas chamber with an X-ray input window made of Al with a thickness of 1 mm filled with Ar a 10 keV X-ray photon produces, on average, approximately 38 times more electron-ion pairs in the gas than a 100 keV X-ray photon. It was described that this is due to the stronger absorption of lower energetic photons. If the chamber is filled with Ne the ratio is ~ 17.4. In this chapter our experiments on soft X-ray generation in gases by means of a pulsed electron beam produced in a high voltage open barrier discharge are presented.

There are a lot of different techniques to generate soft X-rays, e.g., X-ray emission from charge-transfer collisions [1], high harmonics generation [2], femtosecond laser produced plasmas [3, 4], ablative capillary discharges [5], discharge pinches [6], synchrotron radiation [7], transition radiation [8], or Cherenkov radiation [9]. All these methods are complicated in comparison with the frequently used vacuum X-ray tubes. In these tubes electrons are produced and accelerated in vacuum and hit a metal target producing X-rays. On the other hand, this technique has also some serious disadvantages. Firstly, due to the Child-Langmuir law that restricts the electron current in vacuum the photon flux is limited. Secondly, the photon energy of the produced X-rays has to be high enough, typically > 100 keV, to penetrate through the separating window between the vacuum part of the source and the high-pressure gas volume of the discharge chamber. However, as described earlier such high energetic X-rays are not well absorbed in the gas volume even at a gas pressure of a few bar and a gap length of several cm. Therefore, a generator that produces X-rays directly in the gas discharge chamber can be very attractive as a preionizer because in this case no separation window is required and thus the X-ray photon energy can be lower.

X-rays can be generated directly in a gas or a gas discharge only if the exciting electrons are sufficiently fast (~ 10 to 100s keV). X-rays were discovered as early as 1895 by Röntgen [10] via fast electrons in a low pressure (< 1 Torr) gas discharge. However, in high-pressure discharges (> 100 Torr) it is not easy to generate fast electrons, because the short mean free path

of the electrons usually prevents acceleration to a kinetic energy that suffices for X-ray generation. One of the first observations of X-rays in an atmospheric pressure helium discharge was published in 1968 [11], where X-rays were produced at the surface of a metallic discharge electrode. In those experiments fast electrons ran away in the strong electric field and hit the anode. An overview on this, so called, "run away" effect has been presented in chapter 1 (see section 1.3.5) and also can be found in reference 12.

The same method but improved and further developed is described in recent publications by Tarasenko's group in Tomsk, Russia [13 – 15]. In these cases run away electron beams were produced in gas diodes filled with air at atmospheric pressure. Pulses with a rather high voltage (> 150 kV), with a short rise time (200 – 500 ps) and a short duration (1 – 2 ns) had to be applied in order to produce runaway electrons. In reference [15] it was reported that under discharge less favorable conditions for the formation of very fast runaway electrons (> 100 keV), most of the X-ray radiation was produced in the plasma discharge volume, while under more favorable conditions for the generation of runaway electrons most of the X-rays were generated at the anode of the gas diode. In reference [16] it also has been reported that fast electrons in a discharge can generate X-rays directly in a gas. In all these experiments [13 - 16] the runaway effect was achieved due to a high and inhomogeneous electric field in a point-to-plane or a rod-to-plane electrode configuration while the stability of these discharges could only be provided via high voltage pulses with a short rise time, and a short duration.

In addition, in reference [17] it was reported that instead of metal targets as is usual in X-ray sources heavy gases, e.g. Xe, could be utilized for the generation of X-ray bremsstrahlung radiation. In that paper a 100 ns, 500 keV e-beam was produced in vacuum, and after passing the aluminized Mylar foil anode the electrons generated X-ray radiation in a gas volume containing Xe gas at atmospheric pressures.

Recently our group showed the possibility to generate a large area electron beam in an open barrier discharge [18 - 21]. The advantages of this type of electron beam generation is that the generated electrons are relatively fast, with an energy approximately equal to the discharge voltage, and with an efficiency as high as 90% [20]. Other advantages of this method are that such discharges are very stable, with a high shot-to-shot reproducibility, although the area of the produced beam is rather large (10 - 100 cm^2). The open barrier discharge is a modification of the so-called "open" discharge, proposed in the early 80's by the group of P. Bokhan in Novosibirsk, Russia and thoroughly investigated until now, e.g., see the recent publications [22, 23]. A typical open discharge unit includes a plane metal cathode and a plane perforated metal anode (usually a mesh), separated by a narrow (~ 1 mm) gas gap, and a field-free drift space behind the anode. In the open barrier discharge the cathode is made of a dielectric material. This modification improves the discharge stability at high current density. Electron acceleration in the open barrier discharge is achieved by means of the runaway effect, as well as in the usual open discharge.

Large area electron beams can be used for a lot of applications varying from industrial applications like surface processing, surface cleaning and sterilization. As mentioned above electron beams are also very frequently used for X-ray generation. For a special laser application, namely the preionization of the laser gases just before the electrical discharge is initiated, the open barrier e-beam source is very well suited. It is well known that for all kinds of high pressure gas lasers preionization of the gas (creating free electrons in the gas volume) is required before an electrical discharge in a gas or gas mixture is started. Only in this way a homogeneous discharge can be initiated in the gas. Such electrical discharges are used to excite laser gases or gas mixtures homogeneously in order to provide an excited medium that make optical amplification possible. Preionization of gases with X-rays has the advantage, compared to preionization with fast electrons as is usually done, of a larger penetration depth of the X-ray

photons. The e-beam source based on an open discharge has the potential to be able to work directly in gases, so no entrance window is required and thus there are no X-ray photons losses in the entrance window. Because of this it can work at lower kinetic energies where the absorption cross-section for ionization is higher than for higher energetic radiation. Also a much higher e-beam current can be obtained at the same voltage, compared to a vacuum e-beam source where the current is limited by the Child-Langmuir law. As a consequence a higher X-ray photon flux can be generated with our device at the same charging voltage.

In this chapter we describe the design and investigations on this novel source for soft X-ray generation based on an open barrier discharge as described in references 19, 20 and 21. Experiments with the novel soft X-ray generator which proves its capability as a gas preionization source for laser gas mixtures are discussed in this chapter.

2.2 Experimental setup of the soft X-ray generator and X-ray detector

Our setup of the open barrier discharge is shown schematically in figure 2.1. The main features and electrical properties of this type of open barrier discharge are described in reference 18 and 19. The main part of the electron beam generator is a dielectric cylinder (1) with a diameter of 5.3 cm and a thickness of 2.15 cm made out of ceramic material with a high dielectric constant ($\varepsilon \sim 4300$). For these parameters, the specific capacitance of the dielectric is ~ 0.17 nF/cm^2, while its breakdown voltage is ~ 30 kV. A metallic electrode is deposited on the rear side of the dielectric cylinder. The diameter of the active area of the dielectric cylinder serving as cathode was 41 mm. A metal grid (2) of 41 mm in diameter was placed 3 mm apart from the cathode and held by a metal ring. The metal ring and the metal grid served as a composed anode. During experiments generating X-rays from a metallic target, an Al foil (5) with a thickness of ~ 13 μm and diameter 38 mm was fixed inside the discharge chamber by a metal ring 17 mm apart from the grid. Both the anode and the foil were grounded in this case. For experiments aiming on generating X-rays directly in a gas, the Al foil was removed. The whole discharge setup was encapsulated in a discharge chamber (3) consisting of a glass tube 0.5 m long. The X-ray output window (4) with a diameter of 1 cm is made of a 0.1 mm thick Kapton foil. Several pieces of Al foil (9) ~ 1 cm in diameter, placed 3 mm behind the output window, served as variable attenuator for X-rays during the experiments.

The dielectric cathode (1) served as the energy storage capacitor and was charged by a Hipotronics R50B high-voltage power supply (11) through a 10 MΩ resistor attached to its metallic back. A TGI1 1000/25 thyratron in the triggering unit (10) was used to trigger the discharge.

A photomultiplier Philips 56AVP (7) with a piece of scintillating plastic NE102 (6) attached was used as X-ray detector. The scintillator was placed in a special box with an input window (8) of ~ 1 cm in diameter made out of 13 μm thick Al foil to prevent illumination of the photomultiplier by ambient light or by light from the discharge.

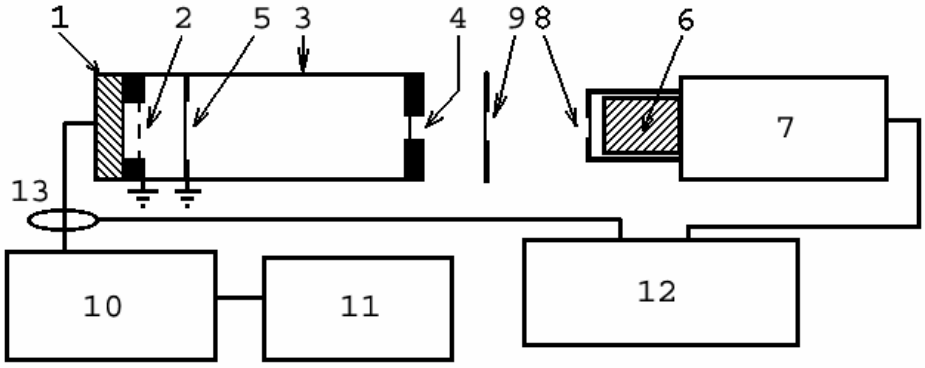

Figure 2.1. Experimental setup
1: dielectric cathode, 2: metal anode grid, 3: discharge chamber, 4: Kapton output window, 5: Al target, 6: scintillator, 7: photomultiplier, 8: Al input window, 9: Al attenuator, 10: triggering unit, 11: high-voltage power supply, 12: oscilloscope, 13: current transformer (Rogovski coil)

A Rogovski coil (Pearson Electronics Inc., model 110, 0.1 V/A) (13) was used to measure the current waveforms. The current waveforms as well as the X-ray signals detected by the photomultiplier were captured by a digital oscilloscope (Tektronix TDS 640A) (12). The current waveform measured by the Rogovski coil is, in fact, not the current of the e-beam produced, but was measured only to check the reproducibility and to compare the discharge conditions.

The recorded X-ray signal amplitude depended on the photomultiplier amplification coefficient governed by its supply voltage. In order to minimize the experimental error in the X-ray intensity measurements the amplification of the photomultiplier in every experiment was chosen such that the signal amplitude was much higher than the noise level but well below the saturation level. The effective amplification for the photomultiplier varies for all figures 2.3 – 2.9 and 2.14, but it is the same in each individual figure. Thus the curves within the same figure can be directly compared. The experimental error in the measured amplification coefficient as well as in the X-ray signal amplitude fluctuation is given by the error bars in all the figures. A detailed description of the recorded signal processing procedure, the origin of errors and the influence of the detector response function is given later in section 2.5 of this chapter.

The generation of X-rays was investigated in He, Ne and Ar with and without an Al foil in the discharge chamber. The discharge chamber was filled with a fresh gas before each new series of experiments on a particular gas or gas pressure. The electron beam device could be operated at a repetition rate of up to several kHz but usually a repetition rate of about 1 Hz was used in our experiments.

2.3 Propagation of a beam of electrons in gases

When the capacitance of the dielectric cathode, formed by the dielectric and its metallic backside (1 in the figure 2.1) is charged and the thyratron in the triggering unit (10 in the figure 2.1) is switched, a glow discharge is ignited between the dielectric cathode and the mesh anode (2 in the figure 2.1). A portion of the electrons in the discharge plasma are accelerated in the discharge gap and penetrate through the perforated anode into the field-free drift space beyond

the anode. These fast electrons are decelerated in the drift space due to collisions with the gas atoms or molecules. Their kinetic energy is partially transferred into the gas atoms or molecules due to an excitation event. The excited atoms/molecules loose their excitation energy by emission of visible radiation in the drift space. This can be seen in figure 2.2 where time-integrated pictures from the drift zone are shown (without Al foil in the discharge chamber).

The color of the visible glow depends on the kind of gas used, for example, in Ne (figure 2.2 a, b) the color is red, and in He (figure 2.2 c, d) the color is light-blue. It can be seen that the spatial distribution of the light intensity depends on the gas pressure, on the kind of gas used and on the charging voltage. In general, for the same gas and the same charging voltage the length of the glow increases with decreasing gas pressure, but at the cost of the light intensity. For the same gas and the same gas pressure the length of the glow increases with the charging voltage. For the same charging voltage and the same gas pressure the glow region is longer for gases with lower atomic weight (e.g. He) than for heavier gases (e.g. Ar). It is also worth mentioning that if the e-beam current is high enough, pinching of the beam is observed, as it shown in figure 2.2 (d).

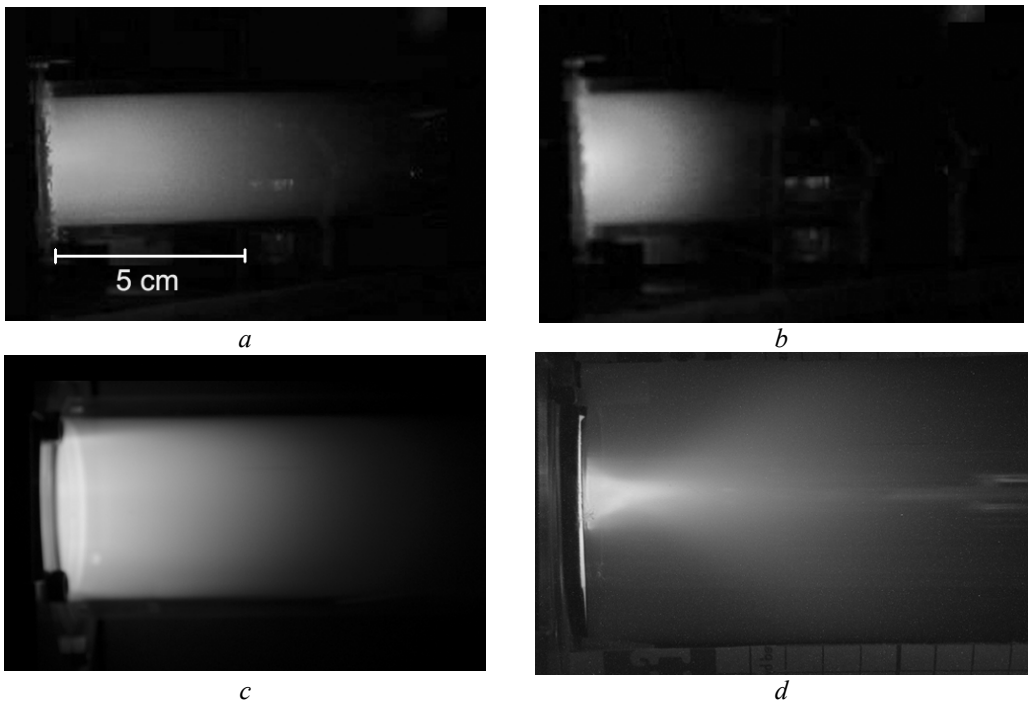

Figure 2.2. Visible spontaneous emission of gas in the field-free drift space beyond the anode. (a) Ne, gas pressure p = 5 mbar; charging voltage V_0 = 15 kV; (b) Ne, p = 10 mbar, V_0 = 15 kV; (c) He, p = 20 mbar, V_0 = 5 kV; (d) He, p = 30 mbar, V_0 = 15 kV

Since there is no external electric field in the gas behind the mesh anode where the glow is observed, one can suppose that the time-integrated spatial distribution of the glow $I_t(x)$, excited

by the e-beam in the drift space, is a function of local energy deposition into the gas by the e-beam. The length of the glow region, determined from the spatial glow distribution, is related to the electron propagation distance in the gas, which is a measure of the initial electron energy in the beam. In order to find how the local time-integrated intensity depends on the local energy deposition into the gas we express the time integrated spatial glow distribution in terms of the e-beam energy distribution function:

$$I_t(\vec{x}) \propto \sum_i \int_\varepsilon n\, p_i\, \sigma_i(\varepsilon) f(\varepsilon, \vec{x}) \sqrt{\varepsilon}\, d\varepsilon \tag{2.1}$$

where n is the neutral atom density, p_i is the probability of the radiative relaxation of the excited state i, neglecting all non-radiative processes, σ_i is the excitation cross-section of state i by the impact of an electron with electron energy ε and f is the electron energy distribution function in the e-beam. The electron energy distribution function is determined by the initial energy spectrum of the electrons entering the field free region behind the mesh anode and the transport equation of the e-beam in the gas. For electron energies in the keV range the continuous slowing down approximation is valid to solve the transport equation (see chapter 1, section 1.3.5). In this approximation the electron dynamics is described by the stopping power *dE/dx*, that is the energy loss per unit path length in terms of eV/cm. It is determined mostly by inelastic collisions of electrons with atoms. The stopping power not only describes the electron energy loss, but also the power deposition into the ambient gas due to the deceleration of electrons in the gas. Therefore, the time-integrated spatial distribution of the glow is proportional to the local energy deposition density, which is the product of the average local energy loss rate for a single electron and the number of electrons passed trough a unit area. It is the time integral of the electron flux, which is proportional to the local e-beam current density j_b:

$$I_t(\vec{x}) \propto \frac{d\hat{E}(\varepsilon(\vec{x}))}{dx} \int_t j_b(\vec{x}) \tag{2.2}$$

As electrons are decelerated during their propagation through the gas, the average electron energy in the beam as well as the e-beam current density decrease. When the average electron energy is higher than the ionization potential of the gas, the stopping power *dE/dx* increases with decreasing electron energy (see figure 1.2 in chapter 1) and thus the electron deceleration rate increases. At lower electron energy the stopping power decreases with decreasing electron energy. When the electron energy is less then the required energy for excitation of the gas atoms or molecules, no light will be produced. Therefore, the length of the visible glow can be used to estimate the range R, that is the penetration depth of the e-beam into the gas. The range R is an indication of the initial electron energy. The length of the glow only roughly shows the range, because for a strict analysis the radial distribution (perpendicular to the path of the e-beam propagation) also should be taken into account, which depends on the angular distribution of the electron scattering during the collisions. However, the longer the glow region, the higher the range R.

In reference 18 it is shown that the range R increases with E^2 and decreases with the mass density of the gas ρ, as follows:

$$R \propto \frac{E^2}{\rho} \propto \frac{E^2}{p\,A} \tag{2.3}$$

where p is the gas pressure and A is the atomic weight of the gas. The average electron energy or electron energy distribution in the e-beam is not easily measurable in gases at moderate pressures. Thus the $R\,p\,A$ product is a good qualitative measure for the average electron energy in the beam. For example, in figure 2.2 (a) the gas pressure of Ne is two times lower than in figure 2.2 (b), while the charging voltage is the same. One can see from these two figures that the range is almost two times longer for the lower gas pressure. This means that the energy of the electrons in the beam is almost the same. On the other hand, the electron energy in the beam depends not only on the charging voltage, but also on the gas pressure and the kind of gas used, as is discussed later in this chapter. For instance, in figure 2.2 (c) the range is almost the same as in figure 2.2 (a), thus the initial electron energy in the two beams is almost equal in both cases. However, the gas pressure of He (c) is 20 mbar and the atomic weight is 4, while the gas pressure of Ne (a) is only 5 mbar and the atomic weight is 20. Correspondingly the $p\,A$ products are 100 (a) and 80 (c) and are of the same magnitude while the charging voltage in the case of He is much less, only 5 kV (c) compared to 15 kV in Ne (a).

The measurements of the e-beam current and the energy efficiency of the e-beam generation in the open barrier discharge have been performed earlier [19, 20]. Both measured quantities are important parameters because the X-ray dose produced by the e-beam in the gas depends on them. The experimental setup in those experiments was the same as in our experiments except for the dielectric cathode. We used a larger dielectric cathode but the specific capacitance was almost the same. It resulted in a higher capacitance of the cathode and a slower voltage rise time compared to the values reported in [19, 20]. However, qualitatively the discharge behavior is the same, and the results given in references 19 and 20 are still valid for a correct understanding of the results of our experiments.

A detailed description of the working principle of the e-beam generation system is given in the earlier mentioned papers so at this place only a short description will be presented. After closing the electrical circuit by the thyratron switch, first a voltage reversal is observed due to the discharge of a stray capacitor that is formed by the rear electrode and the anode holder of the generator. So, under vacuum conditions the maximum potential difference applied to the acceleration gap is twice the charging voltage V_0 of the dielectric (see reference 19 and figure 2 therein). When the chamber is filled with gas, the voltage waveform is the same as the voltage waveform under vacuum conditions until a gas breakdown occurs at a voltage U_{br}. The breakdown voltage U_{br} is determined by the charging voltage V_0, the voltage rise time and the discharge formation time, which is governed by the ion mobility. For example, in He U_{br} is almost constant at a gas pressure less than 30 mbar and then decreases with a pressure increase (see reference 19 and figure 3 therein). On the other hand, U_{br} increases with the charging voltage V_0. U_{br} has apparently a nonstatic character and it is much higher than the static breakdown voltage [24]; at a gas pressure less then 30 mbar it is even higher than V_0. Note that the maximum possible kinetic energy of the generated runaway electrons is determined by the breakdown voltage.

Secondly, the e-beam peak current density j_b increases sharply at low gas pressure and then slowly decreases with an increase of the gas pressure (see reference 19 and figure 4 therein). The peak current density increases with the charging voltage from ~ 15 A cm^{-2} at V_0 = 7.5 kV to ~ 58 A cm^{-2} at V_0 = 20 kV in He [19]. On the other hand, the gas pressure, at which the maximum j_b is observed, slightly decreases with increasing charging voltage from ~ 15 mbar at V_0 = 7.5 kV to ~ 10 mbar at V_0 = 20 kV in He [19].

The energy efficiency of this e-beam generator was measured in [20] (see figure 6 therein) by means of a novel thermo-reflectance bolometer, described also in [20]. For example, in He at a gas pressure of 10 mbar the efficiency is ~ 55% at V_0 = 10 kV and increases up to ~ 95% at V_0 = 15 kV.

2.4 X-ray generation results

We expected from our novel source X-ray pulse lengths in the order of a few tens of ns long. For detection of the pulses a plastic scintillator NE102 with a fast rise and fall time (specified as 0.9 and 2.6 ns respectively), originally designed for a maximum efficiency and linearity in the MeV-range (~ 1.2*10^4 photons/MeV), was used. The radiation of the scintillator was detected by a photo-multiplier. The response time of the photomultiplier was measured to be ~ 5 ns. In our experiments the scintillator was used in the keV-range, although here the efficiency is much lower and the linearity is not specified. The measurements of the X-ray pulses have been performed using a 100 MHz bandwidth oscilloscope. This resulted in uni-polar (negative voltage) signal pulses from the photomultiplier as shown in figure 2.3, with a temporal width of ~ 13 ns (FWHM) for a discharge in Ar at a pressure of 4 mbar without Al foil in the discharge chamber. The shape and the half-width of the X-ray pulse waveforms are almost independent on the charging voltage, the type of gas used, and the way the X-rays have been generated, either in a gas or in an Al target. However, the signal amplitude and the delay of the X-ray signal, with regard to the discharge current and voltage, depended on the above mentioned parameters.

In order to prove the possibility of using even light rare gases, like He or Ne as target for X-ray generation, first the X-ray signal, produced in a discharge in He without Al foil in the chamber, was measured as a function of the discharge voltage at three different gas pressures. The measured dependence of the detected X-ray signal on the discharge voltage is shown in figure 2.4, where the gas pressure is 25 (1), 20 (2) and 15 mbar (3). It is seen that for our configuration the generation of X-rays showed a threshold value at around 8 kV. For higher charging voltages the X-ray signal increased with higher voltages.

Then the X-ray signals were measured with and without an Al foil inside the discharge chamber for different gases and at different gas pressures. The dependence of the X-ray signal on the He pressure is shown in figure 2.5 for a constant discharge voltage of 15 kV. For the trace in this figure denoted (1) the electrons were stopped by an Al foil placed in the discharge chamber (see figure 2.1), while for trace (2) the X-ray radiation was produced by the deceleration of electrons directly by collisions with He atoms (without an Al foil in the discharge chamber). At a pressure above 10 mbar both curves show a similar behavior such as a maximum at about 30 mbar (note that the X-ray signal without the foil is about 5 times smaller). On the other hand, below 10 mbar, with decreasing pressure, the X-ray signal without foil rises and even surpasses the signal obtained with a foil (at few mbar). We believe that this is due to X-rays generated by stopping of electrons in the chamber wall, because for lower gas pressures the visible glow of the gas tends to fill almost the entire volume of the discharge chamber as can be seen from figure 2.2. This can be understood because, for lower pressures, the mean free path and thus the penetration depth of fast electrons in the gas increases leading to a broader and longer visible

glow of the gas. As a result, more fast electrons are scattered towards the wall of the chamber causing there X-ray generation.

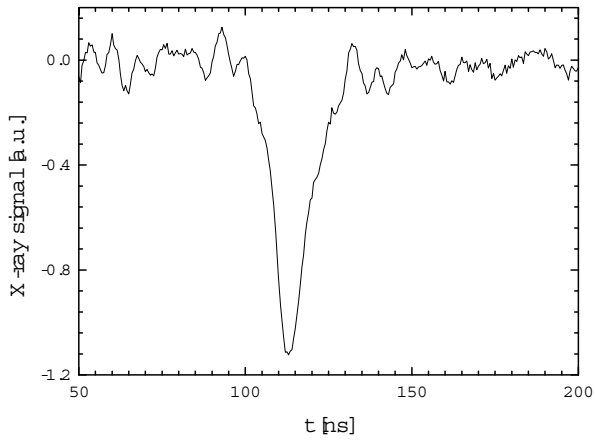

Figure 2.3. Typical waveform of an X-ray signal detected by the scintillator-photomultiplier system. Discharge in Ar at a pressure of 4 mbar. The charging voltage is 15 kV. The X-rays are produced in Ar without an Al foil inside the discharge chamber.

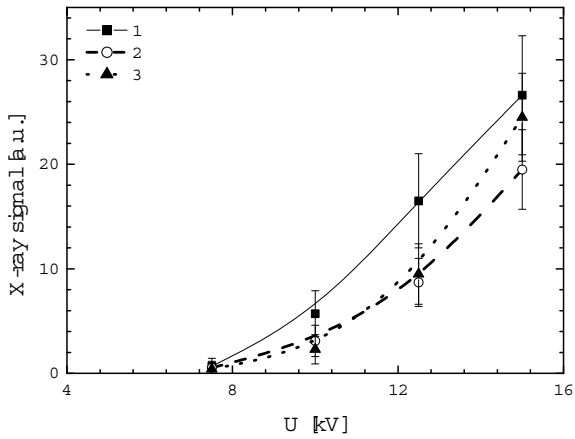

Figure 2.4. Dependence of the X-ray signal, generated in a discharge in He without an Al foil inside the discharge chamber, on the discharge voltage. The gas pressure is 25 (1), 20 (2) and 15 mbar (3).

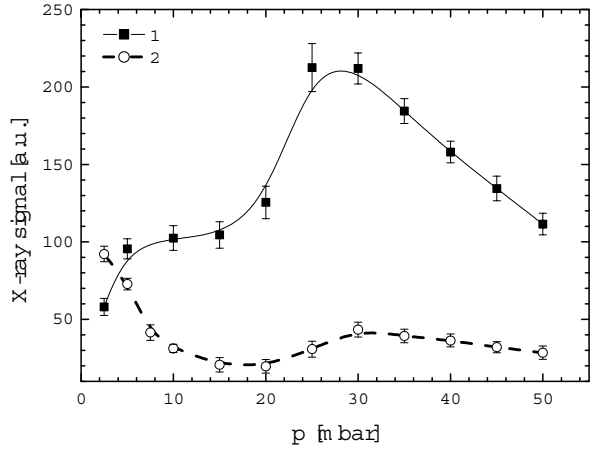

Figure 2.5. Dependence of the X-ray signal on the He pressure. The charging voltage is 15 kV. 1: with Al foil inside the discharge chamber, 2: without Al foil.

For discharges in Ne, the same experiments lead to different results as it is shown in figure 2.6 (charging voltage 15 kV). The trace denoted by (1) represent the case where the electrons were stopped by the Al foil placed in the discharge chamber and in case (2) the foil was removed. In both cases the signal amplitudes are almost equal over the entire observed pressure range and the maximum X-ray signal is observed at a gas pressure of ~ 5 mbar in both cases.

With an Al foil mounted, the pressure dependence for He (figure 2.7; trace 1), Ne (figure 2.7; trace 1) and Ar (figure 2.7; trace 1) were recorded in order to be able to compare the X-ray generation in different types of gases. Note that the maximum X-ray signal is almost the same in all gases, however, the gas pressure of the maximum X-ray signal decreases with increasing atomic weight of the gas. In He the maximum X-ray signal is observed at a pressure of ~ 25 mbar, in Ne at ~ 5 mbar and in Ar at ~ 2.5 mbar.

Also the direct X-ray generation in these three gases (with the Al foil removed) have been measured for comparison (see figure 2.8). The three curves shown in this figure correspond to He (trace 1), Ne (2) and Ar (3). Again it can be seen that the gas pressure at which the maximum X-ray signal is observed decreases with increasing atomic weight of the gas. And again, in He the maximum X-ray signal is observed at ~ 25 mbar, in Ne at ~ 5 mbar, and in Ar at ~ 2.5 mbar. However, now the maximum of X-ray generation is observed in Ar while He shows the lowest efficiency.

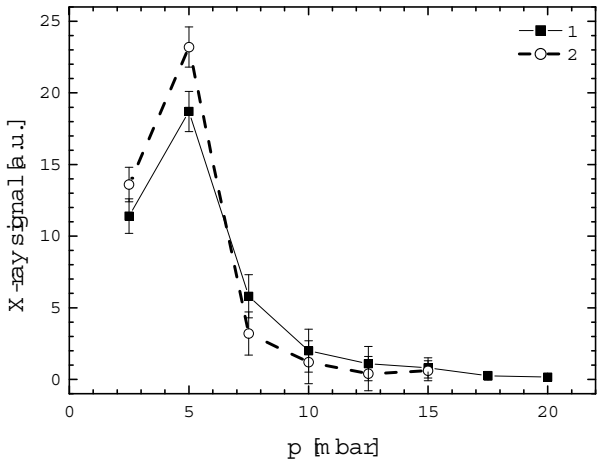

Figure 2.6. Dependence of the X-ray signal on Ne pressure. Charging voltage is 15 kV. 1: with Al foil inside the discharge chamber, 2: without Al foil.

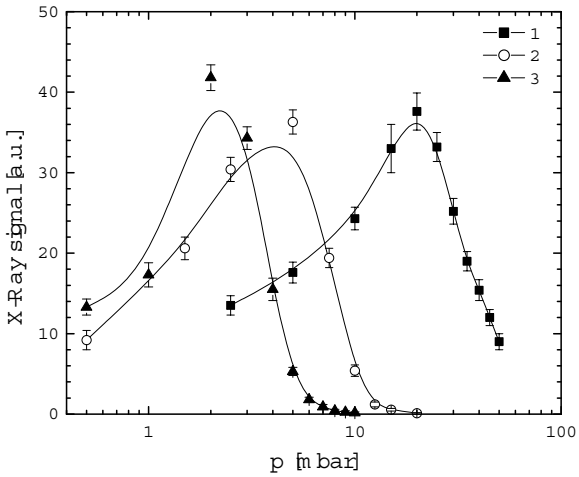

Figure 2.7. Dependence of the X-ray signal, generated in the Al foil target, on gas pressure. Charging voltage is 15 kV. 1: He, 2: Ne, 3: Ar.

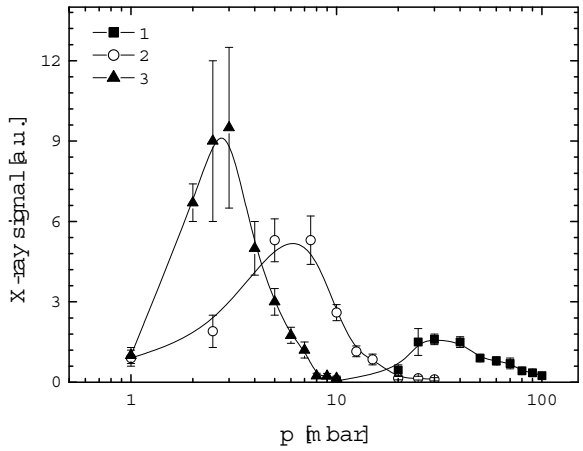

Figure 2.8. Dependence of the X-ray signal generated in gases, without an Al foil target, on gas pressure. Charging voltage is 15 kV. 1: He, 2: Ne, 3: Ar.

For a preliminary estimation of the mean photon energy of the generated X-rays the attenuation of the X-rays through an increasing number of Al foils (with equal thickness) was measured. This method is based on the following assumptions. For a monochromatic beam the attenuation increases exponentially with the number of foils. The rate of this exponent is determined by the mass absorption coefficient. For a non-monochromatic spectrum the total attenuation is the integral of the attenuation coefficients of all spectral components because the attenuation coefficient depends on the photon energy.

Two examples of measured attenuation curves, used for the estimation of the average X-ray photon energy, are shown in figure 2.9. The X-rays were produced with a discharge in He at a pressure of 40 mbar (lower trace) and 20 mbar (upper trace) at a charging voltage of 15 kV. As will be discussed later, only the high-energy part of the X-ray (bremsstrahlung) spectrum (several keV wide) was observed. These photons can be produced only by high-energy electrons with an energy close to the maximum energy. It is expected that for a constant charging voltage the maximum electron energy should decrease monotonically with rising pressure. This is what can be seen in figure 2.9. The best linear fit of curve 1 (40 mbar) gives an average photon energy of ~ 4 keV, while for curve 2 (20 mbar) ~ 6 keV is estimated. Further experiments and a more detailed analysis of the attenuation curves should be used to obtain a complete spectral analysis of the generated X-rays. The preliminary results show, however, that X-ray photons are generated with an energy that is comparable to the charging voltage multiplied with the electron charge.

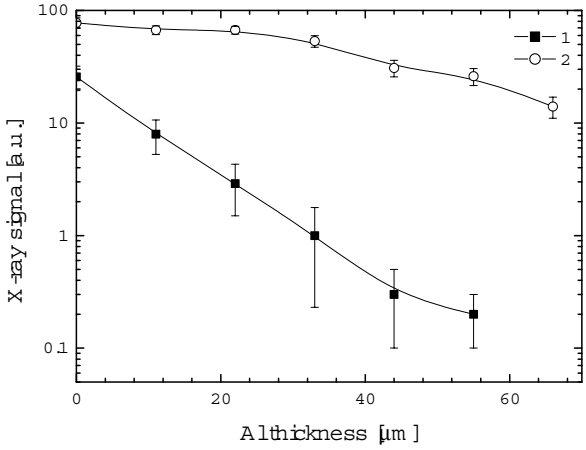

Figure 2.9. Attenuation curve of the X-ray signal generated in an Al foil target. Discharge in He at p = 40 (1) and 20 mbar (2), charging voltage 15 kV.

2.5 Registered signal processing: influence of the detector response function and signal to noise ratio improvement

In this section a detailed analysis is given in which way the measured X-ray signal should be interpreted and how it is related to the real signal. Generally speaking the measured waveform of a signal is always more or less disturbed by two fundamental effects: the response function of the measuring device and noise. In the previous section it has been observed that the FHWM of the measured X-ray signal is almost constant and equal to ~ 13 ns. This constant FWHM value may be due to a constant duration of the X-ray pulse or caused by the detector response function. In order to find how the detector response function influences the width of the detected signal in our experiments, compared to the original signal, a few very general assumptions are discussed.

The response or, also called, apparatus function, $g(t)$, describes the response of the measuring device to a delta-function shaped signal $\delta(t)$. The measured signal, $f_{out}(t)$ is given by a convolution:

$$f_{out}(t) = \int_{-\infty}^{t} f_{in}(\tau) g(t-\tau) d\tau \tag{2.4}$$

where $f_{in}(t)$ is the real (but unknown) shape of the signal. The apparatus or response function leads to various types of changes of the shape of the measured signal, such as, for example, a

delay (e.g., due to long transmission lines), a broadening or a smoothing of the pulse (e.g., due to RC or LC time of the measuring system).

The real signal shape $f_{in}(t)$ can be found from the registered signal $f_{out}(t)$ if the response function $g(t)$ is known. The response function can be measured, for example, with help of narrow input signal. If the response time of the measuring unit is much longer than the width of the input signal, then $f_{in}(t)$ in Eq. 2.4 can be replaced by a delta function:

$$f_{out}(t) = \int_{-\infty}^{t} a\,\delta(\tau) g(t-\tau)\,d\tau = a\,g(t) \tag{2.5}$$

where a is the area (time integral) of the input signal $f_{in}(t)$. Thus measuring with a very slow detector reveals the apparatus function, but the amplitude of this response is proportional to the area of the input signal.

In the opposite case, when a slow signal is measured with a very fast detector, Eq. 2.4 can be written as:

$$f_{out}(t) = \int_{-\infty}^{t} f_{in}(\tau) b\,\delta(t-\tau)\,d\tau = b\,f_{in}(t) \tag{2.6}$$

where b is the area of the response function of the detector. Thus, in this case the measured signal waveform equals the input signal except for a constant scaling factor.

When the signal widths and the apparatus function are comparable, the measured shape of the waveform is more complicated and is given by a convolution of the input signal and the detector response function (see Eq. 2.4). In our experiments the rise and fall time of the scintillator NE102 response function are known to be 0.9 and 2.6 ns respectively, the characteristic response time of the photomultiplier is ~5 ns and the measured X-ray signal width is ~ 13 ns. So the response time of the scintillator and the photomultiplier is less but comparable to the signal width. Thus, neither Eq. 2.5 nor Eq. 2.6 is really valid in our case. Only in some special cases, as discussed in chapter 3, $f_{out}(t)$ can be just a linear combination of a part proportional to the signal's area (like in Eq. 2.5) and a part proportional to the signal itself (like in Eq. 2.6). In our particular experiments, described in the present chapter, it is also not the case.

As mentioned before the input signal waveform can be restored from the measured signal, if the response function is known, by means of the Fourier transformation or by direct numerical deconvolution of Eq. 2.4. Apart from being complex, these procedures require some additional "before hand" assumptions on the initial (input) signal. In some cases, this may lead to the appearance of artificial structures, like oscillations, on the restored signal waveform. In our particular case we are not interested in the shape of the X-ray pulse but only in its real width. In order to find out how the detector response broadens the recorded X-ray pulse and whether the amplitude of the measured signal is proportional to the amplitude of the X-ray pulse we have performed a numerical simulation.

In this numerical model we have assumed that the overall response of the detector is given by a convolution of the scintillator response and the response of the photomultiplier. In figure

2.10 the responses of the scintillator to a short signal < 1 ns, as given in the specifications by the manufacturer NE Technology Ltd. (presented by trace 1), and of the Philips 56AVP photomultiplier (trace 2), are shown. As mentioned above, the rise and the fall time of the scintillator NE102 response function (trace 1) is 0.9 and 2.6 ns respectively. The response function of the photomultiplier (trace 2) has a rise time of ~ 0.5 ns and an exponentially decaying tail with a time constant of ~ 5 ns. Convolution of these two responses in accordance to Eq. 2.4 gives the expected apparatus function of detector (trace 3), which is a combination of these two devices. It can be seen that the resulting response function (trace 3) has a rise time of ~ 5 ns and a relatively long decaying tail, resulting in a FWHM of ~ 9 ns.

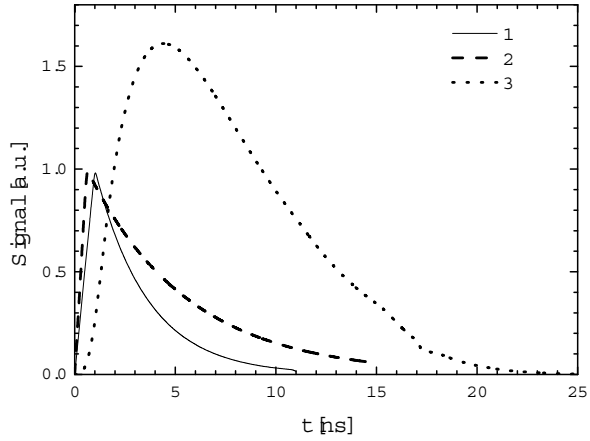

Figure 2.10. Apparatus functions of the scintillator NE102 (1) and the Philips 56AVP photomultiplier (2), normalized to unity, and the resulting response of the combined detector (3).

The resulting width of the detector response function (~ 9 ns) is shorter but comparable to the FWHM of the registered X-ray signal (Fig. 2.3). Therefore, one can suppose that the actual X-ray pulse width is comparable to the FWHM of the detector response function. On the other hand, the shape of the detector response function is asymmetric, while the registered X-ray is almost symmetric.

In order to determine broadening of the input signal by a response function of a comparable width, the expected response function of the detector has been tested against model input signals. Although a test input signal may be of any shape, we have chosen Gaussian signals for a number of reasons: a Gaussian pulse is symmetric; it consists only out of rising and falling slopes without a constant middle part; it has no steep edges, (which is undesirable in a finite difference numerical integration scheme employed in the model) and last but not least, the FHWM of the convolution of the detector response function and a Gaussian pulse, longer than the FWHM of the response function, is predictable in the analytical model. As long as we are interested only in the broadening of the signal and not in its real shape, Gaussian pulses are valid choices for a test signal.

In order to find the expected width of a registered signal, the convolution of two Gaussian-shaped test pulses with the expected detector response function has been investigated. The initial shape of the pulses is given by the formula $f(t) = exp(-(t-\tau)^2/a^2)$. For the first (short) pulse τ = 6 ns and a = 2.5 ns, and τ = 11 ns and a = 5 ns for the second (longer) pulse, corresponding to a FWHM of ~ 4 and 8 ns respectively (see figure 2.11, traces 1 and 2). The results of the convolution of these test pulses with the response curve of the detector is shown in figure 2.11 (traces 3 and 4). It can be seen that there is a significant broadening of the short (4 ns) test signal and almost no broadening of the longer (8 ns) test signal. It can further be seen that the convolution of the short test signal (trace 3) has almost the same shape as the apparatus function of the detector (see figure 2.10 (3)), and the shape of the convolution of the second test signal (trace 4) is much closer to the shape of the original signal (trace 2). In other words, the convolution of the short test signal (a FWHM of ~ 4 ns) with a modeled response function (a FWHM of ~ 9 ns) is close to the prediction of Eq. 2.5, while the width and the shape of the convoluted long test signal (with a FWHM of ~ 8 ns) is close to the prediction of Eq. 2.6. It is obvious that for shorter signals (< 1 ns) and longer signals (> 15 ns) the validity of Eqs. 2.5 and 2.6 respectively is more satisfied regardless of the shape of the input signal. Our numerical model confirms this statement.

The results of our numerical modeling have been used for the estimation of the X-ray signal broadening due to the detector response function. In our experiments neither the FWHM nor the shape of the measured X-ray signal changes significantly. On the other hand, the FWHM of the registered signal is significantly longer than the estimated detector response function width (~13 and ~ 9 ns respectively), while the registered signal waveform is symmetric and the estimated response function is strongly asymmetric. According to the results of our numerical modeling, Eq. 2.6 predicts the convoluted signal shape and width quite accurately (with a precision of ~ 10 %). This means that the actual shape and the FWHM of the signal do not change drastically; the amplitude of the detected signal is proportional to the actual amplitude of the X-ray signal, and the measured FWHM of the signal ~ 13 ns is close to the actual width of the X-ray pulse (estimated to be ~ 11 – 13 ns).

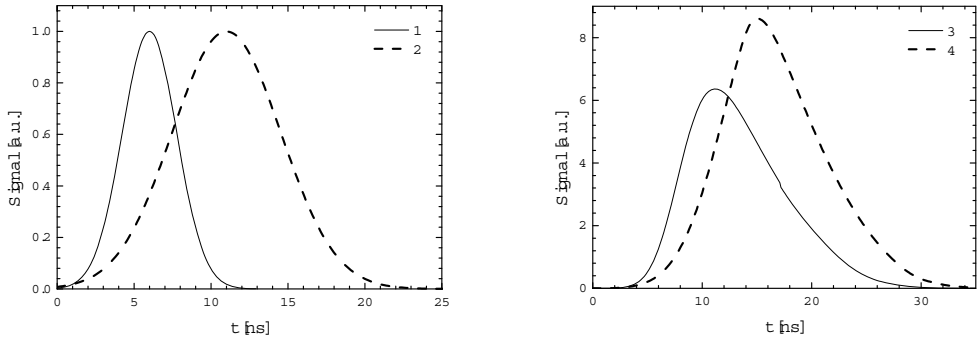

Figure 2.11. Input test signals (1 and 2) and the resulting signals (3 and 4), calculated as a convolution of the test signals with the response function of the detector (see figure 2.10 (3)).

Apart from the detector response function, a measured signal is also influenced by noise, which adds additional details and structures to the measured signal. When measuring a very strong signal or a signal with a very high signal to noise ratio, the additional noise pattern can be neglected. However, when a very weak signal had to be measured it always occurred with a strong noise background. This was the case, when the attenuation curve was measured using a large number of separate attenuators in order to determine the X-ray spectrum (see figure 2.9). In such a situation a noise removal procedure had to be applied.

In order to describe and validate the noise removal procedure, employed in our experiments, we first will explain the types of noise present in our experiments and the differences between those types of noise. Looking to the X-ray generation signals (but also other parameters measured in our experiments and described in this thesis), one observes that the detected noise roughly comes in two different types: random and systematic (regular) noise. The first one, shot or thermal noise, shows due to its fundamental nature a completely random pattern which changes from shot to shot. This kind of noise was seen in our experiments in two different forms: bi-polar noise (shot and/or thermal) and uni-polar noise pulses which come from random counts of the detector because of natural background radiation as is shown in figure 2.12 (a). Systematic or regular noise is usually caused by some electro-magnetic interference in the measuring circuit. The regular noise pattern is the same from shot to shot. The oscillations in the second half of the trace shown in figure 2.12 (a) are an example of regular noise due to interference from the pulsed discharge inside the X-ray source.

As can be seen from figure 2.12, trace (c) regular and random noise patterns were also present in the measured signal without an X-ray pulse falling on the detector, with the input window of the detector shielded by a lead plate. Due to the statistical independence of the various noise sources, the measured signal can be divided in three independent parts:

$$f_{meas}(t) = f_s(t) + f_{irn}(t) + f_{rn}(t) \tag{2.7}$$

where $f_{meas}(t)$ is the measured waveform, $f_s(t)$ is the signal itself, $f_{irn}(t)$ is the random noise and $f_{rn}(t)$ is the regular noise.

To improve the signal to noise ratio of a signal various techniques are applicable: Fourier filtering, adjacent points averaging, multiple curve averaging, etc. We have employed multiple curves averaging due to its simplicity and the accuracy of this method. Additionally, in our experiments the amplitude of the X-ray signal slightly fluctuates. The used averaging method allows us to determine the amplitude of the signal with a higher precision than in a one shot experiment and to measure the experimental error due to the fluctuation of the signal. Multiple curves averaging effectively suppresses the random noise while this approach does not change significantly the signal itself and the regular noise pattern, as shown in figure 2.12, trace b.

In order to remove the regular noise pattern from the measured waveform, the so called background signal has been measured in all experiments without the X-ray signal, when the input window of the detector is shielded completely by a lead plate. In this case the measured background waveform can be written as:

$$f_{bg}(t) = f_{rn}(t) + f^{1}_{irn}(t) \tag{2.8}$$

where the upper index of the irregular noise function denotes that it changes from shot to shot. The regular part of the noise function $f_{rn}(t)$ is the same with or without X-ray pulse. To enhance the background (regular noise) removal procedure the background signal is measured several times (typically from 5 to 10 times with and without the X-ray signal) and averaged.

So the signal to noise ratio enhancement procedure, employed in our experiments, consists of 3 steps: the measurements of the average signal waveforms, the measurements of the background signals and the subtraction of the background signal from the measured signal waveform. This procedure is illustrated in steps in figure 2.12. A raw experimental signal, measured in a single shot is shown in figure 2.12 (a). Uni-polar negative spikes, which are contributed to random counts of the detector, are also present in this case. An average of five similar shots of the signal is shown in figure 2.12 (b). It can be seen that the amplitude of the random counts is suppressed, but they appear more frequently. The average of 5 shots of the background signal is presented in figure 2.12 (c), and one can see that this shows suppressed random counts as well. The restored signal finally, defined as a difference of the averaged measured signal and the averaged background signal, is shown in figure 2.12 (d). The X-ray signal shown in figure 2.3 was obtained also using the same procedure.

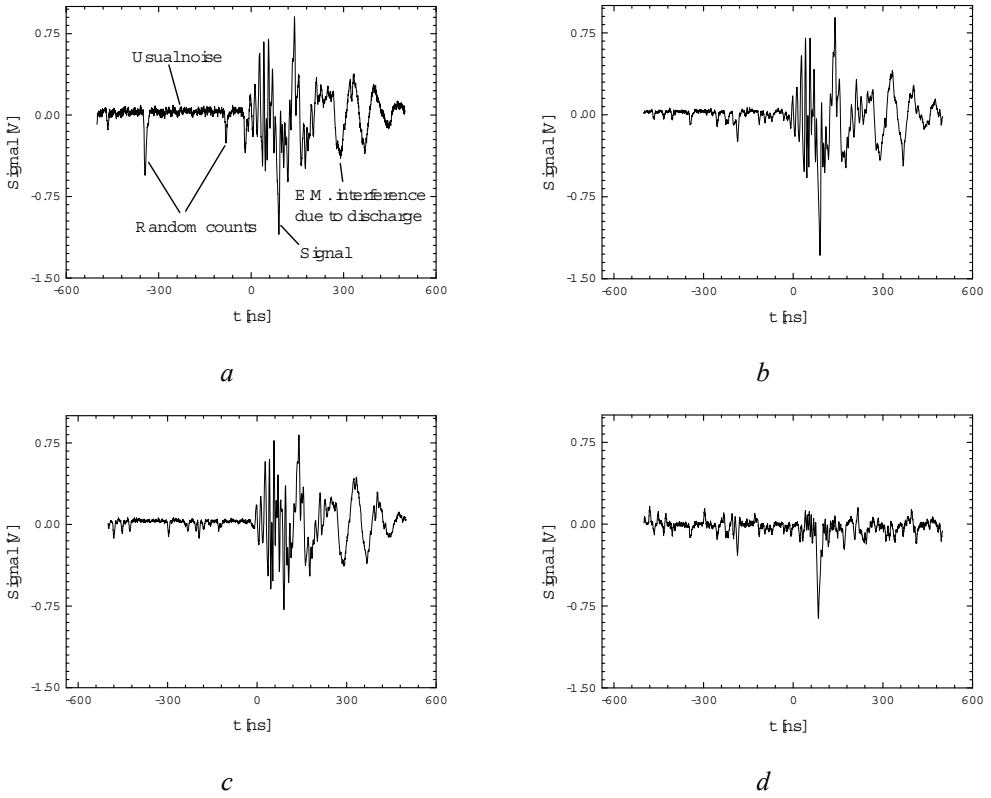

Figure 2.12. Steps of the noise removal procedure: (a) raw signal waveform; (b) average of 5 measured waveforms; (c) average of 5 measured background waveforms; (d) restored signal

In order to estimate the efficiency of the noise removal procedure we conduct the following reasoning. The multiple curves averaging procedure is mathematically described by:

$$\langle f(t)\rangle = \frac{1}{N}\sum_{i=1}^{N} f^{i}(t) \tag{2.9}$$

where N is the number of curves being averaged. Then, because of the linearity of Eq. 2.12, 2.13 and 2.15 and the statistical independence of the various noise sources, the averaged measured and background signals are:

$$\begin{cases} \langle f_{meas}(t)\rangle = \langle f_{s}(t)\rangle + \langle f_{rn}(t)\rangle + \langle f_{irn}(t)\rangle \\ \langle f_{bg}(t)\rangle = \langle f_{rn}(t)\rangle + \langle f_{irn}^{1}(t)\rangle \end{cases} \tag{2.10}$$

where the averaging does not change significantly the shape of the regular noise and the real signal, thus:

$$\begin{cases} \langle f_{s}(t)\rangle \cong f_{s}(t) \\ \langle f_{rn}(t)\rangle \cong f_{rn}(t) \end{cases} \tag{2.11}$$

This averaging changes the random part of the noise. Because the random noise pattern changes from shot to shot we use the maximum of the absolute value of the random noise peak amplitudes over the entire period of measurement to estimate the noise suppresion:

$$|f(t)| = \max(abs(f(t))) \tag{2.12}$$

Since the bi-polar part of the random noise has an average value of zero in the time domain (see figure 2.12) and the uni-polar random noise also has a baseline at zero level, this value is a good qualitative measure of the noise level.

Then the irregular noise suppression, observed in the figure 2.12, can be expressed as:

$$\frac{|f_{irn}(t)|}{N} \le |\langle f_{irn}(t)\rangle| \le \frac{|f_{irn}(t)|}{\sqrt{N}} \tag{2.13}$$

where the left part of the inequality corresponds to the suppression of the uni-polar irregular noise (random counts) and the right part corresponds to the case of bi-polar noise suppression (high frequency bi-polar pattern), achieved by averaging over N traces.

Then, from Eq. 2.10 the restored signal is:

$$\begin{aligned} \left\langle f_{signal}(t) \right\rangle &= \left\langle f_{meas}(t) \right\rangle - \left\langle f_{bg}(t) \right\rangle \\ &= \left\langle f_S(t) \right\rangle + \left\langle f_{irn}(t) \right\rangle - \left\langle f^1_{irn}(t) \right\rangle \\ &= \left\langle f_S(t) \right\rangle + f^2_{irn}(t) \end{aligned} \tag{2.14}$$

where:

$$\left| f^2_{irn}(t) \right| \leq \left| \left\langle f^1_{irn}(t) \right\rangle \right| \cong \left| \left\langle f_{irn}(t) \right\rangle \right| < \left| f_{irn}(t) \right| \tag{2.15}$$

The same averaging and background removal method is also used in the experiments described in the next chapters.

2.6 Discussion of the results

To explain the observed dependence of the X-ray signal amplitude on the different parameters like the applied voltage, gas pressure, target (Al foil or gas: He, Ne or Ar), as shown in figures 2.4 – 2.8, we need to find out which mechanism is responsible for the measured X-ray production. The two options are characteristic or bremsstrahlung radiation. A characteristic radiation spectrum consists of a number of narrow lines, which are typically in a few keV energy range for low atomic number (Z) elements, like Ne, Al, Ar. Moreover the X-ray photon energy from characteristic radiation does not depend on the incident electron energy. In contrast with this the energy spectrum of bremsstrahlung radiation shows a broad continuum, which is spread from zero energy to the high-energy cut-off, determined by maximum kinetic energy of the electrons hitting the target. Therefore, a bremsstrahlung spectrum strongly depends on the electron energy. So the spectrum of a measured X-ray signal is a criterion for the type of X-ray radiation in the observed signal.

In our experimental setup (see figure 2.1) the 0.1 mm Kapton foil output window, the open air gap between the discharge chamber and the photomultiplier housing and the the Al foil used as the input filter for the photomultiplier provide a certain cut-off photon energy, E_{min}. Only X-ray photons with an energy above E_{min} reach the scintillator/photomultiplier and are detectable. So, the observed X-ray spectrum has a low energy cut-off, which is independent on the electron energy and is determined only by the construction of the setup as well as a cut-off at the high-energy part that is depending on the electron energy.

In order to analyze the observed X-ray spectrum we first have to estimate the low energy cut-off E_{min}. The X-ray absorption in the medium is described by the exponential law (see also chapter 1, section 1.4):

$$I(x) = I_0 e^{-(\frac{\mu}{\rho})\rho x} \tag{2.16}$$

where $I(x)$ is the intensity of the beam propagated over a distance x, I_0 is the initial beam intensity, μ/ρ is the mass attenuation coefficient, and ρ is the mass density of the medium.
The exponential attenuation factors of each attenuator in a setup are simply multiplied when the beam is passing through more attenuators:

$$I_{final} = I_0 \prod_i e^{-(\frac{\mu}{\rho})_i \rho_i L_i} = I_0 e^{-\sum_i (\frac{\mu}{\rho})_i \rho_i L_i}, \tag{2.17}$$

where ρ_i and L_i are the mass density and the length of every component of this complex attenuator.

In our case the beam is passing through the Kapton output window of the X-ray source, the air gap between the source and the detector and the Al entrance window of the detector. In order to estimate E_{min} in our particular setup the mass attenuation coefficients of Al and air, provided from Hubbell and Seltzer from the NIST database [25, 26] (see Appendix, figure A.2) have been substituted into Eq. 2.17. For the Kapton foil we used the data from references 25 and 26 for similar kinds of plastics, as the exact absorption coefficient of the used Kapton foil was not known. From this we calculated that almost all 1 keV X-ray photons and more than 96% of the photons with an energy of 3 keV are absorbed on the path to the detector. For 5 keV photons only ~ 40% of the radiation is absorbed. We have estimated the cut-off energy E_{min} ~ 3.5 keV, a value at which ~ 10 % of X-ray photons are transmitted through this complex attenuator. This value can be compared with the energy of the characteristic Kα lines of Ar (2.96 keV), Ne (0.849 keV) and Al (1.49 keV) [27 - 29]. So it is seen that all Kα lines have a lower energy than the estimated cut-off energy. Thus, although characteristic radiation is produced either in the gas or in the Al target, it is too soft to reach the detector because it is absorbed by the Kapton output window, the air gap and the input Al foil filter in front of the detector almost entirely.

Bremsstrahlung radiation, as has been mentioned above, has a continuous spectrum ranging from zero to a maximum value that equals the maximum electron energy in the e-beam. What can be detected with our setup is thus the fraction its spectrum, extending from E_{min} ~ 3.5 keV to the maximum electron energy (~ 10 keV). We conclude that in our case the observed X-ray signal must consist of bremsstrahlung radiation.

From experimental data [30] and theoretical estimations [31] based on the Kramers cross-section [32] it is expected that in our experiments, where X-ray radiation due to bremsstrahlung from an optically thick target is observed, the X-ray signal should increase with the energy of the electrons E and the atomic number Z of the stopping medium. Additionally, the signal should be

proportional to the electron flux and thus to the electron beam current density j_b. So the question arises whether or not these predictions are valid in our experiments.

Suppose that the entire kinetic energy of the e-beam incident onto the target is converted into the X-ray radiation with a spectral energy distribution given by the commonly used Kramers cross-section for the bremsstrahlung process [31, 32]. Although the Kramers cross-section does not predict the fine structure of the bremsstrahlung spectrum, it gives the order of magnitude of the X-ray radiation intensity and a correct dependence of the radiation intensity on the electron energy and the Z-number of the stopping medium (the target). The Kramers cross-section is derived under the following assumptions: a dipole nature of the bremsstrahlung radiation, the dipole momentum of an impinging electron changes instantly during the interaction with an atomic nucleus and the maximum interaction distance between an electron and a nucleus is determined from the energy equality of the Coulomb interaction energy and the kinetic energy of the electron (or the Coulomb energy may be taken as a half of the kinetic etc., it changes only the numerical coefficient). Then the Kramers cross-section of the photon emitting process with a frequency ω (and energy ħω) during the interaction of a nucleus with a charge Z and an electron with a kinetic energy E_0 is:

$$\sigma_{Kr}(\omega) = \begin{cases} k_1 \dfrac{Z^2}{E_0} & for \;\; \omega \le \dfrac{E_0}{\hbar} \\ 0 & for \;\; \omega > \dfrac{E_0}{\hbar} \end{cases} \tag{2.18}$$

where $E_0/\hbar$ is the high-energy cut-off of the spectrum and the constant k_1 includes the electron mass, charge and the speed of light. From Eq. 2.18 it can be seen that the Kramers differential cross-section $\sigma_{Kr}(\omega)$ is constant in the frequency region from 0 to the cut-off $E_0/\hbar$ and is zero for higher frequencies. The total cross-section for an optically thin target is given by the integration of the differential cross-section over the frequency interval. The target is optically thin if the energy loss of the electron is negligible compared to their initial kinetic energy, in other words, the electron stopping range in the material of the target (see chapter 1, section 1.3.5 and Appendix, figure A.1) is much longer than the physical thickness of the target. The integration shows that for a thin target the total cross-section is constant, i.e., independent on the initial electron kinetic energy and proportional to the Z^2, which is a property of the target only.

In our experiments the target (either the Al foil or the gas medium) is optically thick, so the electrons are stopped entirely in the gas or in the Al target. In order to find the spectral distribution of the X-rays P_ω we apply the continuously slowing down approximation (CSDA) and integrate Eq. 1.18 over the path length of the electrons. For this we use the stopping power for electrons as given by Bethe's formula [33] (see also chapter 1, section 1.3.5, Eq. 1.29). The electron density in Eq. 1.29 is $n_e = Z\, n_0$, where Z is atomic number (nucleus charge) n_0 is the atomic concentration. In a condensed matter, e.g. a metal (Al in our case), the atomic concentration n_0 is determined by the packing density (inter-atomic distance), which changes very little compared to the Z-number. In gases the atomic concentration is given by the gas temperature T and the gas pressure $p = n_0\, k\, T$, where k is the Boltzman constant. Thus, at atmospheric pressure and at room temperature, n_0 is the same for all gases. The logarithmic term

changes very slowly compared to *1/E(x)* and can thus be neglected, such that Eq. 1.29 simplifies to the so-called Thompson-Whiddington law [31] (see also Eq. 1.30 in chapter 1):

$$\frac{dE(x)}{dx} \propto -n_0 \frac{Z}{E(x)} \tag{2.19}$$

Integration of Eq. 2.19 results in a simple square-root dependence of the electron energy on the path length x. At the maximum penetration depth of the electron into the medium x_{max} the electron energy is zero. Function $E(x)$ obtained from Eq. 2.19 is substituted into the equation for the differential cross-section Eq. 2.18, multiplied by the atomic density n_0 and integrated over the path length of the electron from 0 to x_{max}. The spectral component of the X-ray intensity P_ω, produced by a single electron with the initial energy E_0 is then:

$$P_\omega = k_2 Z(E_0 - \hbar\omega) \tag{2.20}$$

where constant k_2 again includes the electron mass, charge and the speed of light. Eq. 2.20 shows that the X-ray intensity obtained from a thick target, does not depend on the atomic density, but on the Z-number. More specifically, according to Eq. 2.20, the radiation spectrum of a thick-target decreases linearly with increasing photon energy towards the high-energy cut-off at $E_0/\hbar$.

In order to find the amount of the detectable X-ray radiation S generated by a single electron with a initial kinetic energy E_0 Eq. 2.20 has to be integrated over the photon frequency range from $E_{min}/\hbar$ to $E_0/\hbar$. The lower integration boundary is due to the fact that we can detect only photons with energy higher than E_{min}.. So, the amount of detectable X-ray radiation from a single electron is:

$$S = \frac{k_2}{2\hbar} Z(E_0^2 - E_{\min}^2) \tag{2.21}.$$

To calculate the total amount of radiation generated by the entire electron beam with current density J_b one has to multiply the generated amount of radiation by a single-electron (Eq. 2.21) by the energy distribution function of all the electrons (e-beam current) and integrate this product over the whole energy range. If one considers a normalized energy spectrum for the e-beam current density $j(E)$:

$$\int_0^{E_{\max}} j(E)dE = 1 \tag{2.22}$$

where E_{max} is the maximum electron energy in the beam determined by the discharge conditions; then the total amount of the X-ray radiation S_{total}, produced by the e-beam is:

$$S_{total} = \frac{Zk_2 J_b}{2\hbar e} \int_{E_{\min}}^{E_{\max}} (E^2 - E_{\min}^2)\, j(E) dE \qquad (2.23)$$

Here, the lower integration boundary is set by the fact that only electrons with an energy higher than E_{min} produce X-ray photons that can be detected. E_{max} is the upper limit of the X-ray photon energy, as has been discussed above.

It is important to note that in our experiments the upper limit of the kinetic energy for electrons in the beam E_{max} is related, but not equal to the charging voltage. Rather, the maximum accelerating voltage (potential difference between the cathode and the anode) corresponds to the breakdown voltage of the gas U_{br}. This can be seen from figure 3 in reference 19, where it is shown that for a fixed gas pressure the breakdown voltage increases with the charging voltage. On the other hand it can be seen also that for a fixed charging voltage the breakdown voltage decreases with an increase of the pressure. This is due to the pulsed mode operation where the non-zero discharge formation time allows a very high voltage over the discharge gap provided it can be applied in a time shorter than the discharge formation time.

The current density of the e-beam, J_b, depends on the gas pressure and the charging voltage as has been reported in reference 19 and figure 4 therein. Specifically, for a fixed gas pressure a higher charging voltage leads to a higher e-beam current density. For a fixed charging voltage the e-beam current density increases up to a certain maximum and then decreases with the pressure. This observation, and the pressure dependence of the electron energy described above, is consistent with the pressure dependence of the X-ray signal measured (see figures 2.5 to 2.8).

The increase of the observed X-ray signal with increasing charging voltage (see figure 2.4) can also be explained with this knowledge. A higher breakdown voltage at the same gas pressure leads to a higher e-beam current density J_b, and a higher upper limit of the electron and photon energy E_{max}. Also the e-beam energy spectrum changes in such a way, that more electrons are in the high-energy than in the low-energy part of the spectrum, because a higher electric field strength is more beneficial for the runaway effect. Thus, according to Eq. 2.23, this results in a higher amount of radiation detected. This also indicates that our system could be improved considerably in terms of achieving a higher X-ray flux, a higher X-ray photon energy and a higher optimum gas pressure at which the maximum amplitude of the X-ray signal is observed, by applying a higher voltage pulse with a shorter rise time in the order of nanoseconds.

In order to explain why the maximum X-ray signal amplitude generated directly in gases increases and the optimum gas pressure decreases with increasing atomic weight of the gas, as shown in figure 2.8, we first analyze figure 2.7. In this figure the experimental results are shown with an Al foil as electron stopping target. For the conditions where the maximum X-ray signal is observed (e.g. gases at moderate pressure) the penetration depth of fast electrons in the used gases, is much larger than the gap length between the mesh anode and the Al foil target. Correspondingly, one can neglect the energy loss of the e-beam in front of the Al target such that almost all energy of the e-beam is dissipated in the Al target. As a result, the maximum X-ray signal generated in the discharge chamber with the Al target inside should be the same,

irrespective of the gas that is used, if the current density J_b and maximum kinetic energy of generated electrons E_{max} are the same, as directly follows from Eq. 2.23. From our experiments we see from figure 2.7 that for the same e-beam parameters (current density and electron energy) the maximum X-ray values obtained in discharges with He, Ne and Ar are almost the same but occur at a lower pressure for a heavier gas. From figures 2.5, 2.6 and 2.8 we see that the maximum X-ray signal produced directly in gases, i.e., without Al target, is observed at a lower pressure for a heavier gas and that the maximum X-ray signal in each of the investigated gases is observed at the same pressure as in with the Al target (compare to figure 2.7).

The observed differences in the maximum X-ray amplitudes generated in the Al target and directly in He, Ne and Ar (figures 2.5 – 2.8) can be explained by the difference in the atomic number Z of the different media (see Eq. 2.23). With a Z number for He of 2 the lowest X-ray signal is produced directly in He without the Al target. The Z number of Al is 13 and therefore the X-ray signal measured from the Al target is higher under the same conditions (figure 2.5). Ne and Al have close Z values (10 and 13 correspondingly) and the observed X-ray signal is almost the same (see figure 2.6). It is expected that for Al the signal should be a bit stronger then directly in Ne because of the slightly higher Z, but it appears that the measured signal is slightly lower. This can be explained by the geometry of generation setup. When the electrons are stopped by the Al foil, all the X-ray radiation comes from the foil which is a plane. However, when the electrons are stopped by Ne (no foil), the radiation source is distributed along the entire electron path in the gas. Windows 4 and 8 (see figure 2.1) form a narrow solid observation angle for the amount of radiation to be detected. So for a distributed radiation source (without Al foil) the "effective" solid angle is larger, leading to larger signal on the detector for the same Z value medium. The largest signal is observed when the X-rays are generated directly in Ar (Z = 18) without Al target.

In order to prove validity of the given above explanation for the dependence of the X-ray amplitude on the gas pressure and for the dependence of the optimum gas pressure and maximum X-ray signal amplitude on the Z number of the gas used, we have normalized the data of figure 2.8 with respect to the Z numbers of He (Z = 2), Ne (Z = 10) and Ar (Z = 18). So we introduce here normalized curves with p Z and the X-ray signal/Z as coordinates. The choice of the horizontal scale in terms of p Z and vertical $1/Z$ scaling can be argued in the following way. The breakdown voltage and thus the maximum accelerating electric field strength are determined by the charging voltage and the formation time of the discharge. The discharge formation time depends on the gas pressure; it decreases with increasing pressure. On the other hand, the formation time is inversely proportional to the ion mobility μ_i, which is inversely proportional to the atom mass A and, thus, to Z. Heavier ions are slower. The pressure dependence of the breakdown voltage (see figure 3 in [19]) scaled as 1/Z. The stopping power dE/dx (Eq. 2.19) not only describes the propagation of the e-beam in the medium, but it is also the competitor to the accelerating field in the electron runaway effect (see chapter 1, section 1.3.5). In gases $n_0 \sim p$ and $dE/dx \sim p\,Z$. It is expected that the pressure dependence of the e-beam current J_b (see figure 4 in [19]) scales as $1/Z$ as well, namely in Ar the maximum e-beam current density is reached at lower gas pressure compared to Ne and, specially, to He. The vertical scaling $1/Z$ is given by Eq. 2.20, because at the same J_b and E_{max} the X-ray signal is proportional to Z. Therefore, it is expected that with these coordinates all three traces for He, Ne and Ar respectively, coincide.

The results of the normalization is shown in figure 2.13. The curves for Ne (2) and Ar (3) coincide quite well, taking into account the errors bars and the qualitative nature of our assumptions on the maximum electron energy and e-beam current density dependence on the gas pressure. However, for He (1) the maximum signal/Z value is higher than expected, probably, due to gas impurities which effectively increase the average Z number.

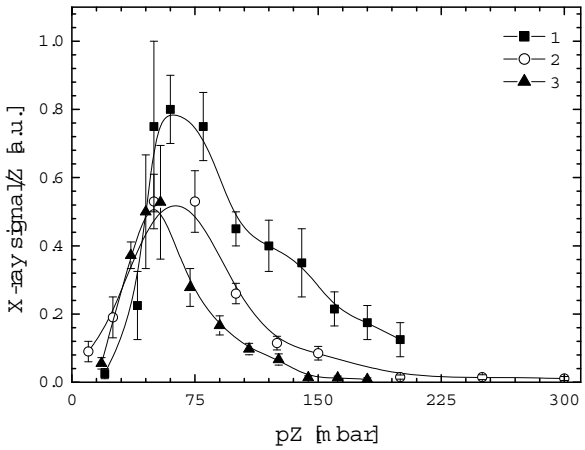

Figure 2.13. Dependence of the normalized X-ray signal amplitude generated in gases without an Al foil target, on the normalized gas pressure. Charging voltage is 15 kV. 1: He, 2: Ne, 3: Ar

Continuing our discussion of the results with the next figure, we observed in figure 2.9 a decrease of the average X-ray photon energy with increasing gas pressure at constant charging voltage. As mentioned above, the breakdown voltage U_{br}, which determines the maximum kinetic energy of the -electrons and the maximum available energy of the X-ray photons E_{max} (see Eq. 2.20), decreases with increasing gas pressure. Thus, a lower breakdown voltage leads to a lower maximum X-ray photon energy. At a lower U_{br} also a lower electric field strength is present near the dielectric cathode of the discharge chamber. As shown in reference 12, a higher electric field strength enhances the run away effect and more electrons are involved; in very strong fields all electrons may experience the run-away effect, resulting in a mono-energetic e-beam with the electron energy equal to the applied voltage. Therefore, at a lower breakdown voltage not only the maximum but the also the average kinetic energy of electrons in the beam is lower due to a shift of the electron energy distribution function towards the lower energy part. So, at a lower breakdown voltage a lower average photon energy should be observed in the detectable region from the threshold E_{min} to the maximum energy E_{max}. For example, the average X-ray energy obtained from the attenuation curve (see figure 2.9) is ~ 6 keV in He at a charging voltage of 15 kV and a gas pressure of 20 mbar and it is only ~ 4 keV at a pressure of 40 mbar.

From our measurements we can conclude that an even higher charging voltage would produce a more intense X-ray beam and also the upper energy limit of the generated X-ray photons would increase with the applied voltage. We have argued already that these improvements should be achievable by using a voltage pulse with a much shorter rise time (less than or comparable to 1 ns) because this would make it possible to apply a significantly higher voltage over the same discharge gap before gas breakdown occurs. By decreasing the voltage rise time to approximately 1 ns in our device and by increasing the charging voltage to ~ 100 kV we expect that electrons with a kinetic energy in the order of 50 – 100 keV can be generated and that the maximum output of X-rays would than occur at a gas pressure of ~ 10^2 – 10^3 mbar, i.e. near to atmospheric pressure. These expectations are supported by experiments from other groups, where

e-beam generation at atmospheric pressure was indeed observed [14] in a gas diode at a voltage of ~ 150 kV, a voltage pulse width of ~ 1.4 ns and a rise time of ~ 0.2 ns. However, the main drawback of the approach described in that paper was that a metal cathode (and not a dielectric one) was used. This gas diode scheme suffered from instabilities typical for all high-voltage metal-electrodes systems, and therefore the voltage pulse length was limited width to a few ns. Our open barrier discharge e-beam generator is free of all this instability problems because of the current limiting dielectric electrode. With these advantages our electron beam generator can be of great importance for all kind of applications where stable and homogeneous irradiation with X-rays is desired for large areas and at atmospheric pressures.

2.7 Conclusion

A new stable, reliable and simple, broad-area soft X-ray source based on an open barrier discharge with a ~ 12.5 cm^2 cross-section was realized and extensively tested. The electron beam produced in this discharge generates X-ray radiation by stopping the electrons either in an Al foil or directly in a gas in the form of bremsstrahlung. We investigated how the X-ray intensity depends on the parameters of the electron beam (like the electron energy and current density) and the stopping material properties (*Z*-number) of the medium. We found that the energy of the X-ray photons is comparable to the charging voltage of the source. The highest obtained energy in the X-ray spectrum depends on the maximum electron energy and the lowest energy is determined by the transmittance of the output window and the window of the detector (~ 3.5 keV).

The device is able to operate at a high repetition rate of up to several kHz. From our results we expect that, with an increase of the charging voltage to ~ 100 kV and by lowering the rise time to ~ 1 ns, the device should be capable to produce e-beams with a current density of ~ $10^2 – 10^3$ A/cm^2 and an electron energy of ~ 50 – 100 keV directly in gases at a pressure of ~ 0.1 – 1 atm. Such an e-beam source may be incorporated directly into the gas vessel or laser chamber filled with a sub- and near atmospheric pressure gas or gas mixture. Thus there is no need for a separation window and it may serve as a highly efficient preionisation source or even as a direct e-beam pumping source for the active laser medium. Such a source, when optimized to high photon energies of ~ 50 – 100 keV, may also be used in connection with a separation window between the source and the high pressure chamber as a powerful external X-ray preionization source for multi-atmospheric pressure gas lasers.

References:

[1] J.L. Barrett and J.J. Leventhal, Appl. Phys. Lett., **36**, 869 (1992)
[2] Z. Chang, A. Rundquist, H. Wang, M.M. Murnane and H.C. Kapteyn, Phys. Rev. Lett., **79**, 2967 (1997)
[3] J.A. Chakera, V. Arora, S. Sailaja, S.R. Kumbhare, P.A. Naik, P.D. Gupta, N.K. Gupta and B.K. Godval, Appl. Phys. Lett., **83**, 27 (2003)
[4] K. Oguri, H. Nakano, T. Nishikawa and N. Uesugi, Appl. Phys. Lett., **79**, 4506 (2001)
[5] D. Hong, R. Dussart, C. Cachoncinlle, W. Rosenfeld, S. Gotze, J. Pons, R. Viladrosa, C. Fleurier and J.-M. Pouvesle, Rev. Sci. Instr., **71**, 15 (2000)
[6] D.A. Hammer, D.H. Kalantar, K.C. Mittal and N. Qi, Appl. Phys. Lett., **57**, 2083 (1990)
[7] A. Heuberger, J. Vac. Sci. Technol., **B6**, 107 (1988)
[8] M.A. Piestrup, D.G. Boyers, C.I. Pincus and J.L. Harris, Appl. Phys. Lett., **58**, 2692 (1991)
[9] W. Knulst, M.J. v.d. Wiel, O.J. Luiten and J. Verhoeven, Appl. Phys. Lett., **83**, 4050 (2003)
[10] W.C. Röntgen, Nature, **53**, 274 (1896)
[11] R.C. Noggle, E.P. Krider and J.R. Wayland, J. Appl. Phys., **39**, 4746 (1968)
[12] L.P. Babych, *High-Energy Phenomena in Electric Discharges in Dense Gases: Theory, Experiment and Natural Phenomena*, ISTC Science and Technology Series, Vol. **2**, Arlington, VA: Futurepast (2003)
[13] V.F. Tarasenko, S.K. Lyubutin, S.N. Rukin, B.G. Slovikovskii, I.D. Kostyrya and V.M. Orlovskii, Technical Physics, **50**, 1462 (2005)
[14] V.F. Tarasenko, Appl. Phys. Lett., **88**, 081501 (2006)
[15] I.D. Kostyrya, V.F. Tarasenko, A.N. Tkachev and S.I. Yakovlenko, Technical Physics, **51**, 356 (2006)
[16] P.B. Repin and A.G. Rep'ev, Technical Physics, **49**, 839 (2004)
[17] V.V. Chorny, O.I. Frolov, V.M. Dubina, V.T. Kolisnyk, G.V. Tsepilov and V.S. Solovjov, Proc. of the 12th Int. Conf. on High-Power Particle Beams, BEAMS'98, Haifa, Israel, vol. **2**, 581-584 (1998)
[18] A.V. Azarov, S.V. Mitko and V.N. Ochkin, Quantum Electronics, **32**, 675 (2002)
[19] S.V. Mitko, Y.B. Udalov, P.J.M. Peters, V.N. Ochkin and K.-J. Boller, Appl. Phys. Lett. 83, 2760 (2003)
[20] S.V. Mitko, A. Yu. Oudalov, Y.B. Udalov, P.J.M. Peters and K.-J. Boller, Rev. Sci. Instr., **76**, 013101 (2005)
[21] A.V. Azarov, P.J.M. Peters, K.-J. Boller, Plasma Sources Sci. Technol. **16**, 110 (2007)
[22] P.A. Bokhan, D.E. Zarkevsky, Technical Physics Letters, **28**, 454 (2002)
[23] A.R. Sorokin, Technical Physics Letters, **10**, 836 (2003)
[24] Yu.P. Raizer, *Gas Discharge Physics*, Springer, London (1992)
[25] J.H. Hubbell, Internat. J. of Appl. Radiation and Isotopes, **33**, 1269 (1982)
[26] S.M. Seltzer, Radiation Research, **136**, 147 (1993)
[27] J.A. Bearden, Rev. Mod. Phys., **39**, 78 (1967)
[28] J. Schweppe, R.D. Deslattes, T. Mooney and C.J. Powell, J. Electr. Spectr. Relat. Phenom., **67**, 463 (1994)
[29] P.J. Mohr and B.N. Taylor, Rev. Mod. Phys., **72**, 351 (2000)
[30] J.G. Chervenak and A. Liuzzi, Phys. Rev. A, **12**, 26 (1975)
[31] M. Lamoureux, P. Waller, P. Charles and N.B. Avdonina, Phys. Rev. E, **62**, 4091 (2000)
[32] H.A. Kramers, Philos. Mag. 46, 836 (1923)
[33] H. Bethe, Ann. Phys., **5**, 325 (1930)

Chapter 3

Measurements of the electron preionization density produced by a vacuum X-ray source

A vacuum X-ray source based on a wired corona plasma cathode has been built and its performance has been investigated. The preionization electron density created by this X-ray source in the gas volume of the discharge chamber has been measured in different gases and with different discharge gap lengths. It is shown for the first time that the preionization of the gas in our setup was produced not only due to X-ray absorption in the gas but also due to photo-electrons generated by the X-ray pulse in the cathode of the discharge chamber. The influence of the photo-electric effect at the cathode on the preionization of the gas is discussed.

3.1 Introduction

The novel soft X-ray source based on an open barrier discharge, described in chapter 2, has a very promising potential for future applications like for X-ray preionization or direct e-beam pumping of gas media as, for example, in active gaseous laser. For this kind of applications the source should be improved in terms of higher charging voltage and shorter rise time. In the current configuration described in chapter 2 the typical operational gas pressure of ~ 10 mbar is too low compared to the typical gas pressure needed for excimer lasers (~ few bar). Due to this the described X-ray source cannot be incorporated inside the laser chamber designed by us without the use of a pressure separation window. On the other hand, the produced X-rays are too soft (~ 5 – 10 keV) to penetrate through a separation window, which is typically made of Al with a thickness of ~ 1 mm. Therefore, instead of a further time consuming improvement of the soft X-ray generator to higher voltages and shorter rise times we have chosen to use another existing and proper working X-ray device, based on a corona plasma cathode [1 – 6], as the X-ray preionization source for all measurements on F_2 based laser gas mixtures presented in this thesis.

So, a wired corona plasma cathode based vacuum X-ray source has been designed and built to be used in all our measurements described in the following chapters of this thesis. In chapter 1 (see section 1.3.6) is estimated that in the laser gas mixture inside the discharge chamber an electron preionization density of at least ~ 10^7 – 10^8 cm^{-3} is required in order to create a stable and homogeneous discharge. In order to prove that the designed X-ray source is capable to produce a spatially uniform preoinization of the laser gas with such a density, measurements of the absolute dose of the X-rays produced by this source, of the spatial dose profile and of the electron preionization density created in the discharge chamber have been performed and will be discussed in the present chapter.

In our experiments it has been found that the electron preionization density in a gas with a low atomic number, e.g., He is much higher than expected from the theory (see chapter 1, section

1.4). The obtained values have been compared with the produced electron preionization density in higher atomic number gases, for instance, Ne and Ar. We have proposed an explanation of the observed phenomenon based on the X-ray photo-electric effect in the cathode, which serves as the separation window in our discharge chamber.

3.2 Experimental setup of the X-ray generator

The X-ray source to be described in this chapter, was designed and built according to the principal idea proposed in reference [6]. It is based on a vacuum corona plasma cathode, which emitted electrons, that are accelerated to an anode made of a high z material thereby producing X-rays, All dimensions were chosen to suit our requirements. The device was designed to provide X-ray preionization in a gas volume suitable for the excitation of small scale high pressure gas lasers. The output window of the X-ray source had a cross-section of 10 x 100 mm^2.

The schematic layout of the X-ray source is shown in figure 3.1. The source is placed in a cylindrical chamber (1) made of stainless steel with an inner diameter of 160 mm and a height of 138 mm with three gauge connections (one – DN 16 and two – DN 40) and two blank clamp flanges. The lower flange is made of stainless steel; the upper one is made of aluminum. One DN 40 gauge connection is used to evacuate the chamber and the second one is used as the high voltage input port. In the upper aluminum flange a cavity (2) (10 x 100 mm^2) is machined serving as the X-ray output window (3). The thickness of this window (3) is 1 mm, while the thickness of the flange itself is 12 mm. A piece of Ta foil 100 μm thick and with an area of 110 x 20 mm^2 is glued on the inner side of the output aluminum window (3) and is serving as the high z target, where the electrons are decelerated and are producing X-ray radiation. The outside of the entire chamber is shielded by a 2.5 mm thick lead cover, only the output window is left uncovered. The corona plasma cathode (4) consists of two identical tubes placed closely together. A schematic cross-section of one of them is shown in the right hand side part of figure 3.1. Inside a quartz glass tube, 110 mm long with an outer diameter of 14 mm and an inner diameter of 10 mm (5), a copper rod 2 mm in diameter (6) is inserted in such a way that it touches the upper side of the inner part of the quartz glass tube (5). This rod (6) serves as the inner trigger electrode. The inner part of tube (5) is filled with an epoxy glue (Stycast 1266) in order to fix the position of the rod and to prevent a discharge inside the tube. A piece of aluminum foil 13 μm thick (7) is glued on the outer surface of the tube leaving approximately 1/4th of the circumference (~ 11 mm) uncovered. The length of the uncovered zone is 70 mm. A tungsten wire 125 μm in diameter (8) is wrapped around the outer Al foil. The pitch of the wiring is 3 mm. Another piece of aluminum foil 13 μm thick and 90 mm long (9) is wrapped around this wiring also leaving the above mentioned zone uncovered, Thus each of these two tubes forms a discharge area of 11 x 70 mm^2 with their long sizes oriented along the long size of the output window (3). Copper anti-corona rings (10) are fixed on both ends of the foil wrapping (9) of the plasma cathode (4) to prevent corona discharges on the edges.

This composed plasma cathode is attached to a metal holder with an adjustable height (11). By changing the height of the holder the length of the acceleration gap, formed by the upper surface of the plasma cathode (4) and the inner surface of the output window (3) with the Ta foil target, is varied. The gap length could be varied between 15 and 25 mm. The cathode holder (11) is fixed on the lower flange of the chamber (1) via a dielectric base holder (12). The cathode holder (11) is in electric contact with the foils (7, 9) and wiring (8) and is connected to a mini-Marx generator by means of a copper rod (13), which is vacuum-tight glued into a glass tube (14). The glass tube (14) and the dielectric insulator (12) insulate the metal parts, that can be charged to a high potential, from the chamber walls, which are grounded. The trigger electrode

(6) is connected to the chamber walls through a capacitor C with a capacitance of ~ 90 pF, forming a capacitive divider with the capacitance of the plasma cathode being ~ 40 pF.

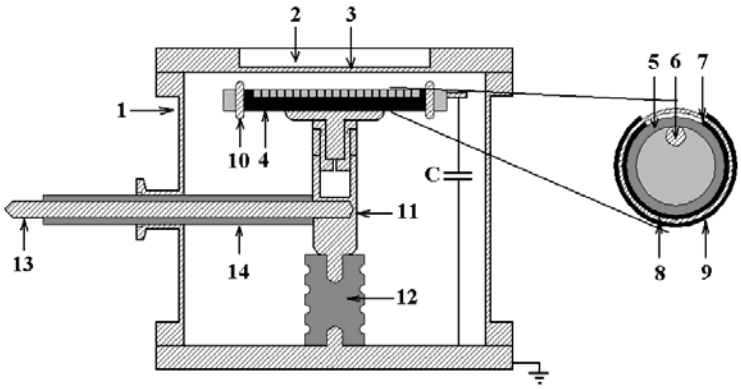

Figure 3.1. Layout of the X-ray source.
1: Source chamber; 2: rectangular cavity in the upper flange; 3: output window for X-rays; 4: corona plasma cathode (shown in cross-section on the right-hand side); 5: quartz glass tube filled with epoxy glue; 6: copper rod (inner trigger electrode); 7: aluminum foil on the surface of the tube; 8: tungsten wiring; 9: aluminum foil wrapped around the tungsten wiring; 10: copper anti-corona rings; 11: cathode holder with adjustable length; 12: dielectric insulator; 13: copper rod connecting to the mini-Marx generator; 14: insolating glass tube.

The experimental setup for preionization electron density measurements is shown in figure 3.2. The corona plasma cathode was powered by a homemade 6 stage mini-Marx generator. The connection of the plasma cathode to the mini-Marx was vacuum-tight and the current flowing from the generator into the source was monitored by a homemade fast (>100 MHz) current transformer (Rogovski coil). The mini-Marx generator was charged by a HV DC power supply (Hipotronics R 60A) and triggered by a homemade triggering unit, based on a thyratron (Perkin Elmer 7665A). The triggering unit was operated by a Farnell PG102 pulse generator. The X-ray source was directly connected to a vacuum pump and was evacuated to a gas pressure of ~ 10^{-4} mbar. The discharge chamber was used to measure the preionization electron density, created in the gas by the X-ray pulse. The same discharge chamber was used in the experiments as described later in chapter 4. The discharge chamber consisted of a cylindrical quartz tube with an inner diameter of 74 mm enclosed by two Al flanges. Two Al electrodes were attached to the flanges. The upper electrode was 50 mm in diameter and served as anode. The lower electrode was 60 mm in diameter and served as grounded cathode. Both electrodes had rounded edges to prevent enhancing of the electric field at the edges and were covered with a thin layer of Ni (~ 30 μm). As can be seen in the figure the lower flange had a round opening of 1 cm in diameter in the middle, and the lower electrode had a cavity 1 cm in diameter, which formed the 1 mm thick input window for the X-ray preionization pulse. The gap between the electrodes was adjustable between 0.5 and 2 cm. The discharge chamber was connected to a gas fill system and to a separate vacuum pumping unit. During the electron density measurements a constant voltage from a HV DC power supply (Philips 9412) was applied to the anode of the discharge chamber through an 80 MΩ resistance. The signals of the preionization electron density

measurements were taken from a serial connection of a 0.9 nF capacitor and a 10 MΩ resistance, formed by a high-voltage probe (Hameg HZ 36, having an attenuation coefficient 1 : 10) connected parallel to the discharge gap. A digital oscilloscope (Tektronix TDS 640A) was used to measure the voltage signal from the resistance by means of this probe. A 2.5 mm thick lead plate with a round aperture 1 cm in diameter was used in these experiments to confine the X-ray radiation to a beam 1 cm in diameter. This aperture and the discharge chamber were centered to the middle of the output window of the X-ray source. The distance from the X-ray output window to the input window of the discharge chamber was ~ 70 mm. The same configuration, as used in the preionization electron density measurements, was employed for the discharge preionization experiments described later in chapter 4.

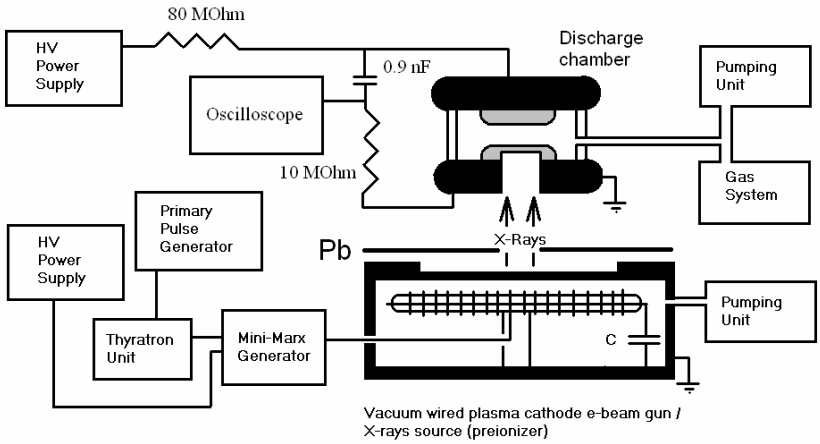

Figure 3.2. Experimental setup for the electron preionization density measurements.

For the measurements on the pulse duration, the absolute X-ray dose and the spatial distribution of the dose, produced by the the X-ray source, the discharge chamber and the lead aperture were removed. The duration of the X-ray pulse was measured by a piece of NE102A scintillating plastic attached to a photomultiplier (Philips 56AVP), placed 10 cm above the X-ray source and in the centre of the output window. A conventional pen dosimeter (SEQ6-0.1 rad) was used in the experiments on the absolute value and the spatial profile of the dose measurements. In these experiments the pen dosimeter was oriented in the transverse direction while the profile was measured in the longitudinal direction of the X-ray output window.

The diameter of the pen dosimeter was 14 mm. In order to make the dose profile measurements more localized the dosimeter was shielded from both sides in the longitudinal direction by two 2.5 mm thick lead plates. Thus these plates formed a 1 cm wide slit perpendicular to the longitudinal direction. Together with the lead shielding of the source and the slit a measuring window of 1 x 1 cm^2 was defined. The pen dosimeter was placed above this window. The window was then moved along the longitudinal axis of the X-ray source to measure the spatial profile of the dose. Two different profile measurements were performed. In the first experiment the dosimeter and lead plates were placed on top of the lead shielding of the X-ray source. In this experiment the distance from the X-ray output window of the source to the 1 x 1

cm^2 measuring window and the dosimeter was ~ 25 mm. In the second experiment the dosimeter was placed on top of a piece of aluminum 1 mm thick and ~ 78 mm above the X-ray source in order to simulate the X-ray absorption in the input window of the discharge chamber,. The distance from the X-ray output window to the dosimeter was ~ 90 mm in this case due to the thickness of the upper flange of the X-ray source.

During the absolute dose value measurements without profile information the dosimeter was placed above the central part of the output window without these slit forming lead plates.

3.3 Experimental results on the X-ray pulse duration, the total dose and the spatial distribution of the dose

In order to determine the duration of the X-ray pulse and to compare it to the duration of the current produced by the Mini-Marx generator the signal waveforms obtained by the photomultiplier with the scintillator attached and by the Rogovski coil have been measured. The typical waveforms of the current, flowing from the mini-Marx generator into the X-ray source, and of the X-ray pulse are shown in figure 3.3. The charging voltage of the mini-Marx generator was 17 kV. The current waveform has a FWHM of ~ 60 ns, and the FWHM of the X-ray pulse is ~ 30 ns. The X-ray pulse appears approximately 40 – 50 ns after the onset of the current. On the other hand, the photomultiplier introduces a delay of the signal due to time-to-flight of electrons inside the tube. With the help of short pulses from a LED the delay is measured to be approximately 50 ns. The response of the homemade current transformer has been tested by means of rectangular pulses from a pulse generator and a matched line. It has been found that this current transformer introduced approximately 8 – 10 ns delay of the measured signal and that the bandwidth of the device was ~ 140 MHz. Thus, the X-ray pulse appeared on the rising front of the current waveform. The current waveform was used in all later experiments as an indicator of the time of the appearance of the X-ray pulse, although it does not give information about the current of the e-beam in the source.

In order to provide spatially uniform gas volume preionization the spatial distribution of the X-ray dose had to be uniform. To check the uniformity of the X-ray dose distribution along the output window of the source, it has been measured by a pen dosimeter, as described in section 3.2 of this chapter. The longitudinal profiles of the X-ray dose distribution measured just above the X-ray source at a distance 25 mm from the output window (trace 1) and after the 1 mm thick Al plate at a distance 90 mm from the output window (trace 2) are shown in figure 3.4. The Al plate was placed in order to simulate the absorption in the input window of the discharge chamber. The bottom of this plate was shielded by lead plates, leaving an uncovered rectangular area of 10 x 100 cm^2 just above the X-ray source output window. The horizontal error bars represent the size of the measuring window 10 mm, formed by two Pb plates. The vertical error bars are due to the measuring scale of the dosimeter, which is 5 mrad. In case (1) the dose is measured in one shot at each position, in case (2) the dose is measured during three shots at each position and then averaged. Because of this fact the vertical error bars in case (2) are smaller.

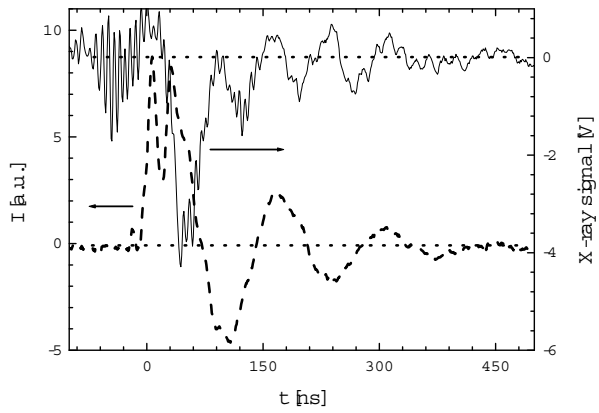

Figure 3.3. Typical waveforms of the current (lower dashed curve), flowing from the mini-Marx generator to the X-ray source, and of the X-ray pulse (upper solid curve), measured at a charging voltage of the mini-Marx 17 kV. The dotted horizontal lines show the zero levels of the current and X-ray signal.

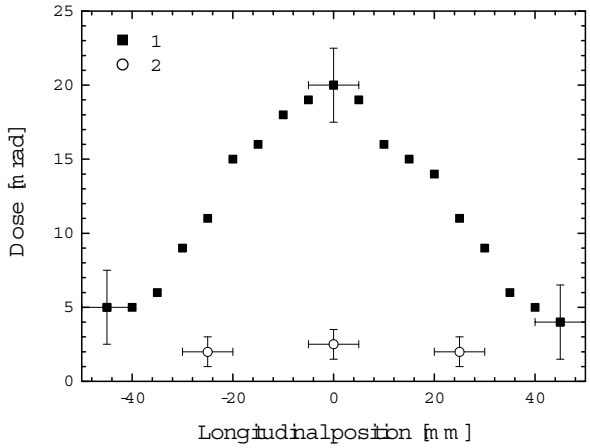

Figure 3.4. The longitudinal profile of the X-ray dose measured at a mini-Marx charging voltage of 17 kV and with an acceleration gap length of 25 mm. (1): 25 mm above the source; (2): 90 mm above the source and after passing a 1 mm thick 100 x 10 mm^2 Al window.

In case (1) the dose profile has a maximum of ~ 20.0 ± 2.5 mrad above the middle of the output window and drops at the edges of the source window. The FWHM of this profile is ~ 60 mm. In case (2) the dose is ~ 2.5 ± 0.8 mrad in the middle and ~ 2.0 ± 0.8 mrad at a position 25 mm apart from the middle of the source window (on both sides). Thus in case (2) the dose in the center is ~ 8 times lower and the dose profile is also flatter compared to case (1).

As shown in reference 6, the X-ray dose, produced by the corona plasma cathode based source, increases with the applied voltage and also depends on the acceleration gap length. The acceleration gap length dependence of the delivered X-ray dose is not linear; there is an optimal gap length at which the delivered dose reaches a maximum value at any charging voltage. In order to find the optimum gap length the dependence of the produced dose on the charging voltage of the mini-Marx generator was measured for different lengths of the acceleration gap of the X-ray source. The dose measurements were performed with a pen-dosimeter, placed above the source in the middle of the output window at a distance of 25 mm from it without the Pb plates, shielding the dosimeter on each side. A gap length of 15 mm was found to be optimal.

The dependence of the delivered dose on the mini-Marx charging voltage is presented in figure 3.5 for two gap lengths: 25 (1) and 15 mm (2). The decrease of the acceleration gap length from 25 to 15 mm caused more than a twofold increase of the dose per shot. However, in both cases the dose per shot grows very slowly with the charging voltage applied to the mini-Marx generator. According to this observation, 17 kV was chosen as the standard mini-Marx charging voltage, because at a higher charging voltage the dose per shot did not increase significantly while the stress on the elements inside the X-ray source was much higher. Thus in all preionization electron density measurements, described below in this chapter and in the gas discharge excitation experiments, described in chapter 4, the acceleration gap length of the X-ray source was 15 mm and the charging voltage of the mini-Marx was 17 kV. Under these conditions the dose per shot, produced just above the source in the middle of the output window, was approximately 53 mrad.

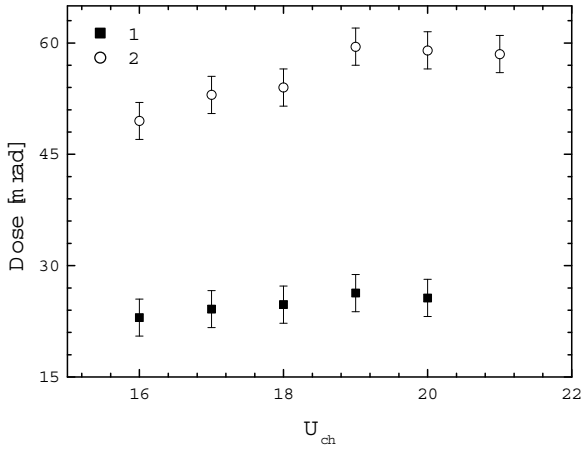

Figure 3.5. Dependence of the dose per shot, produced by the X-ray source, on the charging voltage U_{ch} of the mini-Marx generator. The acceleration gap length was 25 (1) and 15 mm (2).

In order to determine the X-ray dose produced inside the discharge chamber, the chamber was installed above the X-ray source, as is shown in figure 3.2. The X-ray input window in the Al electrode of the chamber (1 mm thick and 1 cm in diameter) was ~ 70 mm above the center of the output window of the X-ray source. The X-ray source was also shielded by a Pb plate with an opening 1 cm in diameter placed on top of it. This configuration has been used later in the discharge experiments and in the preionization electron density measurements. The X-ray dose penetrating into the chamber has been measured to be ~ 1 mrad per shot at a charging voltage of the mini-Marx of 17 kV and at an acceleration gap length in the source of 15 mm.

3.4 Experimental results of the preionization electron density measurements

To check the designed X-ray source, the preionization electron density production in the gas volume of the discharge chamber at a gas pressure of few bar was measured. As mentioned before, an electron density of ~ 10^7 – 10^8 cm^{-3} is required for a homogeneous breakdown (see chapter 1, sect. 1.3.6). The measurements of the preionization electron density were performed with the setup shown in figure 3.2. The gap length between the anode and the cathode in the discharge chamber, which was used as ionization chamber in these experiments, was varied from 0.5 to 2 cm. The measurements were taken in He, Ne and Ar at a gas pressure of 5 bar with a gap length of 0.5, 1, 1.5 and 2 cm. Additionally, the electron density was measured in He : Xe / 99 % : 1 % and He : F_2 / 99.9 % : 0.1 % gas mixtures at a total pressure of 5 bar and a gap length of 1 cm, and in He at gas pressures of 1, 2, 3 and 4 bar and with a gap length of 1.5 cm. The DC voltage applied to the electrodes was varied from ~ 100 V to ~ 5 kV. For each gas or gas mixture a series of measurements was taken at various voltages, gas pressures and gap lengths. The experiments were done this way to reach the saturation electric field strength, that is when the field is strong enough to provide the collection of all electrons produced due to absorption of the X-rays, but still too weak to cause additional ionization of the gas due to collisions of the produced and accelerated electrons with neutrals.

In order to determine the total charge of the preionization electrons produced in the chamber from the measured voltage waveforms, the capacitance of the chamber formed by the electrodes, the flanges and the gap, was measured. It was observed that this capacitance, as expected, depended on the gap length. It was measured to be 92 pF at a gap length of 0.5 cm, 82 pF at 1 cm gap length, 79 pF at 1.5 cm and 76 pF at a gap length of 2 cm.

Typical waveforms of the signals (averaged) measured in He (1), Ne (2) and Ar (3) at a gas pressure of 5 bar, a gap length of 1 cm and an applied voltage of 1 kV are shown in figure 3.6. The first sharp spike at $t = 0$ ms is artificial and has no meaning. The amplitude of this spike changed significantly from shot to shot while the other (slow) part of the waveform was almost the same for each shot under equal conditions. The amplitude of this slow half-wave fluctuated a bit from shot to shot, but the shape and slope of this part of the measured signal were constant for otherwise equal conditions. The amplitude of the signal and slope of the decaying part depended on the gap length, applied voltage, gas pressure and composition. For example, in figure 3.6 all three signals reached their minimum values at almost the same time namely after ~ 0.3 ms, although the amplitude was larger in Ar (3) than in Ne (2), which was on its turn larger than in He (1). After reaching the maximum absolute value all signals decayed. This decay was the fastest in He (1) and the slowest in Ar (3).

The measured amplitude of the signal was multiplied by 10, in order to compensate for the attenuation coefficient of the voltage probe. The total gathered charge, the number of electrons gathered and the electron density are calculated from this value. The total gathered charge is given by the following expression:

$$Q = C_p \, \Delta U \,, \tag{3.1}$$

where C_p is the capacitance of the chamber, and ΔU is the measured (multiplied by 10) voltage change over the gap capacitance.

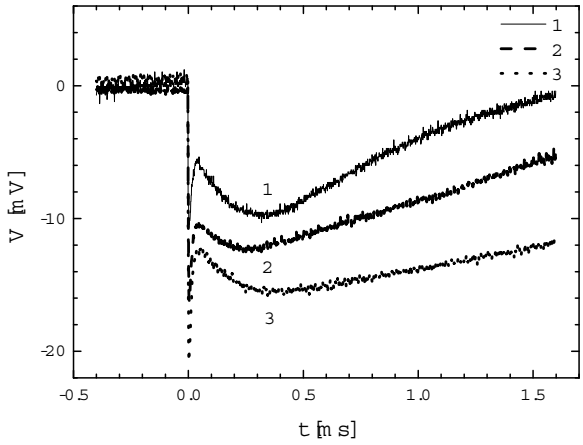

Figure 3.6. Averaged (over 5 waveforms) preionization signal in He (1), Ne (2) and Ar (3) at a gas pressure of 5 bar and a gap length of the ionization chamber of 1 cm. The voltage applied to the electrodes of the chamber was 1 kV.

The number of electrons gathered, N_e, could be calculated by the division of the total charge by the electron charge. We have assumed that in this particular setup only electrons and not ions contributed to the measured amplitude of the signal; the validity of this assumption is discussed later in sect. 3.5 of this chapter. The other assumption that has been made was that the preionization was produced only in volume V, defined by the product of the gap length d and the area S of the input window (which is 1 cm in diameter): $V = d\,S$. The electron density n_e is the ratio of the total number of electrons to this volume, i.e., $n_e = N_e / V$.

As shown in sect. 1.4 of chapter 1, in case of weak absorption, which is relevant in our experiments, the absorbed X-ray dose and, thus, the preionization electron density is proportional to the gas mass density, which is proportional to the gas pressure. Then, the specific electron density n_e/p depends only on the X-ray spectrum and intensity and on the kind of gas used. In our experiments the measured specific electron density is given by:

$$\frac{n_e}{p} = \frac{C_p \, \Delta U}{p \, e \, d \, S}, \tag{3.2}$$

where e is the charge of electron, d is the gap length, S is the area of the input window and p is the gas pressure.

When free electrons and ions are produced in the gas volume and the external electric field is applied, the gas starts to conduct electric current. In absence of secondary ionization due to collisions of electrons with neutral particles this process is the extreme case of a non-self-sustained gas discharge. As usual for gas discharges, the parameters of this extreme form of the gas discharge are determined by the specific electric field strength E/p and not by the applied voltage. The specific electric field strength in our experiments is defined as:

$$\frac{E}{p} = \frac{V_{ic}}{p\,d}, \tag{3.3}$$

where V_{ic} is the voltage applied to the chamber and p is the gas pressure.

In order to find the specific saturation electric field, when all produced electrons are gathered and saturation occurs but still no secondary ionization is present, the dependence of the voltage change ΔU on the applied voltage V_{ic} was measured. The dependence of the voltage change ΔU on the applied voltage V_{ic} (a) and the specific electron density n_e/p on the specific electric field strength E/p (b), calculated with Eqs. 3.2 and 3.3, are shown in figure 3.7. The gap length was 1 cm and the gas pressure was 5 bar during these experiments. The measurements were taken in He (1), Ne (2) and Ar (3). In the cases of He (1) and Ar (3) ΔU and n_e/p at first increased with the charging voltage and, thus, with the specific electric field strength, and then they reached a saturation level. This saturation value of the specific electron density is considered to be the specific preionization electron density. In the case of Ne (2) the voltage change and the specific electron density were almost the same at a charging voltage of 1 and 1.5 kV, but they were much higher at a charging voltage of 2 kV. At higher charging voltages an electric gas breakdown was observed. We believe that at a charging voltage of 2 kV secondary ionization takes place, which caused electron avalanches to grow. The preionization electron density in this case was determined as the electron density value at low charging voltage (<1.5 kV).

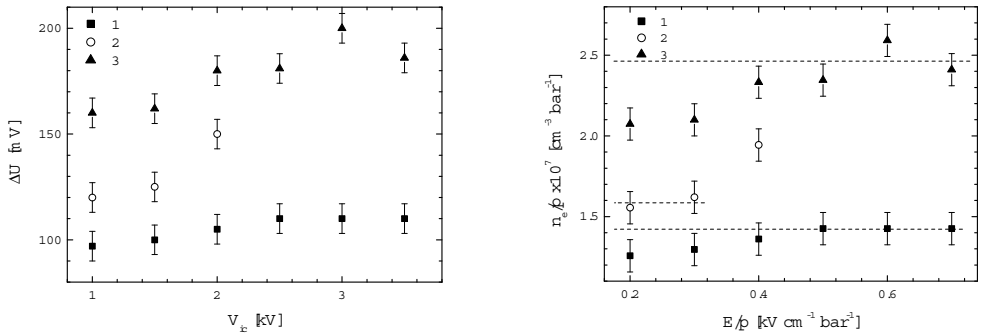

a *b*

Figure 3.7. Dependence of the voltage change ΔU on the voltage V_{ic} (a) and n_e/p on E/p (b), measured in He (1), Ne (2) and Ar (3) at a gas pressure of 5 bar and a gap length of the ionization chamber of 1 cm. Horizontal lines correspond to a saturated electron density.

Following this procedure, the specific preionization electron density has been found to be ~ 1.4 10^7 cm^{-3} bar^{-1} in He, ~ 1.6 10^7 cm^{-3} bar^{-1} in Ne, ~ 2.5 10^7 cm^{-3} bar^{-1} in Ar, ~2.2 10^7 cm^{-3} bar^{-1} in a He : Xe / 99 % : 1 % mixture and ~ 1.6 10^7 cm^{-3} bar^{-1} in a He : F_2 / 99.9 % : 0.1 % mixture at a total gas pressure of 5 bar and a gap length of 1 cm. The preionization electron density (and not specific density) has been observed to be of ~ 10^8 cm^{-3} for all of the investigated gases.

According to Eq. 1.43 in chapter 1, neither the specific preionization electron density, nor the preionization electron density at each given gas pressure depends on the gas gap length. In order to check the validity of this prediction in our experiments the dependence of the specific preionization electron density on the gas gap length was measured. The dependence of the total number of electrons gathered (a) and the specific preionization electron density (b) on the gap length, measured in the saturated region (see figure 3.7), are given in figure 3.8. The gas pressure was 5 bar; the experiments are in He (1), Ne (2) and Ar (3). The dependence of the total number of electrons on the gap length was observed to have a minimum value for Ne (2) and Ar (3), or was slightly growing in the case of He (1). However, due to the vertical error bars, which are determined by the uncertainty in the drawing of the saturation line (see figure 3.7), the total number of electrons is almost independent on the gap length in figure 3.8 (a). This explains why the specific electron density drops almost inversely proportionally to the gap length *d*. The specific electron density in Ar (3) is only ~ 2 times higher than in He (1).

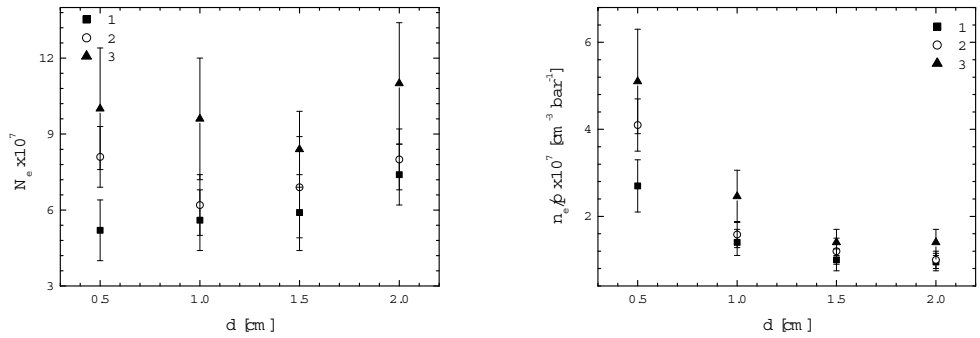

a *b*

Figure 3.8. Dependence of the saturated total number of the electrons gathered (a) and the saturated specific electron density (b) on gap length of the ionization chamber, measured in He (1), Ne (2) and Ar (3) at a gas pressure of 5 bar.

Additional measurements were carried out in He at gas pressures varying from 1 to 5 bar in the chamber with a gap length of 1.5 cm. The results of these experiments together with the previous results for He (figure 3.8 (a, b) (1)) are shown in figure 3.9 as the dependences of the total number of preionization electrons (solid squares) and the specific preionization electron density (open circles) on the specific gap length *p d*.

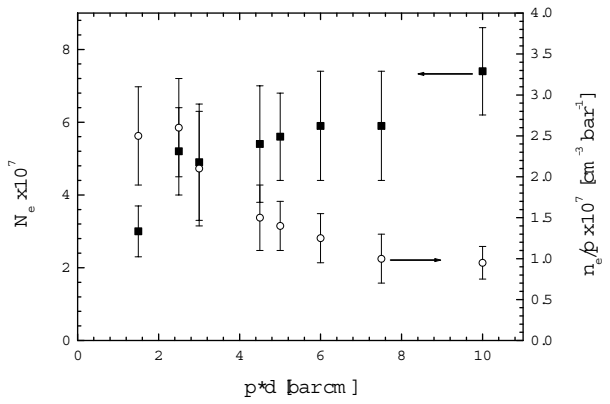

Figure 3.9. Dependence of the saturated total number of electrons gathered (solid squares) and the saturated specific electron density (open circles) on the p d value in the ionization chamber, measured in He.

3.5 Analysis of the measurement scheme

3.5.1 Analytical evaluation of the measuring circuit

The measured specific preionization electron density has been found to be higher in low Z gases (as, for example, He) compared to higher Z gases (like Ar), than predicted by the X-ray absorption theory (see chapter 1, sect. 1.4). In order to prove the correctness of our measurements and the validity of our assumption that the amplitude of the voltage change is proportional only to the electron charge and not to the sum of the electron and ion charges an analytical evaluation and a numerical model of the measuring scheme have been elaborated.

The principle of the preionization electron density measurements was as follows: the capacitance of the ionization chamber was charged to a voltage V_{ic} providing a constant electric field distribution with a specific field strength given by Eq. 3.3. A preionization source created free electrons and free positive ions in pairs in the gas volume. In the electric field the electrons and ions started to move toward the opposite electrodes, and an electric current appeared. This current caused the discharge of the capacitance of the chamber, thus the voltage V_{ic} across electrodes decreased. By measuring the current and integrating it over time one gets the total charge produced in and pulled out from the gas volume. However, the RC circuit integrated the signal by itself. So the alternative way is to measure the voltage change ΔU across the electrodes in the chamber and calculate the charge produced in the gas volume from the simple relation given by Eq. 3.1.

Our approach was based on the following assumptions. First of all, the current from the DC power supply, recharging the capacitance of the chamber, was negligible compared to the ion and electron current in the chamber because of high impedance (80 MOhm) of the current limiting resistance and the high capacitance (0.9 nF) of the storage capacitor connected to the chamber. In this case the measuring scheme could be treated as electrically insulated from the DC source. Secondly, the capacitance of the additional capacitor (0.9 nF) was much higher than

the value of the chamber (typically ~ 70 – 90 pF). In this way the voltage change across the additional capacitor could be neglected compared to the voltage change across the chamber. The third assumption was that the response time of the measuring circuit was much longer than the current duration, so the circuit integrated the current, as was discussed in chapter 2 (see Eq. 2.5 therein). Additionally, in our measurements it was supposed that the circuit integrated only the electron current in the chamber, and for the ion current the circuit was too fast to provide current integration (see chapter 2, eq. 2.6). Therefore the measured ΔU was only proportional to the total charge of electrons gathered, thus there was no need to divide the total charge by 2.

The capacitance of the chamber, C_p, has been measured to vary from ~ 70 to ~ 90 pF depending on the gap length. The capacitance of the additional capacitor C = 0.9 nF was more than 10 times higher. For the charging part of the circuit (see figure 3.2) these two capacitors were connected in parallel, thus their capacitances have been summed up. Taking into account the impedance of the load resistance the RC time of the charging part was ~ 80 ms. For the measuring part of the scheme these capacitances were connected in series, and their total capacitance value was ~ 0.9 C_p. Combined with the effective impedance of the probe the RC time of the measuring part of the scheme was ~ 1 ms, which correlated with the typical rise time of the measured signal of ~ 0.3 - 0.5 ms and with the decay time of the tail of the curves which was several ms. The typical applied voltage was in order of kV, but the voltage change was less than or comparable to 1 V, and the measurements were taking during a couple of ms. Thus we could conclude that the current from the DC supply could be neglected, as well as the voltage change across the additional capacitor C.

It was expected that the current pulse width in the chamber should depend on the electron and ion mobilities in the applied field. The electron drift velocities in the applied field from 0.1 to 1 kV cm^{-1} bar^{-1}, typical for our measurements, in He, Ne and Ar have been taken from references 7, 8 and 9. For all three gases the electron drift velocity was approximately the same varying from ~ 10^5 cm s^{-1} in a weak field of ~ 0.1 kV cm^{-1} bar^{-1} to ~ 10^6 cm s^{-1} in a strong field of ~ 1 kV cm^{-1} bar^{-1}. The ion mobility and drift velocity were usually measured in stronger fields, thus for an estimation of their values in our experiments we have extrapolated the data in reference 10 from 1 - 10 kV cm^{-1} bar^{-1} region to 0.1 – 1 kV cm^{-1} bar^{-1} region. Then, the ion drift velocity was estimated to vary from 10^3 to 10^4 cm s^{-1}. For a gap distance of ~ 1 cm the drift time for electrons has been estimated to be in order of 10^{-6} – 10^{-5} s, and for ions – in order of 10^{-4} – 10^{-3} s, while a value of 10^{-3} s was expected to be more reasonable taking into account the ion to electron mass ratio. Therefore, we have concluded that the measuring scheme integrated the electron part of the current in the chamber, but the type of response to the ion current has to be investigated further (is it the integral of or is it proportional to the ion current).

To clarify this question an analysis of the measuring circuit has been done. A simplified equivalent electric circuit of the measuring scheme is shown in figure 3.10. It is taken from a suggestion in reference 5, where C_p represents the capacitance of the chamber, C the additional capacitor, R the impedance of the probe and the current generator $i(t)$ corresponds to the ion and electron current in the chamber, and $V(t)$ is the measured signal.

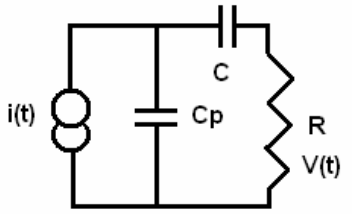

Figure 3.10. Simplified equivalent circuit of the charge collection scheme.

In order to analyze the response of this equivalent circuit to current pulses with varying pulse durations, a simple theory has been elaborated. If the charge of the capacitor C_p is q, and Q is the charge of the capacitor C, then this circuit is described by the following set of equations:

$$\begin{cases} i(t) = \dot{q} + \dot{Q} \\ \dfrac{q}{C_p} = \dfrac{Q}{C} + V(t). \\ \dot{Q} = \dfrac{V(t)}{R} \end{cases} \tag{3.4}$$

From this set of equations it follows that:

$$\dot{q} = \dot{Q}\frac{C_p}{C} + \dot{V}(t)C_p. \tag{3.5}$$

The relation between V(t) and i(t) is:

$$\begin{aligned} i(t) &= \dot{Q}\frac{C_p}{C} + C_p\dot{V}(t) + \dot{Q} = \\ &= \dot{Q}(1 + \frac{C_p}{C}) + C_p\dot{V}(t) = \\ &= \frac{V(t)}{R}(1 + \frac{C_p}{C}) + C_p\dot{V}(t) \end{aligned} \tag{3.6}$$

In the case C>>C_p, as valid for our setup, Eq. 3.6 can be simplified to:

$$i(t) = \frac{V(t)}{R} + C_p \dot{V}(t). \tag{3.7}$$

The exact solution of Eq. 3.7 can be found in form:

$$V(t) = U(t) \exp\left(-\frac{t}{RC_p} \right). \tag{3.8}$$

After substitution the expression given by Eq. 3.8 into Eq. 3.7 a differential equation for *U(t)* is produced:

$$\dot{U}(t) \exp\left(-\frac{t}{RC_p} \right) = \frac{i(t)}{C_p} \qquad \Rightarrow$$

$$U(t) = \int_0^t \frac{i(\tau) \exp\left(\frac{\tau}{RC_p} \right)}{C_p} d\tau \,. \tag{3.9}$$

The solution of Eq. 3.7 is then:

$$V(t) = \frac{\exp\left(-\frac{t}{RC_p} \right)}{C_p} \int_0^t i(\tau) \exp\left(\frac{\tau}{RC_p} \right) d\tau \,. \tag{3.10}$$

For a better understanding of the structure of this exact solution (Eq. 3.10) we have considered two limit cases: the slow and fast response of the measuring circuit compared to the current pulse duration.

If the $R\ C_p$ response time is much longer than the duration of the current, then Eq. 3.7 is simplified to:

$$i(t) \approx C_p \dot{V}(t), \tag{3.11}$$

and the measured voltage change ΔU, which is the amplitude of $V(t)$, is proportional to the gathered charge Q, which is the integral of the current $i(t)$, divided by the capacitance of the chamber C_p. This case is valid for the electron component of the total current in the chamber. In the opposite case, when the current changes slowly compared to the $R\ C_p$ response time, Eq. 3.7 is simplified to:

$$i(t) \approx \frac{V(t)}{R}, \tag{3.12}$$

and the measured signal is proportional to the current in the chamber multiplied by the impedance of the probe R. The validity of this case to the ion current is expected, however, the ion drift time is actually comparable to the $R\ C_p$ time in our experiments. A numerical model based on the exact solution of Eq. 3.7, which is given by Eq. 3.10, has been performed to check validity of this assumption. This numerical model is discussed in the following section 3.5.2 of this chapter.

3.5.2 Numerical model of the electron density measuring circuit

In order to check the validity of the assumption that the response of the measuring circuit is proportional to the time integral of the electron current (Eq. 3.11) and to the ion current waveform (Eq. 3.12) a numerical model of the preionization electron density estimation has been developed. It is based on Eq. 3.10, which describes the relation between the measured signal $V(t)$ and the current in the discharge chamber $i(t)$, which consists of electron and ion components.

The electron and ion components of the current are modeled by triangular pulses according to reference 5. This model assumes that the ions and electrons are distributed homogeneously within the volume. It also assumes that the external electric field is not disturbed by the space charge, mostly due to slow ions, which are left behind after the electron cloud is removed from that volume. Therefore the field strength across the gas gap is constant and does not change because $\Delta U << V_{ic}$. Then, the ion and electron currents are given by:

$$\begin{aligned} i_e &= e\, n_e\, S\, v_e \frac{(d - v_e\, t)}{d} \\ i_i &= e\, n_i\, S\, v_i \frac{(d - v_i\, t)}{d} \end{aligned}, \tag{3.13}$$

where i_e and i_i are the electron and ion current, $n_e = n_i = 6\ 10^7$ cm^{-3} are the electron and ion densities, S is the cross-section area of the gas volume 1 cm in diameter, $d = 1$ cm is the gap length, $v_e = 10^5$ cm s^{-1} and $v_i = 10^3$ cm s^{-1} are the drift velocities of the electrons and ions. Thus,

the current pulse due to the electrons is 100 times higher in amplitude but 100 times shorter than the ion current.

This total current, which is the sum of the two components given by Eq. 3.13, is substituted into Eq. 3.10. The resulting curve *V(t)* is shown in figure 3.11 for $R\ C_p = 10^{-4}$ s (a 1) and 10^{-3} s (b 1). These two values of $R\ C_p$ were chosen to simulate the response to slower (higher *Z*) and faster (lower *Z*) ions, and to simulate the change of the electron and ion velocities due to the varying electric field. Also shown in both parts of figure 3.11 are an exponential discharge of the capacitor with a corresponding $R\ C_p$ time and with an initial charge that is equal to the time integral of the electron part of the current (2) (see Eq. 3.13) or an initial charge twice this value (3),. It is seen that in both cases (slower and faster $R\ C_p$ response time) the amplitude of the signal is almost equal to the electron charge divided by the capacitance of the chamber and not to the double value of the electron charge, which corresponds to the integral response to both components. However, for a smaller RC_p time (a) the tail of the signal, at first, drops fast (with a time constant close to the $R\ C_p$ value) and then follows a straight line, representing the ion current. For a longer $R\ C_p$ time (b) the tail follows the exponential voltage decay of the capacitor charged to twice the electron charge.

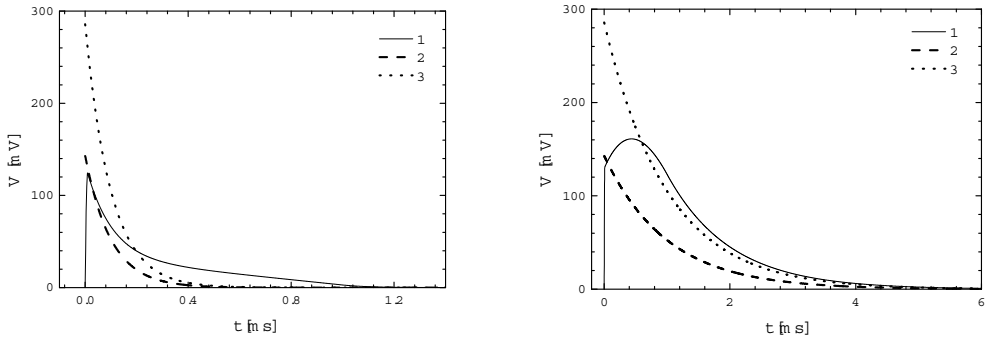

Figure 3.11. Results of the modeling the measured signal following Eq. 3.12 and 3.13 with an RC_p time equal to 10^{-4} s (a) and 10^{-3} s (b). 1: V(t) waveform given by Eq. 3.10; 2: exponential discharge with the corresponding RC_p time and initial charge Q, equal to the integral of the electron current; 3: initial charge is 2 Q.

The electron current in both cases is too fast, thus it is integrated, and the amplitude of the signal in the model is given by the total electron charge divided by the capacitance. In the first case (a) the ion current is longer than the *RC* time of the circuit, and its duration is comparable to the *RC* time of the circuit in the second case (b). Thus case (a) corresponds, on one hand, to lighter gases, where the electron and ion mobilities are higher and, thus the drift velocities are higher; and on the other hand, to stronger electric fields, where the drift velocities are higher even for the same mobilities. The second case (b) describes heavier gases and weaker electric fields. For example, in figure 3.6 the shape of the observed signal is in between these two extreme cases. The position of the maximum of the signal, determined by the response of the measuring

RC circuit to a very fast electron current, is closer to case (b). However, the tail of the signal decays faster and almost exponentially in He. The ions are faster in the same field (figure 3.6 (1)) compared to the heavier gases and thus in Ne (figure 3.6 (2)) and Ar (figure 3.6 (3)) the tail decays slower and almost linearly, as predicted by this model.

The amplitude of the signal in the model in both cases differs less than by 15 % from the expected value which is comparable to the experimental error given by the fluctuation of the measured signal and the uncertainty in the drawing of the saturation line (see figures 3.7 – 3.9). Due to this modeling, we have concluded that the amplitude of the measured signal is proportional to the total charge of electrons only, while the shape of the measured signal tail is determined by the ion component of the current.

3.5.3 Signal to noise ratio enhancement procedure

In order to increase the signal to noise ratio of the measured signal a multiple curve averaging procedure has been employed. This procedure has been discussed already in chapter 2. In the experiments described in this chapter the background signal was obtained with the X-ray source aperture covered by a 5 mm thick Pb plate. In this case the slow (ms range) signal was not observed, only a sharp spike was present in the measured signal. As discussed earlier, there was a large shot to shot variation in the amplitude of this spike. It is assumed that this spike was caused by the electro-magnetic noise produced by the discharge of the mini-Marx generator and / or by the plasma expansion in the acceleration gap of the X-ray source. Thus the background signal during a measurement was almost a straight line with a sharp spike on it. The slope of this straight line fluctuated from shot to shot and could be positive or negative. In fact, a part of the observed signal in figure 3.6 in the negative time domain $-0.5 < t < 0$ ms corresponds to this almost straight line of the background signal. As it is seen for three curves in figure 3.6 for He (1), Ne (2) and Ar (3), the slope of these lines differs. When the background signal was measured in a larger time window of ~ 50 ms, it was observed to be not a straight line, but a sine function with an oscillation period of ~ 20 ms (50 Hz) and an amplitude of ~ 4 mV (without multiplication by a factor of 10, corresponding to the attenuation coefficient of the probe). So the background signal observed in a ~ 2 ms time window was just a part of this 50 Hz sine function with constant amplitude and random phase shift due to insufficient rectification of the DC signal from the HV power supply.

The voltage change ΔU was measured as the difference between the values of the signal $V(t)$ at $t = 0$ ms and at $t \sim 0.5$ ms. During this period of time the background sine signal changed by less than $6\ 10^{-4}$ V, as estimated from the oscillation period of 20 ms and the amplitude of 4 mV. The amplitude of the measured signal on the other hand was ~ 10^{-2} V, and the error introduced by the slope of the background signal is negligible. Thus in these experiments the measured waveforms were averaged but no subtraction of the background signal was made.

The experimental errors are due to the fluctuations of the measured signals and by the uncertainty in the drawing of the saturation level lines.

3.6 Discussion of the results

3.6.1 Total X-ray dose and spatial distribution of the dose

As reported in section 3.3 the X-ray dose was measured to be ~ 50 mrad per shot, measured 25 mm above and in the middle of the output window of the X-ray generator and

without X-ray collimation. In this case the dosimeter captured radiation from the entire surface of output window of the X-ray source. When the dosimeter was placed inside the discharge chamber on top of the lower Al electrode (covered with a 30 μm thick Ni layer) the measured X-ray dose was only ~ 1 mrad per shot. During these measurements the X-ray output window was covered with 2.5 mm thick lead plate, in which a circular aperture of 1 mm in diameter was made. The opening in the lower flange and in the lower electrode of the discharge chamber, both 1 cm in diameter, formed the X-ray input window with a total metal thickness of 1 mm Al. The distance from the X-ray source output window to the pen dosimeter in this case was 70 cm.

In order to check if this 50-fold decrease of the dose is due to absorption in the X-ray input window we estimated in which way this input window attenuated the X-ray flux. The exponential attenuation law is given by Eq. 2.16 (chapter 2). The mass density of Al is 2.7 g/cm^3 and 8.9 g/cm^3 for Ni. The 6-stage mini-Marx generator produced a voltage pulse with an amplitude of ~ 100 kV at a charging voltage of 17 kV. The produced X-ray radiation consists of a continuous bremsstrahlung spectrum with a high-energy cut-off ~ 100 keV and the characteristic lines of Ta, mostly K_α at ~ 56 keV. The mass attenuation coefficient for X-rays in Al at 30, 56 and 100 keV is ~ 1, ~ 0.3 and ~ 0.18 cm^2/g, and for Ni ~ 10, ~ 2 and ~ 0.44 cm^2/g [11, 12] (see also Appendix, figure A.2). The intensity of the X-ray beam after passing this window, consisting of 1 mm Al and a ~ 30 μm Ni layer, is reduced to ~ 0.58, ~ 0.87 and ~ 0.94 of the initial beam intensity for X-ray photons with an energy of 30, 56 and 100 keV correspondingly. The attenuation of the beam in air over ~ 50 mm is negligible due to the very low mass density of air (~ 10^{-3} g/cm^3). So it must be concluded that absorption of the the X-rays in the window can not explain the observed 50-fold decrease of the dose.

Earlier dose experiments have been reported in section 3.3 and the results are presented in figure 3.4. When the dosimeter was shielded by Pb plates, forming a 10 x 10 mm^2 measuring window and placed 25 mm above the source the measured dose was ~ 20 mrad per shot in the middle of the X-ray beam (compared to ~ 50 mrad per shot without this X-ray beam collimating window) and it dropped to ~ 5 mrad near edges of the output window of the source. Thus the dose was observed to be distributed non-homogeneously along the output window of the source. When the same dosimeter was placed behind a 1 mm thick Al plate and installed ~ 90 mm above the output window of the source and shielded by lead plates to form a window with 10 x 100 cm^2 area, the measured dose was only ~ 2.5 mrad per shot in the middle of the window and ~ 2 mrad per shot at the position ~ 1/4th of the window length from any side. Again, the X-ray dose was observed to be much lower, than was expected from the mass absorption coefficient of Al and its thickness (this window transmits ~ 0.76, 0.92 and 0.95 of the X-rays at 30 , 56 and 100 keV respectively). It also can be seen from figure 3.4 that dose distribution profile was flattened at longer distances from the X-ray source.

In order to explain the observed abnormal decrease of the X-ray beam dose due to the beam collimation a numerical model, based on assumption that the generated X-ray beam is highly divergent, has been elaborated. In this model the non-uniform X-ray dose distribution along the X-ray source output window, the decrease of the dose and flattening of the dose spatial distribution with increasing distance from the source have been taken into account.

3.6.2 Numerical model of the X-ray beam divergence

The main assumption in this model is that each point in the output window of the source is an independent point source of radiation with the same brightness as any other point in the window. Every point produces a spherical wave with the same amplitude. The actual source is an incoherent sum, actually a surface integral, of all these point sources of spherical waves from the

10 x 100 mm^2 surface with the brightness homogeneously distributed across its cross-section. Suppose the origin of coordinates (0, 0, 0) in the middle of the output window of the X-ray source. With an infinitely small spherical measuring volume dV with radius $dr \sim dV^{1/3} \rightarrow 0$ placed at position (x_0, y_0, z_0), the number of photons per unit of time, registered in the measuring volume from the point source at position (x, y, 0), is inversely proportional to the square of the distance from the centre of the measuring volume to the point source:

$$n(x_0, y_0, z_0, x, y) \propto \frac{1}{(x - x_0)^2 + (y - y_0)^2 + z_0^2}. \tag{3.14}$$

The x-axis is in the plane of the window and perpendicular to the longitudinal direction of the window. The y-axis is in the longitudinal direction of the window. The z-axis is perpendicular to the window. The total amount of the captured photons from the entire area of the source is:

$$N(x_0, y_0, z_0) \propto \int_{-y_{\max}}^{y_{\max}} \int_{-x_{\max}}^{x_{\max}} n(x_0, y_0, z_0, x, y)\, dx\, dy, \tag{3.15}$$

where for the 10 x 100 mm^2 output window y_{max} = 50 mm and x_{max} = 5 mm. Eq. 3.15 is valid as long as $|x_0| \leq x_{max}$ and $|y_0| \leq y_{max}$ that is the projection of the position of the centre of the measuring volume is inside the cross-section of the output window. Otherwise the integration limits in Eq. 3.15 are determined by the line of sight formed by the position of the measuring point and the edges of the cavity, forming the output window (see figures 3.1 and 3.2). This means that the cavity limited the divergence angle of the source. The integration was made inside this solid angle.

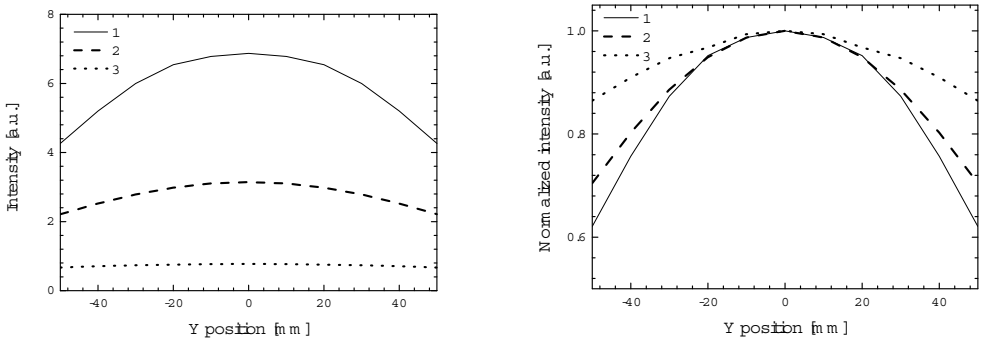

a *b*

Figure 3.12. Longitudinal profiles of the X-ray dose in a.u. (a) and normalized to unity (b) calculated in the 2D model. An imaginary detector is placed 30 (1), 50 (2) and 110 mm (3) from the source.

In a first approximation this model has been investigated in a 2D approach. The output window has been divided into a set of infinitely narrow stripes with the long side of each stripe being perpendicular to the longitudinal direction of the window, i.e., the stripes are oriented in the x-direction. Each stripe has been replaced by a point source in the calculations. The dose distribution has been calculated along y-axes at points (0, y_0, z_0). Thus the profile of the beam in the x-direction has been neglected. The results of this 2D modeling are shown in the figure 3.12 for $z_0 = 30$ (1), 50 (2) and 110 mm (3) in arbitrary units (a) and normalized to unity (b).

This 2D model predicted a decrease of the dose (a) and a flattening of the dose profile (b) with increasing distance from the source.

A 3D model based on Eqs. 3.14 and 3.15 gave almost the same results, as is shown in figure 3.13 for $z_0 = 30$ (a, b) and 110 mm (c, d).

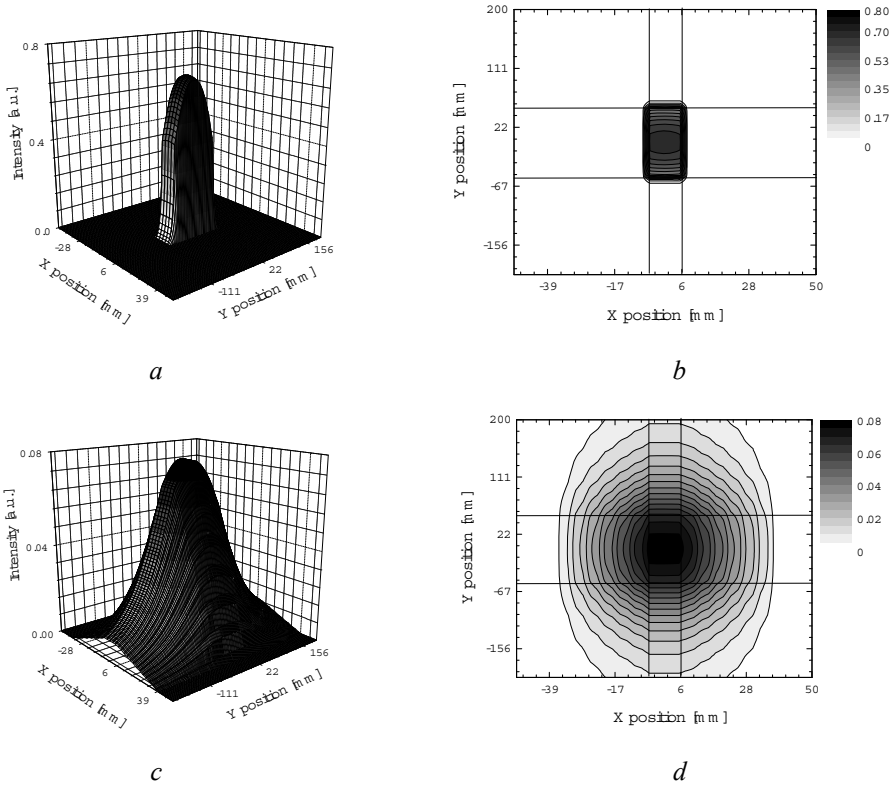

Figure 3.13. Profiles of the X-ray dose in a.u. calculated in the 3D model. An imaginary detector is placed 30 (a, b) and 110 mm (c, d) from the source. Intersection of two horizontal and two vertical solid lines represents the position of the 10 x 100 mm^2 source output window.

It can be seen that due to the divergence of the beam and the finite size of the source in these two models the dose profile was not homogeneous and that the dose decreased with increasing distance from the source. It has been assumed that the brightness of the source was

constant across output window, which means that the e-beam current density was homogeneous over the 10 x 100 mm^2 cross-section of the window. The real dose profile was actually sharper (see figure 3.4). We assumed that the actual length of the X-ray emission zone was closer to the length of the plasma cathode (70 mm) and that the current density was higher in the middle of this zone than on the edges.

In our experiments, discussed above, the dosimeter had a finite diameter of ~ 14 mm and the length of the sensitive part was ~ 20 mm. When this dosimeter was placed just 25 mm above the source, it integrated the calculated profiles (see figure 3.13) over its effective cross-section of ~ 10^2 mm^2, thus it gathered the radiation from every point of the source of ~ 10^3 mm^2 in a solid angle of ~ 10^{-1} radian. When the dosimeter was placed inside the chamber, the radiation penetrated first through an aperture of 1 cm in diameter, machined in the flange of the laser chamber placed 25 mm above the output window, and then through a 1 cm diameter window made in the bottom Al electrode leaving a path length for the X-rays of 1 mm in Al at a distance of 70 mm above the source window. This layout collimated the beam, effectively limiting the integration area in Eq. 3.15 to ~ 10^2 mm^2, and allowed to gather the X-ray radiation in a solid angle of ~ 10^{-2} radian. This collimation reduced the dose approximately 50 times due to the initial beam profile and the divergence of the beam, which corresponded to the observed X-ray attenuation.

3.6.3 Preionization electron density

The numerical model, given in sect. 3.5.2 validated our assumption that the registered signal amplitude was proportional to the total charge of electrons produced by X-ray pulse. However the measured preionization electron density in He was, compared to the measured value in Ar, much higher than expected from theory (see chapter 1, sect. 1.4). Our analysis presented below proved that this was caused by an additional electron generating process in the gas due to the photo-electric effect.

In order to check if the observed preionization electron density in gases indeed was achieved by an X-ray pulse with a dose of ~ 1 mrad, we have calculated the electron density in He, Ne and Ar for such a dose.

It was measured that an X-ray pulse with a dose of ~1 mrad per shot produced ~ 10^7 electrons in cm^3 at a pressure of 1 bar in all investigated gases. By the definition 1 rad is "*the unit of energy absorbed from ionizing radiation, equal to 100 ergs per gram or 0.01 joules per kilogram of irradiated material*". Then, 1 mrad is 10^{-5} J/kg or ~ 6.25 10^{13} eV/kg. The average ionization energy for atoms is in order of ~ 10^1 eV, so 1 mrad should produce ~ 10^{12} – 10^{13} electrons per kg of the matter, if this dose is absorbed. On the other hand, the used pen dosimeter is calibrated for human body tissues, where X-rays are absorbed stronger than in gases. Therefore, it is expected that in gases this X-ray dose should produce less than ~ 10^{12} electrons per kg.

To find the number of electrons per kg produced in gases in our experiments we assumed for the mass density of He: 1.66 10^{-4} g/cm^3, 8.39 10^{-4} g/cm^3 for Ne and 1.66 10^{-3} g/cm^3 for Ar at 1 bar gas pressure from [11, 12]. The preionized volume was ~ 1 cm in height and 1 cm in diameter, thus the gas volume was ~ 0.8 cm^3. This volume of He weights ~ 6.64 10^{-7} kg, ~ 3.36 10^{-6} kg for Ne and ~ 6.64 10^{-6} kg for Ar at a gas pressure of 5 bar. According to this calculations and the data presented in figure 3.8 (a) the X-ray pulse was observed to produce ~ 8 10^{13} electrons per kg in He, ~ 1.8 10^{13} electrons per kg in Ne, and ~ 1.5 10^{13} electrons per kg in Ar. These numbers are higher than expected. Also, according to these calculations the absorbed dose in He was higher than in Ne and in Ar at the same gas pressure and gas volume. The theory

however predicted an inverse relation between absorbed doses in He, Ne and Ar (see chapter 1 sect. 1.4).

In order to find the predicted ratio of the electron densities produced in He, Ne and Ar by the same X-ray pulse we have conducted the following considerations.

Heavier gases like Ne and Ar absorb X-ray radiation better than He at the same gas pressure due to higher mass density ρ and higher mass energy-absorption coefficient μ_E/ρ. The exponential X-ray absorption law is similar for attenuation effects and is given by Eq. 2.16 (see chapter 2), although in this case the mass attenuation coefficient has to be replaced by the mass energy-absorption coefficient. This is because the mass attenuation coefficient describes the attenuation of the X-ray beam including all processes, for example, elastic scattering of photons (without change of the photon energy), while the mass energy-absorption coefficient refers to the energy absorbed by matter due to photo-ionization, Compton scattering and other inelastic processes, leading to absorption of photons and/or changes in their energy.

What is absorbed in the gas is the difference between the initial beam energy intensity and the attenuated energy intensity:

$$\begin{aligned} I_0 - I(x) &= I_0 \left(1 - \exp\left(-\left(\frac{\mu_E}{\rho}\right)\rho x\right)\right) \approx \\ &\approx I_0 \left(1 - \left(1 - \left(\frac{\mu_E}{\rho}\right)\rho x\right)\right) = I_0 \left(\frac{\mu_E}{\rho}\right)\rho x \end{aligned}, \tag{3.16}$$

if the absorption is weak, i.e.:

$$\left(\frac{\mu_E}{\rho}\right)\rho x << 1. \tag{3.17}$$

The number of fast primary electrons, produced by ionization of atoms due to absorption of X-ray photons, is proportional to the left part of Eq. 3.17. These fast primary electrons produce slow secondary electrons with an average energy loss A_I, which is proportional to the ionization energy I. The ionization energy I for He is ~ 24 eV, ~ 21 eV for Ne and ~ 15 eV for Ar. Thus A_I is comparable for these three gases; however, it is the lowest for Ar and is the highest for He. The total number of electrons produced by the same pulse in different gases at the same gas pressure and in the same volume is then proportional to the mass absorption coefficient of a gas, its mass density, and inversely proportional to the average energy loss in an ionization act:

$$N \propto \frac{\left(\frac{\mu_E}{\rho}\right)\rho}{A_I}. \tag{3.18}$$

The $(\mu_E/\rho)\ \rho$ values for He, Ne and Ar at 5 bar gas pressure for X-ray photons with an energy of 30, 56 and 100 keV are given in Table 3.1, according to references 11 and 12 (see also Appendix, figure A.3). It is seen from this table that the absorption is really weak and Eq. 3.17 is valid for the chamber gap length of ~ 1 cm and a gas pressure less than or equal to 5 bar in our experiments.

	30 keV	56 keV	100 keV
He	$7.8\ 10^{-6}$	$1.1\ 10^{-5}$	$1.7\ 10^{-5}$
Ne	$1.5\ 10^{-3}$	$4.7\ 10^{-4}$	$1.2\ 10^{-4}$
Ar	$2.2\ 10^{-2}$	$3.1\ 10^{-3}$	$6.0\ 10^{-4}$

Table 3.1. The $(\mu_E/\rho)\rho$ [cm^{-1}] values for different gases at a pressure of 5 bar and different X-ray photon energies.

According to Table 3.1 Ar absorbs 30 keV photons ~ 2800 times better and 100 keV photons ~ 35 times better than He. For Ne and He the same ratios are ~ 190 and ~ 7. Taking into account the fact that the average energy loss in an ionization act in Ar is less than in He the preionization electron density in Ar should be ~ 10^2 – 10^3 times higher than in He. Our measurements show however that the preionization electron density in Ar is only ~ 2 times higher than in He (see figure 3.8 (a)).

The total free charge produced in a gas is the product of the elementary charge e (the charge of electron) and the total number N of electrons produced in the gas and is given by Eq. 3.18. The mass of the gas volume V is $V\rho$. The dose D absorbed in the gas in terms of electrons per kg is:

$$D = \frac{eN}{V\rho} \propto \frac{\left(\frac{\mu_E}{\rho}\right)}{A_I} \tag{3.19}$$

for a gas volume V. The energy loss in an ionization act A_I differs slightly compared to μ_E/ρ for different gases. Therefore the dose absorbed in different gases is determined mostly by the mass energy-absorption coefficient at the same gas pressure and volume. The mass energy-absorption coefficient drastically depends on the photon energy. Values of μ_E/ρ for He, Ne and Ar and X-ray photon energy of 30, 56 and 100 keV are given in Table 3.2.

	30 keV	56 keV	100 keV
He	$9.4\ 10^{-3}$	$1.3\ 10^{-2}$	$2.0\ 10^{-2}$
Ne	$3.6\ 10^{-1}$	$1.1\ 10^{-1}$	$2.8\ 10^{-2}$
Ar	$2.6\ 10^{0}$	$3.7\ 10^{-1}$	$7.2\ 10^{-2}$

Table 3.2. The (μ_E/ρ) [$cm^2\ g^{-1}$] values for different gases and X-ray photon energies.

According to Table 3.2 and Eq. 3.19 the absorbed dose in He should be less than in Ne and less than in Ar. However, the absorbed dose estimated above from figure 3.8 (a) is ~ 8 10^{13} electrons per kg in He, ~ 1.8 10^{13} electrons per kg in Ne, and ~ 1.5 10^{13} electrons per kg in Ar, so the estimated absorbed dose is higher in He than in Ne and Ar. This result contradicts strongly with the theoretical predictions.

Eqs. 3.17 and 3.18 also predict that for the same gas the number of electrons produced in the volume is proportional to the gap length and gas pressure, because the mass density of a gas is proportional to the gas pressure. Then the specific electron density n_e/p should be constant. However, the experiments showed a different dependence of the total number of electrons N_e and the specific electron density n_e/p on the gas gap length. In figure 3.8 (a) the total number of electrons measured in the volume is almost independent on the gap length, both in Ne and Ar. In He the the total number of electrons grows very slowly with the gap length. So the specific electron density (figure 3.8 (b)) drops almost as $1/d$, where d is the gap length in the ionization chamber.

Therefore we concluded that there should be another mechanism for the electron production for preionization the gas volume in addition to the direct absorption of X-ray photons in a gas.

3.6.4 Photo-electric effect at the cathode

The observed phenomena could be explained by means of taking into account the photo-electric effect at the cathode. When an X-ray photon is absorbed by an atom of metal, the atom is ionized and a free electron is released. The energy of this electron is comparable to the energy of the incident photon, if the ionization took place from one of the outer shells, because the energy of a photon is in the order of ~ 10 – 100 keV, which is much higher than the ionization energy. Then this electron experiences elastic and inelastic collisions and finally may leave the bulk of the metal, penetrating into the gas volume of the chamber. Of course, its energy is less than the initial energy because of the inelastic collisions. However, if the electron escaped from the surface layer with a thickness comparable to the inelastic mean free path (IMFP) λ_{IE}, the energy loss is not very significant. Then this fast electron may cause ionization of the gas volume in the same way as primary electrons, produced due to direct ionization of the gas by absorption of X-ray photons. Primary electrons, produced further from the metal-gas interface surface than IMFP, penetrate into the gas with less kinetic energy. The deeper in the bulk of the metal the electron is produced, the lower is its kinetic energy when it leaves the metal. Therefore, the so-called photo-electrons injected from the metal into the gas may be characterized by the mean escape depth (MED) and the average kinetic energy.

In order to find out if the photo-electric effect can explain the deviation of the experimental results from the theoretical predictions we first estimated the MED of electrons. Auger electron spectroscopy and X-ray photoelectron spectroscopy are based on detection of such photo-electrons, produced by X-ray radiation in the surface layer of samples. In these techniques the energy of the incident X-ray photons E_{ph} is comparable to the ionization energy of the inner shells I_{in}. Photo-electrons with an energy of ~ E_{ph} - I_{in} are observed. These electrons do not loose a significant amount of energy before they escape from the sample. Then the MED for these electrons is comparable to the IMFP λ_{IE} [13]. In our case, however, the energy of the incident X-ray photons is higher and the electrons may loose a significant part of their initial kinetic energy but electrons with a kinetic energy of 10's of keV may still cause a significant contribution to ionization in the gas volume. Thus the MED in our case is definitely longer than the IMFP and comparable to the range of electrons in the material of the electrode.

We have estimated the MED as the half of the electron range in the metal with an initial kinetic energy ~ 50 - 60 keV using the continuous slow-down approximation (CSDA, see chapter 1, Eqs. 1.29 and 1.30, and figure A.1 within Appendix). At half the range the electron loses only ~ $1/4^{th}$ of its initial kinetic energy. The upper surface of the Al cathode is covered with a Ni layer with a thickness of ~ 30 μm. In Ni the CSDA range R of electrons with an initial energy of ~ 50 – 60 keV is ~ 9 μm, which is less than the thickness of the Ni layer 30 μm. So it is only possible for electrons to escape from this Ni layer when the MED d_{es} is ~ 4.5 μm.

In order to find the number of photo-electrons produced in a metal surface layer with a thickness d_{es} we have calculated the amount of energy, absorbed in this layer. If the intensity of the X-ray beam before this 4.5 μm thick layer is I_0, then the intensity of the beam after this layer is:

$$I_1 = I_0 \exp\left(-\left(\frac{\mu}{\rho}\right)_{Ni} \rho_{Ni}\, d_{es}\right) \approx$$
$$\approx I_0 \left(1-\left(\frac{\mu}{\rho}\right)_{Ni} \rho_{Ni}\, d_{es}\right) \approx 0.992\ I_0 \quad , \tag{3.20}$$

while the number of photons absorbed and fast primary electrons produced in and escaped from this Ni layer N_{Ni} is:

$$N_{Ni} \propto I_0 \left(\frac{\mu_E}{\rho}\right)_{Ni} \rho_{Ni}\, d_{es} \approx 6.81 * 10^{-3}\ I_0 . \tag{3.21}$$

In order to estimate the influence of the photo-effect this number of photo-electrons has to be compared to the number of primary electrons, produced by X-ray absorption in the gas, which is:

$$N_g \propto I_1 \left(\frac{\mu_E}{\rho}\right)_g \rho_g d_g \approx 0.992\ I_0 \left(\frac{\mu_E}{\rho}\right)_g \rho_g d_g . \tag{3.22}$$

After substitution of the values from the Table 3.1 for He, Ne and Ar at 56 keV, corresponding to a gas pressure of 5 bar, and d_g = 1 cm, the corresponding values for N_g are ~ 1.1 10^{-5} I_0 in He, ~ 4.7 10^{-4} I_0 in Ne, and ~ 3.1 10^{-3} I_0 in Ar, where I_0 is the X-ray beam intensity.

It can be seen from this estimation that the number of the primary fast electrons, produced due to photo-electric effect in the cathode, is comparable to the number of the primary electrons produced due to direct absorption of X-ray photons in Ar. However, in Ne and especially in He the photoemission from the cathode is the dominant process. The number of the photo-electrons emitting from the cathode is independent of the gas pressure, gap length and gas composition,

however, the number of the secondary slow electrons produced by these fast primary electrons depends on the average energy loss in an ionization act, which decreases with the atomic weight of the gas. So the total number of the electrons produced is constant and independent on the gap length, and the specific electron density drops as *1/d* if the cross-section of the ionized volume is constant, exactly as was measured and is shown in figure 3.8.

3.6.5 Influence of the CSDA range of electrons in gases on the preionization electron density

The influence of the photo-electric effect has been investigated in sect. 3.6.4 assuming that the range of primary electrons (with energy ~ 10 – 100 keV) is less than the characteristic size of the gas volume. Otherwise primary electrons do not loose all their energy on the ionization of the gas, and the total number of electrons produced is expected to depend on the characteristic size of the gas volume.

In order to compare the electron range and the characteristic size of the gas gap we have calculated the CSDA ranges in different gases and for electrons with different kinetic energies. The CSDA ranges in terms of bar cm for He, Ne and Ar and at electron energies of 30, 56 and 100 keV are given in Table 3.3 (see Appendix, figure A.1 and references therein). These numbers also help to estimate the thickness of the gas layer near the cathode, which is affected by the photoemission.

The characteristic size of the gas volume in our experiments is ~ 1 cm (diameter of the cross-section of the preionized volume or gap length), and at a gas pressure of 5 bar the characteristic $p\ d$ value is ~ 5 bar cm. From Table 3.3 it can be seen, that only relatively slow electrons with energy < 30 keV for He, and < 50 keV for Ne and Ar are efficient in transferring their kinetic energy into ionization of the gas volume. It means that photo-electrons are more effective than primary electrons produced in the gas, because they already lost part of their kinetic energy escaping from the cathode. This explains why the number of electrons produced in He grows with $p\ d$ (figure 3.9) and stays almost constant in Ne and Ar (figure 3.8 (2, 3) at the same p = 5 bar and different d). When the range of electrons is longer than the characteristic size of the gas volume, primary electrons do not lose all their energy inside this volume. On the other hand electrons lose more energy, producing more secondary electrons, as their specific path length in terms of $p\ d$ in a gas increases.

	30 keV	56 keV	100 keV
He	10.6	31	88
Ne	2.6	7.6	21
Ar	1.57	4.46	12

Table 3.3. The CSDA ranges [bar cm] values for different gases and different initial kinetic energies of electron.

To summarize, X-ray radiation in the 50 – 100 keV region is not very effective for preionization of a gas volume by direct absorption of X-ray photons for small scale discharge chambers with a characteristic $p\ d$ value ≤ 10 bar cm because of two reasons: the very weak absorption of X-ray photons in gas and the long penetration range of the primary fast electrons. The contribution of electrons from photo-electric emission from the cathode surface to the gas

volume preionization in these small scale discharge chambers is significant and can be even much larger than the contribution from direct X-ray ionization. For example, in Ar at a gas pressure of 5 bar and a gap length of 1 cm the preionization electron density produced by direct absorption of ~ 50 keV X-ray photons is estimated to be comparable to the one created by photo-electrons emitted from the cathode according to Eq. 3.21 and 3.22. In He, under equal conditions, the photo-electrons are estimated to produce a ~ 600 times higher preionization electron density than the direct absorption of X-ray photons in the gas volume.

On the other hand, in large scale discharges ($p\,d$ > 100 bar cm) the influence of the photo-electrons from the chamber walls or electrodes is negligible because of the much stronger absorption of X-rays in the gas and lower ratio of the range of photo-electrons to the characteristic size of the gas volume. Due to this fact photo-emission is usually neglected as a source of the gas preionization, although this effect is well known. For example, the definition of Röntgen as ionization unit of the dose, adopted internationally in 1928, is: "*the quantity of radiation which, when the secondary electrons are fully utilized and the wall effect of the chamber is avoided, produces in one c.c. of atmospheric air at* 0^0 *C. and 76 cm. mercury pressure such a degree of conductivity that one electrostatic unit of charge is measured at saturation current*" [14]. Even a technique for dose measurements was developed, based on the photoemission from the walls surrounding a small gas volume, where the ionization density was measured. It is called the Bragg – Gray dosimetry method and the theory of this technique was desribed, for instance, in references 15, 16 and 17.

3.7 Conclusion

An X-ray source based on a vacuum corona plasma cathode was built and investigated. The typical dose, produced by this X-ray source and measured by a conventional pen dosimeter 25 mm above the source in the middle of the output window, was found to be ~ 50 mrad per shot. The dose is distributed non-homogeneously across the output window of the source (10 x 100 mm^2) at a distance of 25 mm above the window of the source; it was observed to drop to almost 5 mrad at the edges of the window. As the distance to the source increased the dose profile flattened and the local dose value decreased, because of the divergence of the produced X-ray beam. The discharge chamber should be installed as close as possible to the output window of the source in order to achieve the highest dose inside the chamber.

The dose, measured inside the discharge chamber, installed 70 mm above the output window of the X-ray source and with a 1 mm thick Al input window 1 cm in diameter, was found to be ~ 1 mrad per shot. This distance is typical for the discharge experiments described in chapter 4 and is the minimum distance allowed by the design of the experimental setup. The 50-fold decrease of the dose was caused mostly by the fact that only radiation from a small part of the source, confined in a narrow solid angle, due to a set of apertures collimating the X-ray beam, was able to penetrate into the discharge chamber.

The specific preionization electron density, produced in the gas inside the discharge chamber with this ~ 1 mrad per shot X-ray pulse, was measured to be in order of 10^7 electrons per cm^3 per bar in all investigated gases and gas mixtures: He, Ne, Ar, He : F_2 / 99.9 % : 0.1 % and He : Xe / 99 % : 1 %. The specific electron density decreased as $\sim 1/d$ with the gap length d at the same gas pressure. At the same gas pressure and gap length the specific electron density was only 2 times higher in Ar than in He. These observations have been explained by the influence of the photo-electric effect from the cathode. It has been shown that in small scale discharges with a characteristic size $p\,d$ < 10 bar cm the number of primary fast electrons, produced by photo-emission from the cathode, exceeded the number of primary electrons produced by direct

ionization of the gas due to X-ray absorption. So it is shown for the first time that in small scale discharge chambers like in our experimental setup, photo-emission effects from the cathode played the most important role with respect to preionization of the the gas volume.

References:

[1] S. Humphries, J.J. Ramirez and M.G. Wilde, IEEE Trans. Plasma Sci., **8**, 517 (1980)
[2] J.I. Levatter, R.L. Sandstrom and J.H. Morris, Proc. IEEE 4th Pulsed Power Conf., 755 (1983)
[3] S.J. Scott, J. Appl. Phys., **64**, 537 (1988)
[4] S.J. Scott, Appl. Phys., B **56**, 201 (1993))
[5] F.A. van Goor, J. Phys. D: Appl. Phys., **26**, 404 (1993)
[6] H.M.J. Bastiaens, PhD thesis, Univ. of Twente, the Netherlands, ISBN 90-365-141-69 (2000)
[7] R.A. Nielsen, Phys. Rev., **50**, 950 (1936)
[8] J.A. Hornbeck, Phys. Rev., **83**, 374 (1951)
[9] J.S. Townsend and V.A. Bailey, Phil. Mag., **46**, 657 (1923)
[10] J.A. Hornbeck, Phys. Rev., **84**, 615 (1951)
[11] J.H. Hubbell, International Journal of Applied Radiation and Isotopes, **33**, 1269 (1982)
[12] S.M. Seltzer, Radiation Research, **136**, 147 (1993)
[13] A. Jablonski and I.S. Tilinin, Phys. Rev. B **54**, 10-927 (1996)
[14] G.W.C. Kaye and W. Binks, Proc. Roy. Soc. A **161**, 564 (1937)
[15] W.H. Bragg, *Studies in Radioactivity*, Mac Millan and Co, London (1912)
[16] L.H. Gray, Proc. Roy. Soc. A **122**, 647 (1928)
[17] L.H. Gray, Proc. Roy. Soc. A **156**, 578 (1936)

Chapter 4

Investigation of gas discharge pumping schemes for the generation of UV radiation and excimer lasers

Single pulse and double (pre- and main) pulse gas discharge excitation schemes for excimer lasers with X-ray preionization have been investigated. Different rare gases and rare gas – halogen gas mixtures at a total pressure of 2 bar have been used. Single pulse excitation in combination with X-ray preionization of the gas has been found to be an efficient pumping mechanism for excimer laser gas mixtures.

4.1 Introduction

In order to achieve a long optical pulse (~ 100 ns) from a high gas pressure excimer laser it is required to provide a high discharge pumping density or an electric power deposition density of ~ 1 MW cm^{-3}. It has been discussed in chapter 1 that the discharge should be distributed uniformly across the gaseous medium and should last in a homogeneous mode for a time period longer than ~ 100 ns. As mentioned in chapter 1 in such high pressure gas discharges at this high power deposition values discharge instabilities tend to develop. To avoid or, at least, to suppress the formation of discharge instabilities preionization of the gas volume is required, as described also in chapter 1. The design and characteristics of the X-ray source used for the preionization of the gas has been discussed in chapter 3. It was found that this vacuum corona plasma cathode based X-ray source creates a gas volume preionization with a specific electron density of ~ 10^7 cm^{-3} bar^{-1} in He. We have also designed a gas discharge excitation scheme to pump the active medium of fluorine based excimer laser gas mixtures at gas pressures of a few (typically 1 – 5) bar.

Although in our experiments we have used an electrical discharge in a laser gas mixture to pump the active medium of fluorine based excimer lasers, there are different excimer laser excitation schemes. The first excimer laser was reported in 1970 by Basov et al. [1], who observed stimulated emission from Xe_2^* using excitation of liquid Xe by a beam of electrons. In 1972 xenon gas at a high-pressure was excited also by an electron beam [2]. Laser action in rare gas - halogen gas mixtures was reported for the first time in 1975 for $XeBr^*$ and XeF^* [3, 4]. The first ArF^* laser was reported in 1976 [5]. All these high pressure laser gas mixtures were pumped by e-beams. At the same time the transversely excited atmospheric (TEA) gas discharge pumping technique, known from other gas lasers, like for example the CO_2 laser, was further improved and made applicable for excimer lasers. For instance, XeF^*, KrF^* and ArF^* excimer lasers pumped by a TEA discharge in the laser gas mixture were reported also in 1976 [6].

High-pressure gas discharges differ from low-pressure discharges in many parameters. For example, at a low gas pressure the breakdown of the electrode gap occurs in the form of a Tonwsend avalanche, while at a high gas pressure the gap breakdown usually happens via

multiple microscopic streamers [7]. The streamer breakdown mechanism usually leads to sparking or arcing unless the individual streamers overlap and in this way form a uniform avalanche-like breakdown, as shown in sect. 1.3.6 of chapter 1. To provide streamer overlapping they have to be close enough to each other. This means that, because each streamer is initiated from a free electron, the breakdown has to evolve from a sufficiently high initial electron density ($\sim 10^7$ - 10^8 cm^{-3} bar^{-1}). This initial electron density is usually produced by a separate preionization source [8, 9]. The electric field strength in the different parts of a glow discharge, like the cathode sheath or the positive column, is established in such a way that an equilibrium exists between the production and losses of the charged particles. This equilibrium electric field strength E, and thus the discharge voltage across the gap, usually increases proportionally to the gas pressure p [7]. The discharge current density j at the same E/p increases as p^2 [7]. Therefore the discharge current grows as p^2 at an equal discharge cross-section. Thus the power deposition density into a discharge increases steeply with the gas pressure as p^3. An increased power deposition density leads to a stronger gas heating, which on its turn is a source of thermal instabilities in the discharge [7]. In presence of electro-negative gases, e.g., halogens in excimer laser gas mixtures, attachment of electrons to electro-negative atoms and molecules plays an extremely important role in the discharge kinetics and may cause attachment-related discharge instabilities [7, 10, 11].

Various techniques were developed to avoid such discharge instabilities, but they all have in common that, in order to provide a uniform gap breakdown, a proper preionization of the laser gas mixture prior to the onset of the main discharge is applied. Preionization of a gas volume can be done in a lot of different ways as for example by means of UV radiation [6], X-ray radiation [12], an RF barrier discharge [13] or a high voltage pre-pulse with a short duration [12, 14] prior to the main discharge.

The pre- and main pulse excitation technique, also known as pulser / sustainer excitation scheme, was proposed in 1972 [14] for the excitation of a low pressure CO_2 laser. Later this scheme with small modifications was successfully employed for excitation of high pressure CO_2 [15, 16] and $XeCl^*$ lasers [17]. The basic idea of this method is that a short duration high voltage pulse is applied to a discharge gap. The gap is over-voltaged during the pre-pulse compared to the discharge steady-state voltage. The pre-pulse creates a significant electron density in the gas volume, although the power deposition is relatively low during the pre-pulse. The pre-pulse duration is short compared to the duration of the main discharge and to the onset time for instabilities. The main pulse is applied to the created plasma and the energy stored in the capacitor is deposited into the discharge, pumping the laser active medium. The voltage of the main pulse is close to the steady-state discharge voltage. In reference 12 this pre- and main discharge scheme is used in conjunction with X-ray preionization to pump a F_2^* laser emitting in the vacuum ultraviolet (VUV) part of the electro-magnetic spectrum at 157 nm.

A different approach to the double pulse excitation of a gas discharge was proposed in reference 18 for $XeCl^*$ laser pumping. The idea proposed in [18] is based on the stability diagram of a self-sustained discharge in a HCl containing excimer laser gas mixture. The dependence of the specific electron density N_e/p on the specific electric field E/p in the steady-state part of the discharge is nonlinear. In the region $N_e/p < 10^{10}$ cm^{-3} bar^{-1} the steady-state electron density increases with the steady-state electric field strength. This is the lower positive branch corresponding to a low-current discharge. In the region between 10^{10} and 10^{15} cm^{-3} bar^{-1} the higher steady-state electron density requires a lower electric field in the discharge. According to the authors this negative branch is responsible for the discharge ionization instability. At an electron density value higher than 10^{15} cm^{-3} bar^{-1} there is another positive branch corresponding to a high-current discharge. Therefore it is proposed in reference [18] to create first a low-current

discharge and then switch it into a high-current discharge skipping the negative branch. In order to realize their proposal they employed such a double pulse gas discharge excitation in combination with X-ray preionization. In their experiments, an X-ray pulse created the preionization of the gas volume prior to the pre-discharge. The pre-discharge voltage was chosen close to the steady-state voltage of the low-current discharge. The pre-discharge burned at a low current density of ~ 0.1 -10 A cm^{-2}. The pre-discharge duration was ~ 1 μs. The main pulse was applied at the moment when the pre-discharge current reached the peak value. The main discharge voltage was chosen to be ~ 1.5 times higher that the steady-state voltage of the low-current discharge. After applying the main pulse the discharge was transformed into a high-current discharge form. The main discharge current density was typically ~ 200 – 300 A cm^{-2} and the current pulse width was ~ 400 - 800 ns. According to [18] this excitation scheme was successfully employed for excitation of a $XeCl^*$ laser at a total gas pressure of 2 bar.

In this chapter of the thesis we describe our experiments on an X-ray preionized pre- and main pulse excitation scheme. In our design we were able to vary to a large extent all the parameters for the pre – and main pulses such as pulse duration, charging voltage, current and power deposition. In order to find the optimal pre-pulse parameters, we have varied them from typical for the usual pre-pulse schemes [12, 14] to values typical for the Bychkov scheme [18]. From our experiments it appeared that the double pulse excitation scheme had no advantages compared to a much simpler single pulse X-ray preionized excitation scheme. On the other hand, the single pulse excitation scheme in our case has been proven to be capable of efficient excitation of F_2 containing high pressure laser gas mixtures with discharge pulse durations of ~ 100 ns. The experimental results with our discharge excitation scheme are reported in the present chapter.

4.2 Description of different discharge excitation schemes

The setup for the investigation of the pre- and a main pulse discharge excitation is shown schematically in figure 4.1. The discharge chamber (1) is the same as has been used in the preionization density measurements (see chapter 3). It consists of a cylindrical quartz tube with a length of 60 mm and an inner diameter of 74 mm with two Al flanges attached at either side. The lower Al electrode is attached to the lower flange directly, whilst the upper electrode is attached to the upper flange through a set of Al inserts, which allow discharge gap variation in the range from 0.5 to 4 cm. Both electrodes have rounded edges to prevent enhancing of the electric field at the edges and are covered with a thin layer of Ni (~ 30 μm). The upper electrode is 50 mm in diameter and serves as the anode. The lower electrode is 60 mm in diameter and serves as the grounded cathode. The lower flange has a round opening 10 mm in diameter in the middle, and the lower electrode has a cavity 10 mm in diameter, which form an input window for the X-ray preionization pulse. The thickness of this window is 1 mm. The space between electrodes (the discharge gap) is 10 mm in all experiments described below. The chamber is connected to a vacuum pumping unit and a gas filling system. Prior to each series of experiments the chamber is passivated with a 5% fluorine containing gas mixture, evacuated to a gas pressure of ~ 10^{-6} mbar and then filled with the required gas or gas mixture,. In the experiments with the double discharge excitation scheme, four peaking capacitors, with a capacitance of 50 pF each, have been mounted symmetrically around the circumference of the glass tube. These peaking capacitors were electrically connected in parallel to the discharge gap. A 47 kΩ resistance is electrically connected in parallel to the discharge gap in order to define the voltage level during the charging phase of the pre- and main pulse capacitors.

The preionization X-ray pulse is generated by an electron beam source based on a wired plasma cathode (2) described in chapter 3. The source has an output window with an area of 10 x 100 mm^2. The whole X-ray source is shielded by a 2.5 mm thick lead cover, leaving uncovered only the central part of the output window 10 mm in diameter. The discharge chamber is installed such that the round opening in the shielding of the X-ray source, the opening in the lower flange and the cavity in the lower electrode of the discharge chamber have the same axis. The distance from the X-ray source output window to the input window of the discharge chamber is 70 mm. This is the minimal distance, allowed by the design of the X-ray source and the discharge chamber and its mounting. The dose produced by the X-ray source inside the discharge chamber has been measured to be ~ 1 mrad per shot. Such X-ray pulse has been found to create a specific electron preionization density in the discharge chamber of ~ 10^7 cm^{-3} bar^{-1} in He (see chapter 3).

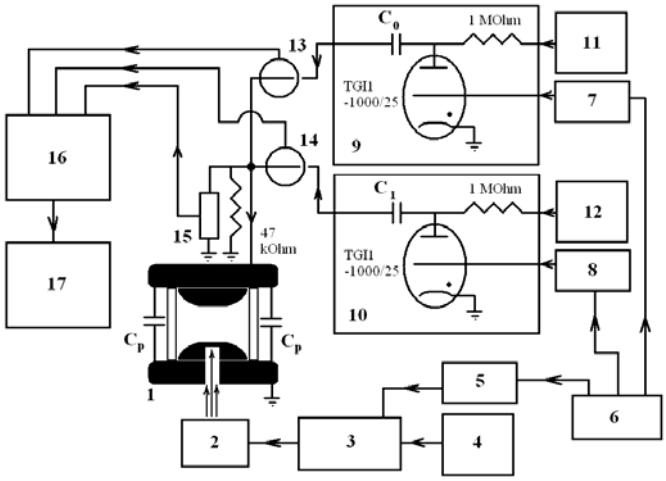

Figure 4.1. Experimental setup for pre- and main pulse discharge excitation.
1: discharge chamber, C_p is a set of 4 peaking capacitors 50 pF each; 2: X-ray source; 3: mini-Marx generator; 4: HV DC power supply; 5: triggering unit for mini-Marx generator; 6: primary pulse generator; 7, 8: triggering units for thyratrons; 9, 10: pre- and main pulse forming units, C_0 and C_1 are storage capacitors; 11, 12: HV DC power supplies; 13, 14: current transformers; 15: HV fast voltage probe; 16: oscilloscope; 17: PC.

The X-ray source (2) is powered by a home-made 6-stage mini-Marx generator (3), which is charged by HV DC power supply (Hipotronics R 60A) (4) and triggered by a home-made thyratron (Perkin Elmer 766A) based trigger unit (5). The trigger unit (5) on its turn is triggered by a primary pulse generator (6), which consists of two coupled pulse generators: Farnell PG 102 and Hewlett-Packard 8003A. This primary pulse generator (6) is also used to trigger two identical home-made pulsers (7 and 8) each designed to switch a TGI1 – 1000/25 thyratron installed in the pre- (9) and main pulse (10) forming units. These pulse forming units are almost identical except for the capacitance of the storage capacitors. The storage capacitor C_0 of the pre-pulse unit (9) is charged by a HV DC power supply (Hipotronics 8100-10) (11) through a current limiting resistor with an impedance of 1 MΩ. The capacitance of C_0 has been either 0.8 nF or 3 nF in different experiments. The storage capacitor C_1 of the main pulse circuit (10) is charged by

another HV DC power supply (Philips 9412) (12) through another limiting resistor with an impedance of 1 MΩ. The capacitance of C_1 has been either 30 nF or 42 nF in different experiments. The actual capacitances of C_0 and C_1 are indicated for every set of experiments in the text. The pre-pulse is applied by discharging C_0 in the gas of the discharge chamber (1) after switching the thyratron by the trigger unit (7). The main pulse is applied by discharging capacitor C_1 in the gas chamber (1) after a trigger pulse from trigger unit (8).

The waveforms of current in the pre- and main discharges are measured by two home-made and calibrated current transformers (13 and 14). Each of these current transformers has a bandwidth of ~ 100 MHz. The voltage waveform of both (pre- and main) discharges together is measured by a home-made and calibrated HV probe (15) with a bandwidth of ~ 100 MHz electrically connected parallel to the discharge gap. The voltage and current waveforms are recorded by a digital oscilloscope (Tektronix TDS 640A) (16) connected to a PC (17).

In the single pulse excitation experiments the main pulse forming unit (10 in Fig. 4.1), has been disconnected from the discharge chamber. Also the peaking capacitors, connected parallel to the discharge gap, have been removed during these experiments. In the single pulse discharge excitation experiments the pre-pulse forming unit (9 in Fig. 4.1) is used alone, and it is referred to as the pulse forming unit.

4.3 Experimental results of the different discharge excitation schemes

4.3.1 Investigation of pre- and main pulse excitation schemes with X-ray preionization

In our experimental setup the discharge has always been ignited in the center part of the discharge electrodes, where the preionization by the X-rays entering through the cathode window, occurs. Depending on the gas mixture composition, the storage capacitances and the charging voltage a discharge has been observed either in a diffuse or in a dense mode. In the diffuse form the visible glow of the discharge occupies an area of ~ 2 – 4 cm in diameter, depending on the above mentioned parameters. The glow is less bright compared to the glow of the dense form of the discharge. In the dense mode the brightness of the discharge is higher, and the glow occupies an area of less than or equal to 1 cm in diameter. In the dense form the visible width of the glow increases with the charging voltage and discharge current until its diameter is ~ 1 cm. Both forms of the discharge are characterized by a steady-state voltage of ~ 0.5 – 4.5 kV, depending on the gas mixture composition. If, in some experiments, a spark appears and leads to the ignition of an arc discharge, it can be clearly distinguished from the glow discharge by the steep voltage drop to almost zero, the drastic increase of the discharge current and by the appearance of oscillations later on in the voltage and current waveforms.

Typical measured voltage V, current I and calculated power deposition P waveforms of a pre-discharge in a He : F_2 / 99.95 : 0.05 gas mixture at a total pressure of 2 bar and a charging voltage U_0 = 10 kV are shown in figure 4.2. The X-ray preionization pulse was applied at the moment indicated by the vertical dashed line. We see that the X-ray pulse is applied during the rising phase of pre-pulse voltage. The capacitance of the pre-pulse storage capacitor C_0 was 3 nF. We see from this figure that the voltage V first rises in ~ 70 ns from 0 to ~ - 10 kV (determined by the charging voltage U_0). After a delay, corresponding to the discharge formation time, the gas gap electrically broke down and the pre-discharge was ignited. In this case the delay was ~ 20 ns, however at lower charging voltages the delay times were much longer, for example, at U_0 = 6 kV the delay time was ~ 200 ns. When no discharge started at all the voltage decreased exponentially

with a typical duration of ~ 140 ms, determined by the capacitance C_0 = 3 nF and the 47 kΩ resistance connected in parallel to the discharge gap. From the moment that the pre-discharge was ignited the voltage dropped down to a steady-state value of U_d ~ 4.3 kV for this He : F_2 gas mixture during ~ 50 ns. The steady-state voltage did not depend on the charging voltage. The current I started to increase at the same time. The peak value of the current of ~ 160 A was reached ~ 100 ns after ignition of the pre-discharge. After reaching the peak value the current was constant for ~ 50 ns in this case. The voltage was equal to the steady-state value during this time. Then both the current and the voltage decreased to zero in ~ 100 ns. The FWHM value of the current was measured to be ~ 150 ns. The calculated power deposition P was found to have a peak value of ~ 600 kW and a FWHM of ~ 120 ns.

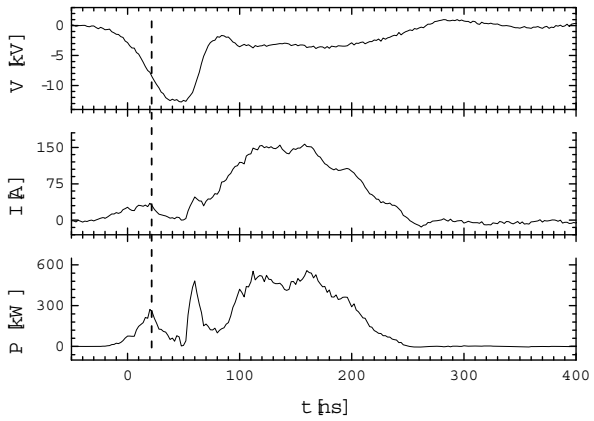

Figure 4.2. Typical measured voltage V, current I and calculated power deposition P waveforms of a pre-discharge in a He : F_2 / 99.95 : 0.05 mixture at a total gas pressure of 2 bar and charging voltage U_0 10 kV. The storage capacitance of the pre-pulse circuit C_0 = 3 nF. The vertical dashed line shows the position in time of the X-ray preionization pulse.

The pre-discharge form was extensively investigated in He, Ne, He : F_2 / 99.95 : 0.05, Ne : He: F_2 / 99 : 0.95 : 0.05 and 97 : 2.85 : 0.15, Ne : Ar / 99 : 1 and Ne : Ar : HCl / 98.9 : 1 : 0.1 at a gas pressure of 2 bar and with a pre-pulse storage capacitance of C_0 = 3 nF. In figure 4.3 the dependence of the charging voltage on the pre-discharge peak current I (a), the FWHM current (b), the peak power deposition P (c), the FWHM power (d), the total transferred charge Q (e) and the energy E (f) deposited into the pre-discharge is shown for the different gases and gas mixtures mentioned above. It can be seen that for the same charging voltage U_0 the lowest peak current was observed in He : F_2 / 99.95 : 0.05 gas mixture (3), and the highest peak current was observed in Ne : Ar / 99 : 1 mixture (6). In general, in He (1) and He : F_2 (3) mixtures the peak current was less than in Ne and Ne based mixtures. Halogen addition was found to decrease the peak current as can be seen from a comparison of (1) and (3), (4) and (5), (6) and (7). The addition of Ar caused an increase of the peak current (compare (2) and (6)).

In all investigated gases or gas mixtures the peak current increased linearly with the charging voltage U_0 as:

$$I = k(U_0 - U_L) \tag{4.1}$$

where the values for k and U_L were determined from the coefficients of the best linear fit. The determined values of k, U_L and the measured steady-state voltage U_d are given in Table 4.1.

	U_d [kV]	U_L [kV]	k [A/kV]
He	3.5±0.5	4.7	31
Ne	1.0±0.2	1.7	32.5
He:F_2 (99.95%:0.05%)	4.3±0.3	4.9	29.8
Ne:He:F_2 (99%:0.95%:0.05%)	1.7±0.2	2.1	31.3
Ne:He:F_2 (97%:2.85%:0.15%)	2.0±0.5	4.5	39.5
Ne:Ar (99%:1%)	0.5±0.2	1.7	32.8
Ne:Ar:HCl (98.9%:1%:0.1%)	2.3±0.4	3.0	30.6

Table 4.1.
Measured quasi-steady-state voltage U_d and U_L and k parameters from a linear fit of the dependence of the pre-discharge current on the charging voltage U_0 for different gases and gas mixtures at a total pressure of 2 bar. Storage capacitance C_0 = 3 nF.

The measured current FWHM (fig. 4.3 b) was observed to decrease with increasing charging voltage until it reaches a value of ~ 110 – 160 ns after which it stayed at a constant value. The measured FWHM of the calculated power deposition (d) also decreased with increasing charging voltage until a value of ~ 100 – 120 ns is reached. Also here it was seen that for higher charging voltages the FWHM of the power deposition stayed constant. The calculated peak power deposition P (c) is the product of the steady-state voltage U_d, which is independent on the charging voltage, and the peak current I, which increases linearly with U_0 according to Eq. 4.1. Therefore, the peak power deposition increases linearly with U_0. In He (1) and in a He : F_2 (3) mixture U_d has the highest values and the peak power deposition grows faster with U_0. In a Ne : Ar (6) mixture U_d has the lowest value and the peak power deposition grows much slower with U_0. The absolute values of the peak power deposition in a Ne : Ar : HCl / 98.9 : 1 : 0.1 mixture (7), a Ne : He : F_2 / 97 : 2.85 : 0.15 mixture (5), He (1) and a He : F_2 / 99.95 : 0.05 mixture (3) are close to each other because the lower peak current in He (1) and in the He : F_2 mixture (3) compared to Ne based mixtures (7 and 5), is compensated by the higher U_d.

The total charge Q transferred into the discharge is calculated as the integral of the current waveform (figure 4.2 b) and is roughly equal to the product of the peak current (figure 4.3 a) and the current FWHM (figure 4.3 b). The solid line (8) in figure 4.3 e corresponds to the total charge stored in the capacitor C_0 charged to a voltage U_0. Since the current FWHM changes with U_0 slightly compared to the peak current, the total transferred charge is mostly determined by the peak current of the discharge. For example, about 95 % of the stored charge is transferred into the discharge in a Ne : He : F_2 / 99 : 0.95 : 0.05 mixture (4), and only about ~ 40 % into a He discharge (1).

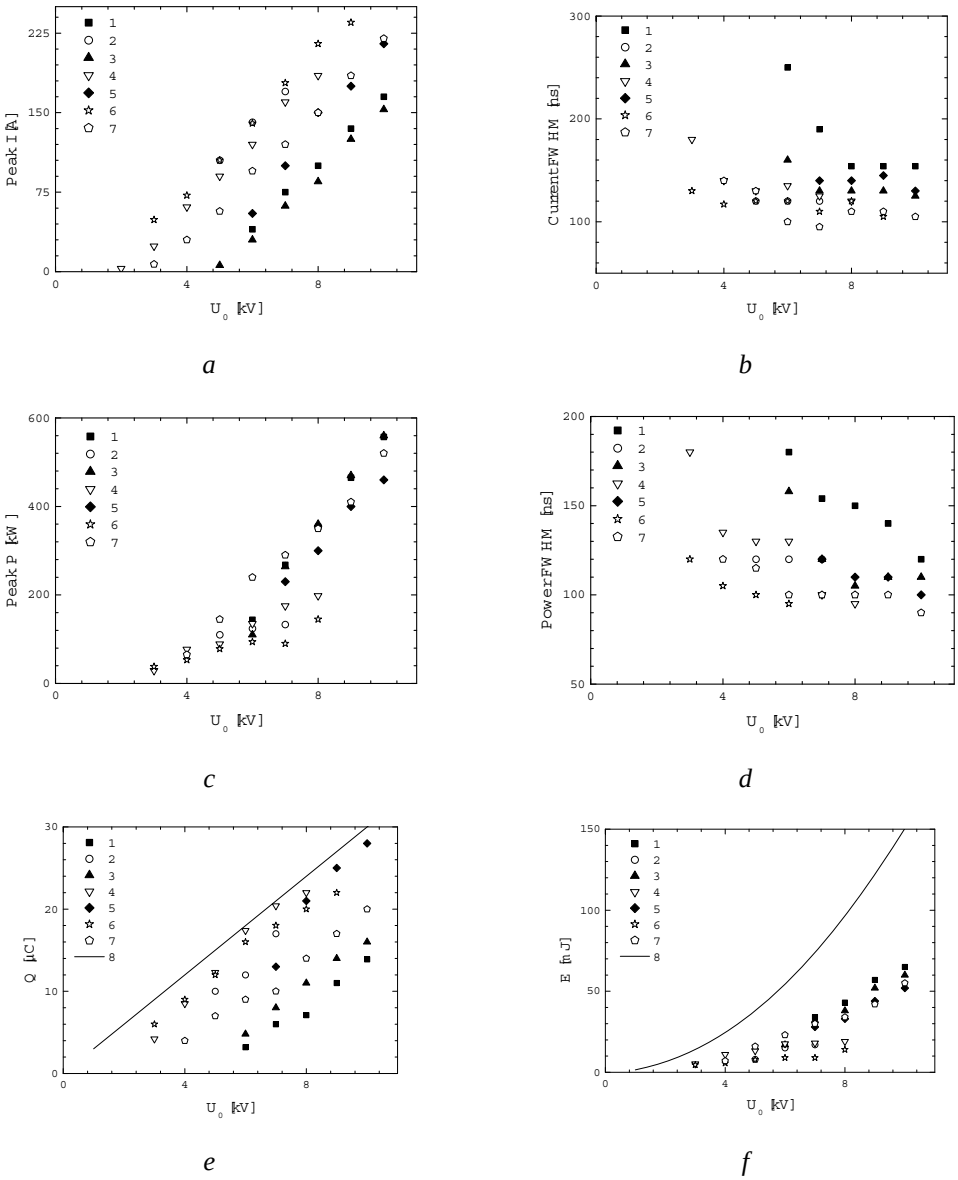

Figure 4.3. Dependence of the pre-discharge peak current I (a), current FWHM (b), peak power deposition P (c), power FWHM (d), total transferred charge Q (e) and energy E (f) deposited into the pre-discharge in He (1), Ne (2), He : F_2 / 99.95 : 0.05 (3), Ne : He : F_2 / 99 : 0.95 : 0.05 (4) and 97 : 2.85 : 0.15 (5), Ne : Ar / 99 : 1 (6) and Ne : Ar : HCl / 98.9 : 1 : 0.1 (7) at a gas pressure of 2 bar on the charging voltage of the pre-pulse circuit U_0. (8) In (e) values for the total charge and in (f) for the energy stored in the capacitor of the pre-pulse circuit charged to a voltage U_0 are added. Storage capacitance of the pre-pulse circuit C_0 = 3 nF.

The total energy E transferred into the discharge is calculated as the integral of the waveform for the power deposition (figure 4.2 c) and is roughly equal to the product of the peak power deposition (figure 4.3 c) and the FWHM power deposition (figure 4.3 d). The solid line (8) in figure 4.3 f corresponds to the total energy stored in the capacitor C_0 charged to the voltage U_0. Since the power deposition FWHM changes with U_0 slightly compared to the peak power deposition, the total transferred charge is mostly determined by the peak power deposition into the discharge. The total transferred power grows almost linearly with U_0, while the total stored energy increases as U_0 squared. For example, in He (1) at a charging voltage of 8 kV ~ 50 % of the stored energy is transferred into the discharge, and only ~ 40 % of the stored energy is transferred at U_0 = 10 kV. On the other hand, in a Ne : Ar / 99 : 1 mixture (6) at a charging voltage of 8 kV only ~ 15 % of the stored energy is transferred into the discharge.

Next the capability of the designed double (pre-pulse main-pulse) discharge excitation scheme with X-ray preionization was investigated. It was checked how to ignite and maintain a uniform and stable discharge in high pressure halogen containing laser gas mixtures. In order to find the optimum performance of the excitation scheme, system parameters, like e.g., the charging voltages, storage capacitances, delay times etc. have been varied and for all settings the discharge voltage and current waveforms have been measured.

In the double (pre- and main) pulse excitation scheme the delays between the preionization X-ray pulse, the pre-discharge and the main discharge are usually set in such a way that the X-ray pulse is applied during the rising phase of the pre-pulse voltage, and the main pulse is applied after ignition of the pre-pulse discharge. Thus the X-ray pulse creates a certain homogeneous preionization level throughout the discharge volume, which facilitates a homogeneous breakdown of the electrode gap due to the pre-pulse. Next to this the main pulse circuit transfers additional energy into the plasma, produced by the pre-discharge, and sustains the discharge at a much higher power deposition level.

Properties of the main discharge in Ne and Ne based mixtures have been observed to differ drastically from the main discharge properties in He and He : F_2 mixture. Typical measured voltage (V) waveform, pre- (I_{pre}) and main discharge current (I_{main}) waveforms of a discharge in Ne at a gas pressure of 2 bar are shown in figure 4.4 a. The calculated power deposition waveforms into pre- (P_{pre}) and main discharge (P_{main}) and total power deposition (P_{total}) are shown in figure 4.4 b.

The vertical dashed line shows the time at which the X-ray preionization pulse was applied. The vertical dotted line indicates the moment the main pulse was applied. The capacitance used in the pre-pulse circuit was 3 nF and the pre-pulse charging voltage was 7 kV. The capacitor of the main pulse circuit was 42 nF and main pulse charging voltage U_1 was 6 kV. The delay time between the pre-pulse and the ignition of the discharge was ~ 150 ns in this case. Then a pre-discharge with a peak current of ~ 180 A and FWHM ~ 120 ns was observed. The voltage dropped to a steady-state value of ~ 1 kV. After ignition of the pre-discharge the main pulse was applied. The peak current of the main discharge was ~ 700 A. The FWHM value of main current was ~ 450 ns and the shape of the main current pulse was observed to resemble half a period of a sine function. The power deposition into pre-discharge reached a peak value of ~ 180 kW and had a FWHM of ~ 120 ns. The power deposition into main discharge reached a peak value of ~ 600 kW with a FWHM of ~ 300 ns. The oscillations on the main discharge power deposition waveform are due to slight oscillations of the voltage waveform in the steady-state voltage region, where the steady-state voltage was rather low in Ne (~ 1 kV). The total power deposition is the sum of power deposition into the pre- and main discharges.

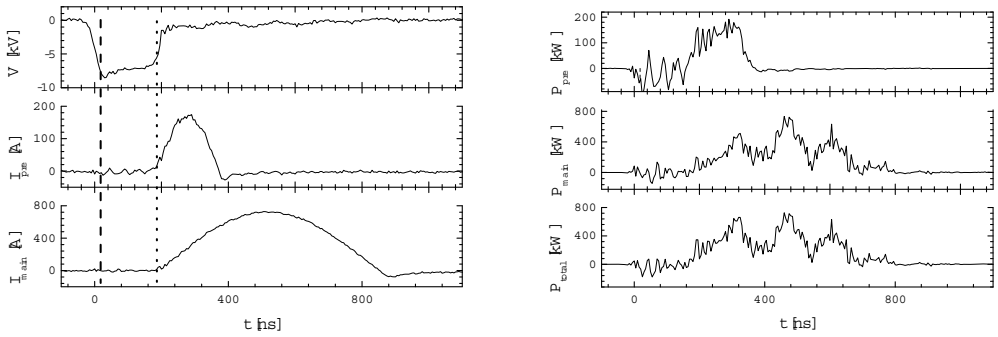

a *b*

Figure 4.4. (a) Typical measured voltage (V) waveform, pre- (I_{pre}) and main discharge current (I_{main}) waveforms of a discharge in Ne at a gas pressure of 2 bar. (b) The calculated power deposition waveforms into pre- (P_{pre}) and main discharge (P_{main}) and total power deposition (P_{total}). Pre-discharge: C_0 = 3 nF, U_0 = 7 kV; main discharge: C_1 = 42 nF, U_1 = 6 kV. The vertical dashed line corresponds to the time of the X-ray preionization pulse; the dotted line shows the moment the main pulse was applied.

Neither the peak current nor the current FWHM of the main discharge in Ne and Ne based mixtures depends on the charging voltage of the pre-pulse. For example, in figure 4.5 the dependence of the peak current I of the main discharge in Ne at a gas pressure of 2 bar on the charging voltage of the main pulse circuit U_1 is shown. The main discharge was ignited without pre-pulse (1) and with pre-pulse at a charging voltage of U_0 = 5 (2), 6 (3) and 7 kV (4). The storage capacitance of the pre-pulse circuit C_0 = 3 nF and the capacitance of the main pulse circuit C_1 = 42 nF. All experimental points lay on a straight line, given by Eq. 4.2:

$$I = 129.6\ (U_1 - 0.6) \tag{4.2}$$

where the current I is in A and the main pulse charging voltage U_1 is in kV. The only parameter affected by the pre-discharge in Ne and Ne based mixtures is the minimum value of the main pulse charging voltage required to ignite the main discharge. In absence of a pre-discharge U_1 had to be higher than the breakdown voltage at the electron preionization density provided by X-ray pulse, in our case ~ 3 kV (see figure 4.5 (1)). When the pre-pulse was applied, it created highly conductive plasma, and the main pulse voltage did not have to break down the gas gap. Thus, the charging voltage of the main pulse needed to be just higher than the steady-state voltage in order to maintain a self-sustained discharge, which was in our case ~ 1 kV (see figure 4.5 (2 – 4).

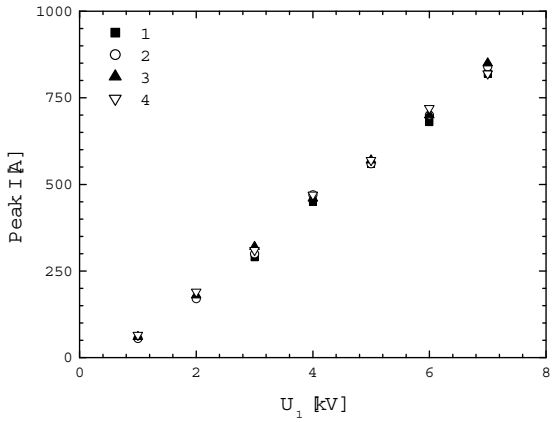

Figure 4.5. Dependence of the peak current I on the charging voltage of the main pulse circuit U_1. Discharge in Ne at a gas pressure of 2 bar without pre-pulse (1) and with pre-pulse at a charging voltage U_0 = 5 (2), 6 (3) and 7 kV (4). The capacitance of the pre-pulse circuit was C_0 = 3 nF and the capacitance of the main pulse circuit C_1 = 42 nF.

The dependence of the discharge peak current I (a), peak power deposition P (b), total transferred charge Q (c) and energy E (d) deposited into the main discharge on the charging voltage U_1 is shown in figure 4.6. The discharge was investigated in Ne at U_0 = 6 kV (1), in a Ne : He : F_2 / 99 : 0.95 : 0.05 mixture at U_0 = 6 kV (2), in a Ne : He : F_2 / 97 : 2.85 : 0.15 mixture at U_0 = 10 kV (3), and in a Ne : Ar / 99 : 1 mixture at U_0 = 10 kV (4). The total pressure of all laser gas mixtures was 2 bar. The total charge (c) and energy (d) stored in the capacitor of the main pulse circuit charged to the voltage U_1 are shown by the solid lines (5). Again the capacitance of the pre-pulse circuit C_0 was 3 nF and the capacitance of the main pulse circuit C_1 was 42 nF. The peak current values are almost the same in all cases at the same charging voltage. The voltage dependence of the peak current (figure 4.6 a) follows a linear dependency given by Eq. 4.2. The peak power deposition (figure 4.6 b) slightly differs in different gas mixtures due to different steady-state voltages in these mixtures. The total charge transfer into the main discharge (figure 4.6 c) is very efficient in all investigated mixtures and it is close to 100 %. The energy deposition into the main discharge grows linearly with the charging voltage, while the total energy stored in the capacitor increases as charging voltage squared. Thus at U_1 = 2 kV the energy transfer efficiency is ~ 40 %, and it is ~ 20 % at U_1 = 6 kV.

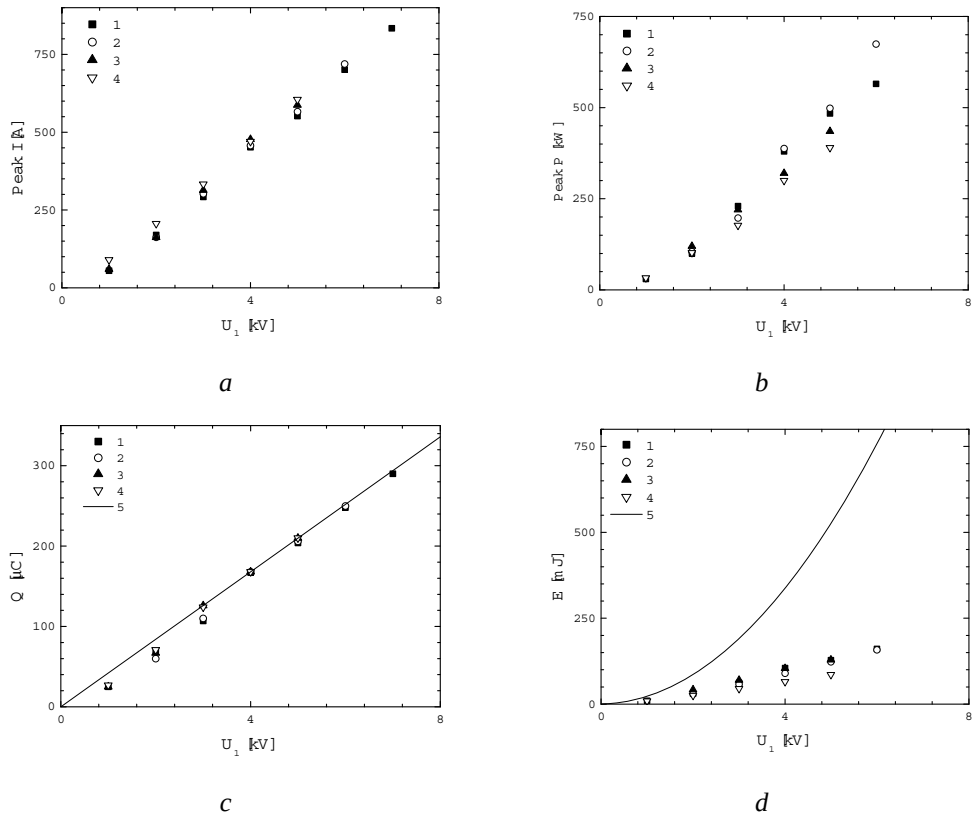

Figure 4.6. Dependence of the discharge peak current I (a), peak power deposition P (b), total transferred charge Q (c) and energy E (d) deposited into the main discharge on the charging voltage U_1. Discharge in Ne at U_0 = 6 kV (1), Ne : He : F_2 / 99 : 0.95 : 0.05 at U_0 = 6 kV (2) and 97 : 2.85 : 0.15 at U_0 = 10 kV (3), and Ne : Ar / 99 : 1 at U_0 = 10 kV (4) and at a total gas pressure of 2 bar. (5) The total charge (c) and energy (d) stored in the capacitor of the main pulse circuit charged to the voltage U_1. Capacitance of the pre-pulse circuit C_0 = 3 nF and the capacitance of the main pulse circuit C_1 = 42 nF.

In our experiments with He and He : F_2 mixtures the pre-pulse main-pulse excitation scheme failed with respect to produce homogeneous discharges. We were able to produce a stable and homogeneous pre-discharge with pre-pulse storage capacitor C_0 = 3 nF charged to a voltage up to 19 kV. However, if the storage capacitor of main pulse circuit C_1 = 30 or 42 nF was charged to a voltage U_1 higher than the steady-state voltage, the main discharge always developed into an arc discharge. At U_1 less than the steady-state voltage main discharge appeared however in the form of a homogeneous non-self-sustained discharge. Non self-sustained means that the discharge can not sustain itself or in other words the discharge does not produce enough new free charge carriers to compensate for the losses. The consequence is that the discharge extinguishes gradually.

In figure 4.7 typical measured waveforms of the voltage V, the pre-discharge current I_{pre} and main discharge current I_{main} (a) in He at a gas pressure of 2 bar are shown. The calculated power deposition into the pre-discharge P_{pre} and main discharge P_{main} and the total power deposition P_{total} waveforms (b) are also shown in this figure. The pre-pulse storage capacitance C_0 = 3 nF was charged to U_0 = 10 kV while C_1 = 42 nF was charged to U_1 = 3 kV. The time at which the X-ray preionization pulse was applied is shown by the vertical dashed line. The vertical dotted line corresponds to the moment the main pulse was applied.

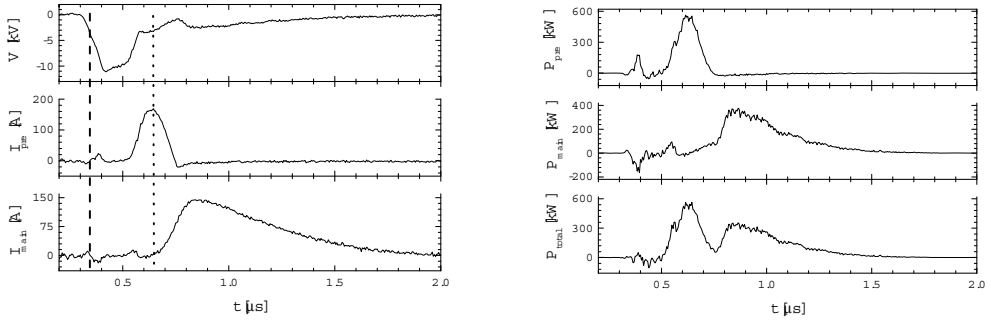

a *b*

Figure 4.7. (a) Typical measured waveforms of the voltage V, the pre-discharge current I_{pre} and main discharge current I_{main} in He at a gas pressure of 2 bar. (b) The calculated power deposition into the pre-discharge P_{pre} and main discharge P_{main}, and the total power deposition P_{tot}. Pre-discharge: C_0 = 3 nF, U_0 = 10 kV; main discharge: C_1 = 42 nF, U_1 = 3 kV. The vertical dashed line corresponds to the X-ray preionization pulse; the dotted line shows the moment the main pulse was applied.

The pre-discharge at U_0 = 10 kV was observed to appear ~ 100 ns after the moment when voltage waveform reached its maximum value. The pre-discharge current had a peak value of ~ 190 A and a FWHM of ~ 120 ns. At the peak value of the pre-discharge current the main pulse was applied. The rise time of the main discharge current was ~ 200 ns, and the peak current was ~ 150 A. After reaching the peak value the main discharge current exponentially decayed with a time constant of ~ 500 ns. This current waveform is typical for a non-self-sustained discharge. The power deposition into the pre-discharge had a peak value of ~ 550 kW and a FWHM of ~ 100 ns. The peak value of the power deposition into the main discharge was ~ 350 kW. As can be seen from this figure the power deposition into main the discharge decreased exponentially in time.

It has been found that in the non-self-sustained form of the main discharge the peak current, power deposition, current and FWHM of the power deposition depend not only on the main pulse charging voltage but on the pre-pulse charging voltage as well. In figure 4.8 the dependence of the discharge peak current I (a), FWHM of the current (b), peak power deposition P (c), power FWHM (d), total transferred charge Q (e) and energy E (f) deposited into the discharge in He on the main voltage U_1 is shown. The total gas pressure was 2 bar He and the charging voltage of the main pulse circuit U_1. All parameter were measured at three different pre-

pulse charging voltages U_0 namely 8 kV (1), 9 kV (2) and 10 kV (3). The total charge (e) and energy (f) stored in the capacitor of the main pulse circuit C_1 = 42 nF charged to voltage U_1 are additionally given by solid lines (4) in figures 4.8 e and 4.8 f. The value of the storage capacitance of the pre-pulse circuit C_0 was 3 nF. One can see that a higher pre-pulse charging voltage U_0 leads to a slightly higher peak current and slightly higher power deposition into the main discharge. The FWHMs of the current and power deposition are much more affected by the pre-pulse charging voltage. For example, at U_0 = 8 kV the FWHM of the main discharge current was ~ 700 – 750 ns and the power deposition FWHM was ~ 400 – 450 ns, while at U_0 = 10 kV the values were ~ 500 ns and ~ 250 – 300 ns respectively. The transferred charge and energy into the main discharge at a given U_1 were almost equal for the pre-pulse charging voltage varied from 8 to 10 kV. The transfer efficiencies of the charge and energy were ~ 45 % and ~ 50 % respectively.

This double pulse excitation scheme with the main discharge working in the non-self-sustained form was also investigated in He : F_2 gas mixtures. For a He : F_2 / 99.95 : 0.05 mixture at a total gas pressure of 2 bar in figure 4.9 the dependence of the main discharge peak current I (a 1), transferred charge Q (a 2), power deposition P (b 1), transferred energy E (b 2), FWHM current (c 1) and FWHM power deposition (c 2) on the main pulse charging voltage is shown. The main pulse capacitance C_1 was 30 nF. For these measurements the pre-pulse storage capacitance C_0 = 3 nF was charged to U_0 = 19 kV. All six parameters have been found to grow almost linearly with the main pulse charging voltage. The highest values of the previously mentioned parameters obtained at U_1 = 3.5 kV were ~ 200 A, ~ 68 μC, ~ 630 kW, ~ 120 mJ, ~ 300 ns and ~ 200 ns respectively. For higher main pulse charging voltages the main discharge showed the tendency to transform into a self-sustained regime and finally ended up in an arc.

In a He : F_2 / 99.95 : 0.05 gas mixture at a total gas pressure of 2 bar the parameters of the main discharge in the non-self-sustained form have been found to depend also on the pre-pulse charging voltage and the pre-pulse storage capacitance. In figure 4.10 this dependence of the main discharge peak current I (a), peak power deposition P (b), total transferred charge Q (c) and energy E (d) deposited into the discharge on the pre-discharge charging voltage U_0 is shown. A capacitor of 30 nF was used as C_1 in the main pulse circuit. Three different combinations of parameters were used in the electrical circuit and denoted in figure 4.10 as (1): C_0 = 0.8 nF and the charging voltage of the main pulse circuit U_1 was 2.75 kV; (2) C_0 = 0.8 nF and U_1 = 3 kV and (3): C_0 = 3 nF and U_1 = 3 kV. We see from this figure that with a pre-pulse storage capacitance of C_0 = 0.8 nF (1, 2) the peak current I, peak power deposition P, transferred charge Q and energy deposition E have increase with increasing pre-pulse charging voltage U_0. With C_0 = 3 nF (3) the same main discharge parameters are almost independent of U_0. However, one can also see from the figure that an increase of the pre-pulse charging voltage leads to a more powerful main discharge for (1) and (2): a slightly higher value of the main pulse charging voltage for the same values of C_0 and U_0 creates a more powerful main discharge. An increase of the pre-pulse capacitance also enhances the main discharge at the same charging voltages of pre- and main discharges (compare 2 and 3).

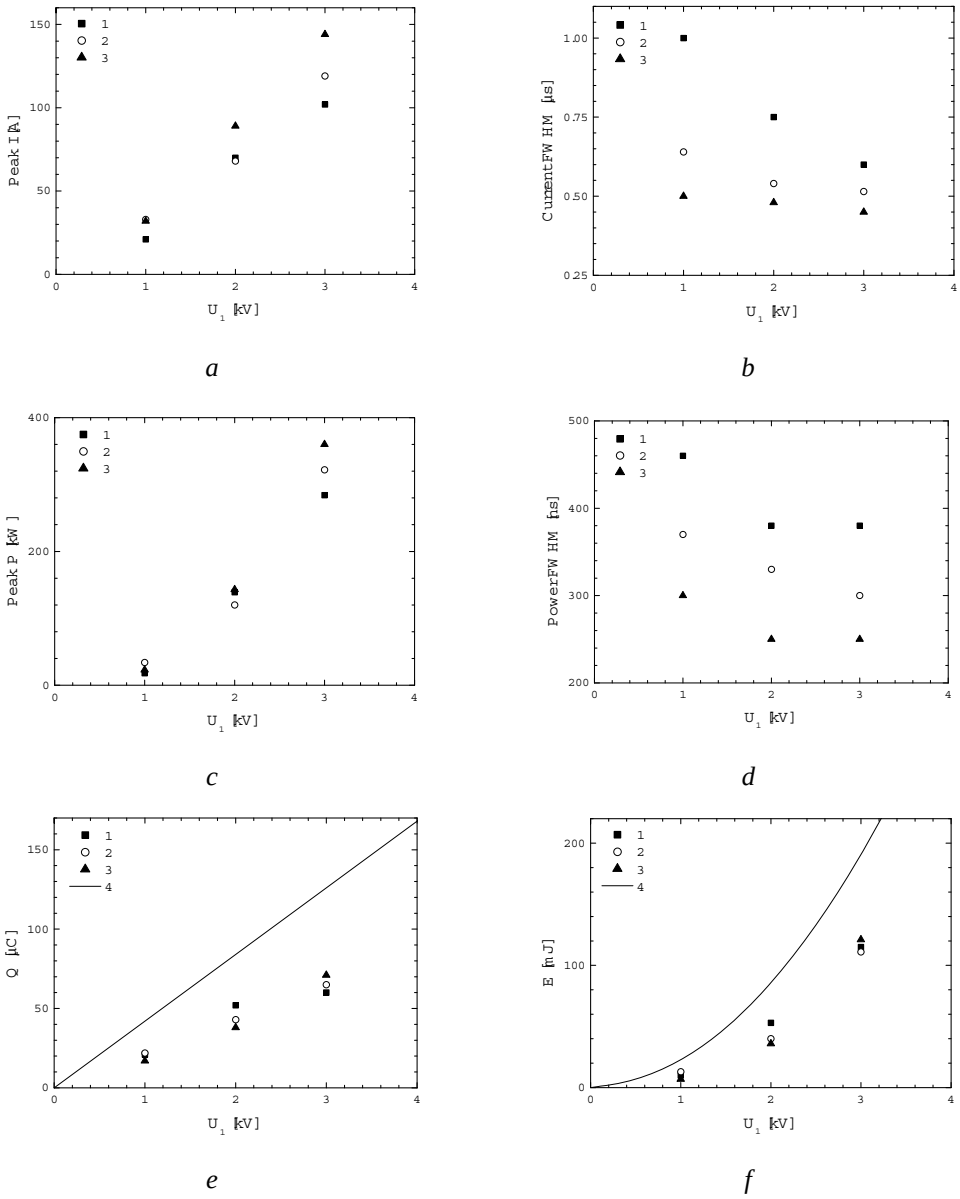

Figure 4.8. Dependence of the discharge peak current I (a), current FWHM (b), peak power deposition P (c), power FWHM (d), total transferred charge Q (e) and energy E (f) deposited into the discharge in He at a gas pressure of 2 bar on the charging voltage of the main pulse circuit U_1. The pre-pulse charging voltage U_0 is 8 (1), 9 (2) and 10 kV (3). (4) The total charge (e) and energy (f) stored in the capacitor of the main pulse circuit C_1 = 42 nF charged to the voltage U_1. The capacitance of the pre-pulse circuit C_0 = 3 nF.

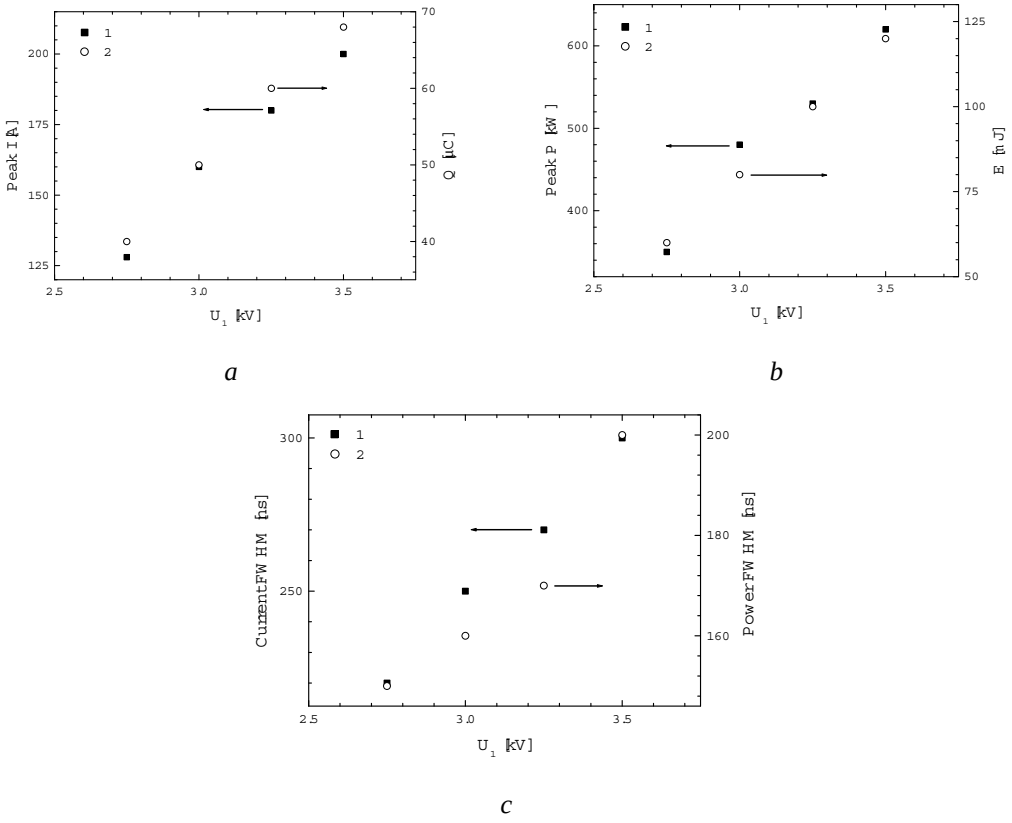

Figure 4.9.(a) Dependence of the peak current I (1) and total transferred charge Q (2) on the main pulse charging voltage U_1; (b) dependence of the peak power P (1) and total transferred energy E (2) on U_1; (c) dependence of the FWHM current (1) and FWHM power deposition (2) on U_1. Discharge in He:F_2 / 99.95:0.05 at a total gas pressure of 2 bar. Capacitance of the main pulse circuit C_1=30 nF. Capacitance of the pre-pulse circuit C_0=3 nF and the charging voltage U_0=19 kV.

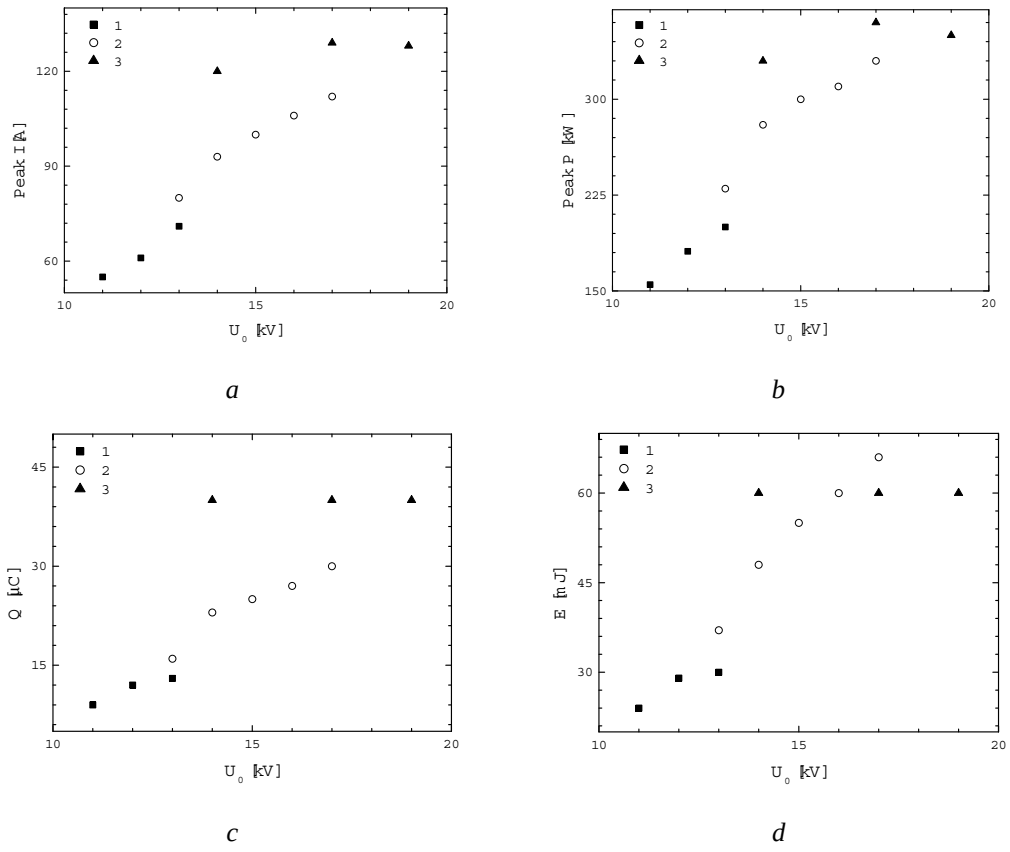

Figure 4.10. Dependence of the main discharge peak current I (a), peak power deposition P (b), total transferred charge Q (c) and energy E (d) deposited into the discharge on the pre-discharge charging voltage U_0. Discharge is in He : F_2 / 99.95 : 0.05 at a total pressure of 2 bar. Capacitance of the main pulse circuit C_1 is 30 nF. Capacitance of the pre-pulse circuit C_0 is 0.8 (1, 2) and 3 nF (3). The charging voltage of the main pulse circuit U_1 is 2.75 (1) and 3 kV (2, 3).

4.3.2 Single pulse excitation scheme with X-ray preionization

As discussed above in sect. 4.3.1, we were able to transfer efficiently the energy stored in the main pulse capacitor into the gas in the form of a self-sustained discharge in gas mixtures with Ne as buffer gas. In gas mixtures with He as buffer gas the main discharge was only stable in a non-self-sustained form where the energy transfer is inefficient and the power deposition is low. On the other hand, the pre-pulse discharge alone has been found to be able to deposit a significant amount of power of ~ 200 – 600 kW during ~ 100 ns in a gas. Therefore the single pulse excitation scheme has been thoroughly investigated as an alternative and simple way to pump excimer laser gas mixtures. In the single pulse discharge excitation experiments only one of the two pulse forming circuit was used, namely the former pre-pulse circuit. The peaking capacitors were removed from the circuit as well. In this sub-section the results of these

investigations are reported. As mentioned before in such a system only one capacitor is used. In order to investigate the influence of the capacitance of this capacitor on the discharge parameters, its value was varied from 0.8 to 12 nF.

In figure 4.11 typical waveforms are shown of the measured voltage *V* and current *I*, and the calculated power deposition *P* from a single pulse discharge in a He : F_2 / 99.95 : 0.05 mixture at a total gas pressure of 2 bar at a charging voltage 9 kV. The storage capacitance C_0 was 6 nF. The vertical dashed line shows the time when the X-ray preionization pulse was applied. The discharge current had a peak value of ~ 250 A and a FWHM of ~ 180 ns. The power deposition reached a peak value of ~ 900 kW with a FWHM of ~ 150 ns.

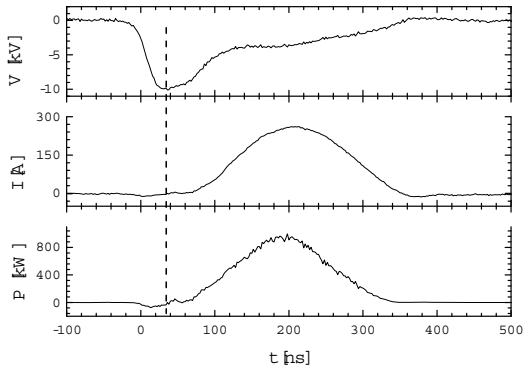

Figure 4.11. Typical measured voltage V, current I and calculated power deposition P of a single pulse discharge in He : F_2 / 99.95 : 0.05 gas mixture at a total gas pressure of 2 bar. The charging voltage was 9 kV. Storage capacitance C_0 = 6 nF. The vertical dashed line shows the time when the X-ray preionization pulse was applied.

In figure 4.12 the dependence of the peak current *I* (a), the FWHM of the current (b), the peak power deposition *P* (c), the FWHM of the power (d), total transferred charge *Q* (e) and energy *E* deposited into the discharge (f) on the charging voltage U_0 is shown for different capacitances. The gas mixture used was He : F_2 / 99.95 : 0.05 at a total pressure of 2 bar. Values for the capacitance used were 0.8 (1), 3 (2), 6 (3) and 12 nF (4). As can be seen from the figure the peak current, peak power deposition, the transferred charge and energy deposition grows linearly with charging voltage. For higher storage capacitances at the same charging voltage higher values were found so with increasing charging voltages the values grew steeper. The FWHM current and the power FWHM deposition decreased with increasing U_0 until they reached a constant value. This charging voltage dependence of the current and FWHM power deposition is observed better for lower capacitances at C_0 = 0.8 (1) and 3 nF (2). When C_0 was 12 nF (4) constant values of the FWHM current and power deposition were not reached at the investigated charging voltages. The measured values did not change significantly. On the other hand an increase of the FWHM current and the FWHM power deposition with increasing storage capacitance C_0 is observed in figure 4.12. The peak current increases linearly with U_0 according

to Eq. 4.1. Coefficients U_L and k are taken from the best linear fits parameters and are given in Table 4.2.

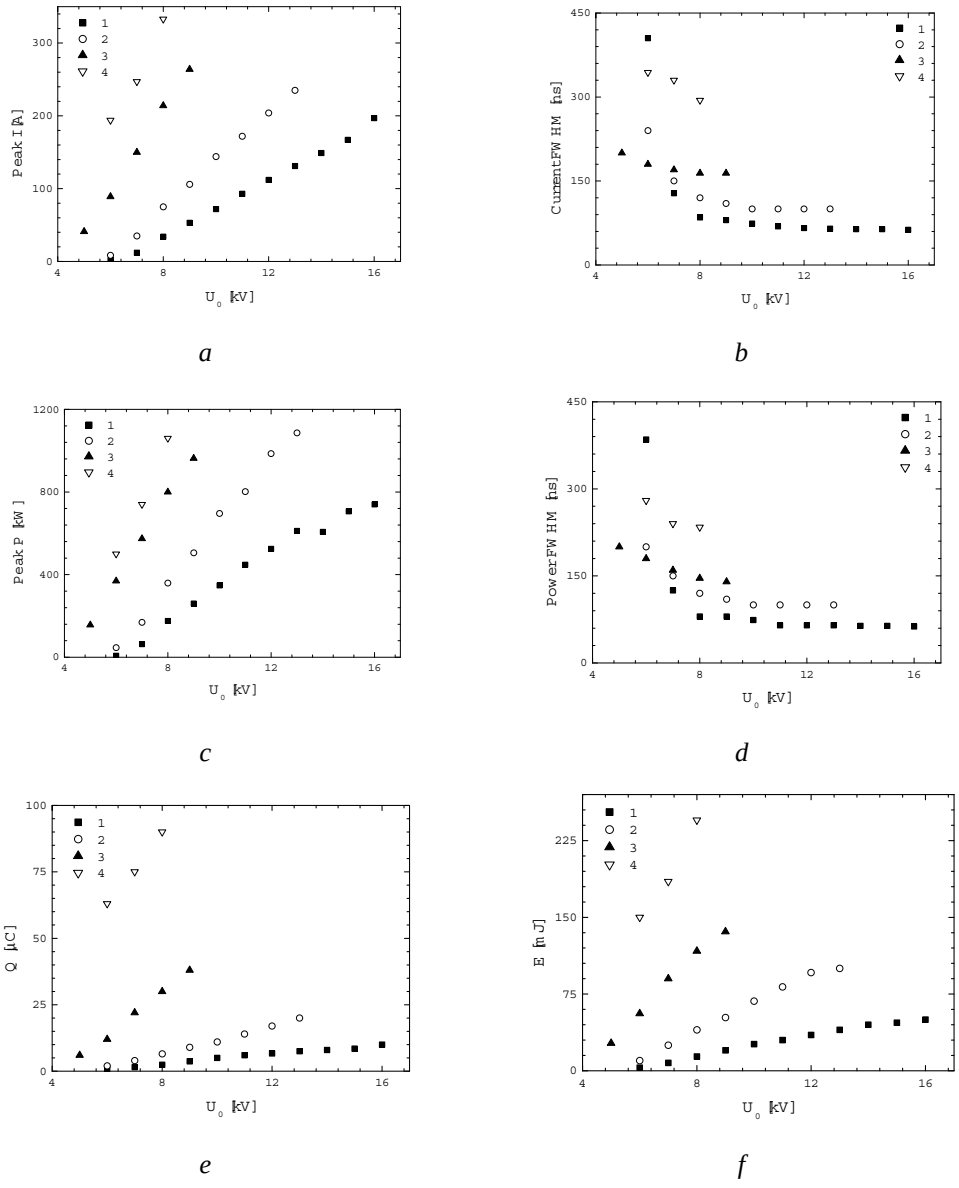

Figure 4.12. Dependence of the discharge peak current I (a), current FWHM (b), peak power deposition P (c), FWHM of power deposition (d), total transferred charge Q (e) and energy E deposited into the discharge (f) on the charging voltage U_0. Discharge in He : F_2 / 99.95 : 0.05 at a total pressure of 2 bar. Capacitor values: 0.8 (1), 3 (2), 6 (3) and 12 nF (4).

For all different capacitor values shown in figure 4.12 the discharge was observed in the diffuse form at low power deposition for low charging voltages, and in the dense form at high power deposition at higher charging voltages. In the diffuse form the discharge glow was ~ 2 cm in diameter. The brightness of the glow increased with the charging voltage. In the dense form the discharge glow was much brighter and was constricted to a narrow channel (several mm in diameter). The width of this channel increased with a further increase of the charging voltage. The transition from the diffuse to the dense form usually occurred when the discharge current exceeded ~ 200 – 250 A and the power deposition was higher than ~ 750 – 850 kW. These conditions were reached at a charging voltage of 16 kV for case 1 (C_0 = 0.8 nF) and at a charging voltage of 7 kV in case 4 (C_0 = 12 nF).

C_0 [nF]	U_d [kV]	U_L [kV]	k [A/kV]
0.8	4.3 ± 0.5	6.2	19.5
3	4.3 ± 0.5	5.7	32.6
6	4.3 ± 0.5	4.4	57.1
12	4.3 ± 0.5	3.3	69.5

Table 4.2.
Measured quasi-steady-state voltage U_d and U_L and k parameters of the linear fit of the dependence of single pulse discharge current in He:F_2 / 99.95%:0.05% mixture at a total gas pressure 2 bar on the charging voltage U_0 for different storage capacitors C_0.

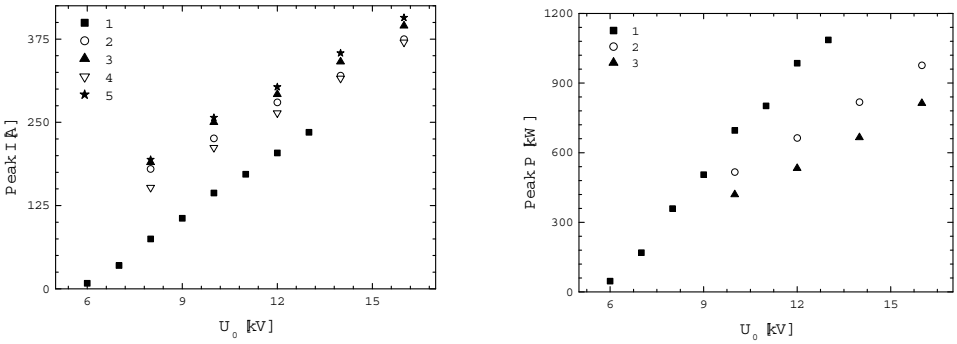

a *b*

Figure 4.13. Dependence of the peak current I (a) and peak power deposition P (b) into the discharge in He : F_2 / 99.95 : 0.05 (1), He : Ar : F_2 / 94.9 : 5 : 0.1 (2), Ne : Ar : He : F_2 / 93 : 5 : 1.9 : 0. (3), He (4) and Ne (5) on the charging voltage at a total gas pressure of 2 bar. The capacitance is 3 nF.

The dependence of the peak current *I* (a) and peak power deposition *P* (b) into the discharge in He : F_2 / 99.95 : 0.05 (1), He : Ar : F_2 / 94.9 : 5 : 0.1 (2), Ne : Ar : He : F_2 / 93 : 5 :

1.9 : 0.1 (3), He (4) and Ne (5) on the charging voltage at a total gas pressure of 2 bar is shown in figure 4.13. The capacitance C_0 = 3 nF. The discharges in the F_2 containing laser gas mixtures (1 – 3) were in the dense form; the discharges in He (4) and Ne (5) were in the diffuse form. The peak current in all five cases have been found to grow linearly with the charging voltage according to Eq. 4.1. The coefficients U_L and k were calculated from the best linear fits parameters and are given in Table 4.3. At the same charging voltage the lowest peak current was observed the in He : F_2 mixture (1) and the highest peak current measured was in pure Ne (5). In the F_2 containing mixtures (1 – 3) the highest power deposition was observed in the He : F_2 mixture (1). The lowest power deposition was found in a Ne : Ar : He : F_2 mixture (3), although in case 1 the peak current was the lowest and in case 3 the highest peak current was measured. The power deposition was not measured in He (4) and Ne (5).

	U_d [kV]	U_L [kV]	k [A/kV]
He : F_2 / 99.95 : 0.05	4.3 ± 0.5	5.7	32.6
He : Ar : F_2 / 94.9 : 5 : 0.1	3.7 ± 0.5	0.6	24.2
Ne : Ar : He : F_2 / 93 : 5 : 1.9 : 0.1	2.0 ± 0.5	0.3	25
He	3.5 ± 0.5	2.6	27
Ne	1.0 ± 0.2	0.4	26.2

Table 4.3.
Measured quasi-steady-state voltage U_d and U_L and k parameters from a linear fit of the dependence of single pulse discharge current on the charging voltage U_0 for different gases and gas mixtures at total pressure 2 bar. Storage capacitance C_0 = 3 nF.

In order to determine the specific power deposition in terms of kW cm^{-3} from the measured power deposition the discharge volume should be known. Since the gap length (1 cm) is known, we have measured visually the width of the glow discharge. The discharge volume has been calculated as the product of the gap length and the width of the glow discharge.

In figure 4.14 typical time-integrated photos of the discharge in different gases and gas mixtures at a gas pressure of 2 bar and different charging voltages are shown. The vertical size of the glow was limited by the discharge gap (1 cm). The horizontal size of the glow was determined by discharge conditions. In He : Ar : F_2 / 94.9 : 5 : 0.1 (a) and Ne : Ar : He : F_2 / 97 : 5 : 1.9 : 0.1 gas mixtures (b) the discharge appeared in the dense form. The positive column of the discharge had a cylindrical shape with a diameter of several mm. With an increase of the charging voltage from 8 (1) to 16 kV (5) the width of the glow increased. In He (c) and Ne (d) a diffuse form of the discharge was seen. The positive column glow was also cylindrical in shape and the width of the glow, measured as the width of the central brightest part of the glow, was ~ 2 cm. For this type of discharge the width of the glow did not change significantly with increasing charging voltage. Around the bright central part of the glow there was a faint glow barely visible by eye. The width of this glow was ~ 2.5 cm in Ne (d) and ~ 3 cm in He (c). Also here the width of this glow was independent on the charging voltage.

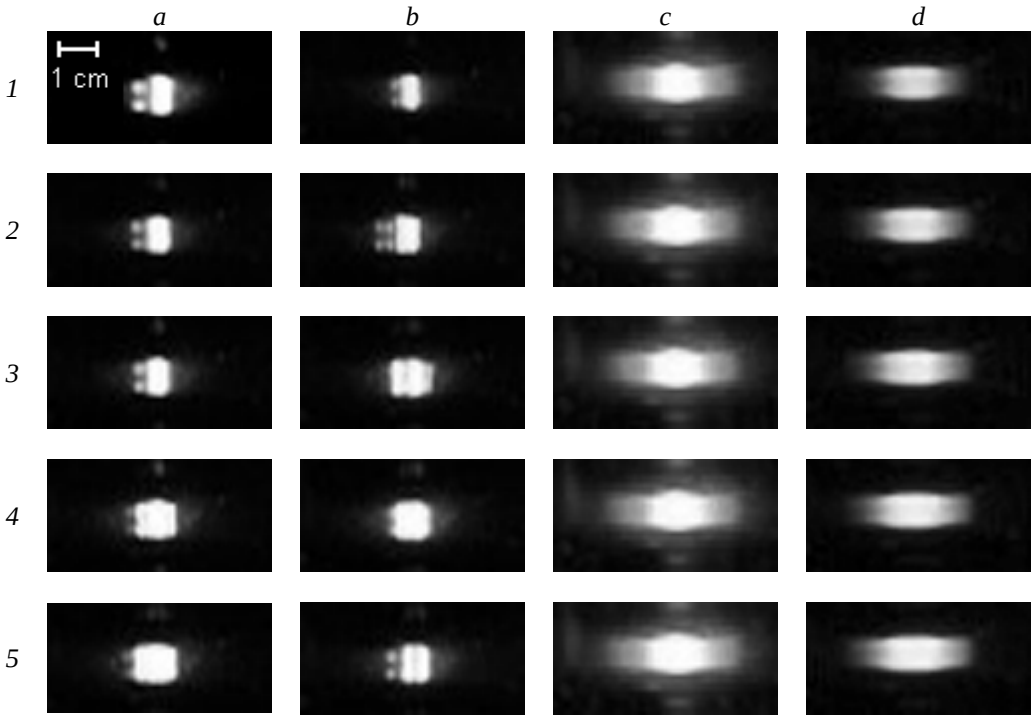

Figure 4.14. Typical time integrated photos of the discharge glow in He : Ar : F_2 / 94.9 : 5 : 0.1 (a), Ne : Ar : He : F_2 / 97 : 5 : 1.9 : 0.1 (b), He (c) and Ne (d) at total gas pressure 2 bar and charging voltage 8 (1), 10 (2), 12 (3), 14 (4) and 16 kV (5).

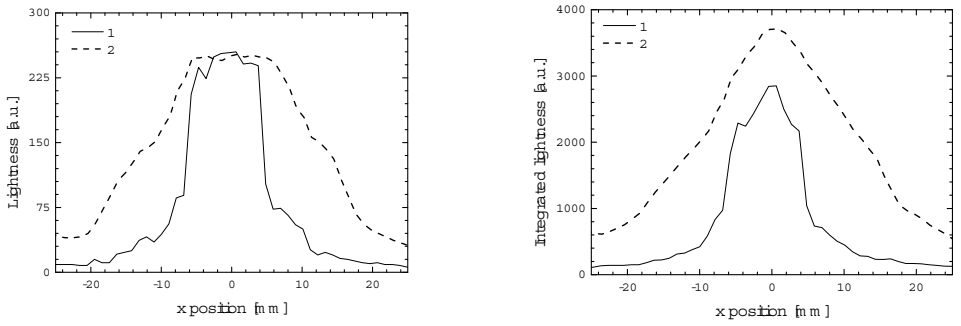

a *b*

Figure 4.15. Horizontal spatial light intensity profile of the time-integrated photos of the discharge glow in the middle of the discharge gap (middle of the glow in the vertical direction) (a), and the profile integrated along the discharge gap (b). Discharge in He : Ar : F_2 / 94.9 : 5 : 0.1 (1) and He (2) at the charging voltage 14 kV and a total gas pressure of 2 bar.

From the time integrated photos of the discharge glow spatial light intensity profiles were made. In figure 4.15 the horizontal profile in the middle of the discharge gap (a) and the horizontal spatial light intensity profile integrated in the vertical direction (along the gap axis) (b) obtained are shown. Photos of the discharge glow in a He : Ar : F_2 / 94.9 : 5 : 0.1 gas mixture (1) and in He (2) at a gas pressure of 2 bar and a charging voltage of 14 kV were taken to obtain these profiles. The width of the discharge was estimated in two ways: as a FWHM of the profile in the middle of the discharge gap and as a FWHM of the integrated profile.

As mentioned above, it has been observed that the width of the discharge in the dense form increased with the discharge current. For a normal glow discharge we expect that the current density in the positive column of the discharge, which is responsible for the visible glow, is constant, i.e., the discharge current is proportional to the discharge cross-section area. In order to check this assumption in the dense form of the discharge the current density in He : Ar : F_2 / 94.9 : 5 : 0.1 and Ne : Ar : He : F_2 / 97 : 5 : 1.9 : 0.1 gas mixtures was measured at a total gas pressure of 2 bar. In each gas mixture 5 consecutive time-integrated photos of the discharge glow were made in darkness (ambient light was absent) and 5 photos were made in presence of the ambient illumination at a charging voltage of 8, 10, 12, 14 and 16 kV. The current waveform of the discharge was measured simultaneously. From every photo the profile of the light intensity of the photo in the middle of the discharge gap and the integrated spatial profile as in shown figure 4.15 were produced. The FWHM of the horizontal spatial profile d and the FWHM of the integrated profile d_I were measured for every photo. To enhance the precision of our estimations of the discharge area, both values of d and d_I have been calculated from the squared average of 5 values:

$$\langle d \rangle^2 = \left(\frac{1}{5} \sum_{k=1}^{5} d_k \right)^2$$
$$\langle d_I \rangle^2 = \left(\frac{1}{5} \sum_{k=1}^{5} d_{I\,k} \right)^2 \qquad (4.3)$$

and from the average of 5 squared values of d and d_I:

$$\left\langle d^2 \right\rangle = \frac{1}{5} \sum_{k=1}^{5} d_k^2$$
$$\left\langle d_I^2 \right\rangle = \frac{1}{5} \sum_{k=1}^{5} (d_{I\,k})^2 \qquad (4.4)$$

The squared average width (Eq. 4.3) and the average of the squared width (Eq. 4.4) determined from a middle-line profile and integrated profile were calculated at every charging voltage separately and for photos obtained in total darkness and in the presence of the ambient light.

The dependence of the square of the diameter of the discharge glow on the discharge current in a Ne : Ar : He : F_2 / 93 : 5 : 1.9 : 0.1 gas mixture at a total gas pressure of 2 bar is shown in figure 4.16. The presented values 1 – 4 are obtained from photos made in total darkness. Values 5 – 8 are obtained in the presence of the ambient illumination. Sets 1 and 5 represents $\langle d \rangle^2$ from Eq. 4.3), 2 and 6 $\langle d^2 \rangle$ from Eq. 4.4, 3 and 7 are $\langle d_I \rangle^2$ from Eq. 4.3, and finally 4 and 8 are representing $\langle d_I^2 \rangle$ from Eq. 4.4. The error bars represent the standard deviation of the experimental values. The dotted line represents the $d^2 = 1$ cm^2 level, and the uncertainty range in the determination of the $k_j = d^2/I$ coefficient is shown by two dashed lines. The current density j in the positive column of the discharge in a dense form is:

$$j = \frac{I}{S} = \frac{4I}{\pi d^2} = \frac{4}{\pi k_j} \tag{4.5}$$

where I is the discharge current, S is the cross-section of the positive column, d is the diameter of the positive column, and k_j is the slope of the fitted straight line (solid line in figure 4.16).

The positive column current density has been calculated from Eq. 4.5 to be 800 ± 300 A cm^{-2} in a He : Ar : F_2 / 94.9 : 5 : 0.1 gas mixture and 500 ± 200 A cm^{-2} in a Ne : Ar :He : F_2 / 93 : 5 : 1.9 : 0.1 gas mixture at a total gas pressure of 2 bar.

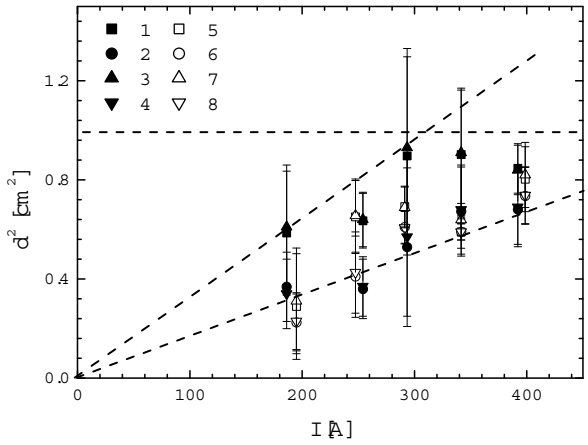

Figure 4.16. Dependence of the square of the diameter of the discharge glow on the discharge current, obtained from the time-integrated photos of discharge glow. Discharge in Ne : Ar : He : F_2 / 93 : 5 : 1.9 : 0.1 at a total gas pressure of 2 bar. (see text for details).

4.4 Discussion of the results

In the experiments with pre- and main discharge excitation schemes it appeared that the pre-discharge was always in the self-sustained form, while the main discharge was observed in either a non-self-sustained or a self-sustained form depending on the excitation conditions and the composition of the gas mixture. These two discharge forms are very distinct by their properties. In this section we are describing the differences between the self-sustained and non-self-sustained form. Also the observed charging voltage dependencies of the discharge current, power deposition, FWHMs of the discharge current and the power deposition are explained.

In our experiments it appeared to be possible to create a main discharge in the non-self-sustained form in He and in a He : F_2 / 99.95 : 0.05 gas mixture. First, an analysis of this type of discharge will be given here. The pre-discharge creates plasma between both electrodes in the gas volume. Then additional voltage is applied to the electrodes creating additional electric field in the plasma already present. However, this applied voltage is less than the steady state voltage of the self-sustained discharge, thus the electric field strength is also lower than in the self-sustained discharge. Although ionization takes place in the applied field, its rate is not sufficient to overcome electron losses due to very strong recombination or attachment of electrons in case an electro-negative gas, as for example F_2, is added to the mixture. So there is a decrease of charges in the plasma by the applied external field and the discharge exponentially decays in time, as shown in figure 4.7.

As higher voltage is applied to the main discharge it results in higher external electric field, which leads to a higher degree of ionization of the plasma. As a consequence the discharge current and power deposition into the discharge increases.

The duration of the discharge current pulse is determined by many factors: the discharge rate of the storage capacitor, which is higher at higher current; the ionization rate and the rate of the removal of free charges from the plasma volume. For example, at higher applied voltage free charges are removed faster from the plasma; on the other hand ionization is also stronger. The free charges removal rate is determined by the mobilities of the charged particles and is directly proportional to the applied field. The ionization rate increases with the field strength much faster, but it is still less than rate of volumetric losses and charges removal combined, otherwise it would not be the non-self-sustained discharge. However the increased ionization rate slows down the plasma decay in the constant applied field. In our case the applied field is not constant as the storage capacitor discharges into the plasma through the discharge current, and it happens faster at higher discharge current. As a result, the current pulse duration may increase or decrease with a change of the applied main discharge voltage. In figure 4.8 it is seen that the discharge current width decreases with increasing main or pre-discharge charging voltage. In the last case higher pre-discharge voltage leads to higher pre-discharge current, which creates denser plasma. Denser plasma results in higher current at the same main discharge voltage and faster discharge of the main pulse storage capacitor. In figure 4.9 discharge current width, on contrary, increases with the main pulse charging voltage.

An increase of the pre-pulse charging voltage or pre-pulse capacitance at the same charging voltage results in more powerful pre-discharge, which creates denser initial plasma with higher free electron density and, thus, higher conductivity. As a consequence, at the same main discharge voltage, the current, the power and the energy deposition into the main discharge are higher, as shown in figure 4.10.

If the main pulse charging voltage is higher than the steady state voltage of the self-sustained discharge, usually the main discharge switches into the self-sustained mode. However,

in our experimental setup stable self-sustained glow discharge in He and in a He : F_2 / 99.95 : 0.05 gas mixture was not observed. Arc discharge was ignited in these gases instead.

In Ne and Ne based mixtures stable homogeneous main discharge was observed in the self-sustained mode. The properties of the main discharge were found to be independent of the pre-pulse parameters. They were even the same in absence of a pre-pulse (see figure 4.5). The only parameter that was affected by the pre-pulse was the minimum main pulse voltage required for ignition of the main discharge. For example, the main discharge in Ne was ignited at a minimum charging voltage of ~ 3 kV without a pre-pulse, while on the other hand with a pre-pulse, a voltage of just higher than the steady state discharge voltage (~ 1 kV) was required.

The main discharge current in this mode depended linearly on the charging voltage according to Eq. 4.2 and has the shape of a half-period sine function. The FWHM of the current was ~ 430 ns and it was almost independent on the charging voltage and gas mixture composition.

As mentioned before with our design, the pre- and main pulse excitation scheme has been found to operate separately in Ne based gas mixtures while in He based mixtures this scheme failed at all. On the other hand, a pre-discharge alone was found to be capable of delivering a power deposition of ~ 1 MW/cm^3 with reasonable pulse duration of ~ 100 ns. For that reason further experiments were performed with the single pulse excitation scheme. The peaking capacitors (four of them in parallel, 50 pF each) were also found unnecessary and were removed.

The properties of the self-sustained discharge with the single pulse excitation scheme employed were the same as the properties of the pre-discharge, so the excitation scheme was the same except for peaking capacitors. These properties were also very similar to the properties of the main discharge of the double pulse excitation scheme in the self-sustained form. The current has been observed to increase also linearly with the voltage according to Eq. 4.1. With an increase of the charging voltage and the discharge current, the FWHM of the current waveform decreases first and then reaches a constant value which does not change with a further increase of the charging voltage. This constant value of the FWHM slightly depends on the gas mixture composition and increases with an increase of the storage capacitance. For high values of the charging voltage and discharge current the current waveform has the shape of a half period sine function.

The same voltage dependence of the peak current was observed in UV preionized electrical gas discharges in CO_2 : N_2 : He / 10 : 10 : 80 gas mixtures reported in [19]. In this paper the pulse forming network (PFN) was formed by a storage capacitor C and an inductor L and the observed discharge current properties were contributed to parameters of this excitation scheme. The discharge impedance was much lower than the wave impedance of the PFN and the discharge current was limited by the inductor. If the storage capacitor was charged to a voltage V_c and the discharge burned at a voltage V_p, the peak current value observed in [19] was represented by:

$$I_{\max} = (V_c - V_p)\sqrt{\frac{C}{L}} \tag{4.6}$$

and the oscillation period was:

$$\tau = 2\pi\sqrt{LC} \tag{4.7}$$

It can be concluded that Eq. 4.6 from ref. [19] is similar to Eqs. 4.1 and 4.2. Although in our experimental setup, no inductor was included in PFN, there is always a total inductance L_0 consisting of parasitic inductances of the electrical connections, the inductance of the discharge chamber and the inductance of the discharge itself. These inductances were not measured; however one can estimate them from the current FWHM or the k coefficients in Eqs. 4.1 and 4.2, which has the meaning of a conductance or inverse impedance.

In order to check the validity of this assumption we have performed some calculations. For example, in He the current pulse FWHM reached a constant value of ~ 130 ns at a storage capacitance C_0 = 3 nF (see figure 4.3). When the pulse has a shape of half a period of a sine function, the FWHM of this pulse is 1/3 of the oscillation period of the sine function. Then the estimated value of L_0 is ~ 1.9 μH. The wave impedance of the PFN Z is ~ 25 Ω. The value of the k coefficient in Eq. 4.1 is measured to be ~ 31 A kV^{-1} for He (see Table 4.1). On the other hand, according to Eqs. 4.1 and 4.6 $k = 1/Z$, while $1/Z$ is ~ 39 A kV^{-1}, which is closed to the calculated values of k.

The measured values of k in different gas mixtures (see Table 4.1) vary from 29 to 39 A kV^{-1}, and the FWHMs reach constant values from 100 to 160 ns (see figure 4.6). These changes are due to slightly different inductances of the discharges resulting in different values of L_0. However, L_0 is of ~ 10^{-6} H in all cases.

With an increase of C_0 in the single pulse excitation scheme the measured FWHM τ of the current and the k coefficient grow (see figure 4.12 and Table 4.2). According to Eqs. 4.6 and 4.7 τ and k have to be proportional to the storage capacitance. If τ_0 is the FWHM of the current pulse at C_0 = 0.8 nF and k_0 is measured at the same C_0, then τ and k measured at a different value of the storage capacitance C are related to τ_0, k_0 and C_0 as:

$$\frac{\tau}{\tau_0} = \frac{k}{k_0} = \sqrt{\frac{C}{C_0}} \tag{4.8}$$

and in the double logarithmic scale:

$$\ln\left(\frac{\tau}{\tau_0}\right) = \ln\left(\frac{k}{k_0}\right) = \frac{1}{2}\ln\left(\frac{C}{C_0}\right) \tag{4.9}$$

In figure 4.17 the dependence of the discharge FWHM (1) and coefficient k (2) on the storage capacitance, measured in a He : F_2 / 99.95 : 0.05 gas mixture at a total pressure of 2 bar is shown in the double logarithmic scale. In this figure the theoretical dependence $\ln(C/C_0)/2$, predicted by Eq. 4.9, is given by the dashed line (3). It can be concluded that all measured values are very close to the predicted ones.

The offset voltage U_0, which has a meaning of the discharge voltage at zero current, determined experimentally from the best fit lines is close to the measured directly steady-state

voltage of discharge U_d (see Tables 4.1 – 4.3). In the ideal case U_0 should be equal to U_d, but as can be concluded in our case, they are slightly different but well within the experimental error boundaries.

Thus our conclusion is that in the described single pulse setup the discharge in the self-sustained mode burns at a steady-state voltage regardless of the charging voltage, while the discharge current is determined and limited by the combined inductance of the PFN and the discharge. This conclusion is valid not only for the single pulse excitation scheme, but also for the main pulse circuit of the double pulse scheme. For example, when the double pulse excitation circuit was used in Ne with C_0 = 3 nF and C_1 = 42 nF, the square root of the capacitances' ratio was ~ 3.74. The observed FWHM of the pre- and main discharge pulses are ~ 120 and ~ 450 ns respectively. The FWHM ratio is ~ 3.75. In this case the k coefficients in the voltage dependence of the peak current (see Eq. 4.1, 4.2 and Table 4.1) are ~ 32.5 and ~ 129.6 A kV^{-1} respectively, and their ratio is ~ 4.

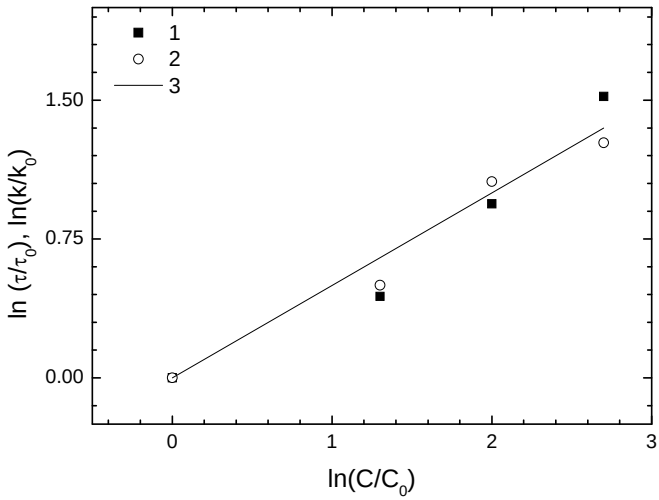

Figure 4.17. Dependence of the normalized current FWHM (1) and normalized "conductance" (2) on the normalized capacitance of the storage capacitor in double logarithmic scale. Discharge in a He : F_2 / 99.95 : 0.05 gas mixture, total gas pressure 2 bar. (3) Calculation of the dependence of $ln(C/C_0)/2$.

Due to the fact that the PFN (or the pre-pulse circuit) works as an *LC* contour, the discharge pulse duration increases as the square root of the storage capacitance. On the other hand, the peak discharge current and the power deposition into the discharge grow as the square root of the storage capacitance at the same charging voltage. Thus higher storage capacitance leads to steeper increase of the discharge current and the power deposition with the charging voltage. A transition from glow discharge into an arc occurs when the power deposition exceeds a certain value. Due to the higher power deposition at the same charging voltage this transition

happens at lower charging voltage when the storage capacitance is higher, although the charging voltage cannot be lower than the steady-state discharge voltage. Thus a higher value of the storage capacitance shortens the charging voltage region where stable glow discharge can be produced. As a result of all the measurements and the analysis of the results, the described pre-pulse circuit with a capacitance of 3 nF as the optimum value was chosen for the experiments described in the next chapter. In chapter 5 the spontaneous emission and laser gain parameters of fluorine doped excimer laser gas mixtures are investigated. This electrical excitation circuit provides a reasonable discharge current pulse duration of ~ 120 ns and it allows, depending on the gas mixture composition, a wide range of charging voltages: from ~ 5 kV to ~ 20 kV. In the diffuse discharge form the visible width of the glow is ~ 2.5 – 3 cm, and in the dense form it is less than or equal to ~ 1 cm, depending on the discharge current and gas composition. Larger width of the discharge means also larger volume of the active medium for a laser and from this point of view the diffuse discharge form might be preferable to use for the laser pumping. However, the maximum power deposition density that could be obtained in a diffuse discharge form is much lower than could be obtained in the dense form. For example, in a He:F_2 mixture the maximum power deposition density is ~ 200 kW cm^{-3}. At higher power deposition values the discharge appears in the dense form where a power deposition density of ~ 1 - 2 MW cm^{-3} has been observed in different gas mixtures. It can be concluded that the dense discharge form has to be used for the excimer laser pumping experiments described in chapter 5.

In the remaining part of this discussion some short comments on some additional discharge properties like the voltage characteristics and the transition from the diffuse to dense form are given. The assumption that the discharge current is limited by the inductance, composed by the discharge self-inductance and residual inductances of the PFN and the discharge chamber, also explains the observed effect of the constant positive column discharge current density in the dense form (figure 4.16). The voltage drop across the discharge consists of two major components: a voltage drop over the positive column and over the cathode sheath. The latter depends mostly on two parameters: the gas composition and the specific cathode sheath current density j/p^2 [7] and is typically a few hundreds volt [7] even in an abnormal glow discharge. It is higher in He-based mixtures and lower in Ne-based mixtures. We have estimated that in our experiments the voltage drop over the cathode sheath contributes less than or equal to 10% of the total discharge voltage, therefore almost the entire voltage drops across the positive column. Since the steady-state discharge voltage is independent on the discharge current, the voltage across the positive column is almost constant. Therefore, at the given gas pressure p the specific electric field strength E/p inside the positive column is also constant. This means that the free electron density in the positive column is constant, thus the conductivity of the positive column is proportional to the discharge cross-section area, and the current density is constant. Hence, in order to conduct a higher total current the positive column should occupy a broader area.

We have seen that the discharge appears in a dense and not in a diffuse form only when the power deposition density exceeded a certain value, which was different for each gas composition. The transition from a diffuse into a dense discharge form is due to contraction of the positive column due to the thermal effects as was reported in many papers [20 – 24]. For example, discharges in He : Ar : F_2 / 94.9 : 5 : 0.1 and Ne : Ar : He : F_2 / 93 : 5 %:1.9 : 0.1 gas mixtures at a total pressure of 2 bar which are typical for laser gain measurements, have always been observed in a dense, constricted form at a charging voltage from 8 to 16 kV and C_0 = 3 nF.

Before contraction occurs in a low current diffuse discharge, there is a radial electron density gradient. The electron density has a maximum value in the middle of the discharge and drops to zero on the edges. However, the radial distribution of the electron density is smooth and broad. Higher current through the positive column leads to higher power deposition into the gas

discharge, leading to higher electron density and stronger gas heating. Since the heat removal is a rather slow processes compared to ionization, attachment and recombination, a radial temperature gradient exists in the discharge plasma. The ionization frequency increases very strongly with the gas temperature and with the electron density. The attachment and recombination frequencies change slower than the ionization frequency. Thus the gas is heated non-uniformly, the maximum gas temperature is observed in the middle of the discharge plasma. At the same time the power deposition is the highest in the middle as well due to radial electron density distribution. These effects lead to a further increase in ionization rate, electron density and power deposition in the middle of the plasma. Usually, diffusion of charged particles and heat transfer are competitors to this increase of the electron density and gas temperature in the middle of the plasma. If the power deposition is low, these two processes smooth the radial distributions of the electron density and gas temperature. So, if the power deposition is high enough, starting from a broad diffuse glow the thermal contraction of the positive column occurs leading to a narrow highly conductive channel. In a He : F_2 / 99.95 : 0.05 gas mixture at a total pressure of 2 bar this transition was observed at a current of ~ 200 – 250 A and a power deposition of ~ 750 – 850 kW.

In the dense plasma, where the electron density is high, electron-electron collisions lead to thermalization of the electron energy distribution function into a Maxwellian distribution function. This process sharpens the discharge contraction, especially in rare gases, like Ne or He. In electro-negative gas mixtures, for example, in F_2 containing mixtures electron attachment is also a mechanism that contributes to the contraction mechanism. Due to non-uniform electron density radial distribution most of the negative ions are constricted in the narrow central part of the discharge. The width of the radial negative ion density distribution is narrower than the radial electron density distribution. Since the negative ions and gas atoms are of comparable mass and a significant fraction of the current being carried by the negative ions, a higher rate of energy transfer into the gas is observed at the same current. This energy transfer occurs in the narrow central part of the discharge, thus making the gas heating even more non-uniform.

4.5 Conclusion

The designed and investigated single pulse gas discharge excitation scheme works as an LC-like PFN due to the inductances of the circuitry, the discharge chamber connections and the discharge itself. No additional inductor was incorporated in the scheme. A self-sustained discharge excited by this scheme burns at the steady-state voltage which is independent on the charging voltage and the storage capacitance of the excitation scheme as long as the charging voltage is higher than the steady-state discharge voltage. Also the power deposition should be lower than the critical power deposition above which a transition into an arc discharge occurs. The peak discharge current is limited by the inductance of the circuit and increases as the square root of the storage capacitance. The discharge pulse width is determined by the half-period oscillation of the LC contour and increases as a square root of the storage capacitance. The LC contour efficiently stabilizes the discharge, acting like a high impedance load resistance and it suppresses discharge instabilities due to the limitation of the current.

A self-sustained discharge in F_2 containing laser gas mixtures is ignited in a diffuse form at low total power deposition and low discharge current. In the diffuse discharge form the positive column glow occupies an area ~ 3 cm in diameter. At higher discharge current and total power deposition, depending on the composition of the gas mixture, the discharge appears in a dense, constricted form which is due to the thermal contraction of the positive column. In the dense discharge form the positive column current density and the power deposition density are

constant. The discharge width however, increases from several mm to ~ 1 cm in diameter with increasing discharge current and total power deposition at a higher charging voltage.

In a Ne : Ar : He : F_2 / 93 : 5 : 1.9 : 0.1 gas mixture at a total pressure of 2 bar a peak current density in the positive column of 500 ± 200 A cm^{-2} and a peak power deposition density of ~ 1 MW cm^{-3} were measured at a charging voltage from 8 to 16 kV and the storage capacitance of 3 nF. In a He : Ar : F_2 / 94.9 : 5 : 0.1 gas mixture at a total pressure of 2 bar a peak positive column current density of 800 ± 300 A cm^{-2} and a peak power deposition density of ~ 1.8 MW cm^{-3} were obtained under equal excitation conditions. The FWHM of the discharge current was ~ 120 ns and the FWHM of the power deposition was ~ 100 ns in both mixtures at a charging voltage from 8 to 16 kV. An energy deposition density of ~ 100 mJ cm^{-3} in the Ne based mixture and ~ 180 mJ cm^{-3} in the He based mixture was reached.

A single pulse gas discharge excitation scheme has been found to be an effective pumping source for (V)UV excimer laser gas mixtures. It provides a homogeneous discharge in halogen/rare gas mixtures with a high energy deposition over a reasonably long period of time namely ~ 100 ns.

References:

[1] N.G. Basov, V.A. Danilychev, Y.M. Popov and D.D. Khodkevich, JETP Lett., **12**, 329 (1970)
[2] H.A. Koehler, L.J. Ferderber, D.L. Redhead and P.J. Ebert, Appl. Phys. Lett., **21**, 198 (1972)
[3] S.K. Searles and G.A. Hart, Appl. Phys. Lett., **27**, 243 (1975)
[4] C.A. Brau and J.J. Ewing, Appl. Phys. Lett., **27**, 435 (1975)
[5] J.M. Hoffman, A.K. Hays and G.C. Tisone, Appl. Phys. Lett., **28**, 538 (1976)
[6] R. Burnham and N. Djeu, Appl. Phys. Lett., **29**, 707 (1976)
[7] Yu.P. Raizer, *Gas Discharge Physics*, Springer, London (1992)
[8] A.J. Palmer, Appl. Phys. Lett., **25**, 138 (1974)
[9] J.I. Levatter and Sh.-Ch. Lin, J. Appl. Phys., **51**, 210 (1980)
[10] W.L. Nighan, Phys. Rev. A **15**, 1701 (1977)
[11] W.L. Nighan, Phys. Rev. A **16**, 1209 (1977)
[12] H.M.J. Bastiaens, S.J.M. Peeters, X. Renard, P.J.M. Peters and W.J. Witteman, Appl. Phys. Lett., **72**, 2791 (1998)
[13] S. Nagai, K. Takehisa, T. Enami, T. Nishisaka, J. Fujimoto, O. Wakabayashi, H. Mizoguchi and A. Takahashi, Jpn. J. Appl. Phys., **38**, 7013 (1999)
[14] J.P. Reilly, J. Appl. Phys. **43**, 3411 (1972)
[15] A.E. Hill, Appl. Phys. Lett., **22**, 670 (1973)
[16] O.R. Wood II, P.W. Smith, C.R. Adams and P.J. Maloney, Appl. Phys. Lett., **27**, 539 (1975)
[17] W. H. Long, M.J. Plummer and E.A. Stappaerts, Appl. Phys. Lett., **43**, 735 (1983)
[18] Yu. Bychkov, I. Kostyrya, M. Makarov, A. Suslov and A. Yastremsky, Rev. Sci. Instrum., **65**, 793 (1994)
[19] O.P. Judd and J.Y. Wada, IEEE J. Quant. Electr., **10**, 12 (1974)
[20] G.M. Petrov and C.M. Ferreira, Phys. Rev. E **59**, 3571 (1999)
[21] P.G. Daniels, R.N. Franklin and J. Snell, J. Phys. D: Appl. Phys., **23**, 823 (1990)
[22] E.I. Toader, J. Phys. D: Appl. Phys., **28**, 75 (1995)
[23] P. Mezei, T. Cserfalvi and M. Janossy, J. Phys. D: Appl. Phys., **34**, 1914 (2001)
[24] M. Makarov and Yu. Bychkov, J. Phys. D: Appl. Phys., **29**, 350 (1996)

Chapter 5

Optical measurements on a compact source of UV excimer radiation at 193 nm pumped by a gas discharge

A single pulse discharge excitation scheme with X-ray preionization, described in chapter 4, has been used as an efficient pumping source for halogen – rare gas mixtures that are typical for excimer lasers. The spontaneous emission and small-signal gain coefficient at a wavelength of 193 nm have been measured in gas mixtures containing He : Ar : F_2 or Ne : Ar : F_2. A very high peak net small-signal gain value of 34 ± 20 % cm^{-1} was measured in the He based laser gas mixture.

5.1 Introduction

As mentioned in the introduction of this thesis and in the introduction of chapter 4, excimer lasers are nowadays widely employed in industry and in scientific research as powerful sources of coherent UV and VUV radiation. On the other hand, most of the commercially available excimer lasers suffer from short optical pulse duration typically of few tens of ns. The short pulse duration allows only a small number of round-trips of the generated radiation inside the laser cavity leading inevitably to a poor beam quality. The two most obvious ways to increase the number of round-trips in the laser chamber are to produce longer optical pulses or to shorten the length of the resonator, provided that the gain is high enough to overcome the losses in the resonator. In this chapter we will describe our approach in this field with the aim to create a long lasting, stable discharge in F_2 doped excimer laser gas mixtures with a high gain coefficient. Because a high power deposition and long discharge pulse duration are necessary for the production of a high gain value and for long optical excimer laser pulses, the discharge has to be stable and homogeneous under these conditions. In order to find out if the designed single pulse excitation scheme with X-ray preionization, described in the previous chapter, is capable of providing the pumping power density required for lasing and to determine the achievable duration of the laser pulse, were have performed experiments with this scheme. The spontaneous UV radiation produced and the laser signal gain obtained in the discharge plasma generated in fluorine – rare gases mixtures were measured. The spontaneous emission and small-signal gain coefficients at a wavelength of 193 nm (ArF^*) have been obtained from discharges in gas mixtures containing Ar and F_2 diluted in He or Ne. The results will be presented and discussed in this chapter.

5.2 Experimental setup

5.2.1 Gas discharge excitation scheme and signal acquisition system

For the experiments described in this chapter a single pulse excitation circuit with X-ray preionization has been utilized. It consisted of a pair of metallic electrodes, usually 1 cm apart each with a diameter of 5 cm (upper electrode, anode) and 6 cm (lower electrode, cathode) and located in the discharge chamber. The discharge in the laser gas mixtures was created by applying a high voltage pulse to the electrodes. Immediately before this event an X-ray pulse was applied trough the bottom electrode in order to preionize the gas mixture. The gas discharge excitation scheme and circuit, is described in more detail in chapter 4 (Sec. 4.2). The discharge chamber is also described more in detail in chapter 4 (Sec. 4.2) and in chapter 3 (Sec. 3.2). Here we repeat only the main features of the layout of the setup shown in figure 5.1.

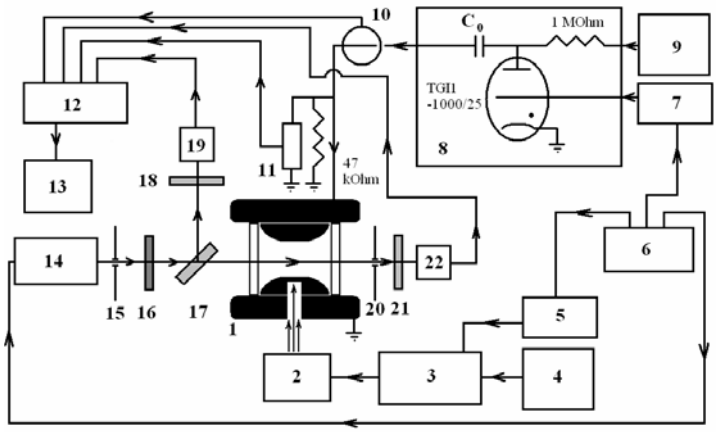

Figure 5.1. Experimental setup for single pulse discharge excitation.
1: discharge chamber; 2: X-ray source; 3: mini-Marx generator; 4: HV DC power supply; 5: triggering unit for mini-Marx generator; 6: primary pulse generator; 7: triggering unit for thyratron; 8: pulse forming unit, C_0 is storage capacitor; 9: HV DC power supply; 10: current transformer; 11: HV fast voltage probe; 12: oscilloscope; 13: PC; 14: ArF probe laser; 15: aperture; 16: neutral density filter; 17: beam-splitting mirror; 18: 193 nm filter; 19: photo-diode; 20: aperture; 21: 193 nm filter; 22: photo-diode.

The gas volume of the discharge chamber (1) is preionized by the X-ray source (2) which is powered by a mini-Marx generator (3). The mini-Marx generator is charged by a HV DC power supply (4) and triggered by a triggering unit (5). The primary pulse generator (6) made of two coupled pulse generators triggers the mini-Marx triggering unit, the triggering unit (7) for the thyratron of the pulse forming unit (8) and the ArF probe laser (14). The capacitance $C_0 = 3$ nF of the pulse forming unit (8) is charged by a HV DC power supply (9) through a 1 MΩ current limiting resistor. The 47 kΩ resistor, connected parallel to the discharge gap, closes the charging

loop. The storage capacitor C_0 is discharged into the gas chamber when the thyratron of the pulse forming unit is switched.

The current waveform of the discharge is measured by a current transformer (10). The voltage waveform of the discharge is measured by a HV probe (11) connected in parallel to the discharge gap. The voltage and current waveforms are recorded by a digital oscilloscope (Tektronix TDS 640A) (12) connected to a PC (13).

It has been found that this excitation scheme was capable to produce stable and homogeneous glow discharges with a cross-section area of ~ 0.8 cm^2 in an electrode gap of 1 cm in different rare gases, rare gas mixtures and fluorine – rare gas mixtures (~ 0.1 % F_2) at a total gas pressure of several bar (2 bar typically in our experiments). In typical ArF^* excimer laser gas mixtures containing ~ 5 % Ar and ~ 0.1 % F_2 diluted in either He or Ne, the discharge pulse has a FWHM of ~ 100 ns, a peak specific power deposition density of ~ 1 MW cm^{-3} bar^{-1} and a specific energy deposition of ~ 100 mJ cm^{-3} bar^{-1}. Such a homogeneous discharge in a laser gas mixture provides the excitation of the gaseous medium needed to create optical amplification characteristics ultimately required for laser action.

The rest of the experimental setup is used for optical measurements of the spontaneous emission and laser gain at 193 nm (ArF^* excimer wavelength). A probe beam from the small ArF laser (TuiLaser ExciStar XS-200-193) (14) passes an aperture (15) ~ 6 mm in diameter and a neutral density filter (16). The purpose of the aperture (15) is to separate the laser beam from the highly divergent spontaneous radiation present in the output of the probe laser. It appeared to be extremely important for the absolute calibration of the photo-diodes and the measurements of the transmission and reflection coefficients of the optical components. The semi-transparent mirror (17) splits the beam probe beam in two parts. One part goes through a 193 nm filter (LC-193 BP 20) (18) directly to a photo-diode (FND 100Q) (19) and serves as the control channel. The other part of the beam passes the discharge chamber (1), an aperture (20), another 193 nm filter (21) and is detected by the second photo-diode (UV 444BQ) (21). This pathway is called the signal channel. The waveforms from both photo-diodes are registered by the oscilloscope (12).

This optical part of the layout has been used in the measurements of the spontaneous emission and the laser gain as well as for the estimation of the temporal profile of the gain. More detailed description of the optical part of the setup is given below in the next sub-section. For the spatial profile measurements of the laser gain a different layout has been used. This is described later in sub-section 5.2.4.

5.2.2 Setup for the spontaneous emission measurements

For the spontaneous emission measurements the probe laser is not required. In these experiments only the spontaneous emission radiation, emitted by the discharge, was detected by the signal photo-diode (UV 444BQ) (22 in figure 5.1) together with the waveforms of the discharge voltage and current. The probe laser was used for absolute calibration of the photo-diode, to check the linearity of the photo-diode, to measure the transmittance of the discharge chamber wall (quartz glass) and the 193 nm filter (LC-193 BP 20) (21 in figure 4.2). These tasks were performed with help of a Molectron EnergyMax500 energy meter.

The spontaneous emission experiments have been conducted in the following sequence. After application of an X-ray preionization pulse the single pulse excitation circuit ignited a homogeneous discharge in the discharge chamber, filled with a suitable laser gas mixture. The spontaneous emission from the excited laser gas mixture in the discharge chamber (1 in figure 5.1) was detected by means of a photo-diode (22 in figure 5.1) placed at a distance of 13 cm from the center of the discharge chamber. The sensitive area of this photo-diode was 12 mm in

diameter. The measured sensitivity of the detector was ~ 578 mV W^{-1} in the linear response region. The 193 nm filter with a diameter of ~ 20 mm (21 in figure 5.1) was attached directly to the photo-diode. According to the specification this filter has its maximum transmittance of 23 %. at a wavelength of 193 nm. The measured transmittance of the filter at 193 nm was indeed ~ 23 %. An aperture (20 in figure 5.1) with a diameter of 15 mm was placed 1 cm in front of the filter. In this configuration the photo-diode detects radiation emitted by the discharge in a solid angle of ~ 6.7 10^{-3} srad. The measured transmittance of the wall of the discharge chamber was ~ 23 %.

5.2.3 Setup for the laser gain measurements

The ArF^* probe laser (TuiLaser ExciStar XS-200-193) (14 in figure 5.1) together with the control photo-diode (FND 100Q) (19 in figure 5.1) was used in our experimental setup for the measurements of the peak net laser gain and for the temporal and spatial profile measurements of the laser gain. The transmittance and reflectance of the beam-splitting mirror and the linearity of the reference photo-diode response to the incident light pulse energy were checked by means of the Molectron EnergyMax500 energy meter. A schematic layout (top view) of the optical part of the setup is shown in figure 5.2.

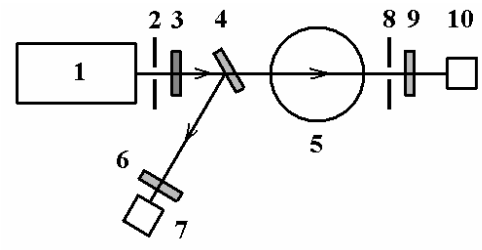

Figure 5.2. Optical part of the experimental setup for measurements of the spontaneous emission and temporal profile of the gain. Top view.
1: ArF probe laser; 2: aperture; 3: neutral density filter; 4: beam-splitting mirror; 5: discharge chamber; 6: 193 nm filter; 7: photo-diode; 8: aperture; 9: 193 nm filter; 10: photo-diode.

The dimensions of the probe laser beam (1) are 3 mm in the plane of the figure (perpendicular to the discharge gap) and 6 mm perpendicular to the plane of the figure. The probe laser is aligned such that the laser beam passes through the center of the discharge chamber (5). The discharge gap (between the two metallic electrodes) in the chamber (5) is 1 cm. The diameter of the first aperture (2) is 6 mm and of the neutral density filter (3) 20 mm. This filter attenuates the probe beam intensity by a factor of ~ 500. Such a high attenuation factor is necessary to be able to measure the small signal gain. The semi-transparent beam-splitting mirror (4) reflects ~ 12 % of the incident laser light towards the reference photo-diode (7) and transmits ~ 66 % of the light towards the discharge chamber (5). The transmittance of the 193 nm filter (6) is 23 %. The sensitive area of the reference photo-diode (7) is 3 mm in diameter, which is 2 times lower than the vertical dimension of the probe beam. The discharge chamber wall is made of a cylindrical quartz glass tube. The probe beam passes through the chamber wall 2 times, each time only 23 % of the light is transmitted. The signal photo-diode (10) in this configuration is placed 21 cm from the center of the discharge chamber. A 193 nm filter (9) is attached directly to the photo-diode, and the second aperture (8) with a diameter of 6 mm is placed 1 cm in front of the photo-diode. In this configuration the photo-diode detects the laser probe beam and the radiation emitted by the discharge in a solid angle of ~ 7 10^{-4} srad. Thus the spontaneous emission signal is

suppressed ~ 10 times compared to the experiments on measurements of the spontaneous emission due to ~ 10 times narrower solid angle in which the spontaneous emission is observed.

5.2.4 Setup for measuring the spatial gain profile

The optical part for measuring the spatial profile of the laser gain is shown in figure 5.3 (top view). The beam from the probe laser (1) goes to the first beam-splitting mirror (2), which transmits ~ 10 % of incident light towards the second mirror (3) and reflects ~ 50 % of the light towards the third mirror (4). Mirror (3) reflects ~ 70 % of the light to the control photo-diode (8). In front of the control photo-diode there a 193 nm filter (7) and an aperture (6) with a diameter of 2 mm is placed. The aperture is used to limit the total amount of light in order to reduce the signal amplitude from the control photo-diode. Mirror (4) reflects ~ 50 % of the light towards the discharge chamber (9). An aperture (5) with a diameter of 0.8 mm is attached to mirror (4). The combination of this mirror and the attached aperture is placed on a translation table. Thus the probe beam passing through the discharge chamber can be shifted in the plane of the figure perpendicular to the 1 cm wide discharge gap. In this way the probe beam with a diameter of 0.8 mm passes the active gain volume and can be shifted through the whole plane in the middle of the discharge gap. The signal photo-diode (12) is placed on another translation table 45 cm away from the center of the discharge chamber. Another 193 nm filter (11) and an aperture (10) with a diameter of 8 mm are attached to the control photo-diode. In this configuration the signal photo-diode detects the laser probe beam and the radiation emitted by the discharge in a solid angle of ~ 2.7 10^{-4} srad. The spontaneous emission signal is, compared to the amplified probe beam signal more suppressed by the aperture at this distance.

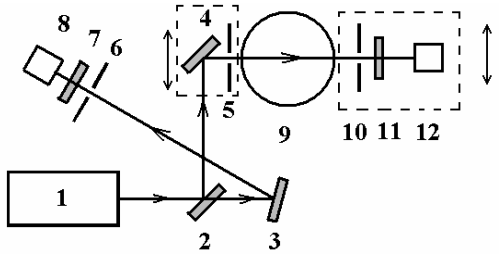

Figure 5.3. Top view of the optical part for measurements of the spatial gain. .
1: ArF probe laser; 2, 3, 4: beam-splitting mirrors; 5, 6: apertures; 7: 193 nm filter; 8: photo-diode; 9: discharge chamber; 10: aperture; 11: 193 nm filter; 12: photodiode.

By moving both mirror (4) and the signal photo-diode (12) by the translation tables, the discharge could be scanned in the mid-plane of the electrode gap and perpendicular to the discharge gap. In this way the spatial profile of the laser gain was measured.

5.3 Measurements of the spontaneous emission and laser gain at the ArF* wavelength of 193 nm

5.3.1 Spontaneous emission measurements

Spontaneous emission measurements were performed in He : Ar : F_2 and Ne : Ar : He : F_2 excimer laser gas mixtures at different power deposition levels, at different gas pressures and for different concentrations of Ar and F_2 in the mixture. The presence of He in Ne based mixtures is due to the fact that all F_2 containing mixtures were prepared using a pre-mixed He : F_2 / 95 : 5

gas bottle. All measurements were carried out at the wavelength of 193 nm (ArF^* excimer line) by using an LC-193 BP 20 filter. The transmittance curve of this filter has a peak transmittance value of 23 % centered at 193 nm and a FWHM of ~ 20 nm.

In gas mixtures without Ar or F_2 added to the laser gas mixture no spontaneous emission in the UV region at 193 nm was detected from the discharge volume. Spontaneous emission was detected only if both Ar and F_2 were presented in the laser gas mixture with He or Ne as the main buffer gas.

Typical measured waveforms of the discharge voltage (a), current (b), the calculated power deposition (c) and the spontaneous emission (d) measured by the signal photo-diode are shown in figure 5.4. A laser gas mixture of He : Ar : F_2 / 94.9 : 5 : 0.1 at a total pressure of 2 bar, and a charging voltage of 14 kV was used. As discussed in chapter 4 the discharge appeared in the dense form under these experimental conditions. As can be seen from the figure the discharge current reached a peak value of ~ 320 A and had a FWHM of ~ 120 ns. The peak power deposition was ~ 750 kW, and the FWHM of the power deposition waveform was approximately 100 ns. The half-width of the spontaneous emission signal was approximately 50 ns, and was shorter than the duration of the pumping pulse. Roughly, the shape of the spontaneous emission signal followed the pumping density waveform. The maximum of the spontaneous emission appeared at the maximum of the pumping density deposition. Since the photodiode was calibrated by means of the probe laser, the transmittance of the chamber wall and the 193 nm filter as well as the solid angle, within which the spontaneous emission is gathered, was known also, it was possible to calculate the emitted spontaneous light intensity in terms of power emitted per unit solid angle. For the above mentioned conditions the peak value was approximately 4.5 kW $srad^{-1}$ at 193 nm.

From the measurements it appeared that the peak intensity and FWHM of the emission waveform depended on the gas mixture composition and gas pressure. The peak spontaneous emission intensity increased with the power deposition into the discharge. The dependence of the peak spontaneous emission intensity on the peak power deposition is shown in figure 5.5 for different gas mixtures. Each point is the average of 5 measured values, the error bars show the standard deviation of the measured values of the peak light intensity (vertical bars) and the peak power deposition (horizontal bars).

In figure 5.5 (a) the total gas pressure of the F_2 : Ar : He mixture is 2 bar, the concentration of Ar is 5 % and the concentration of F_2 is varied from 0.05 % (1), 0.1 % (2) to 0.15 % (3). In figure 5.5 (b) the total gas pressure of the F_2 : Ar : He mixture is 2 bar, the F_2 concentration is kept constant at 0.1% and the Ar concentration is 2.5 % (1), 5 % (2) and 10 % (3). In figure 5.5 (c) the results for the same F_2 : Ar : He / 0.1 : 5 : 94.9 gas mixture but at different total pressures of 1.5 (1), 2 (2) and 3 bar (3) are shown. Finally, in figure 5.5 (d) the results for two different F_2 : Ar : He / 0.1 : 5 : 94.9 and F_2 : He : Ar : Ne / 0.1 : 1.9 : 5 : 93 gas mixtures are shown. In all cases the peak spontaneous emission intensity was observed to grow with the peak pumping power deposition and then to reach a saturation value. This saturation appeared roughly to occur when the discharge reached its maximum cross-section ~ 1 cm in diameter, defined by the preionization area. The saturated light intensity and the power deposition, at which the saturation was reached, were found to depend on the gas mixture composition and total pressure. For example, in figure 5.5 (c) it is shown that at a lower total gas pressure the saturation appears at a lower pumping power and that the saturated spontaneous emission intensity is lower. A higher concentration of F_2 leads to a higher saturation pumping power and higher saturated light output, as is shown in figure 5.5 (a). The spontaneous emission from the discharge in excimer laser gas mixtures with Ne as buffer gas was slightly stronger than from discharges in He-based mixtures, as shown in figure 5.5 (d). For various Ar concentrations

(figure 5.5 (b)) the situation was more complicated: the emission at a high power density was the weakest from a gas mixture with 5% Ar (2) and the strongest in a 2.5 % Ar mixture (1), while the discharge in a mixture with 10 % of Ar (3) produced values in between.

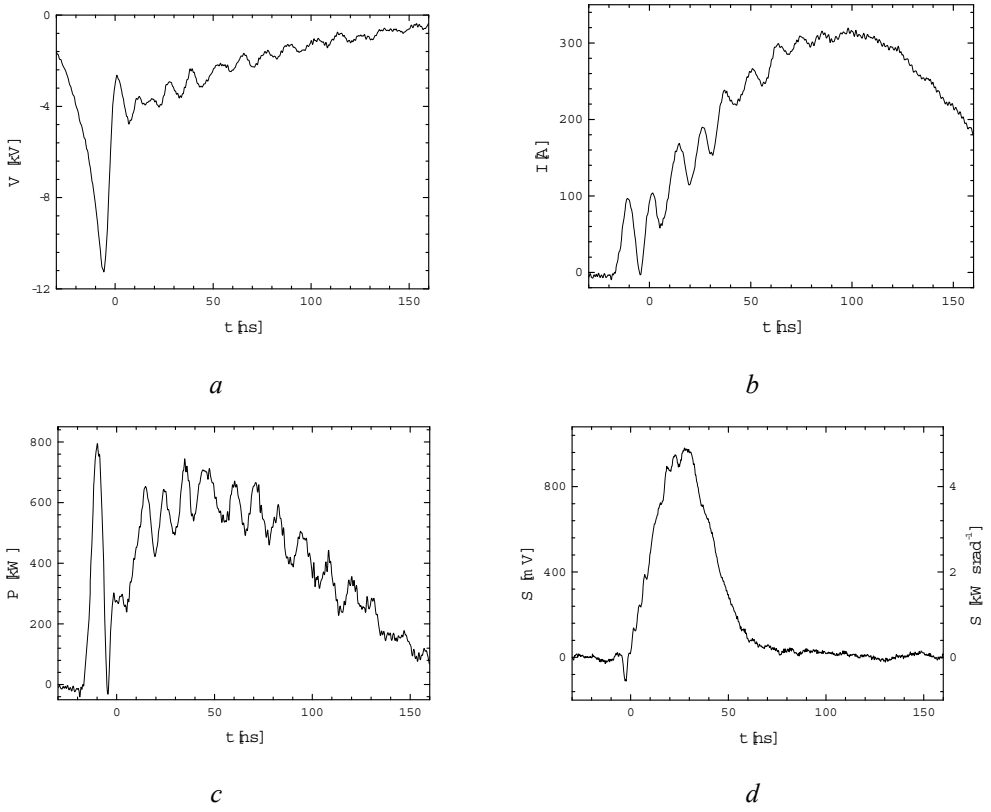

Figure 5.4. Typical measured voltage V (a) and current I (b), calculated power deposition P (c) and measured spontaneous emission light intensity S (d) waveforms, obtained in a discharge in He:Ar:F_2 / 94.85:5:0.15 at a total gas pressure of 2 bar and a charging voltage of 14 kV.

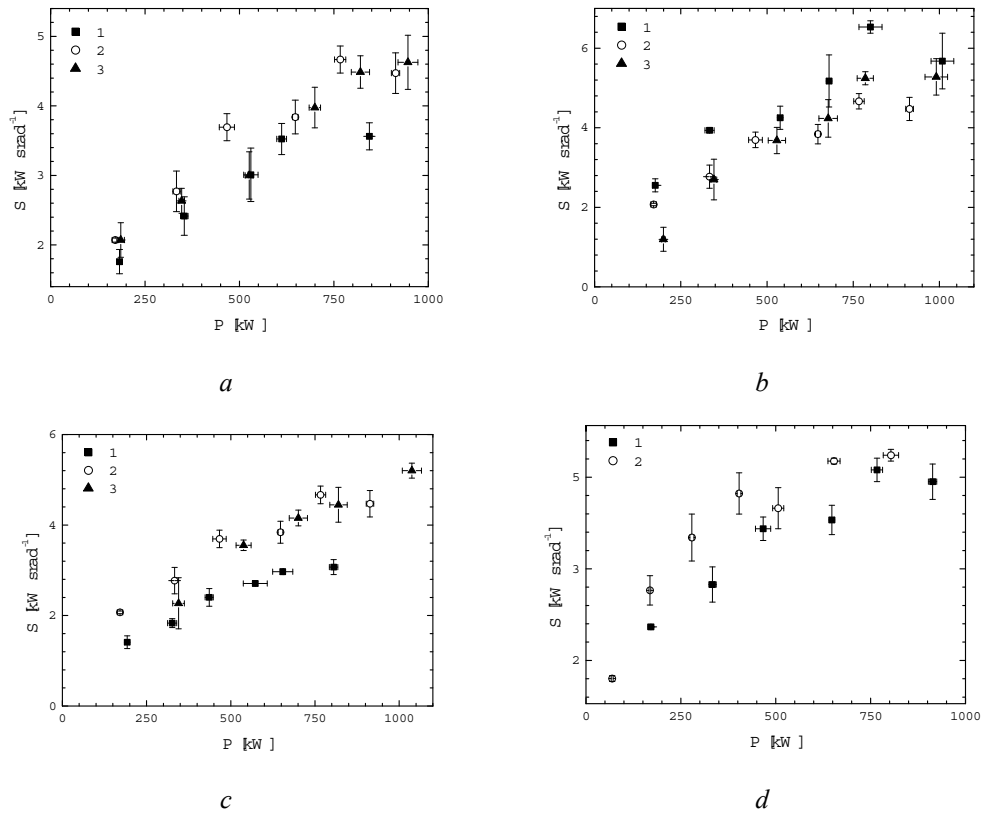

Figure 5.5. Dependence of the peak of the spontaneous emission light intensity S on the peak power deposition into the discharge P. a: Mixture of 0.05 (1), 0.1 (2) and 0.15 % (3) of F_2 and 5 % of Ar in He as a buffer gas at a total pressure 2 bar. b: Mixture of 0.1 % of F_2 and 2.5 (1), 5 (2) and 10 % (3) of Ar in He as a buffer gas at a total pressure 2 bar. c: He : Ar : F_2 / 94.9: 5: 0.1 mixture at total pressure 1.5 (1), 2 (2) and 3 bar (3). d: He : Ar : F_2 / 94.9: 5: 0.1 and Ne : Ar : He : F_2 / 93: 5: 1.9: 0.1 mixtures at a total pressure of 2 bar.

At the same charging voltage the peak power deposition into the discharge and FWHM power deposition were different in different gas mixtures. Differences in the Ar and F_2 concentration in the laser gas mixture have impact on the formation kinetics and affected the peak light intensity and the FWHM of the emission pulse. In figure 5.6 the average of 5 spontaneous emission waveforms measured in a He : Ar : F_2 gas mixture at a total pressure of 2 bar at a charging voltage of 14 kV are shown for different F_2 concentrations of 0.05 (1), 0.1 (2) and 0.15 % (3). The concentration of Ar was 5 % in all three gas mixtures. The peak power deposition into the discharge was ~ 840 (1), 780 (2) and 820 kW (3). It can be seen from this figure that there was a broadening of the emission waveform and a shift of the position of the maximum light intensity with a decrease of the F_2 concentration. The peak emission intensity did not vary much in these three cases. For case (1) the peak power deposition was the highest and

the emission intensity was the weakest. In the case (2) the peak power deposition was the lowest and the peak emission intensity was the highest.

It was found that the spontaneous emission decreased gradually when the discharge was fired a large number of times without refreshing the laser gas mixture. In figure 5.7 the decrease of the spontaneous emission intensity and the broadening of the emission waveform with an increasing number of shots in the same gas mixture are shown. The measurements were performed in a He : Ar : F_2 / 94.9 : 5 : 0.1 gas mixture at a total pressure of 2 bar and a charging voltage of 14 kV. The waveforms shown in this figure are averaged from the consecutive shots number 1 – 35 (1), 31 – 65 (2), 61 – 95 (3) and 91 – 125 (4). The total duration of the experiment was ~ 30 min. It can be seen that with an increasing number of shots the peak intensity decreased, the FWHM of the pulse was found to increase and the peak intensity was observed later. This effect is probably due to F_2 depletion, outgasing of the discharge chamber or due to poisoning of the laser gas mixture by air because of a small vacuum leakage in the connecting pipes to the discharge chamber. This effect was taken into account in the later experiments on the laser gain measurements.

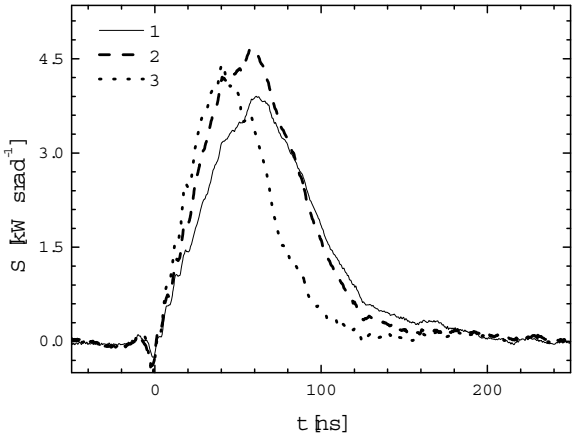

Figure 5.6. Average of 5 spontaneous emission waveforms measured in a He : Ar : F_2 gas mixture at a total pressure of 2 bar and a charging voltage of 14 kV. Concentration of Ar was 5 %. The F_2 concentration was 0.05 (1), 0.1 (2) and 0.15 % (3).

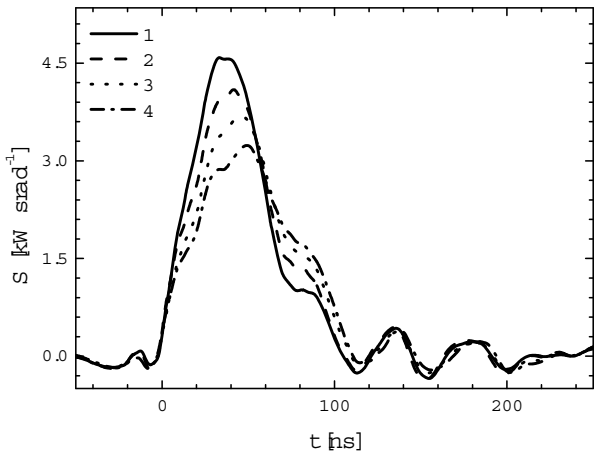

Figure 5.7. Decrease of the spontaneous emission intensity and broadening of the emission waveform with increasing number of shots in the same Ar : F_2 / 94.9 : 5 : 0.1 gas mixture at a total pressure of 2 bar and a charging voltage 14 kV. The waveforms were averaged from the consecutive shots number 1 – 35 (1), 31 – 65 (2), 61 – 95 (3) and 91 – 125 (4).

5.3.2 Gain measurements

For all measurements on the peak net gain and the temporal and spatial profile of the gain the dual channel, control – signal measuring scheme was employed. As described before with this technique the beam from the probe laser was split into two beams. One beam came directly to the control photo-diode, which produced a control signal S_c. The other beam passed through the discharge and was recorded by the signal photo-diode as signal S_s. A change in the ratio S_s/S_c reflected a change of the optical properties of the medium through which the signal beam passed. If in the medium optical gain occurred, this ratio should increase. In case of absorption of the signal beam, the ratio should decrease.

The advantage of this method is that it is not sensitive to fluctuations of the probe laser beam intensity. If the probe beam intensity, for instance, increases 5 % in a shot following the previous shot, both the control and the signal beam also are increased with the same amount after splitting. If the absorption or gain of the medium under investigation is not saturated, then the attenuated or amplified signal in the medium is also increased with the same amount compared to the previous shot. Thus S_s/S_c is not changed due to fluctuations of the initial probe beam.

Because the pulse energy of our probe laser was not stabilized it was very important that the intensity fluctuations were not critical in our measuring system. According to the specifications of the manufacture this laser should have less than 1 % deviation of the pulse energy at a repetition rate of 100 – 200 Hz even without a stabilization unit. In our experiments the laser was used in single pulse operation mode with one pulse every 10 – 20 sec. In the single pulse mode the fluctuation of the pulse energy was measured to be ~ 10 %, while the FWHM of the pulse (~ 10 ns) and the shape of the laser pulse were found to be constant.

If the signal beam passes through the discharge chamber filled with a laser gas mixture, it experiences attenuation due to photo-ionization and photo-dissociation of the gas components of the mixture even when the discharge is not ignited. These and other absorption processes are referred to as steady absorption with the coefficient α_s. When a discharge is ignited in a proper gas mixture population inversion can be created in the gaseous medium and the signal beam will be amplified or attenuated according to the gain coefficient g. In the discharge plasma also species like ions, excited atoms and molecules will be created and these new species may cause additional absorption. However, this absorption is present only when a discharge plasma exists and only in the plasma. This absorption is referred to as transition absorption with the coefficient α_t. By measuring the S_s^v/S_c^v ratio, when the discharge chamber is evacuated, the S_s^f/S_c^f ratio, when the chamber is filled with the laser gas mixture but no discharge is excited, and the S_s^d/S_c^d ratio under discharge conditions, it is possible to measure the steady absorption coefficient α_s and the net gain coefficient g-α_t. They are given by the formulas:

$$\alpha_s = \frac{100\%}{L_g} \ln\left(\frac{S_s^f / S_c^f}{S_s^v / S_c^v} \right) = \frac{100\%}{L_g} \ln\left(\left(\frac{S_s^f}{S_s^v} \right) \left(\frac{S_c^v}{S_c^f} \right) \right) \tag{5.1}$$

and:

$$g - \alpha_t = \frac{100\ \%}{L_d} \ln\left(\frac{S_s^d / S_c^d}{S_s^f / S_c^f} \right) = \frac{100\ \%}{L_d} \ln\left(\left(\frac{S_s^d}{S_s^f} \right) \left(\frac{S_c^f}{S_c^d} \right) \right) \tag{5.2}$$

where L_g is the full path length in cm of the signal beam in the gas (~ 7 cm) and L_d is the path length in cm of the signal beam through the discharge (~ 1 cm or less).

As can be seen from Eqs. 5.1 and 5.2, we looked for the change of the amplitude of the photo-diode signal due to amplification or absorption of the laser pulse in the excited gas during

the discharge S_s^d/S_s^f and corrected this ratio by the factor S_c^f/S_c^d which describes the fluctuations of the initial probe laser beam intensity.

Peak net gain measurements were performed in gas mixtures that are used in ArF excimer lasers like He : Ar : F_2 / 94.9 : 5 : 0.1 and Ne : Ar : He : F_2 / 93 : 5 % :1.9 : 0.1 at a total pressure of 2 bar and for a charging voltage of 10, 12, 14 and 16 kV. In our experiments the sequence of measurements was as follows. First the discharge chamber was evacuated to a pressure of ~ 10^{-6} mbar and the S_s^v/S_c^v ratio was measured in 10 laser shots. From this the average $<S_s^v/S_c^v>$ value and the typical standard deviation of ~ 5 % were determined. Then the chamber was filled with the required gas mixture to a pressure of 2 bar and now the S_s^f/S_c^f ratio was measured in 10 shots. Again the average $<S_s^f/S_c^f>$ value and the typical standard deviation of ~ 5 % were determined. It appeared that the difference between the average $<S_s^v/S_c^v>$ value and the $<S_s^f/S_c^f>$ value was less than the standard deviation. Thus a determination of the steady absorption coefficient α_s according to Eq. 5.1 was not possible.

In the next step the charging voltage was set to the required value between 10 and 16 kV. At every charging voltage the spontaneous emission waveform was 5 times measured without firing the probe laser. The onset of the laser pulse had a jitter of ~ 10 ns. After the probe laser was turned on and the delay between the laser pulse and the ignition of the discharge was adjusted in such a way that the probe beam passed through the discharge at the moment the peak power deposition was reached. Then the S_s^d/S_c^d ratio, corrected for the spontaneous emission waveform and noise pattern, was measured 10 times for this charging voltage. The exact procedure of the signal correction is described in section 5.4. The average net peak gain over the path of the beam in a discharge $<(g-\alpha)\,L>$ was calculated according to:

$$\left\langle (g-\alpha)\,L \right\rangle \;=\; \ln\left(\left\langle \frac{S_s^d / S_c^d}{\left\langle S_s^f / S_c^f \right\rangle} \right\rangle \right) x\,100\% \qquad (5.3)$$

The discharge voltage and current waveforms were measured simultaneously and the average peak power deposition was calculated. After that a new charging voltage was chosen and the procedure was repeated.

In figure 5.8 a typical measured control (top) and signal waveform (middle) together with the corrected waveform (bottom), in which the spontaneous emission and electro-magnetic interference related noise are removed, are given. This signal correction procedure is described later in section 5.4. The control photo-diode (FND 100Q) has sub-nanosecond rise and fall times thus the control signal waveform (top) followed the laser pulse shape which had a FWHM of 10 ns. The signal photo-diode (UV 444BQ) has a rise time of 5 ns and an exponential decay time with a time constant of ~ 8 ns. The FWHM of the corrected signal waveform was ~ 16 ns (bottom). The response of the control photo-diode signal was proportional to the energy of the laser pulse, as it was checked during the absolute calibration of the control photo-diode. Since neither the FWHM of the laser pulse nor the pulse shape changed when the pulse energy was varied, as it was checked with help of the fast control photo-diode, the amplitude of the signal from the control photo-diode was proportional to the light intensity of the laser pulse. The

amplitude of the control waveform (top) was named S_c^d, and the amplitude of the signal waveform corrected to the noise pattern and spontaneous emission waveform (bottom) was named S_s^d.

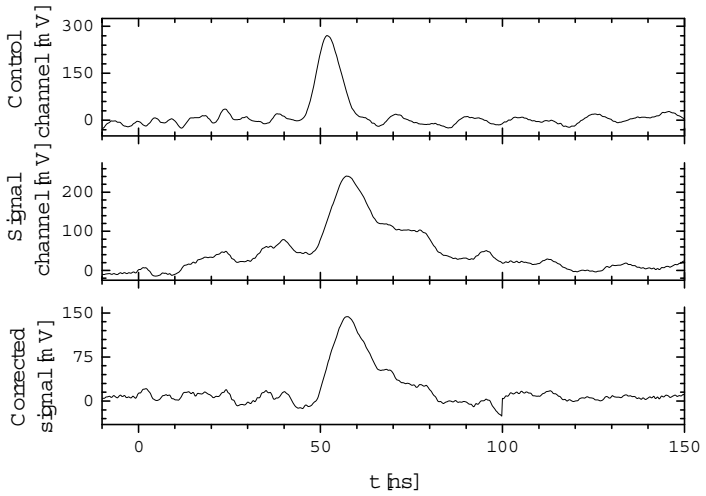

Figure 5.8. Typical signal waveforms, measured by the control (top) and signal photodiode (middle), and the signal waveform corrected for the spontaneous emission and noise pattern (bottom).

In figure 5.9 the dependence of the peak net gain over discharge length $(g-\alpha)\,L$ (top) and peak spontaneous emission intensity S emitted in the unit solid angle (bottom) on the peak power P deposited into the discharge is shown. The measurements have been performed for a He : Ar : F_2 / 94.9 : 5 : 0.1 (1) and a Ne : Ar : He : F_2 / 93 : 5 : 1.9 : 0.1 laser gas mixture (2) at a total pressure of 2 bar and a probe laser beam intensity of 14 ± 2 W cm^{-2}. All values of the peak net gain are averaged over 10 measurements according to Eq. 5.3, the spontaneous emission values are averaged over 5 measurements. The error bars show the standard deviation of the measured values. The peak net gain in the He : Ar : F_2 mixture (1) was observed to increase from 0 at P ~ 500 kW to ~ 20 ± 8 % at P ~ 1 MW. The spontaneous emission signal was found to increase from ~ 2.3 kW srad^{-1} to ~ 4.5 kW srad^{-1} respectively. In the Ne : Ar : He : F_2 mixture (2) the gain was measured to increase from 0 at P ~ 420 kW to ~ 20 ± 8 % at P ~ 660 kW, and was the same at a higher P of ~ 800 kW. The spontaneous emission was observed to increase from ~ 4.2 kW srad^{-1} at P ~ 420 kW to ~ 6.6 kW srad^{-1} at P ~ 660 kW, and to have the same value at a higher value of ~ 800 kW for P.

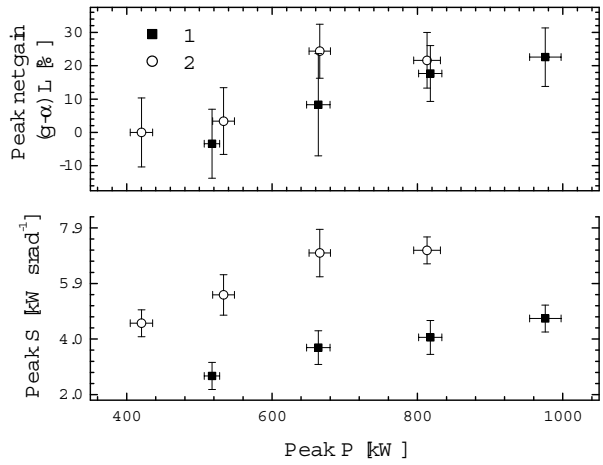

Figure 5.9. Dependence of the peak net gain over discharge length (g-α) L and the peak spontaneous emission intensity S emitted in the unit solid angle on the peak power P deposited into the discharge. Gas mixtures: He : Ar : F_2 / 94.9 : 5 : 0.1 (1) and Ne : Ar : He : F_2 / 93 : 5 : 1.9 : 0.1 (2). The gas pressure was 2 bar. The probe laser beam intensity was 14 ± 2 W cm^{-2}.

In both mixtures the discharge was burning in the dense form. At 10 kV the power deposition was ~ 500 kW in the He based mixture and ~ 420 kW in the Ne based mixture while at a charging voltage of 16 kV the power deposition was ~ 1 MW and ~ 800 kW. Although it was observed that the discharge was narrower at a charging voltage of 10 kV than at the charging voltage of 16 kV, the power deposition density was expected to be constant, as has been discussed in chapter 4. In order to determine the discharge width at every charging voltage we took the average peak current I at the each charging voltage and divided it by the current density j of the positive column measured in the same mixtures, as discussed in chapter 4 (see Sec. 4.3.2, Fig. 4.14). The positive column cross-section area S_d is:

$$S_d = \frac{I}{j} \tag{5.4}$$

where j was 800 ± 300 A cm^{-2} in the He based mixture and 500 ± 200 A cm^{-2} in the Ne based mixture. From the calculated discharge area the width of the discharge was derived. The discharge gap length was 1 cm, thus also the discharge volume is known. When the volume is known for every charging voltage and for the two gas mixtures all results shown in figure 5.9 can be presented in terms of power deposition density, i.e. per cm^3, of specific emission output in terms of kW srad^{-1} cm^{-3} and the peak net gain per cm as given in figure 5.10.

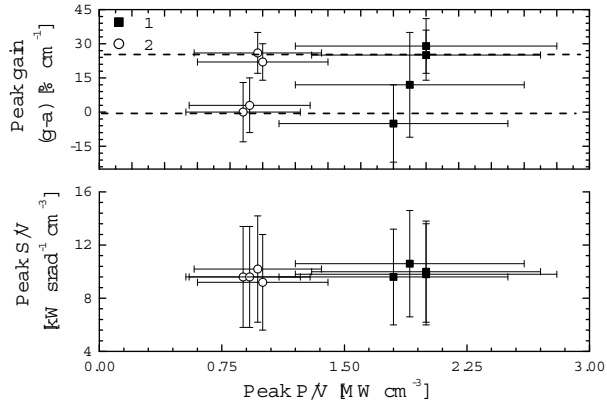

Figure 5.10. Dependence of the peak net gain (g-α) and specific peak spontaneous emission intensity S/V emitted in the unit solid angle from a unit volume of the discharge plasma on the peak power density P/V deposited into the discharge. Gas mixtures : He : Ar : F_2 / 94.9 : 5 : 0.1 (1) and Ne : Ar : He : F_2 / 93 : 5 : 1.9 : 0.1 (2). The gas pressure was 2 bar. The probe laser beam intensity was 14 ± 2 W cm^{-2}.

The error bars become larger because of the large uncertainty in the calculated current density (~ 40%). The specific power deposition density at every charging voltage has been found to be ~ 1 MW cm^{-3} in the Ne based mixture (2) and ~ 1.8 MW cm^{-3} in the He based mixture (1). Although the power deposition density was almost 2 times higher in the He based mixture than in the Ne based mixture, the specific emission output was observed to be the same ~ 9.5 kW srad^{-1} cm^{-3}. The dependency of the peak net gain per cm on the power deposition density was measured to be different for the two gas mixtures. In the Ne based mixture (2) the calculated gain per cm was around 0 at charging voltages of 10 and 12 kV and about 26 % cm^{-1} at the charging voltages of 14 and 16 kV. In the He based mixture the calculated gain was more linear: ~ 0 % cm^{-1} at a charging voltage of 10 kV, ~ 10 % cm^{-1} at 12 kV and ~ 26 % cm^{-1} at 14 and 16 kV.

5.3.3 Net gain temporal profile measurements

In order to check if the temporal profile of the net gain over the beam path length depends on the probe laser beam intensity and to measure the temporal width of the gain waveform, the net gain was measured in a He : Ar : F_2 / 94.9 : 5 : 0.1 mixture. The total gas pressure was 2 bar and the charging voltage 14 kV (peak P ~ 800 kW). For the probe laser we used three different beam intensities: 14 ± 2, 29 ± 3 and 52 ± 3 W cm^{-2}. The discharge chamber was pumped down and filled with a fresh gas mixture before each set of measurement at one particular value of the probe beam intensity.

In the beginning of each set of measurements (at the given probe beam intensity) the S_s^f/S_c^f ratio was measured 10 times and the average value of $\langle S_s^f/S_c^f \rangle$ was calculated. Then the spontaneous emission signal waveform was measured 5 times and also averaged. After these measurements the probe laser was added. The delay between the probe laser pulse and the

ignition of the discharge was set in such a way that the probe laser pulse appeared prior to the discharge. Due to the jitter of ~ 10 ns the probe pulse appeared from shot to shot at slightly different moments compared to the discharge ignition. Then the S_s^d/S_c^d ratio was measured 5 times at that particular delay value. After these measurements the delay was increased by ~ 15 – 25 ns, and 5 more measurements of the S_c^d/S_r^d ratio were performed at that delay value. The spontaneous emission signal waveform measurements were repeated after each 25 measurements of the S_s^d/S_c^d ratio. This procedure of increasing the delay time between the probe and the discharge ignition was repeated until a delay value of ~ 150 – 160 ns after the ignition of the discharge was reached. At the end of the whole series of measurements control measurements of the S_s^f/S_c^f ratio were performed.

The measured data were sorted in ascending order by the moment the probe pulse was applied. The entire set was divided into equal intervals of 10 ns each. The data in every interval were averaged. Thus the average values and the standard deviation of the the S_s^f/S_c^f ratio and the time were calculated for every non-empty interval.

In figure 5.11 the temporal profile of the peak net gain over the beam path is shown for three different probe laser beam intensities: (a) 14 ± 2, (b) 29 ± 3 and(c) 52 ± 3 W cm^{-2}. The laser gas mixture was: He : Ar : F_2 / 94.9: 5: 0.1 at the total pressure of 2 bar and the charging voltage was 14 kV (peak P ~ 800 kW). The discharge width under these conditions was d = 7 ± 2 mm. The solid squares (1) are the actual measured values and the open circles (2) are the averaged values. The error bars represent the standard deviations of the measurements. As can be seen from this figure the measured gain fluctuates very strongly, and it is difficult to draw conclusions about the shape of the temporal gain profile. However, the net gain was definitely positive in the time interval 30 – 100 ns after the ignition of the discharge (t = 0 ns) and the maximum gain has been observed ~ 60 ns after start of the discharge.

5.3.4 Net gain spatial profile measurements

For the measurements of the spatial gain profile a different optical layout was employed, as discussed in section 5.2.4. The discharge volume was scanned in the direction perpendicular to the probe beam and the discharge gap with help of a mirror installed on a translation table (see figure 5.3). The diameter of the aperture limiting the probe beam cross-section was 0.8 mm and the scanning step was 0.5 mm. The signal photo-diode was installed on the other translation table and also shifted each time by 0.5 mm. The position of the photo diode was adjusted every step such that the probe beam fell always onto the center of the photo-diode. The S_s^f/S_c^f ratio was measured 5 times during each step position and averaged. This was done to take into account slight changes in the attenuation of the probe beam by the cylindrical chamber walls at different positions of the probe laser. When the probe beam passes exactly along the diameter of the chamber the wall thickness is less compared to the situation when the beam passes aside from the diameter due to the curvature of the cylindrical wall. This effect was actually observed in our experiments. The spontaneous emission was measured 10 times and averaged prior to the gain spatial profile measurements. The spontaneous emission measurements were repeated after each 4 spatial steps (each 2 mm) and at the end of the experiment. At every position the S_s^d/S_c^d ratio was measured 10 times and the average gain was calculated.

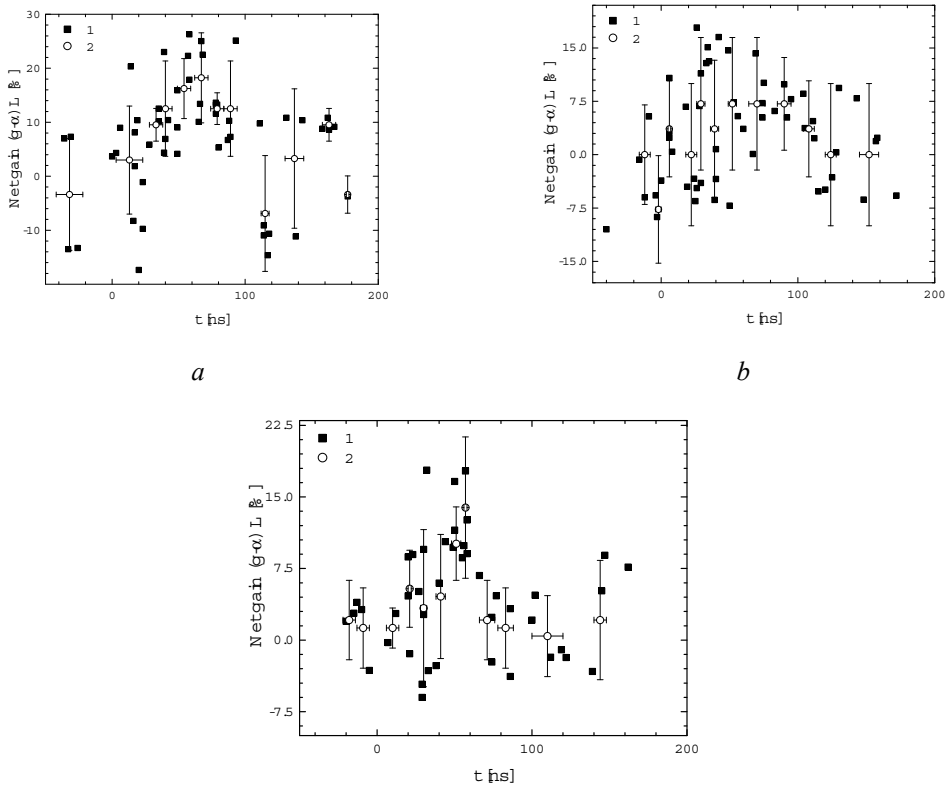

Figure 5.11. Temporal evolution of the net gain (g-α)L measured in a He : Ar : F_2 / 94.9: 5: 0.1 mixture at a total pressure of 2 bar, a charging voltage of 14 kV (peak P ~ 800 kW) and a probe laser beam intensity of 14 ± 2 (a), 29 ± 3 (b) and 52 ± 3 W cm^{-2} (c). 1: Experimental points; 2: averaged values.

All measurements were performed in a He : Ar : F_2 / 94.9 : 5 : 0.1 gas mixture at a total pressure of 2 bar, a charging voltage of 14 kV (P ~ 800 kW) and a probe laser beam intensity of 14 ± 2 W/cm^2. The spatial profile of the net gain over the beam path is shown in figure 5.12. Every point in the graph is the average of 10 measurements. The vertical error bars represent the standard deviation of the measured values. The horizontal error bars correspond to the spatial step of measurements. The gain was observed to reach the maximum value of 17 ± 10 % in the center and to have a full width of ~ 5 mm. The discharge width, estimated from the discharge current and current density (see Eq. 5.4), was 7 ± 2 mm in this case. Visually the discharge width was closer to 1 cm in diameter than to 0.5 cm. The effective value of the gain per cm calculated from the full width of the gain spatial profile was measured to be ~ 34 ± 20 % cm^{-1} and ~ 26 ± 14 % cm^{-1} if calculated from the estimated discharge width.

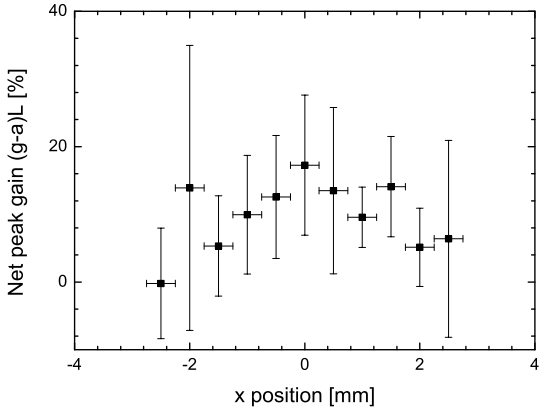

Figure 5.12. Spatial profile of the net gain (g-α)L measured in a He : Ar : F_2 / 94.9 : 5 : 0.1 gas mixture at a total pressure of 2 bar, a charging voltage of 14 kV (P ~ 800 kW) and a probe laser beam intensity 14 ± 2 W/cm^2.

5.4 Discussion of the signal analysis procedure and the error bars

In all gain measurements described in sub-sections 5.3.2 and 5.3.3 the signal waveform was measured on a background of spontaneous emission. Therefore the measured signal has to be corrected for the spontaneous emission signal prior to determination of the S_s^d/S_c^d ratio. The basic idea of the used method is to subtract the averaged spontaneous emission waveform from the measured control signal waveform. As the spontaneous emission intensity fluctuates a bit, the averaged waveform has to be multiplied by a factor $f \sim 1$. The exact value of f was determined experimentally for every signal waveform such that the scaled averaged spontaneous emission signal fits the background before and after the peak corresponding to the laser pulse in the best possible way (least standard deviation of the fit curve from the measured control signal on the wings apart from the laser pulse position).

Another difficulty with respect to the measured signals described in sub-sections 5.3.1, 5.3.2 and 5.3.3 was caused by electro-magnetic interference. Looking to all measured signals it could be seen that fast oscillations appeared in the measured waveforms (see figs. 5.4, 5.6 – 5.8). The origin of these oscillations was the electro-magnetic signals produced by the mini-Marx generator, the X-ray source and the discharge itself. The amplitude and shape of these oscillations did not depend on the spontaneous emission intensity or on the probe beam intensity. They were present also in the averaged spontaneous emission signal. When the scaled by factor f averaged emission signal is subtracted from the control signal the oscillations are not suppressed completely if the scale factor f differs from 1, since the electro-magnetic noise pattern is constant and independent on the spontaneous emission intensity. In order to obtain a better corrected control signal the following procedure of the signal correction was employed.

Firstly, the averaged spontaneous emission waveform in absence of the laser pulse $<S_{es}(t)>$ was obtained. Then averaged waveform was smoothed by the adjacent points averaging method and a so-called smoothed emission signal $S_{ses}(t)$ was produced. After that the $S_{ses}(t)$ signal was subtracted from the $<S_{es}(t)>$ signal and the resulting signal $S_{rn}(t)$ was contributed to the noise

pattern. Then the corrected signal waveform $S_{cs}(t)$, corresponding to the amplified laser pulse, was produced from the measured in a single shot spontaneous emission plus amplified laser pulse signal $S_s(t)$ as:

$$S_{cs}(t) = S_s(t) - S_{rn}(t) - f\, S_{ses}(t) \tag{5.5}$$

where the scaling factor $f \sim 1$ is chosen for every waveform such that the resulting waveform $S_{cs}(t)$ is flat before and after the response of the photo-diode to the laser pulse, which fact follows from the least standard deviation of the fit curve $S_{rn}(t) + f\, S_{ses}(t)$ from the measured control signal $S_s(t)$ on the wings apart from the laser pulse position.

Due to the fact that the spontaneous emission signal slightly changed during a series of experiments (see i.e. figure 5.7) the spontaneous emission waveform, in absence of the probe laser pulse, was measured after each 25 – 40 discharge pulses, and new values for $<S_{es}(t)>$, $S_{ses}(t)$ and $S_{rn}(t)$ were obtained.

By this procedure the corrected signal waveform $S_{cs}(t)$ was calculated for each laser shot (see figure 5.8 (bottom)) and its amplitude was taken as S_s^d (see Eq. 5.3). For the control photo-diode the spontaneous emission was not present in the waveform, and the electro-magnetic interference pattern was much less in the amplitude and typically apart from the laser pulse waveform, therefore no correction procedure was applied and the amplitude of the measured in a single shot control waveform was taken as S_c^d. In absence of the gas discharge no electro-magnetic noise and spontaneous emission was present in the signal and control waveforms, thus their amplitudes were taken as S_s^f and S_c^f respectively (see Eq. 5.3). Their averaged ratios were used to determine net gain coefficient in according to Eq. 5.3, as presented in figures 5.9 – 5.12.

The error bars of the gain in figures 5.9 – 5.12 are also estimated values. Due to the correction procedures described above sometimes large uncertainties are introduced. According to Eq. 5.3 the value of the gain is determined from four numbers: the peak values of signal S_s^f and the control signal S_c^f measured when the chamber is filled with the laser gas mixture but no discharge is ignited and the peak values of the signal S_s^d and the control signal S_c^d measured during the discharge.

It was estimated that the signal S_s^f and the control S_c^f waveforms were also disturbed by thermal and shot noise with a signal to noise ratio of $\sim 10^2 – 10^3$. Thus the noise influence could be neglected compared to the actual fluctuation of the S_s^f/S_c^f ratio itself, which has been measured to be ~ 5 %. The origin of the fluctuation of this signal ratio is not clear but it is supposed that it is connected to the splitting of the initial laser beam into two parts by a semi-transparent mirror, probably due to non-ideal mirror coating and fluctuation of the laser beam polarization and distribution of the power density in the laser beam. Thus $<S_s^f/S_c^f>$ has been measured with a precision of ~ 5 %.

The influence of thermal and shot noise on the measured signal S_s^d and control S_c^d waveforms was also negligible due to the signal to noise ratio of $\sim 10^2 – 10^3$. However, the mini-Marx generator and the discharge produced electro-magnetic signals, which also affected the measured waveforms. The control photo-diode was placed much further from the discharge chamber and mini-Marx generator than the signal photo-diode. The last one had also less capacitance than the control photo-diode. As a result, the electro-magnetic interference on the control waveform S_c^d was much less than on the signal waveform S_s^d and was actually neglected. The electro-magnetic interference pattern from the signal diode was removed very efficiently from the measured signal by the procedure described above and given by Eq. 5.5. An additional

error source in the determination of the S_s^d amplitude was introduced by the removal of the background spontaneous emission signal, given by Eq. 5.5. In all measurements the amplitude of the emission signal was comparable or less than the amplitude of the photo-diode response signal of the probe laser pulse. The scaling factor *f* was determined for every waveform with a precision of ~ 5 %. If the scaling factor f differed from the best fit value by ~ 5 % or more, the difference between $S_{rn}(t) + f\ S_{ses}(t)$ and $S_s(t)$ was clearly visible and the corrected waveform $S_{cs}(t)$ was definitely concave (wings upwards) or convex (wings downwards) instead of being flat before and after the part of the signal corresponding to the response of the photo-diode to the probe pulse. Thus the background removal procedure given by Eq. 5.5 was found to introduce an error of ~ 5 % or less on the actual value of S_s^d.

The fluctuations of the discharge current and voltage resulted necessarily in fluctuations of the power deposition. The fluctuations of the power deposition on its turn led to fluctuations of the spontaneous emission intensity which was originated by fluctuations in the number of excited ArF^* molecules. Thus the amplification of the probe beam also fluctuated with the power deposition. Additionally the S_s^d/S_c^d ratio was observed to fluctuate due to the splitting of the initial probe laser beam in the same way as the S_s^v/S_c^v and the S_s^f/S_c^f ratios did. All the above mentioned factors resulted in a fluctuation of the S_s^d/S_c^d ratio of ~ 10 – 15 %. So the average $<(S_c^d/S_r^d)/< S_c^f/S_r^f>>$ ratio was determined with a precision of ~ 15 % (relative error was 0.15).

For the estimation of the coefficients for absorption, gain and peak gain over the beam path length contain a logarithmic function is used as can be seen in Eqs. 5.1 – 5.3. The logarithmic function in these equations increases the relative error as can be seen in the following way. If a value *b* is measured or calculated with an absolute error δb, the relative error is $\varepsilon_b = \delta b/b$. The logarithm of $b \pm \delta b$ is (for $\varepsilon_b << 1$):

$$\begin{aligned} \ln(b \pm \delta b) &= \ln(b(1 \pm \varepsilon_b)) = \ln(b) \pm \ln(1 \pm \varepsilon_b) \\ &\approx \ln(b) \pm \varepsilon_b \end{aligned} \tag{5.6}$$

In our case the logarithm of a value for *b* which was close to 1, with a relative error of ~ 0.15, had to be calculated. Thus the value of the logarithm was close to zero and was comparable to the relative error. It will be clear that due to this approach the error bars in figures 5.9 – 5.12 are large.

5.5 Discussion of the results

5.5.1 Discussion of the spontaneous emission measurements

In sub-section 5.3.1 the results of our spontaneous emission measurements are presented. In order to be able to explain the observed dependency of the spontaneous emission (and later on the laser gain) on the charging voltage and gas composition, the origin of the spontaneous emission will be discussed.

For both the spontaneous emission and laser gain measurements a LC-193 BP 20 band pass filter centered around 193 nm was used in front of the detectors. This filter has a transmission bandwidth of ~ 20 nm with the maximum transmittance of 23 % at a wavelength of 193 nm. So all the measured signals are originating from radiation at a wavelength of 193 nm

emitted by ArF^* excimer molecules. No spontaneous emission was observed if either Ar or F_2 were absent in the gas mixture.

The intensity of the spontaneous emission and of the laser gain are proportional to the concentration of excimer molecules (ArF^*). This is because the lower state of this excimer molecule is repulsive, the transition is bound-free and the spontaneous lifetime of the excited molecule is very short, namely in the order of 10 ns. In order to derive the rate equations for the excimer molecule density, and for the spontaneous and the stimulated emission, we need to consider the formation kinetics of the excimer molecules.

The ArF^* excimer molecule can be formed by three different processes [1, 2]: a "harpooning" reaction between an excited argon atom Ar^* and molecular fluorine F_2; the ionic recombination process between Ar^+ and F^- in presence of a third partner mostly a rare gas atom (He, Ne or Ar in our case, usually called the buffer gas) or between the molecular ion $Ar_2^+$and F^-. All excited or ionic species can be formed in the gas discharge.

The contributions of these three processes are different. The "harpooning" process is believed to be the most important in the electrical gas discharge while the last process is the least important [3]. It is reported in reference 4 that the "harpooning" process is found to be the dominant channel for the ArF^* formation process in the early stages of the discharge and that the second process becomes more important later on in the discharge.

Atoms in excited states like Ar^*, Ne^* and He^* are produced by collisions of electrons and atoms. In a gas discharge ions like He^+, Ne^+ and Ar^+ are mostly formed by step-wise ionization via the excited states He^*, Ne^* and Ar^* and to a lesser extent by direct ionization. This because in a gas discharge only a small fraction of the electrons are in the high energy tail of the electron energy distribution function and only these electrons contribute to the direct ionization channel. Molecular ions like Ar_2^+ as well as Ne_2^+ and He_2^+ are formed in several ways: via an atomic ion in a three-body collision or from an excited diatomic rare gas molecule (Ar_2^*, Ne_2^*, He_2^*; produced from excited atoms in three-body collisions) by a photo-ionization process.

The formation of negative fluorine ions F^- can proceed in two ways: dissociative attachment of electrons to fluorine molecules F_2 and dissociation of vibrationally excited fluorine molecules F_2^*.

Excited ArF^* molecules decay to the unbound ground state with a spontaneous emission lifetime τ of ~ 4.2 ns [1], thereby emitting photons with a wavelength of 193 nm. In presence of a high photon flux at the same wavelength of ~ 193 nm, for example, in case of strong spontaneous emission or a probe laser beam, or inside the laser cavity stimulated emission occurs. The cross-section σ_{se} for this stimulated emission process is ~ 2.7 10^{-16} cm^2 [1].

Apart from decaying by emitting photons excited ArF^* molecules are also quenched in different collisions processes, for instance with electrons, fluorine molecules and rare gas atoms, resulting in a non-radiative decay. The most effective quenching mechanisms are by electrons and by F_2 [5].

Once generated, the 193 nm photons can be absorbed in the discharge medium by negative atomic fluorine ions F^-; by excited rare gas atoms like Ar^*, Ne^* and He^* (photo-ionization), as well as by dimer or trimer molecules also formed in the discharge like Ar_2^*, Ne_2^*, He_2^*, F_2 or Ar_2F^* [3 – 5]. Additionally, trace impurities of organic molecules and O_2 (the Schumann-Runge bands) strongly absorb 193 nm photons [6].

Since the lower level is repulsive or unbound, it can be excluded from the kinetic equation for the upper level, in absence of a strong radiation field (see chapter 1, sect. 1.2):

$$\frac{dN}{dt} = P_{ul}(t) - \frac{N}{\tau_r} - \frac{N}{\tau_{nr}} \equiv P_{ul}(t) - \frac{N}{\tau_d} \tag{5.7}$$

where N is the population of the upper level, $P_{ul}(t)$ is the production rate of the upper level, τ_r is the radiative lifetime, τ_{nr} is the non-radiative lifetime and τ_d is the efficient lifetime of the upper level due to radiative decay and quenching. The production rate strongly depends on the gas mixture composition, gas pressure (especially for three-body collisions), the pumping power density and the electron temperature in the discharge. It is obvious that the production rate increases with the pumping power density as more excited and ionic species are formed. The non-radiative lifetime also depends strongly on the gas mixture composition, gas pressure, the pumping power density and the electron temperature in the discharge. At high gas pressures and high power deposition the non-radiative lifetime can be even shorter than radiative lifetime, since the non-radiative lifetime is determined by ion – neutral collisions rate, which increases with the gas pressure [1, 2].

If the production rate changes slowly compared to the effective lifetime of the upper level τ_d, the upper level population follows the production rate:

$$N(t) = P_{ul}(t)\,\tau_d \tag{5.8}$$

The spontaneous emission intensity is determined by the upper level population divided by the radiative lifetime:

$$S(t) \propto \frac{N(t)}{\tau_r} \equiv P_{ul}(t)\frac{\tau_d}{\tau_r} \tag{5.9}$$

Eq. 5.9 gives the photon emission probability. Absorption of photons in the gas mixture is not included in Eq. 5.9. The absorption probability however, is proportional to the density of the absorbing species, the absorption cross-section and the photon flux which is proportional to $S(t)$. Therefore, the observed spontaneous emission intensity should be proportional to the instant pumping rate and the ratio of the effective and radiative lifetimes of the upper level.

As could be seen in figure 5.4 the spontaneous emission signal appeared just after the ignition of the discharge and increased with the power deposition. The peak value of the spontaneous emission was observed when the power deposition reached the maximum value. However, later in the discharge the spontaneous emission decreased faster than the power deposition, resulting in a FWHM pulse width of ~ 50 for the spontaneous emission and ~ 100 ns for the power deposition respectively. So the relation of the production rate $P_{ul}(t)$ to the power deposition density is not straightforward and requires a complex numerical kinetic model.

In our experiments the steady-state voltage of the discharge in the constricted self-sustained form was observed to be the same regardless of the charging voltage and the total discharge current. The discharge cross-section was linearly proportional to the total current and positive column current density was constant. Therefore the power deposition density was

constant, while the discharge volume increased with the total discharge current and power deposition (see figure 5.5 for each specific gas mixture).

On the other hand, the production rate depends strongly on the gas mixture composition. For example, the peak power density P/V deposited into a discharge in a He : Ar : F_2 / 94.9 : 5 : 0.1 gas mixture at a total pressure of 2 bar was ~ 2 times higher than in a Ne : Ar : He : F_2 / 93 : 5 : 1.9 : 0.1 gas mixture, although the spontaneous emission output per cubic cm was the same in both cases (see figure 5.10). We assume that this phenomenon is due to differences in the rate constants or cross-sections of the various processes. For instance, one of the processes is the Penning ionization of Ar atoms in collisions with excited metastable He^* and Ne^* atoms, leading to formation of Ar^+ ions. The cross-section of the Penning ionization is proportional to $T_g^{-1/2}$, where T_g is the gas temperature. The cross-section of the He^* + Ar Penning ionization process is ~ 1.53 times lower than the Ne^* + Ar process at the same gas temperature [7]. On the other hand the power deposition density was higher in the He based mixtures than in Ne based mixtures and therefore the gas temperature is higher in the He based mixtures compared to the Ne based mixtures. As a consequence the Penning ionization cross-section is even more than 1.53 times lower in mixtures with He as buffer gas compared to mixtures with Ne as buffer gas. Although Penning ionization is not the dominant Ar^+ formation channel, it may be an important mechanism for the Ar^+ production [8].

In our experiments the spontaneous emission was measured within a narrow solid angle of ~ 6.7 10^{-3} srad. The discharge width of less or equal to 1 cm and the discharge gap of 1 cm are small compared to the distance from the discharge to the photo-diode, which was varied in different experiments from ~ 13 to ~ 45 cm. Therefore in our calculations of the spontaneous emission intensity in terms of kW $srad^{-1}$ from the measured signal in mV the discharge is assumed to be a point-like source and to emit isotropically in all directions. An equal peak specific emission output of ~ 9.5 kW $srad^{-1}$ cm^{-3} was measured from discharges in He : Ar : F_2 / 94.9 : 5 : 0.1 and Ne : Ar : He : F_2 / 93 : 5 : 1.9 : 0.1 gas mixtures at a total pressure of 2 bar (see figure 5.10). Assuming an isotropic emission the peak spontaneous emission from the discharge was ~ 119 kW cm^{-3} at the wavelength of ~ 193 nm in both cases, while the peak power deposition density was ~ 1 MW cm^{-3} in the Ne based mixture and ~ 1.8 MW cm^{-3} in the He based mixture. So the peak power efficiency was ~ 12 % in the Ne based mixture and ~ 6.6 % in the He based mixture. Taking into account the typical FWHM of the spontaneous emission waveform of ~ 50 – 60 ns and the typical FWHM of the power deposition of ~ 100 ns, the discharge was observed to emit ~ 6 mJ cm^{-3}, while the energy deposition density was ~ 100 mJ cm^{-3} in the Ne based mixture and ~ 180 mJ cm^{-3} in the He based mixture. Therefore, the energy efficiency of the spontaneous emission was ~ 6 % and ~ 3.3 % respectively.

5.5.2 Discussion of the laser gain measurements

In order to explain the observed dependence of the laser gain on the charging voltage and the gas composition, a term describing the stimulated emission has to be included into Eq. 5.7. The population density N of the upper level in this case is governed by the following equation:

$$\frac{dN}{dt} = P_{ul}(t) - \frac{N}{\tau_d} - c\rho\sigma_{se}N \qquad (5.10)$$

where c is the speed of light, ρ is the photon density, $\sigma_{se} = 2.7\ 10^{-16}$ cm^2 is the cross-section for stimulated emission. The effective lifetime of the upper level τ_d is composed of the radiative lifetime due to spontaneous emission (for ArF^*: $\tau_r = 4.2$ ns) and the non-radiative life time due to quenching of the upper level τ_{nr}. According to reference 5 the most important quenching mechanisms are due to collisions of F_2 and electrons with ArF^*. The F_2 density is ~ 5 10^{16} cm^{-3} in mixtures containing 0.1 % of F_2 at a total gas pressure of 2 bar. The electron density in our experiments is estimated to be ~ 10^{14} – 10^{15} in the positive column of the discharge, according to the positive column current density, discharge steady state voltage and electron drift velocities in different gases. The estimated electron density is the same as the value predicted in discharge modeling ~ 10^{14} – 10^{15} [4, 9 – 11] calculated for similar gas mixtures, with the same electric field strength in the positive column and same specific power deposition density. Rate constants of 2.4 10^{-9} cm^3 s^1 for the quenching of ArF^* by F_2 and of 2 10^{-7} cm^3 s^{-1} for the quenching by electrons are taken from reference 12. The estimated non-radiative life time is ~ 8 ns for the F_2 channel and ~ 1 – 10 ns for the electron quenching channel. Therefore, the effective upper level lifetime is:

$$\tau_d = \frac{\tau_r \tau_{nr}}{\tau_r + \tau_{nr}} < \min(\tau_r, \tau_{nr}), \tag{5.11}$$

which is less than minimum of radiative and non-radiative decay time.

In our gain experiments the typical probe beam intensity was ~ 14 W cm^{-2} with a pulse duration of 10 ns which means that the spatial length of the laser pulse was ~ 3 m. The 193 nm photon energy is ~ 6.4 eV, thus the average photon density ρ in our experiments was ~ 4.6 10^8 cm^{-3} and the $c\ \rho\ \sigma_{se}$ rate was ~ 3.8 10^3 s^{-1}. The rate of the stimulated emission process is much less than $1/\tau_d$ ~ 10^8 – 10^9 s^{-1}. It means that the probe beam light intensity was much less than the saturation intensity so the probe beam did not destroy the upper level population significantly. The upper level population density was described by Eq. 5.9. Therefore, the measured net gain can be treated as a small signal net gain.

The probe beam duration of 10 ns was much shorter than the FWHM of the spontaneous emission waveform of ~ 50 – 60 ns and the FWHM of the power deposition of ~ 100 ns. On the other hand the probe beam pulse width was comparable or longer than the effective lifetime of the upper level $\tau_d < 4.2$ ns. Therefore, each part of the 3 m long laser pulse, passing through the discharge with a length of less than of equal to 1 cm at a different time, was amplified in the discharge according to the instant upper level population density, which did not change significantly during the probe pulse propagation due to slowly changing power deposition.

The probe beam amplification in this situation can be described by the usual exponential law:

$$\frac{dI(x)}{dx} = (g - \alpha)\, I(x) \tag{5.12}$$

where I is the light intensity, g is the gain coefficient and α is the absorption coefficient. The gain coefficient is proportional to the cross-section of the spontaneous emission and the upper level population density:

$$g \propto \sigma_{se} N \propto P_{ul} \propto S \tag{5.13}$$

where P_{ul} is the production rate of the upper level (see Eqs. 5.7, 5.8 and 5.10) and S is the spontaneous emission intensity (see Eq. 5.9). Thus the gain depends on the pumping density of the discharge and the gas mixture composition. The absorption coefficient α is determined by all processes leading to the absorption of 193 nm photons, therefore α is:

$$\alpha \propto \sum \sigma_a N_a \,, \tag{5.14}$$

where σ_a and N_a are the cross-section of process a and the absorbing species density involved in this particular process. The absorption coefficient also depends on the pumping power density and the gas mixture composition.

As discussed above, the power deposition density in the constricted self-sustained discharge was constant for the same gas composition, while the discharge cross-section increased proportionally to the total power deposition. Therefore the rates of the different processes did not change with increase of the total power deposition, leading to a constant specific spontaneous emission output in terms of kW srad^{-1} cm^{-3}. In this case the net gain *(g-α)* is expected to be constant. However, the net gain measured in He : Ar : F_2 / 94.9 : 5 : 0.1 and Ne : Ar : He : F_2 / 93 : 5 : 1.9 : 0.1 gas mixtures at a total pressure of 2 bar (figure 5.10) was almost zero at the lowest total power deposition, then increased and became constant and equal to ~ 26 ± 10 % cm^{-1} at high power depositions (see figure 5.9). We believe that this fact is due to the relatively large cross-section of the probe beam. Because of the cylindrical symmetry of the discharge the central part of the probe beam traveled a longer distance inside the discharge than the edge of the beam when the probe beam diameter had a certain width. Thus the central part of the probe beam was amplified more than the part of the edge. If the net gain was higher in the middle of the discharge than at the edge of the discharge, this effect would become even more prominent. Therefore the net amplification of the probe beam was less than the case in which the probe beam had an infinitely narrow aperture and passed through the center of the discharge. On the hand, the net amplification was divided by the full width of the discharge, although only the central part of the probe beam passed this path length inside the discharge. Additionally, the discharge width was small at low total power deposition and in this case even the central part of the probe beam was only slightly amplified. This small net amplification was very difficult to distinguish from the background due to the large experimental errors.

Due to the radial distribution of the discharge it is likely that the power deposition in the middle of the discharge is larger than at the edges and consequently also the gain will show a certain radial dependency in its distribution. On its turn such a radial distribution of the gain will have a strong impact on the way the amplitude of the probe beam is amplified. In order to test this assumption a simple analytical model with different gain distributions was developed. In this model two different assumptions for the radial distribution of the net gain *(g-α)* were used: a rectangular radial distribution:

$$(g(r)-\alpha(r)) = \begin{cases} 0.26 & r \le R_0 \\ 0 & r > R_0 \end{cases} \tag{5.15}$$

and a triangular radial distribution:

$$(g(r)-\alpha(r)) = \begin{cases} 0.52\,\dfrac{R_0 - r}{R_0} & r \le R_0 \\ 0 & r > R_0 \end{cases} \tag{5.16}$$

where R_0 is the width of the active medium in cm, and the net gain is in cm^{-1}. The effective net gain along the diameter was 26 % cm^{-1}. The radial gain distributions (Eqs. 5.15 and 5.26) are given in figure 5.13 (a, b) for R_0 = 10 (1), 5 (2), 2.5 (3) and 1 mm (4).

In the model the x-axis is perpendicular to the discharge gap and the direction of the probe beam propagation. The discharge is scanned along the x-axis in the model. The y-axis is opposite to the beam propagation direction and the z-axis is along the discharge gap. The origin of the axes is in the middle point of the discharge. Any point of the discharge is characterized by a z coordinate and a radial coordinate:

$$r = \sqrt{x^2 + y^2} \tag{5.17}$$

The net gain was assumed to be homogeneous in the z-direction and the light intensity was supposed to be homogeneously distributed over the cross-section of the probe beam.

The net gain profile in % along the x-axis was calculated as:

$$\begin{aligned} G_{\mathrm{inf}}(x) = ((g-\alpha)\,L)_{\mathrm{inf}}(x) &= \int_{-\infty}^{\infty} g(\sqrt{x^2 + y^2})\,dy \\ &= \int_{-\sqrt{R_0^2 - x^2}}^{\sqrt{R_0^2 - x^2}} g(\sqrt{x^2 + y^2})\,dy \end{aligned} \tag{5.18}$$

where $L = R_0$ is the active medium width. The values of R_0 are the same as in figure 5.13 (a, b). The calculated profiles are shown in figure 5.13 (c, d). These profiles correspond to imaginary measurements with an infinitely narrow probe beam.

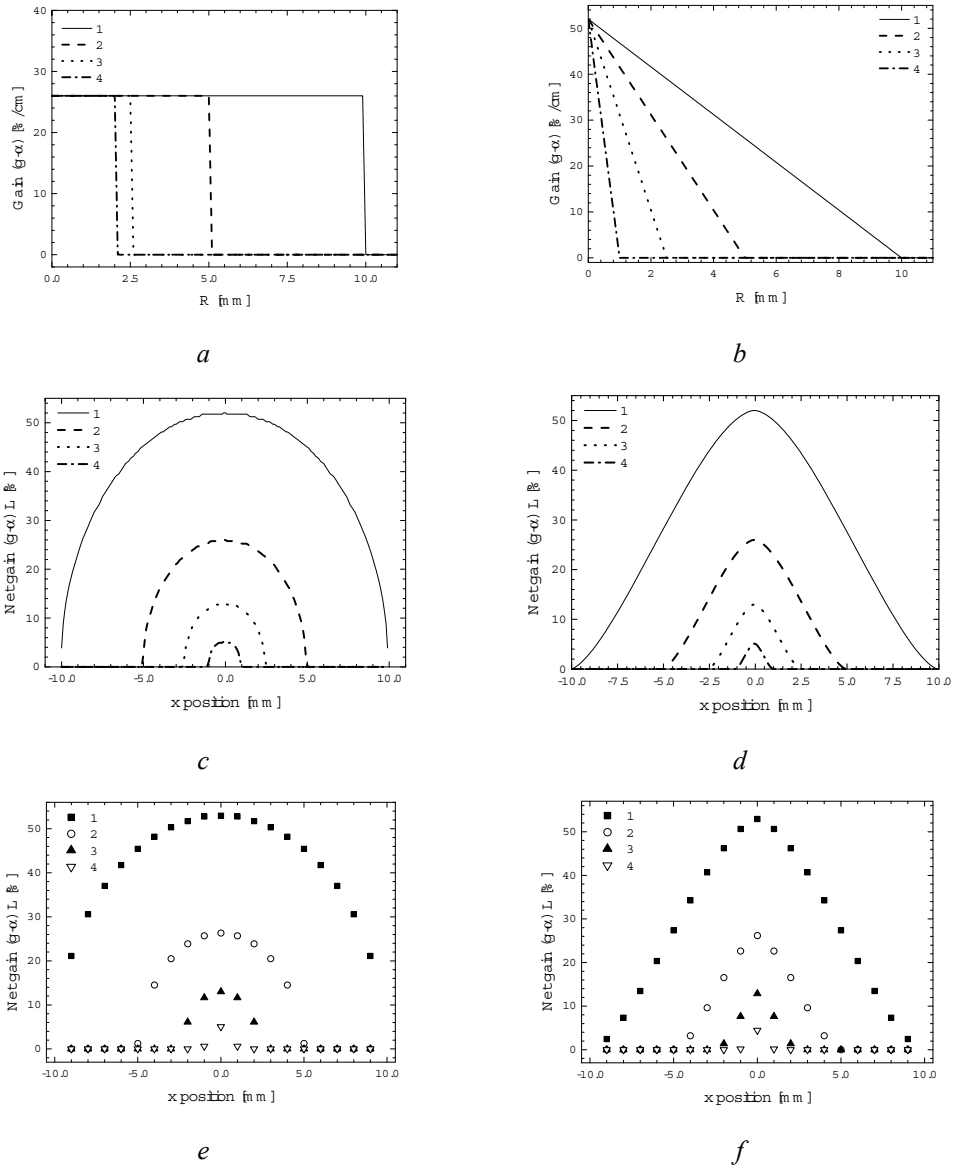

Figure 5.13. Results of the gain profile modeling.
Model radial distribution: a: Rectangular distribution of the gain (g-a) [%/cm].; b: Triangular distribution. Calculated net gain (g-a) L [%] profile for infinitely narrow probe beam. c: Rectangular gain distribution. d: Triangular gain distribution. Calculated net gain (g-a) L [%] profile for a circular probe beam with a diameter 0.8 mm. e: Rectangular gain distribution. f: Triangular gain distribution. In all figures R_0 = 10 (1), 5 (2), 2.5 (3) and 1 mm (4).

In the real spatial net gain profile measurements we used a probe beam with an aperture of 0.8 mm (see section 5.3.4). The calculated net gain in % in this case is:

$$G_{0.8mm}(x) = ((g-\alpha)L)_{0.8mm}(x) = \\ = \frac{4}{\pi d^2} \int_{-\frac{d}{2}}^{\frac{d}{2}} dz * \int_{-\sqrt{d^2/4 - z^2}}^{\sqrt{d^2/4 - z^2}} G_{\inf}(x+w)\,dw \tag{5.19}$$

where d = 0.8 mm. The calculated net gain profiles for the triangular and the rectangular distribution are given in figure 5.13 (e, f). Values of R_0 are the same as in figure 5.13 (a, b). All calculations were performed with a 1 mm step in the x-direction. It is seen that an aperture of 0.8 mm in diameter is sufficiently narrow to introduce no distortion in the measured profile due to its finite diameter.

In the peak net gain and temporal gain profile measurements (see section 5.3.2 and 5.3.3) the probe beam cross-section was 3 mm in the x-direction and 6 mm in the z-direction defined by the probe laser design. The calculated net gain in % in this case is:

$$G_{3mm} = ((g-\alpha)L)_{3mm} = \frac{1}{D} \int_{-\frac{D}{2}}^{\frac{D}{2}} G_{\inf}(x,z)\,dx \tag{5.20}$$

where D = 3 mm. The net gain in % was calculated for the triangular and the rectangular radial distributions and with R_0 = 10, 5, 2.5 and 1 mm (4).

The calculated net gain in % was divided by the length of the discharge (2 R_0) to calculate net gain in % cm^{-1}. The results are shown in figure 5.14. It can be seen that for R_0 = 1 and 2.5 mm the specific net gain calculated according to Eq. 5.20 is much less then the actual effective gain of 26 % cm^{-1} in the model. For R_0 = 5 and 10 mm the results are close to the expected value of 26 % cm^{-1}. These results explain the data presented in figure 5.10. At low total power deposition the discharge width is comparable to the probe beam width and the measured specific gain is lower, compared to the case when the total power deposition is higher and the discharge is wider. In case of a triangular radial gain distribution (2) the gain is higher in the middle of the discharge than at the edge, and the influence of the probe beam width becomes more prominent.

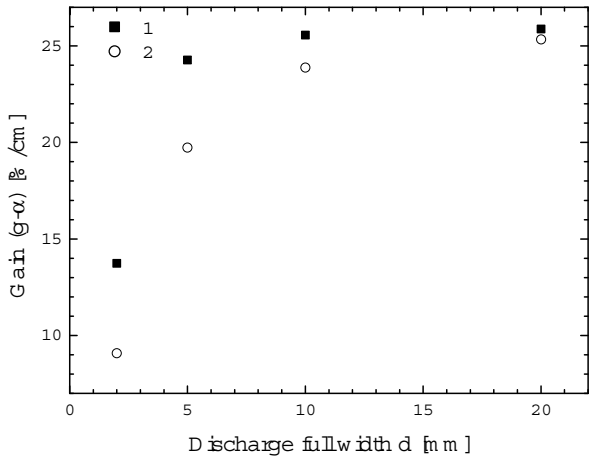

Figure 5.14. Dependence of the calculated gain, as if it was measured by a probe beam with a rectangular aperture of 3 x 6 mm^2, on the discharge full width d = 2 R_0. The radial gain distribution was rectangular (1) and triangular (2). The effective gain along the discharge diameter was 26 % cm^{-1}.

In order to determine the net gain taking into account the finite width of the discharge and the probe beam, the results of the model were applied to the measured spatial net gain profile as shown in figure 5.12. Due to the linearity of Eqs. 5.18 and 5.19 the numerical coefficients 0.26 and 0.52 in Eqs. 5.15 and 5.16 corresponding to an effective specific net gain of 26 % cm^{-1} could be taken out from the integrals. Therefore the net gain in Eq. 5.19 scaled linearly with the effective specific net gain. The discharge width determined from the discharge current and positive column current density for the conditions mentioned in figure 5.12 was 7 ± 2 mm, although the measured full width of the gain profile was estimated to be 5 mm (see Fig. 5.12). Thus R_0 was taken to be 2.5 mm to fit the full width of the gain profile, while the numerical coefficients were taken to be 0.34 for the rectangular distribution (Eq. 5.15) and 0.68 for the triangular distribution (Eq. 5.16) in order to fit the maximum value of the measured gain ~ 17 % at x = 0 (see Fig. 5.12). The measured data (1) and the calculated profiles for a rectangular (2) and a triangular gain distribution (3) are shown in figure 5.15. The calculated profile for the triangular distribution $g_t(x)$ (2) fits the measured values almost perfectly except for two points. The calculated profile for the rectangular distribution $g_r(x)$ (3) overestimated most of the actual data. The best fit was determined as a linear composition of $g_t(x)$ and $g_r(x)$:

$$g_f(x) = \delta\, g_r(x) + (1-\delta)\, g_t(x) \tag{5.21}$$

where $0 < \delta < 1$. The least deviation (RMS) of the fitted profile is obtained at $\delta = 0.55$. This best fitted profile is shown in figure 5.15 (4).

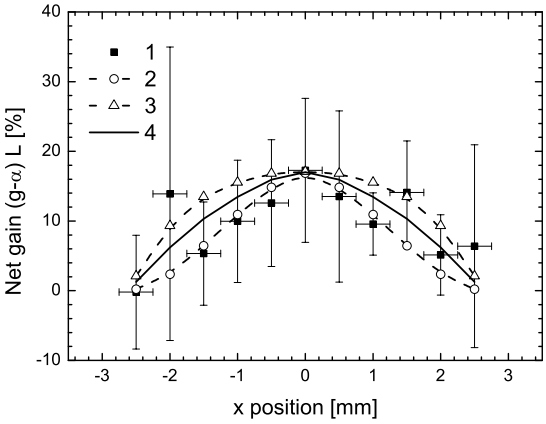

Figure 5.15. Measured spatial profile of the net gain (g-a) L (1) and the calculated profiles for a triangular $g_t(r)$ (2) and rectangular radial gain distribution $g_R(r)$ (3). Curve (4) shows the best fit with the least RMS as a linear composition 0.55 $g_r(r)$+0.45 $g_t(r)$. In the model the radius R_0 was 2.5 mm and the effective gain along the discharge diameter 34 % cm^{-1}.

The radial net gain distribution corresponding to the best fit of the measured points (Eq. 5.21) is shown in figure 5.16. It was mentioned before that for the calculations presented in this figure an effective specific net gain is along the discharge diameter of 34 % cm^{-1} and a radius R_0 of 2.5 mm have been used.

From this figure it can be concluded that a value of 34 ± 20 % cm^{-1} determined from our spatial net gain profile analysis is closer to reality than the value of 26 ± 14 % cm^{-1} estimated from the discharge width as presented in figure 5.10. It follows directly from the non-uniformly distributed spatial gain over the discharge cross-section.

Our estimated value for the small signal gain in ArF* laser gas mixtures is much larger than the small-signal gain values reported in theoretical papers [1, 13] and also much larger than experimentally estimated values reported in [14]. In reference [1] a 4 bar mixture of 4.9 % Ar and 0.1 % F_2 diluted in Ne and in He was evaluated in a numerical model. In a He based mixture it was reported that the small-signal gain g_0 increased from ~ 7 to ~ 12 % cm^{-1} for an increase pumping power density from 5 to 11 MW cm^{-3}. At the same time the absorption α_0 increased from ~ 1.5 to ~ 2.5 % cm^{-1}. The resulting net small-signal gain in a He based ArF* laser gas mixture was ~ 6 – 10 % cm^{-1}. In the Ne based mixture g_0 was ~ 6 % cm^{-1} and α_0 was ~ 1 % cm^{-1} at a pumping power density from 2.5 to 4 MW cm^{-3}. Thus in the Ne based mixture ($g_0 - \alpha_0$) was ~ 5 % cm^{-1} according to [1]. In reference [13] values for g_0 = 3.5 % cm^{-1} and α_0 = 0.2 % cm^{-1} were calculated from experimental data obtained in a He : Ar : F_2 / 90.6 : 9.2 : 0.17 gas mixture at a total pressure of 2 bar. On the other hand a small-signal net gain of 17 % cm^{-1} was measured in reference [14] in a commercially available discharge pumped ArF* laser (Lambda Physik EMG-101). We believe that the reasons for so high laser gain value are high power deposition density (~ 1 MW cm^{-3} bar^{-1}) into the gas discharge volume and higher average electron energy in the single pulse discharge, compared to double pulse discharges, which is preferable for production of the excited atoms (especially for Rydberg states) and ions in the gas discharge. In fact, in the

double pulse excitation scheme the pre-pulse creates a cloud of low energy electrons, which is then pumped by the main pulse with relatively low electric field strength, determined by the conductivity of the plasma. In the single pulse excitation scheme the initial conductivity of the plasma created by X-ray preionization pulse is low, and the applied electric field is stronger, at least in the initial stage of the discharge. Thus, the electron energy distribution function is shifted towards higher electron energy region.

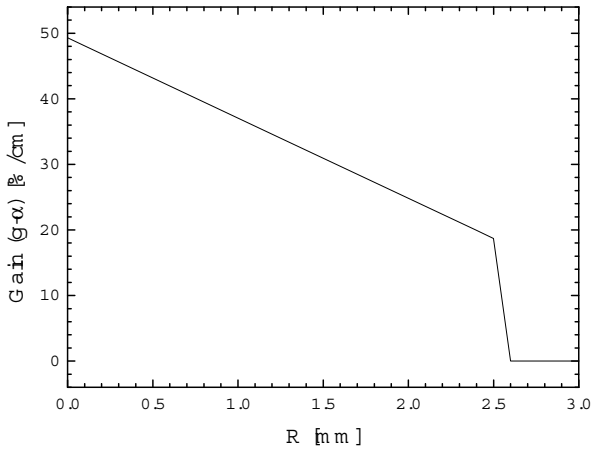

Figure 5.16. Radial gain distribution of the best fit in figure 5.15 (4) for the measured spatial gain distribution with R_0 = 2.5 mm and effective gain along the discharge diameter 34 % cm^{-1}.

5.6 Conclusion

A single pulse gas discharge excitation scheme in combination with an X-ray preionization source, described in chapter 4, has been proven to be a very effective pumping system for ArF^* excimer laser gas mixtures. This compact system appeared to be a powerful UV radiation source. The system was capable to ignite and maintain stable homogeneous glow discharges in fluorine – rare gases mixtures at a total pressure of ~ 2 bar with a FWHM of ~ 100 ns, a peak specific power deposition of ~ 1 MW cm^{-3} bar^{-1} and a specific energy deposition of ~ 100 mJ cm^{-3} bar^{-1}. The excitation system also provided reasonably long duration and high output spontaneous emission pulses from the discharge. Furthermore an extremely high laser signal gain over a time interval comparable to the duration of the spontaneous emission pulse was measured.

The spontaneous emission and small-signal net gain in constricted self-sustained discharges were measured at a wavelength of 193 nm in two different ArF^* laser gas mixtures, one with He and one with Ne as buffer gas, under the same excitation conditions. The spontaneous emission signal was observed simultaneously with the discharge; it was found to reach a peak value at the same time as the maximal power deposition into the discharge, and then to drop faster than the power deposition, resulting in a FWHM of ~ 50 – 60 ns. In the two above mentioned mixtures at the total pressure of 2 bar the same spontaneous emission power of ~ 119 kW cm^{-3} and the same energy of ~ 6 mJ cm^{-3} were measured. The efficiency determined as the

ratio of the peak emission power to the peak power deposition density was ~ 12 % in the Ne based mixture and ~ 6.6 % in the He based mixture. The efficiency determined as the ratio of the emission energy to the deposited energy density was ~ 6 % and 3 % respectively.

From the gain measurements we observed that the temporal profile of the net gain followed the spontaneous emission waveform. The peak net small-signal gain coefficient was determined from the measured amplification of a probe laser pulse (λ = 193 nm) with a duration of ~ 10 ns. The width of the active medium was determined in two ways: from the measured discharge current and the positive column current density which was estimated from the measured width of the visible discharge glow at different currents, and from the full width of the spatial gain profile. In both mixtures a peak net small-signal gain ($g - \alpha$) = 26 ± 14 % cm^{-1} was found using the first method. For ($g - \alpha$) a value of 34 ± 20 cm^{-1} was measured in the He based mixture by using the second method which was closer to the reality according to our spatial net gain profile analysis.

Finally we concluded that the measured net small-signal gain in F_2 based excimer laser gas mixtures, normally used in ArF^* lasers, was much higher than all values reported earlier in the literature. The UV source, described in this thesis and based on a single pulse gas discharge excitation circuit combined with an X-ray preionization source, is a very attractive approach for the construction of a short cavity excimer ArF^* laser due to its high gain. In such a system the moderate pulse length of the discharge and spontaneous emission is compensated by the short round-trip time of the light pulse inside the cavity, resulting in a better laser beam quality compared to long cavity configurations working with the same discharge duration.

References:

[1] M. Ohwa and M. Obara, J. Appl. Phys., **63**, 1306 (1988)
[2] H.M.J. Bastiaens, PhD thesis, Univ. of Twente, The Netherlands, ISBN 90-365-141-69 (2000)
[3] S. Nagai, M. Sakai, H. Furuhashi, A. Kono, T. Goto and Y. Uchida, IEEE J. Quant. Electr., **34**, 40 (1998)
[4] H. Akashi, Y. Sakai and H. Tagashira, J. Phys. D: Appl. Phys., **27**, 1097 (1994)
[5] A.M. Boichenko, V.I. Derzhiev, A.G. Zhidkov and S.I. Yakovlenko, Sov. J. Quant. Electr., **22**, 444 (1992)
[6] Yu.A. Kudryavtsev and N.P. Kuzmina, Appl. Phys., **13**, 107 (1977)
[7] K.A. Temelkov, N.K. Vuchkov and N.V. Sabotin, J. Phys.: Conference Series, **44**, 116 (2006)
[8] Yu.P. Raizer, *Gas Discharge Physics*, Springer, London (1992)
[9] H. Akashi, Y. Sakai and H. Tagashira, J. Phys. D: Appl. Phys., **28**, 445 (1995)
[10] D. Lo, A.I. Shchedrin and A.V. Ryabtsev, J. Phys. D: Appl. Phys., **29**, 43 (1996)
[11] A.V. Demyanov, L. Feenstra, P.J.M. Peters, A.P. Napartovich and W.J. Witteman, Appl. Phys., B **72**, 823 (2001)
[12] A. Mandl, J. Appl. Phys., **59**, 1435 (1986)
[13] S. Watanabe, A. Obara, T. Sato and H. Kashiwagi, Appl. Phys. Lett., **35**, 365 (1979)
[14] K. Mossavi, Th. Hofmann, G. Szabo and F.K. Tittel, Optics Letters, **18**, 435 (1993)

Conclusion

In the frame of the present work we have designed and build the X-ray preionization source, based on the wired vacuum corona plasma cathode, and the discharge chamber and the single pulse discharge excitation unit.

The X-ray preionization source generates photons with the energy up to ~ 100 keV, while the major part of the photons is believed to be attributed to the K_α-line of Ta (~ 56 keV). This X-ray source produces ~ 1 mrad per shot dose inside the discharge chamber, which leads to the specific electron preionization density of ~ 10^7 cm^{-3} bar^{-1} in all investigated rare gases and rare gas – halogen mixtures.

The single pulse forming network (PFN) in conjunction with the discharge has been observed to operate like LC-contour due to inductance of the PFN, connection cables, discharge chamber and the discharge itself, although no inductor has been incorporated in the scheme and the setup has been designed to minimize the residual inductance. The LC-contour (PFN in conjunction with the discharge) determines the discharge FWHM (typically ~ 120 ns by current and ~ 100 ns by power deposition) and limits the discharge current (typically from ~ 50 to ~ 500 A depending on the applied voltage and the gas composition). The current limitation, in fact, stabilizes the discharge and suppresses the discharge instability formation due to LC-contour acting like high impedance resistor. With help of the designed single pulse discharge excitation scheme the power deposition density of ~ 1 MW cm^{-3} in Ne : Ar : He : F_2 and of ~ 1.8 MW cm^{-3} in He : Ar : F_2 gas mixtures at the total pressure of 2 bar has been obtained for the period of ~ 100 ns in the form of uniform, stable gas discharge. The typical Ar concentration of 5 % and F_2 concentration of 0.1 % have been used in our experiments.

With help of this excitation scheme the spontaneous emission from the discharge in helium / neon – argon - fluorine mixtures at the wavelength of 193 nm (ArF^* excimer line) has been observed at the level of up to ~ 7 kW srad, depending on the applied voltage. The discharge has been ignited in the dense form with diameter less or equal to ~ 1 cm, depending on the applied voltage, and the gas gap length of 1 cm. The ratio of the total irradiated power to the discharge volume has been found to be constant and equal to ~ 119 kW cm^{-3} for both investigated gas mixtures. The typical FWHM of the spontaneous emission has been ~ 50 – 60 ns, resulting in the irradiated energy to the discharge volume ratio of ~ 6 mJ cm^{-3}.

Under the conditions discussed the small signal laser gain of the record-high value of ~ 35±20 % cm^{-1} has been measured with the FWHM ~ 50 -60 ns. Due to high gain value and reasonably long gain duration achieved the designed and investigated single pulse excitation scheme can be of interest for pumping short optical path (few cm) excimer lasers, especially fluorine based excimer lasers. Short length of the laser cavity in conjunction with reasonably long optical pulse (~ 50 ns) can provide higher number of round-trips of the beam inside the resonator and build-up of the resonator modes, resulting in the better optical quality (focusability, coherence, etc.) of the output laser beam.

The present work has also two major side-outcomes: we have discovered the influence of the X-ray photo-effect at the discharge cathode, which the radiation penetrates through, on the

electron preionization density; and we have designed the soft X-ray (~ 5 keV) source, based on the X-ray generation in either gases or solid target (Al foil) by means of fast electrons beam (~ 10 keV) generated in the open barrier discharge at moderate gas pressure (~ 10 – 100 mbar).

The X-ray photo-effect takes place in the thin (few μm) surface layer of the cathode, where X-ray photons are absorbed and fast free electrons (~ 50 - 100 keV) are produced. These free electrons penetrate into the gas volume and cause ionization of the gas volume. Since their average energy is less than but comparable to the initial X-ray photon energy (~ 50 – 100 keV) but electrons interact with the gas medium much more efficiently than the X-ray photons, they produce significant amount of the electron – ion pairs. This effect is more prominent in low Z gases (like He) than in higher Z gases (like Ar). According to our calculation electron preionization density produced by the photo-electrons in Ar at $p\,d \sim 2$ bar cm is comparable to the electron density produced by direct X-ray absorption. In He the photo-effect even overcome the direct X-ray absorption, as follows from our calculations. Due to this the electron preionization density is significantly higher than predicted from the X-ray absorption theory, especially in the case of low Z gases (He, Ne). Therefore the X-ray photo-effect is in favour for gas volume preionization, since it increases the produced electron density. On the other hand, due to this effect the produced electron density n_e (e.g., in terms of electrons per cm^{-3}) and even the specific electron density n_e/p (in terms of electrons per cm^3 per bar) depends on the specific gas gap $p\,d$. On contrary, according to the X-ray absorption theory n_e/p should be independent on the $p\,d$ product (as well as on gas pressure p and gap length d independently) and should be determined only by parameters of the X-ray pulse and the gas composition, as long as X-ray absorption is weak, which is valid for $p\,d < 10$ bar cm typical for our experiments.

The designed soft X-ray source has proven the possibility of X-ray generation directly in the gas medium by deceleration of fast electrons. At the present moment the operating gas pressure is too low (~ 10 – 100 mbar) for incorporation of this source into the excimer laser chamber (typically at few bar gas pressure) without separation window. The X-ray photon energy, on the other hand, is too low (~ 5 keV) to use this source for gas volume preionization through the separation window. However, it has been predicted that with increase of the operation voltage to ~ 100 kV the operation gas pressure could be increased up to atmospheric pressure and the X-ray photons energy is expected to increase to ~ 50 – 100 keV, which is typical for vacuum X-ray sources based on generation of the characteristic X-ray radiation. The huge advantage of the proposed X-ray generation method is that the source operates in gases rather than in vacuum. In vacuum the electric current is limited by the Child-Langmuir law, while under gas discharge conditions the electric current is several orders of magnitude higher at the same voltage applied to the gap, resulting in much higher X-ray photon flux. Therefore, being optimized to higher operation voltage (~ 100 kV) this X-ray source may be of high interest.

Appendix

Dependence of the continuous slow-down approximation (CSDA) range of fast electrons in different matters on the electron energy, mass attenuation and mass energy-absorption coefficient of X-rays in different matter on the photon energy, used in calculations through the thesis, are presented here.

Dependence of the CSDA range of fast electrons on their energy in Al (1), He (2), Ne (3), Ar (4) and Ni (5) is shown in figure A.1. Calculations are performed by the ELSTAR computer code in the NIST database [1], based on [2 – 8].

In figure A.2 dependence of the mass attenuation coefficient of X-ray photons on their energy in He (1), Ne (2), Al (3), Ar (4) and air (5) is given. Data are taken from the NIST database [9] based on the works [10-12].

Dependence of the mass energy-absorption coefficient of X-ray photons on their energy in He (1), Ne (2), Al (3), Ar (4) and air (5) is presented in figure A.3. Data are taken from the NIST database [9] based on the works [10-12].

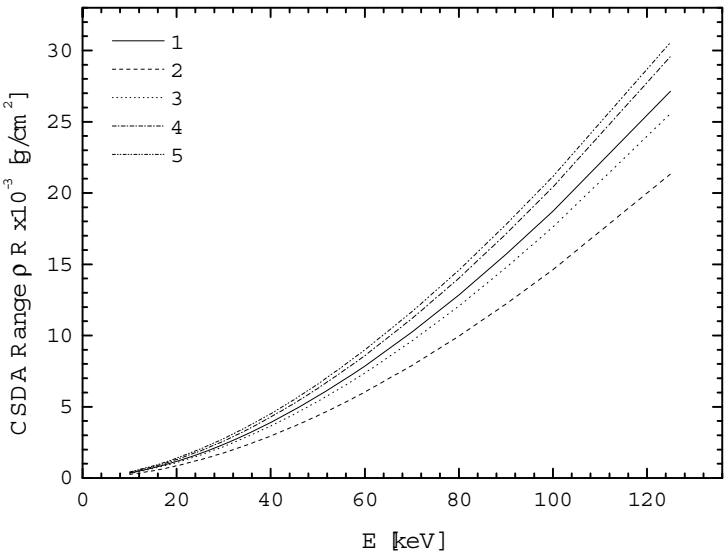

Figure A.1. Continuous slow-down approximation (CSDA) range of electrons in Al (1), He (2), Ne (3), Ar (4) and Ni (5). Data are calculated by ELSTAR code in the NIST database [1]. Calculations are based on the following works [2 – 8].

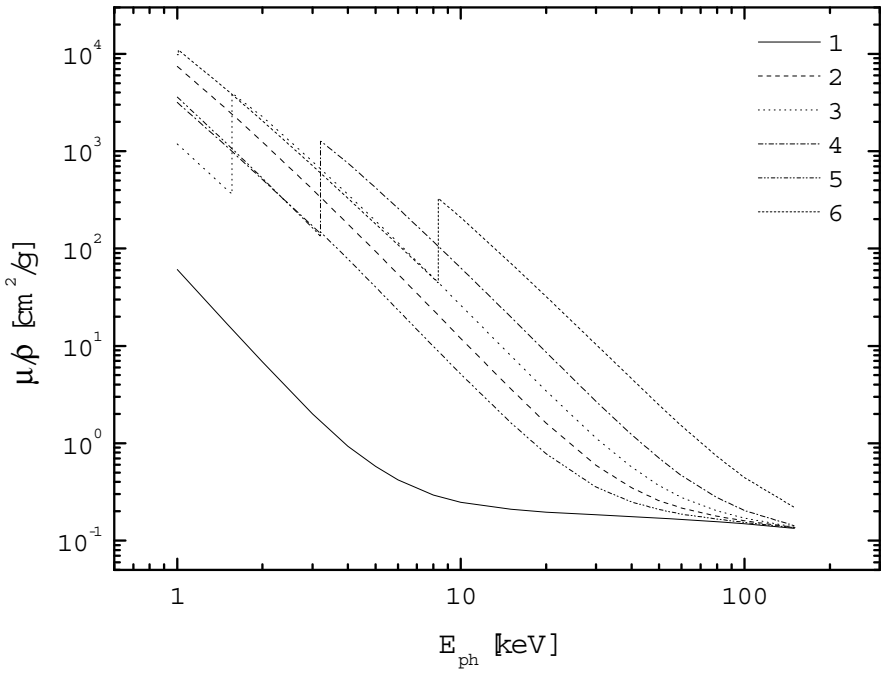

Figure A.2. Mass attenuation coefficients of X-ray photons in He (1), Ne (2), Al (3), Ar (4) and air (5). Data are taken from the NIST database [9] based on the works [10-12].

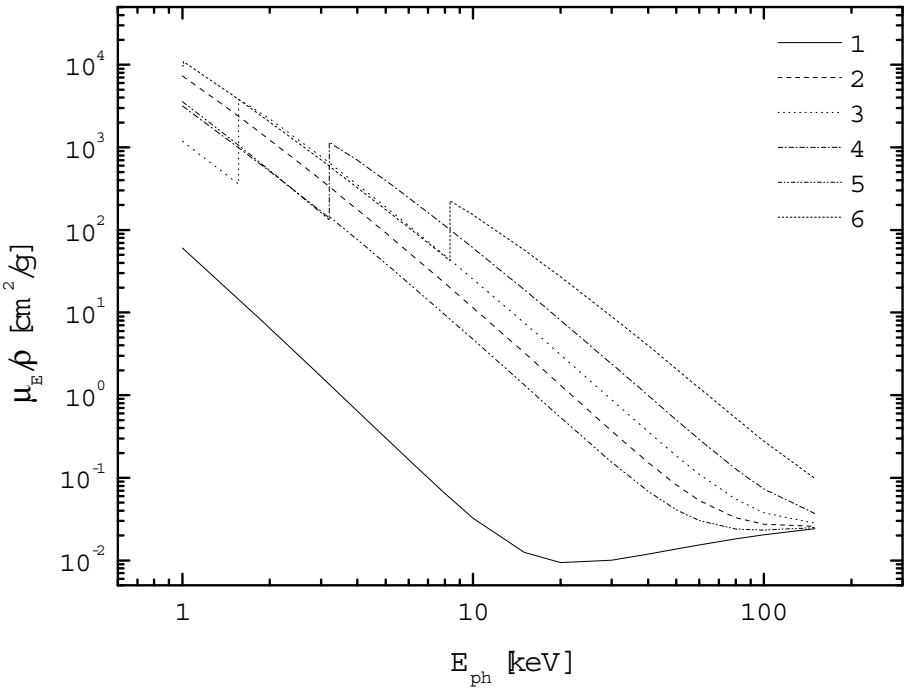

Figure A.3. Mass energy-absorption coefficients of X-ray photons in He (1), Ne (2), Al (3), Ar (4) and air (5). Data are taken from the NIST database [9] based on the works [10-12].

References:

[1] NIST database, ELSTAR, *http://physics.nist.gov/PhysRefData/Star/Text/contents.html*
[2] Bethe H A, Ann. d. Physik **5,** 325 (1930)
[3] Bethe H A, Z. Phys. **76,** 293 (1932)
[4] Sternheimer R M, Phys. Rev. **88,** 851 (1952)
[5] Sternheimer R M, Seltzer S M and Berger M J, Phys. Rev. B **26,** 6067 (1982)
[6] International Commission on Radiation Units and Measurements *ICRU Report 49, Stopping Powers and Ranges for Photons and Alpha Particles* (1993)
[7] Seltzer S M and Berger M J, Nucl. Instr. Meth. B **12,** 95 (1985)
[8] Prarr R H, Tseng H K, Lee C M, Kissel L, MacCallum C and Riley M, Atomic Data Nucl. Data Tables **20,** 175 (1977)
[9] NIST database, Tables of X-Ray Mass Attenuation Coefficients and Mass Energy-Absorption Coefficients, *http://physics.nist.gov/PhysRefData/XrayMassCoef/cover.html*
[10] Seltzer S M, Rad. Res. **136,** 147 (1993)
[11] Hubbell J H, International Journal of Applied Radiation and Isotopes **33,** 1269 (1982)
[12] Seltzer S M and Hubbell J H, *Tables and Graphs of Photon Mass Attenuation Coefficients and Mass Energy – Absorption Coefficients for Photon Energies 1 keV to 20 MeV for Elements Z=1 to 92 and Some Dosimetric Materials*, in: *51st National Meeting of the Japaneese Society of Radiological Technology*, Aplril 14-16, 1995, Nagoya, Japan

Acknowledgements

I am greatly indebted to my promoter, head of the Laser Physics and Non-Linear Optics group Prof. Dr. Klaus Boller for offering me the opportunity of joining the group and for his fruitful discussions and suggestions.

I am especially grateful to my daily scientific supervisor and co-promoter Dr. Peter Peters for his wise guidance. Thank you, Peter, for being always open for discussions and ready to help. I also wish to thank you for your efforts in “fine-tuning” my English in publications, contributions to conferences and in this thesis.

My gratitude as well is to Gerard Oudemeijers, Jacobus Coupers and Ab Nieuwenhuis. Thank you for your help in designing a building my experimental setups, your help cannot be underestimated.

I wish to express my gratitude to Simone ter Hedde-Sloot, who numerous times helped me with administrative and organizational questions.

I thank Dr. Fred van Goor, Dr. Peter van der Slot, Dr. Petra Groß, Dr. Chris Lee, Dr. Marvin Klein and Dr. Ian Lindsay for helpful and fruitful discussion of my results presented during group colloquia. But the most special thanks are to Dr. Bert Bastiaens, who also participated a lot in preparation of experiments and discussion of the preliminary results, and to Dr. Arsen Khachatrryan, who was more than just a colleague. Arsen and his wife Gayana were good friends to me and my family.

To my former colleagues, formerly PhD students and nowadays doctors, Balaji Adhimoolan, Lars Casper, Isabel de la Fuente Valentin, Denny Mathew and Liviu Prodan I am grateful for their friendship and big support. But my most gratitude is to Lars and Denny, who were great friends and colleagues and shared with me not only conferences experience but “a hard day’s night” relaxing afterwards. Our stay in Bad Bentheim and Gmunden will always be in my heart.

Thank you to many other members of LPNO group, you were good colleagues. I apologize for not mentioning all your names here.

I am greatly indebted to head of Control Engineering Group of EWI faculty, Prof. Dr. Ir. J. van Amerongen, who let me join his for the last one and half year and to work on the exciting new project. And my special gratitude is to Prof. Dr. Ir. Paul Regtien, the coordinator of this project. Thank you, Paul, you have provided me with great support and encouragement.

The very special gratefulness is to Dr. Sergey Mitko, who was my supervisor during my University years back in Russia. Sergey, you taught me to be a scientist and researcher, encouraged me to come to the Netherlands, and since then continued to be my wise tutor, colleague, guiding star and friend. I am very grateful as well to Dr. Yuri Udalov, whom I also consider to be my teacher, colleague and friend. Thank you, Yuri, for your help, support and for pointing to my errors and wrong actions. Also thank you, Sergey and Yuri, and thanks to your wives Galina and Elena for your company and guidance not only in science but in life.

I met plenty of new Russian friends in the University of Twente: Elena and Yuri Volokhine, Katya and Denis Deriga, Natasha and Aleksey Kharine, Yulia and Andrey Zinine, Ivan Nikolaev and Nina Demkina. Thank you all, friends, for your friendship and felling of being slightly closer to the motherland.

Special thanks to Dutch friends of mine and my family: Ireen and Adri, Karen and Harm. You showed us new sides of Dutch character and culture, which cannot be found in books for tourists and expatriates.

And I am more than grateful to my family for the patience, understanding, encouragement and inspiration. To my mother Olga Borisovna and father Vladimir Aleksandrovich I am thankful for encouraging me being a scientist, for providing me all the opportunities to study and for their understanding and patience of not seeing me for years. To my sister Katya, my parents-in-law Nadezda Nikolaevna and Valeri Petrovich I am indebted for their support. But most of all to my daughter Daria for being of such joy and inspiration for me, and to my wife Nadia for being of support, for her understanding and her will to follow me wherever I have to go due to my job I pay my gratitude. Daria and Nadia, thank you for being my family. Everything I do, I do for you.

Thank you all!